New techniques of multiple integral field spectroscopy

Ren, Deqing

Ren, Deqing (2001) *New techniques of multiple integral field spectroscopy*, Durham theses, Durham University. Available at Durham E-Theses Online: http://etheses.dur.ac.uk/3800/

New Techniques of multiple integral field spectroscopy

Deqing Ren

M.Sc., B.Sc.

Department of Physics
University of Durham

May 2001

A thesis submitted to the University of Durham
in accordance with the regulation for
admittance to the Degree of Doctor of Philosophy

Abstract

The work of this thesis is to investigate new techniques for Integral Field Spectroscopy (IFS) to make the most efficient use of modern large telescopes. Most of the work described is aimed at the FMOS for the SUBARU 8m telescope. Although this is primarily a system for Multiple Object Spectroscopy (MOS) employing single fibres, there is an option to include a multiple-IFS (MIFS) system. Much of this thesis is therefore aimed at the design and prototyping of critical systems for both the IFS and MOS modes of this instrument.

The basic theory of IFU design is discussed first. Some particular problems are described and their solutions presented. The design of the MIFS system is described together with the construction and testing of a prototype deployable IFU. The assembly of the pickoff/fore-optics, microlens array and fibre bundle and their testing are described in detail. The estimated performance of the complete module is presented together with suggestions for improving the system efficiency which is currently limited by the performance of the microlens array. The prototyping of the MIFS system is supported by an extensive programme of testing of candidate microlens arrays.

Another critical aspect of the instrument is the ability to disconnect the (IFS and MOS) fibre input which is installed on a removable prime focus top-end ring from the spectrographs which are mounted elsewhere on the telescope. This requires high-performance multiple fibre connectors. The designs of connectors for the MOS and IFS modes are described. Results from the testing of a prototype for the MOS mode are presented. This work is supported by a mathematical model of the coupling efficiency which takes into account optical aberrations and alignment errors.

The final critical aspect of FMOS which has been investigated is the design of the spectrographs. The baseline system operates in the near-infrared (NIR) but an additional visible channel is an option. Efficient designs for both the visible and NIR systems are presented. The design of the NIR spectrograph presents challenges in the choice of materials for the doublet and triplet lenses employed. The choice of material and the combinations in which they can be used are described.

This thesis shows that all these critical aspects of FMOS have good solutions that will result in good performance of the whole instrument. For the multiple IFU system, the prototype demonstrates acceptable performance which can be made excellent by the use of a better microlens array. The multiple fibre connector prototype already indicates excellent performance. Finally, the spectrograph designs presented should result in high efficiency and good image quality.

Preface

More than three years have passed since I begun to study for a PhD. In this time, I have learnt a lot from so many people. I studied in a top research group in a top department. I want to thank the whole Astronomical Research Group and here every one is so kindly and ready to help.

The first person that I must mention is my supervisor Dr. Jeremy Allington-Smith for his careful guide and supervision. He is always kindly to provide help and advice when I need. I also thanks for his check for my thesis, including spelling and grammar of the English. I thank my supervisor and Professor Roger Davies for the helps for my application of Oversea Studentship Awards. Without the helps, it is difficult to imagine that I can study at Durham. I would thank Dr. Ray Sharples for his helpful advice and discussion about the FMOS work. I should mention George Dodsworth who helps for the mechanical design. I cannot forget Graham Murray who is always happy to show his experience and I often used his goods free of charge. Thanks also go to Dr. Colin Dunlop who can always help for my experiment test.

I must thank my office mate James Turner and Harold Dyson for tolerating my occupation of more office space. They are always available for helps for anything.

I also need to mention Dr. David Lee and Dr. Roger Haynes at Anglo-Australian Observatory for the discussion about microlenses. They have done excellent work for the characterization of microlens arrays and are always interested in searching good microlenses.

I thank Ms. Judy Low. She kindly provided the careful correction of English spelling and grammar for my thesis.

Some publications have arisen as a result of this work:

1. Deqing Ren, Ray Sharples, Jeremy.R. Allington-Smith, George Dodsworth and David Robertson, G.J. Murray and G. Dalto "The design and construction of a fibre bundle connector using microlenses", Accepted for publication by ***Optical Engineering*** (2001).
2. Lee, D., Haynes, R., Ren, D and Allington_Smith, J., "Characterisation of microlens arrays for astronomy". Submitted to ***PASP*** (2001).
3. Maihara, T., Ohta, K., Tamura, N., Ohtani, H., Akiyama, M., Noumaru, J., Kaifu, N., Karoji, H., Iye, M., Dalton, G. B., Parry, I.R., Robertson, D., Sharples, R., Ren, D., Allington-Smith, J., Taylor, K., and Gillingham, P., "Fiber-Multi-Object Spectrograph (FMOS) for Subara Telescope," ***SPIE Proc.*** **4008** 1111-1118 (2000)
4. J.R.Allington-Smith, Content, R. and Ren, D., "Integral field spectroscopy with the GEMINI Multiobject Spectrograph", ***SPIE Proc.*** **4008** (2000).
5. Deqing Ren, J.R.Allington-Smith, "Apochromatic lenses for near-infrared astronomical instrument", ***Optical Engineering***, **38** (1999).
6. Dalton, G., Parry, I., Allington-Smith, J., Sharples, R., Ren, D., Taylor, K., Gillingham, P., Karoji, H., Iye, M., Noumaru, J., Akiyama, M., and Ohta, K., "FMOS: A Fibre-fed spectrograph for SUBARU," ***FMOS design document*** (1999)
7. Deqing Ren, J.R.Allington-Smith, B.J. Rauscher "Compact all-reflective IR spectrograph and imager for UKIRT", ***SPIE Proc.*** **3122** (1997).
8. B.E.Carrasco, S. Vazquez, Deqing Ren, R.M.Sharples, et. al. "Multi-Fibre Spectroscopy at the Observotorio Guillermo Haro", ***Fibre Optics in Astronomy III***, **Vol. 152**, edited by S. Arribas (1997).

For my wife and daughter

Contents

Chapter 1

Introduction

Abstract

This chapter presents an introduction to the work of the thesis. Different available techniques of spectroscopy are described. The motivation for the thesis is discussed. The main work is to provide an integral-field spectrograph which can work at visible and near infrared wavelengths simultaneously for the FMOS project which aims to provide a multiple object and integral field spectroscopy capability for the Subaru 8-m telescope.

1.1 Introduction

There is no doubt that the forthcoming era of the ground-based astronomy will be dominated by results coming from modern large telescopes recently completed, presently under construction, or planned. As we see from inspection of the current literature, important new results are already flowing from observations obtained with the Keck Telescope (Kraft 1995). Modern large telescopes normally have an aperture larger than 8 meters. The Keck I and II telescope have 10-meter apertures, the VLT Unit consists of 4 telescopes and each one has an 8.2-meter aperture, the Subaru telescope has an 8.3-meter aperture, and the Gemini telescope has an 8-meter aperture. These huge apertures make it possible to collect light from distant and faint objects in the universe which are too faint to be observed with 4-meter telescopes.

As distant objects can be detected, infrared observations are naturally required, so these telescopes are also optimized in optical and infrared wavelengths. The goal for the emissivity of Gemini North telescope is a mere 2% and this will be achieved by using a silver-coated mirror (Mclean 1997). Many of the distant and faint objects, like that in the Hubble Deep Field, are at high redshift and many of the well-established optical spectral diagnostics are shifted beyond 1 micron. Infrared wavelengths are much more penetrating than visible or UV light, and can therefore reveal the processes in star-forming regions which are typically enshrouded in clouds of gas and dust. The need for superior optical and infrared capability will continue into the future (Faber 1980).

Modern large telescopes are normally equipped with adaptive optics which can dramatically improve the spatial resolution. For the Gemini telescope, at 2.2 μm in the infrared the goal is near diffraction-limited imaging using adaptive optics. One of the major drivers for the Gemini telescope is optimized performance in the infrared. High angular resolution through the earth's atmosphere is much more easily achieved at longer wavelengths. Adaptive optics systems are more complex in visible than in infrared because of the large number of actuators that are needed to correct the wave aberration, although in principle there is no limit to achieve the diffraction limit in the visible. Good seeing is important for spectrograph efficiency, which is driven principally by the linear width of slit needed to pass most of the light for the classical spectrograph.

Traditionally, work in high-resolution spectroscopy has been limited to studies in the fields of stellar astrophysics (e.g., magnetic fields, convection, seismology), stellar abundances, and absorption lines associated with cold interstellar matter. However, the new large telescopes will open new vistas: High-resolution echelle-mode spectroscopy can be employed to attack forefront problems in the flux-limited domain formerly reserved exclusively for low-resolution work (Kraft 1995). Obvious examples include the studies of star formation, early stellar evolution, intergalactic matter, AGNs, GSGs, and so on. Since high spectral resolution ($R>10^4$) is necessary in these fields for adequate velocity accuracy, the observations are in a domain where a large telescope is superior to a small one. A review of high-resolution spectrographs designed or built for very large telescopes, including the Keck, Gemini, Hobby-Eberly, MMT and the ESO-VLT, is given by Pilachowski et al. (1995).

For some observations, larger aperture, high angular resolution and infrared ability are necessary for the telescope. An example is the infrared studies of the structure of the galactic center (Faber 1980). The rotation curve of the region close to the nucleus has recently been determined using the Ne II line at 12 μm. These measurements hint at the existence of a large compact mass in the very centre. Higher angular resolution is needed to tell whether this mass is in fact a black hole. The high flux rate and higher resolution of a 10-meter are vital to this problem, not only for further measurements of the Ne II line but also for the spatial distribution of the continuum radiation. Infrared observations of the galactic centre are among the most exciting to be made with a larger ground-based telescope.

However, the new large telescopes are expensive. A 10-m telescope is more expensive than a 4-m telescope. So it is particularly important to use the telescope in the most efficient way.

The construction of the 8 to 10 meter telescopes has brought new opportunities for astrophysical research. The designers of the astronomical instrumentation for larger telescopes must not only improve on the performance of the classical spectrographs, but also respond to the new challenges inherent in modern technology.

In this chapter, different possible technologies for astronomical spectrographs will be discussed first. The advantages and disadvantages of each technology are compared. After these discussions, it will be very clear which one is best fitted to the large telescope. Following these is a description of the construction of the thesis.

1.2 Spectroscopic Instruments for Telescope

1.2.1 Long-slit Spectroscopy

This is the classical spectrograph. A simple long slit spectrograph consists of a slit, a collimator, a camera and a 2-dimensional detector. The object on the telescope focal plane is positioned onto the slit accurately. The light from the slit is collimated first by the collimator, dispersed by the grating and then focused onto the detector. The spatial information along the slit is preserved and this makes it easy for sky subtraction. The width of the slit needs to be adjusted according to the seeing. A wide slit may result in a low spectral resolution and a narrow slit may result in a light loss of the object on the slit. Normally there is only one slit on the focal plane. If the surface density of the objects is high enough then there may be more than one object contained in the slit length. A set of gratings and slits is required to allow both low and high-resolution spectroscopy. Some high-resolution spectrographs are still of this type but this technique cannot make best use of the telescope field and much of the detector area is wasted because there are no spectra of the observed object in this area.

Examples of this instrument include a faint object spectrograph for William Herschel telescope (Allington-Smith et al. 1989), the HIRES high-resolution spectrograph for Keck 10-m telescope (Vogt et al. 1994), a Cryogenic Spectrometer (CRSP) at Kitt peak National Observatory (Joyce et al. 1994), the FAST spectrograph for 1.5-m Tillinghast telescope (Fabricant et al. 1998).

1.2.2 Multi-slit Spectroscopy

The need for multi-object spectroscopy is obvious for faint object astronomy. This is because the greater the spectral resolution, the fewer the number of photons on any detector pixel. Typically, the signal of the spectrum on the CCD detector will be several hundred times fainter than the signal in the direct image of the source. Thus, simultaneous observations of a large number of objects are the only possibility for carrying out the observation within a reasonable time.

One approach is the multi-slit spectrograph which employs an entrance slit composed of multiple sub-sections which can be positioned on the telescope focal plane to pick up many different objects in the field of view. This technique retains many of the advantages of the long-slit spectrograph in that they offer good sky subtraction, and the spatial information in the spectra can be used to optimize the extraction of the object signal (Robertson 1986).

To avoid the loss of light, the slits need to be accurate positioned. Normally an imaging mode is used to determine the precise location of spectroscopic aperture for selected targets and this can be done by replacing the grating with a flat mirror. Unlike other multi-object spectroscopy, multi-slit observing requires a considerable amount of planning and preparation so that a multi-slit configuration can be accurately and quickly set up when it is required. The multi-slit devices are either pre-manufactured aperture plates or re-usable mechanical devices. The positions of the multi-slits must be optimized in the design to avoid or minimize overlap among the spectra. Other examples of this system include a Low Dispersion Survey Spectrograph (LDSS) for the AAT (Taylor 1989), LDSS-2 for the William Herschel Telescope (Allington-Smith et al. 1994), a multi-object spectrograph at CFHT (Le Fevre et al. 1994) and the LRIS spectrograph for the Keck 10-m telescope (Oke et al. 1995).

1.2.3 Multi-fibre Spectroscopy

Multi-object spectroscopy can also be done by using optical fibres. This technique was proposed by Vanderriest (1980). The basic idea is to position one end of each of the several fibres in the focal plane of the telescope at the points corresponding to the interesting objects and to stack up the other ends along the entrance slit of the spectrograph. The spectrum of each object is therefore recorded simultaneously. It can therefore make use of existing long-slit spectrographs well-established, small detectors because the fibre-slit is fixed and totally independent of the field arrangement (Parry 1986). Objects from the entire telescope's field can be observed and all the spectral resolution options of the traditional spectrograph are available.

Fibre optical coupling between a telescope and a spectrograph has several potential advantages over conventional slit spectroscopy. These advantages have been discussed by Angel et al. (1977), Hubbard et al. (1979), and Hill et al. (1980). They include:

(1) The possibility of simultaneous high and low-resolution spectroscopy of many objects in the telescope field of view. This makes it suitable for multi-object and integral field spectroscopy.

(2) Stable, well scrambled images for velocity measurements without slit effects. A system of this kind has been discussed by Heacox (1980).

(3) One advantage of using fibre for multi-object spectrograph is that the spectrograph can be placed on an optical bench on the telescope dome floor. The bundle of fibres is led away from the telescope and fed to the spectrograph at the other end. The spectrograph is therefore completely stationary at all times, which greatly enhances the stability of the apparatus. The fibre trains can be connected or disconnected to the spectrograph by the fibre slits or by a specially design fibre connector. This technique is used for FMOS where a fibre connector is adopted to provide the connection and disconnection between the telescope and spectrographs.

(4) The telescope field of view can be fed to several spectrographs simultaneously. This can make best use of the telescope efficiently. An example is FMOS project, where 4,000 small fibres are fed to 4 spectrographs simultaneously.

Sky subtraction is important for faint-object spectrograph because of the low flux from the object. It has been believed that precise sky subtraction cannot be achieved with multi-object fibre spectrograph system, so that slit observations are most suitable for study of the faintest objects, in spite of their loss in multiplex advantages over multi-fibre systems. An algorithm presented by Wyse and Gilmore (1992) allows data from fibre-fed spectrographs to be sky-subtracted with both precision and reliability close to its limit.

The number of the simultaneously observable objects is limited by the telescope field, the density with which the fibre can be placed on the telescope field and the size of the spectrograph field. More than 100 simultaneous spectra can be obtained in this way. Similar to the multi-slit spectrograph, this technique requires preparation to arrange the fibres on the telescope focal plane before the observations are made. It is important that the fibres are accurately placed on the telescope focal plane to collect the light of the object. The position error may result in a light loss and thus result in a low coupling efficiency for the fibres. The first multi-object fibre spectrograph was built and used by Hill et al. (1980, 1982). The system, called MEDUSA, links the Cassegrain focus of the telescope to a spectrograph with up to 40 short lengths of optical fibres. The fibres are fixed on the focal plane by means of an aperture plane, which has been pre-drilled with holes corresponding to the positions of the target objects. A multi-object fibre spectrograph is being built for the Subaru 8-m telescope, which can record the spectra from 400 fibres simultaneously (Dalton et al. 1999). Other examples include a multi-object spectrograph at a 3.6-m telescope (Lund and Enard 1983), An automated multiobject fibre optics coupler for the AAT (Parry and Gray 1986), Autofib-2 for WHT (Parry et al. 1994), FUEGOS high resolution spectrograph for VLT (Casse et al. 1994), a Low Resolution Spectrograph for 4-m LAMOST telescope (Zhu and Xu 2000).

A common problem for both multi-slit and multi-fibre spectroscopy is the need for precise target positions. In addition, no (multi-fibre) or very limited (multi-slit) spatial information can be obtained.

1.2.4 Integral-field Spectroscopy

Multi-object spectroscopy is more efficient and powerful for point source but this technique is limited in producing spatially resolved spectra of extended sources. Both problems for multi-object spectroscopy, i.e. the need for precise target-positions and the lack of spatial information, will be overcome by a spectrograph with Integral-Field Spectroscopy (IFS) ability which is achieved by using an Integral-Field Unit (IFU). The IFU spectrograph provides a spectrum of each spatial element in a two-dimensional field. The IFS technique can be achieved by using microlenses. This technique was first proposed by Courtès (1982). The image at the telescope focus is enlarged by auxiliary optics and projected on a lenslet array. Each lenslet gives at its focus an image of the entrance pupil of the telescope and any beam collected by the front surface of one of the lens forms an exit pupil which can be considered as the slit for a spectrograph. The matrix of the exit pupils is then fed to the spectrograph. The IFS can also be done using a bare fibre bundle, a microlens array plus fibre bundle, or by imaging slicer. The techniques of sky subtraction for fibre IFU have been discussed by Allingtom-Smith et al. (1998). The imaging slicer only uses mirrors to sample and re-arrange the telescope focal plane images to project them onto the slit of the spectrograph. This makes the imaging slicer the best choice for cryogenic device since the device can be made from metal mirrors. The microlens array + fibre bundle IFU has the advantage of both microlens and fibre and is a good solution for modern spectrograph operating at non-cryogenic temperatures (Vanderriest 1998). In this case, 100% coverage of the focal image is ensured by microlenses, while the redistribution of the pupils by the fibre bundle ensures the best coverage of the detector area and a large spectral range. The details of different IFU techniques will be discussed in Chapter 2.

The IFS technique is suitable to study both extended and single unresolved objects because light from the full extent of the object is collected simultaneously without the need for a wide slit which would degrade spectral resolution. Target acquisition is easier because it is not necessary to position the object carefully on a narrow slit. There is no slit loss for IFS and the image of each source can be reconstructed by software.

The technique of multiple deployable IFUs is very attractive because they can record the spectra of several extended objects simultaneously. Each deployable IFU system consists of several IFUs which can move to the position of the object on the telescope image plane. Sky subtraction can be done for each IFU individually or using a separate IFU which is dedicated to sky subtraction. This technique has the advantages of both Multi-object and integrated field spectroscopy, i.e. it can obtain the spectra of several extended objects over a wide field of view and precise object position is not needed. This will make most efficient use of telescope time and is definitely important for the large new generations of telescopes.

Modern large telescopes are expensive and cover the wavelength from visible to infrared. So, it will be an advantage if the IFU can work in the visible and NIR wavelengths simultaneously. For the spectrograph, it is not necessary to work in both bands simultaneously, as a dichromatic beam splitter can be used to feed the beam to visible and NIR spectrographs separately.

Compared with other "3D" techniques, such as scanning Fabry-Perot interferometer and Fourier transform interferometer, an important advantage of the IFU technique is that all the information is recorded simultaneously. Atmospheric variation doesn't ruin the measurement.

The disadvantage of IFS compared with the MOS is that the field of view is small because the detector must record the spectrum of all parts of the field even if they are empty. However, even hence, it is possible for IFS devices to rival the multiplex advantage of MOS devices. An example is the proposed IFMOS instrument for NGST (Content, R. et al. 2000).

It is clear that the fibre IFU combines the advantages of optical fibre and IFS and will be a dominant instrumentation for large telescope, while the other techniques, such as the image slicer, are also appropriated in some special applications (such as for cryogenic instrument).

1.3 The Scientific Motivation and Thesis Structure

The modern large telescopes provide unprecedented opportunity for spectroscopy at high resolution for extremely faint objects.

For maximum efficiency, it will be a great advantage to carry out simultaneous spectroscopy of as many objects as possible. This is a standard domain of the multi-object spectrograph. However, if objects are to be resolved, and if one is interested in their complex structure, integral-field spectroscopy is the best choice. On the other hand, the problem of accurate slit-position for the diffraction-limited image will require the extension of the multi-object technique towards the multi-IFU approach. Finally, simultaneous use of visible and near infrared is also an advantage for the observation efficiency.

The general scientific drivers for integrated-field spectroscopy have been discussed in several papers (Allington-Smith et al. 1998, Vanderriest 1998). Application examples include: (1) Studies of the distribution of star formation in distant galaxies in the field and clusters. (2) Kinematical studies of galaxies at intermediate redshift. (3) Distance estimation at intermediate redshift. (4) Reconstruction of lensed galaxies. Some of these require a full two-dimensional and a near infrared capability.

FMOS is a project which will provide multi-object and, optionally, integral field spectroscopy for the Subaru telescope. The scientific cases for FMOS IFU spectroscopy include: (1) The study of protostars and young stellar objects. IFS in the NIR will allow detailed velocity mapping of the gas and dust associated with protostellar disk and the molecular outflows from young stars in this and similar star forming regions. The ability to deploy several small IFUs will allow systematic studies of large numbers of these objects in a relatively small amount of telescope time. (2) The evolution of galaxies and large-scale structure. For galaxies at redshift $z > 1$, the spectral features normally observed in the optical bands at low redshift will shift into the near infrared. A study of the evolution of the star formation rate at $1 < z < 2$ will require spectroscopy from 0.9 to 1.8 μm. A survey would require careful random sampling to select galaxies with typical distribution of colour, size etc and this can be done by using integral-field spectroscopy. The studies of dwarf galaxies in the Coma cluster are best matched to a deployed IFU system. (3) Studies of planetary Nebulae. A large IFUs can be used to study the planetary nebulae populations of individual galaxies with a single exposure to cover both detection and analysis. For FMOS, the NIR wavelength range is over 0.9 – 1.8 μm due to the limit of instrumental thermal background because extending the wavelength coverage beyond 1.8 μm will require the whole instrument to be cooled cryogenically. A more detailed description can be found in Dalton et al. (1998). It is evident that the above studies will need the IFU with optical and near infrared ability.

The work of this thesis is to investigate new techniques for integral field spectroscopy to make the most efficient use of modern large telescopes. The main work is to provide a Multiple IFS system with simultaneously optical and near infrared ability for FMOS project for the 8-m Subaru telescope. This includes the design and construction of an IFU which can simultaneously work at visible and near infrared, a design of optical spectrograph for FMOS. The prototyping of the Multiple IFS system is supported by an extensive programme of testing of candidate microlens arrays.

Another critical aspect of the instrument is the ability to disconnect the (IFS and MOS) fibre input which is installed on a removable prime focus top-end ring from the spectrographs which are mounted elsewhere on the telescope. A fibre connector will allow the instrument to be used effectively. The design of connectors for the MOS and IFS modes are described. Results from the testing of a prototype for the MOS mode are presented.

The contents of this thesis are organized as followings:

Chapter 2: Although fibre + microlens IFU system is becoming more and more important for large telescope observation, at the time of writing there is still no publication about the systematic design theory. The aim of this chapter is to present the design theory for the IFU system using microlenses and fibres. The IFU design theories about the fore-optics, microlens and fibre FRD are discussed. The effects of the fibre oversizing and Focal Ratio Degradation (FRD) on the IFU performance are discussed from different aspects. A mathematical model is given which can be used to calculate the fibre core size according to the required coupling efficiency. Finally a figure of merit for IFU system is derived, which can be used to estimate or compare the performance of IFU systems. The design theory will serve as a necessary tool in the whole thesis for the IFU and spectrograph designs.

Chapter 3: Many existing spectrographs are dedicated to long slit or multi-slits and make use of the telescope Cassegrain hole in the beam to position an on-axis fold mirror or detector within the un-illuminated central portion of the pupil. However this spectrograph will result in a light loss when using fibres.

In this chapter, the design of a Compact All-reflective near InfraRed (1-2.5 μm) Spectrograph and imager (CAIRS) is described. CAIRS is designed for the UK Infrared Telescope (UKIRT). When working in slit mode, CAIRS will provide a comprehensive spectroscopic and imaging capability in the near infrared. It uses one slit or two slits for use with image slicers so that it can provide two-dimensional spectroscopy over an extended field. It can also work with a fibre IFU for two-dimensional spectroscopy. The instrument uses only mirrors, there is no chromatic aberration and all primary aberrations are almost completely eliminated over a large field of view.

Compared with some spectrographs, there is no light obstructed by the mirrors, this makes CAIRS suitable for fibre integral-field or fibre multiple-object spectroscopy.

This chapter is based on a SPIE paper (Ren, Allington-Smith et al. 1997a).

Chapter 4: With the fast evolution of modern infrared arrays, there is an increased trend for using lenses in the 1-2.5 μm wavelength range for NIR astronomical instruments. Refractive systems are attractive for many applications because they can accommodate wide fields of view, fast focal ratios while permitting a compact and un-obscured optical design.

The control of chromatic aberration through the selection of glasses is one of the most extensively studied subjects in the field of lens design. However, most of these studies were done at visible wavelengths. Little attention has been given in the Near Infrared (NIR) wavelengths (1 – 2.5 μm). The use of a doublet is often limited by the small number of available glasses and the inability of a doublet to achromatize over the whole NIR wavelength range. At the time of writing, there is no published work about the theoretical choice of glasses for triplet for the NIR astronomical instruments.

In this chapter, a method based on the Herzberger approach has been investigated for the selection of glasses for the apochromatic correction at near-IR wavelength. The method avoids algebraic complexity and simplifies the glass selection processes. Doublet and triplet glass combinations can be chosen directly from the partial dispersion versus v number plot. Good combinations of NIR doublet and triplet are given. This work can be used as a guideline for the selection of glasses for the NIR optical design.

This chapter is based on a paper in Optical Engineering (Ren and Allington-Smith1999).

Chapter 5: Microlenses are the key element for integral-field spectroscopy using microlens arrays. Microlenses are not perfect. Many commercial microlenses suffer from low encircled energy and this will result in much light loss for the IFU. With the improvement of other techniques, such as fibre bundle construction, the quality of microlens becomes a limiting factor for the IFU performance. Continued investigation of the image quality of microlens array is of great importance to the IFU instrument.

In this chapter, two types of microlens arrays, i.e. polymer and monolithic glass microlens arrays are described. The manufacture technologies are discussed. Design theories are given. Different test methods and the experiment apparatuses are presented. Finally, microlens arrays from different manufacturers are tested and compared according to the encircled energy using a mathematical model. The work will be valuable to find the best microlens array for a given application.

Chapter 6: In this chapter, the scientific requirements for the FMOS project are described. The FMOS instrument concepts are also described. The requirements and specifications for these instruments are presented and these will be used as a design guide for the following chapters for the FMOS project. Most specifications in this chapter are from the FMOS design document (Dalton et al. 1998).

Some of this chapter appeared in a SPIE paper (Maihara et al. 2000).

Chapter 7: In this chapter, the optical designs for FMOS optical collimator, camera and spectrograph are described. As many FMOS scientific studies are about faint and distant objects, the work is to design a spectrograph with high throughput. This is achieved by using the minimum number of lenses or mirrors. A white-pupil design is used to keep the size of the camera as small as possible. The vignetting and aberrations found in some conventional spectrographs are eliminated by the white-pupil design. The collimator is a Schmidt type optical system and the basic layout is based on CIRPASS (Parry et al. 2000), however the chromatic aberration is well corrected in the wavelength range of 0.45 –0.9 μm. The F/1.46 optical camera consists of 10 elements in four groups with all spherical surfaces. The optical aberrations are also well corrected for both collimator and camera and this results in good image quality for the spectrograph. The spectrograph performance is estimated and it is shown that the spectrograph meets the requirements for the FMOS project.

Chapter 8: This chapter discusses the optical design of a deployable IFU for the FMOS project. In order to make best use of the telescope time, the IFU is required to work in the optical and near infrared bands simultaneously. The challenge for the design is simultaneous optical and near infrared ability for the IFU. This requires that the chromatic aberration needs to be well corrected in both the optical and near infrared (0.45-1.8 μm) simultaneously. The optical glasses will need to have a high transmission in the optical and near infrared. A simple and compact fore-optics design is also necessary for the deployable IFUs considering that many of these modules will be distributed in the telescope focal plane. The design of the microlens arrays and array fibre bundle are also presented in detail.

Chapter 9: This chapter continues the work of chapter 8. It describes the construction and testing of the IFU.

Chapter 10: FMOS includes a multi-object fibre positioner (Echidna), a fibre connector and a near infrared spectrograph. As Echidna is installed at the Subaru primary focal plane, a fibre connector is necessary to provide a connection and disconnection in the fibre train between the Echidna positioner and the infrared spectrograph. The design and construction of a prototype of the fibre connector is described in this chapter.

The fibre bundle connector also provides the important function of converting the focal ratio from F/2 to F/5 because the F/2 is too fast for the spectrograph. Each fibre bundle connector consists of 100 coupling fibres. It works at 0.9 – 1.8μm wavelength range simultaneously and the chromatic aberration is well corrected in the design. The design principle and the construction of the fibre bundle connector are also discussed. The coupling efficiency is measured and compared with the theoretical estimation. Further possible improvement is also investigated.

This chapter was accepted for publication by Optical Engineering.

Chapter 11: This chapter summarizes the work presented in this thesis and look towards future work.

Chapter 2

Design Theory of IFU for Imaging Spectrometer

Abstract

In this chapter, different IFU techniques are compared. The discussion is concentrated on the IFU systems which use microlenses and fibres. The IFU design theories relating to the fore-optics, microlens and fibre FRD are discussed. The effects of the fibre oversizing and FRD on IFU performance are discussed from different aspects. A mathematical model is given which can be used to calculate the fibre core size according to the required coupling efficiency. Finally a figure of merit for IFU system is derived, which can be used to compare the performance of the IFU system. In this chapter, the IFU for FMOS project is used as a practical design example to show the applications of theses theories.

2.1 Introduction

Imaging spectroscopy means that at every position of a field a spectrum can be obtained and the information content is a 3 dimensional data cube, which comprises the spatial information about the observed object in two dimensions and the spectral information in the third dimension.

There are two approaches so far, which can provide imaging spectroscopy ability. One is Integral-Field Spectroscopy (IFS), which can simultaneously gather the 3 dimensional date cube in a single integration. Another one is scanning, which uses time as a third dimension.

For the scanning approach, three techniques have been applied so far:

1. Long slit scanning, which steps the long slit of the spectrometer across the object. For a long slit spectrometer, an image of the scene cannot be recorded unless the measurements are repeated many times with slight displacements of the telescope. This is the working principle of the scanning long slit spectrometer and this strategy was pioneered at the Anglo-Australian Telescope (Mclean 1997). The slit stepping or scanning can provide large wavelength coverage but it is difficult to obtain good quality images along the scanning direction for most telescopes.

2. The Fabry-Perot interferometer, which is formed by placing a device called etalon in the collimated beam of a typical camera system. The etalon normally consists of two plane parallel plates. By adjusting the distance between theses plates, spectrum information can be obtained. The throughput is high for this instrument. Examples for astronomical applications include Boulesteix et al. (1983), Anandarao (1983), Wade (1983). Resolution of high to 50,000 was reported by Hailash et al. (1983).

3. Fourier transform interferometer (FTS), which is a scanning Michelson interferometer with collimated light as input. The spectrum can be determined by a time sequence of scanning. FTS can have a very high resolving power. Moreover, as there is no slit, all light fall on the detector, so in principle the throughput is high. Examples include Connes (1970), Hall et al. (1979), Maillard and Michel (1982), Ridgway and Brault (1984), Simmons et al. (1997).

Disadvantages of these scanning systems are

- This system can only gather two of the three dimensions data cube at any time. The third dimension has to be obtained sequentially by scanning.
- The atmospheric conditions during the scanning process may change and introduce systematic noise to the data. These may make the construction of a homogeneous data cube more difficult or impossible.

Compared with the scanning approach, IFS provides the 3-dimension data cube simultaneously in a single integration by reformatting the two dimensional telescope images into a slit before entering the classical spectrograph. IFS with a large telescope is most efficient for objects that need the highest possible spatial resolution and when this resolution is indeed achievable, i.e. at very good sites or with adaptive optics. As a result, most of the new large telescopes will be equipped with IFS (Vanderriest 1998).

The aim of this chapter is to present the design theory of IFU system. First, different IFS techniques are discussed, and then the discussions are concentrated on the IFU systems which use microlenses and fibres.

2.2 IFU System

There are three major IFS techniques (Allington-Smith and Content 1998), i.e., lenslets, fibre bundle and image slicers. The fibre bundle system can be further developed as "lenslet+fibre +lenslet" and "lenslet +fibre". The principles of these types are schematically shown in Fig. 2-1.

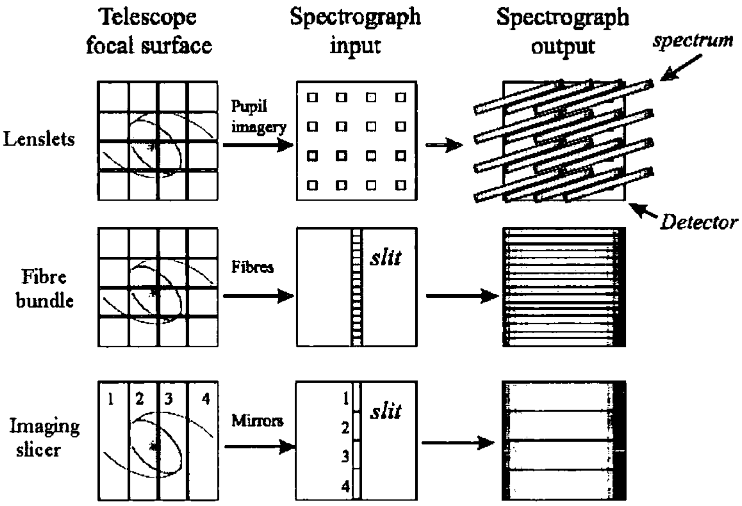

Figure 2-1. Schematic of different types of IFU techniques, which can obtain the 3-D data cube simultaneously.

2.2.1 Lenslet IFU

One way to implement the IFU mode is to subdivide the focal plane or sky image into numerous small segments by using a microlens array. This concept is proposed by Courtes (1982) and is also called TIGER mode. The integral field spectrograph TIGER was the first realization of the concept (Bacon 1995). Normally the sky image is magnified to be suitably sampled by microlenses. The magnified image is then fed to microlens array, which slices up the image before it is fed to the spectrograph. The spectrograph output on the detector is complicated, with some small strips which contain spectral information. This process is schematically shown in Fig. 2-1 on the top. The field of view can be large and is only limited by the detector size. This method doesn't make good use of the detector in order to avoid overlap of the spectra between two microlenses, and the spectral resolution cannot be too high.

Examples include TIGER (Bacon 1995), which has a resolution up to 1800. Other example of this kind of instrument is given by Herbst (1998), which has a resolution up to 2000. This IFU is very simple and the whole system can work at cryogenic temperature. This makes it suitable for infrared astronomy.

2.2.2 Bare Fibre IFU

This technique, first realized by Vanderriest (1980), use fibres to sample the two-dimensional sky image into a pseudo-slit at the entrance of a classical long slit spectrograph. In principle, the IFU field of view is only limited by the detector size and the design is quite simple. As there are dead areas between fibres even though the fibres are closely packed and due to the limitation of fibre core/clad ratio, the typical fill factor is about 70 %. In order to reduce FRD, the fibres should be fed with focal ratios faster than about F/5. For slow beams, FRD will be a problem, which may introduce light loss in the spectrograph because of vignetting or the spectrograph needs to be oversized to accept the light that is faster than the input on the fibres. Although one can use extra optics to speed the input beam, however the demagnification optics will decrease the physical size of the input fibre bundle, which may lead to great problem with the filling factor (Allington-Smith and Content 1998). Examples of this IFU are SILFID at CFHT (Vanderriest 1980), the ARGUS mode of the ALBIREO spectrograph (Herpe et al. 1998), INTEGRAL for William Herschal Telescope (Arribas et al. 1998), a Integral-Field Spectroscopy for Hobby-Eberly Telescope (Bershady et al. 1998).

2.2.3 Lenslet + Fibre System

Because of the disadvantages of the bare fibre IFU system, an improved IFU, which combines the advantages of both bare fibre IFU and TIGER approaches into a single system was first proposed by Courtes (1982). At the fibre input ends, a microlens array is used to segment the sky image and couple the telescope pupil image onto the entrance of each fibre. The input light at the fibre entrance can be fast enough (with a typical value of F/5) to reduce the FRD and the fill factor can be as high as ~100 % with commercial microlens arrays. At the output ends of the fibres, a linear microlens array can be used to convert the light to a suitable focal ratio, which is consistent with an existing spectrograph. Obviously this IFU system has the advantages of both lenslet and bare IFU systems. In principle, there is no light lost even though FRD exists. The FRD at the fibre output end only causes an increase in the size of the pseudo-slit if microlenses are used at the output end of the fibre. For this lenslet+fibre+lenslet IFU system, the throughput could be very high, at least in principle. For the lenslet+fibre system, as there is no lenslet at the output end of the fibre, FRD will introduce some light loss because of vignetting if the spectrograph is not oversized. However, the loss will still be less than the bare fibre IFU system because the beam can be fast at the fibre entrance.

The drawbacks are that high quality microlens array is needed. Each fibre needs to be accurately registered to the microlens. This makes the construction of the fibre bundle very difficult. Perhaps the biggest drawback is that it is not clear currently whether this system can survive at cryogenic temperature for a long time, although some work (Haynes et al. 2000, Tecza and Thatte 1998) has demonstrated this possibility. This makes it only suitable for visible and infrared in J, H bands where cryogenics is not necessary. However, this design is the optimal solution for many modern spectrographs. Examples include the IFU of the GEMINI Multi-Object Spectrograph (Allington-Smith et al. 1998a), a Wide-Field IFU for the VLT-VIRMOS (Prieto et al. 1998), SINFONI: a high-resolution near-infrared imaging spectrometer for VLT (Tecza and Thatte 1998), AOIFU: AOB OSIS Infrared Fibre Unit (Guérin 1998), SMIRFS-II: Multi-Object and Integral-Field Unit Spectroscopy at the UKIRT (Haynes and Allington-Smith 1998).

2.2.4 Image Slicer

Even the lenslet+fibre IFU system suffers from the fact that the IFU may not survive at cryogenic temperature. Another IFU technique called image slicing, which uses a mirror with many facets to subdivide the sky image into many narrow strips which are then stacked along the length of a spectrograph slit using other mirrors. As only mirrors are used, this IFU can work at cryogenic temperature.

This slicer was first proposed by Bowen (1938). A Bowen image slicer was constructed by Pierce (1965) for the McMath Solar Telescope. A well-known image slicer, called 3D (Weitzel 1996), was the first to be used for infrared. It consists of two sets of plane mirrors. The first one is located on telescope focal plane. The second one guides the light to the slit of the spectrograph. As only flat mirrors are used, the telescope focal ratio is conserved. A disadvantage is that some light will be lost due to the shadow areas between the first set of mirrors because no one mirror is exactly in focus. There is a defocus between each strip at the pseudo slit (Weitzel 1996). This requires that the spectrograph can tolerate this defocus or that the input beam fed to the pseudo slit is slow. These problems can be partly compensated by using an *advanced image slicer*, which uses spherical mirrors to transfer the telescope sky image and pupil image (Content 1997). The disadvantage of this IFU is the complexity of design, manufacture and alignment. Optical off-axis aberrations, such as coma and astigmatism, need to be carefully corrected.

Mostly, this IFU system is used in the infrared because it can tolerate cryogenic temperatures. As normally infrared spectrographs are designed to accept slow beam, this imaging slicer is suitable for this application.

The technique was first exploited and realized by Weitzel et al. (1996), with 3D, which was developed at Max Planck Institute. Other examples include a Cryogenic Integral Field Spectrograph for Palomer 200 Inch Telescope (Murphy 1999), Near-infrared Integral-Field Spectrograph (McGregor et al. 1999), GIRMOS: an infrared multi-object spectrograph for Gemini (Wright et al. 2000), an in planning system for ESA-NGST integral field slicer (Content 2000). Note that all these examples are for infrared where cryogenics is necessary.

2.3 Fibre Lenslet IFU Modeling

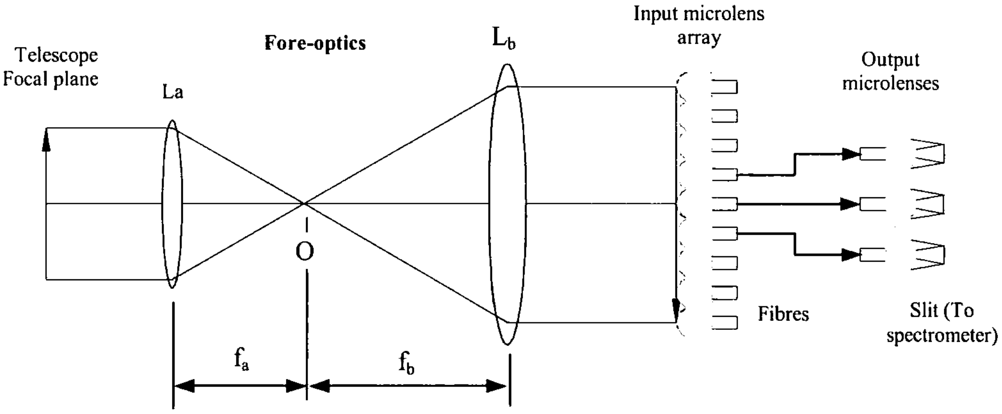

Figure 2-2. Schematic of lenslet + fibre + lenslet IFU system. For clarity, only chief rays are shown in the fore optics. Note that the chief rays are parallel to the optical axis after the fore optics and this means that the sky images on the input microlens front surface are telecentric.

The principle of lenslet + fibre +lenslet IFU system is schematically shown in Fig. 2-2. The telescope focal plane sky image is magnified by the fore-optics, which is composed of lens L_a

and L_b. The magnified sky image is formed on the microlens front curved surface. Each microlens forms a telescope pupil image on its back flat surface, where the fibre entrance is located. The input microlens array is a 2-D array of microlenses. The filling factor can be ~100% and the sky image is well sampled almost without light loss in the lens-to-lens gap. At the output end of the fibre, a linear microlens array is used to convert the sky image to a suitable focal ratio at the pseudo slit, which can be directly fed to a spectrograph.

2.3.1 Fore-optics

In principle, one can place the input microlens array directly on the focal plane of the telescope. However there are some advantages for having a fore-optics between the focal plane of telescope and the microlens array. These include being able to use a microlens array at a suitable size, allowing pupil-segmentation and making the system from the input microlens array onwards independent of the telescope and therefore potentially useful on many telescopes including 8m telescopes (Parry et al. 1997).

The fore-optics is a key element for the IFU system. Its main function is to magnify the telescope focal plane image (i.e. sky image) and make it suitably sampled by a 2-dimensional microlens array. The magnified sky image on the microlens surface must be telecentric in order to avoid pupil image shift on the microlens, which may result in a light loss.

In Fig. 2-2, the sky image on the telescope focal plane is magnified and imaged onto the surface of microlens array. Assume that telescope pupil is infinite or distant (this is the case for FMOS and most telescopes). The sky image is magnified by lens L_a and L_b. In order to keep the magnified sky image telecentric, Lens L_a needs to form a telescope pupil image at the focal point O of lens L_b in either case, i.e. for both telecentric and non-telecentric images on telescope focal plane. In the case that the telescope focal plane image is telecentric or telescope exit pupil is distant, it is obvious that the lateral magnification is given by

$$M = \frac{f_b}{f_a} = \frac{F_S}{F_{tel}} \qquad (2-1)$$

Where F_s is the focal ratio of the sky image on the microlens after the fore-optics and F_{tel} is the focal ratio of sky image on the telescope focal plane.

Another advantage of telecentricity is that the magnification M is independent of distance between the object (here it is telescope focal plane) and the fore-optics. Conventional optical system produces images with higher magnification when the object is closer to the lens. A telecentric system acts as if it has an infinite focal length. An object moved from far away to near the optical system goes into and out of sharp focus, but its image size is constant.

2.3.2 Input Microlens

The functions of input microlenses are to sample the sky image and project the telescope pupil image onto their back surfaces where the fibre entrances are located. The fibres can be fed with a fast beam in order to reduce FRD. The microlenses form a two dimensional contiguous array with ~100% filling factor between two microlenses.

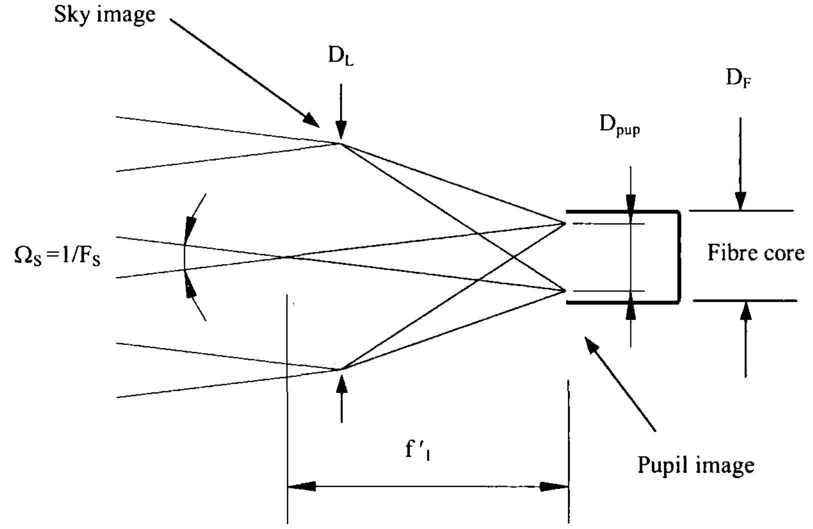

Figure 2-3. Schematic of microlens sampling. The input microlens is used to sampling the sky image. The telescope pupil image is formed on the back surface of the microlens. Note that the fibre core is oversized.

In Fig. 2-3, assume that microlens refractive index is n_l and focal length is f_l in air. The microlens thickness is one focal length in the refractive medium and is given by

$$f_1' = f_1 n_1 \qquad (2-2)$$

As the microlens thickness is equal to the focal length in the medium, the telescope pupil image size on the fibre entrance is

$$D_{Pup} = \frac{f_1}{F_S} \qquad (2-3)$$

Where F_S is the F-number of the sky image after fore-optics.

The pupil image focal ratio at the fibre entrance converted in air is

$$F_{pup} = \frac{f_1}{D_L} \qquad (2-4)$$

From equation (2-1), (2-2) and (2-3), the telescope pupil size projected onto the fibre entrance is

$$\begin{aligned} D_{pup} &= \frac{F_{pup}}{F_S} D_L = \frac{D_L}{M} \frac{F_{pup}}{F_{tel}} \\ &= \frac{D_{samp} F_{pup}}{F_{tel}} \end{aligned} \qquad (2-5)$$

Where D_{samp} is the diameter of microlens projected on telescope focal plane. For an optimal sampling, at least two microlenses are used to sample the seeing disk (FWHM).

From equation (2-5), it is evident that the fore-optics has no affect on the pupil image size projected onto the fibre entrance. From equation (2-4), it is also obvious that the pupil image f-number is only decided by the microlens. One can place the microlens directly on the telescope focal plane and the pupil image is the same as that after the fore-optics. The function of the fore-optics is only to magnify the sky image and then make it suitable to be sampled by a microlens of suitable size.

In practice, the fibre core can be oversized to facilitate the pupil image. For a fibre with a diameter of D_F, the oversizing factor is expressed as

$$K_{pup} = \frac{D_F}{D_{pup}} \qquad (2-6)$$

2.3.3 Output Microlens

The functions of output microlens are different from that of the input microlens. The output microlens has two functions. One is to convert the sky image at the pseudo-slit, which is fed to an existing spectrograph. Another function is to convert the focal ratio to a suitable value for the spectrograph. This is a very important advantage of this lenslet + fibre + lenslet than other kinds of IFU systems. The fibre output end is shown in Fig. 2-4. The telescope pupil image is at the fibre output end, which is transferred from the fibre entrance. At the fibre output end, the chief ray is perpendicular to the end face at every point for the pupil image and the pupil image is telecentric. Obviously, the sky image is at infinity. The infinite sky image is converted to a real image at a distance of one focal length in the air after the microlens, where the pseudo slit located. The microlens thickness, which is one focal length in the medium, ensures that the sky image at the pseudo slit is also telecentric. More details about the advantages of this arrangement will be discussed in section 2.5.

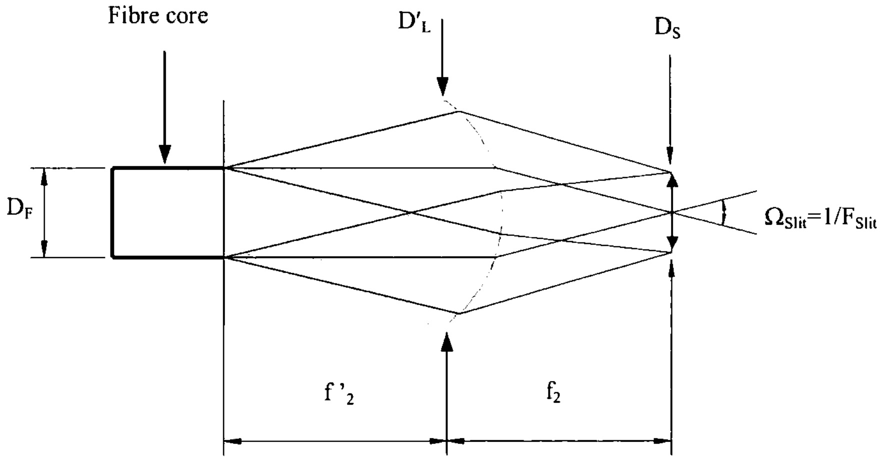

Figure 2-4. Schematic of output microlens. The output microlens is used to convert the sky image onto the slit. The output focal ratio can also be converted to a suitable value for a existing spectrograph. Note that the pseudo-slit image is telecentric.

The thickness of microlens is given by the focal length in the medium with a refractive index n_2

$$f_2' = f_2 n_2 \qquad (2-7)$$

Where f_2 is the microlens focal length in the air.

The focal ratio at the pseudo-slit can be expressed as

$$F_{Slit} = \frac{f_2}{D_F} \qquad (2-8)$$

After the fibre core size D_F is decided, by adjusting the microlens focal length the focal ratio at the pseudo slit can be adjusted to a value that is suitable to a existing spectrograph. Because of the fibre scrambling, the fibre output end is very uniform in illumination, so the focal ratio is well defined in the cone shape. This well-defined beam is then fed to a spectrometer and results in no loss in throughput.

It needs to be noted that the focal ratio at the slit is only decided by the fibre core size and the output microlens focal length. Fibre FRD has no effect on it. This means that fibre FRD introduces no vignetting at the spectrograph and there is no light loss if an output microlens of the correct size is used.

Assure that fibre FRD is expressed by a constant K_F

$$K_F = \frac{F_{pup}}{F_o} \qquad (2-9)$$

Where F_O is the focal ratio at the fibre output end. F_{pup} is the fibre input focal ratio and is decided by equation (2-4). K_F is always bigger than 1. It is not important how to define F_O provided that one controls the aperture size of the microlens (see Fig. 2-4). The aperture size of the output microlens is expressed as

$$D_L' = D_F + \frac{1}{F_O} f_2 \qquad (2-10)$$

Equation (2-9) and (2-10) decide the actual value of F_O that the microlens system can accept.

The pseudo slit diameter is given by

$$D_s = \frac{f_2}{F_O} = \frac{f_2}{F_{pup}} K_F = \frac{D_F F_{slit}}{F_{pup}} K_F \qquad (2-11)$$

Combined with equation (2-6), one has

$$D_s = \frac{D_{pup} F_{Slit}}{F_{pup}} K_{pup} K_F \qquad (2-12)$$

This equation is independent of the output microlens. One can clearly see how the fibre FRD affects the performance of the spectrometer. It is evident that the slit size is decided by the FRD factor K_F and fibre oversizing factor K_{pup}. The pupil imaging optics will convert the effects of the fibre FRD into an increased image size at the slit. Both the fibre FRD and oversizing factors will increase the slit width, which will decrease the spectral resolution of the spectrometer. The oversizing of the fibre core has the same effect as the FRD to the performance of the spectrometer. It needs to be noted that the slit size is independent of output microlens if F_{Slit} is fixed or decided by an existed spectrometer. The function of the output microlens is only to convert the pupil image to sky image at the fibre output end.

2.3.4 Output End Without Microlens

When the fibre end is without microlens, the situation is simple. The bare fibres are located at the pseudo slit and directly fed to spectrograph. The size of pseudo slit is decided by the fibre core diameter, which can be decided by equation (2-5) and (2-6). The oversizing of fibre core will increase the pseudo slit width. The focal ratio at the pseudo slit is decided by fibre FRD and fibre input focal ratio at the fibre entrance end. The focal ratio can be calculated according to equation (2-9). FRD will introduce vignetting or require that the spectrograph be oversized to accommodate this fast beam. In order to reduce the vignetting, this kind of IFU needs a dedicated spectrometer.

2.4 Non-telecentric Image

Ideally the sky image from the telescope focal plane is absolutely telecentric. However, in practice, this is difficult considering the difficulty in design. In this case, it will be useful to work out the allowed non-telecentric angle.

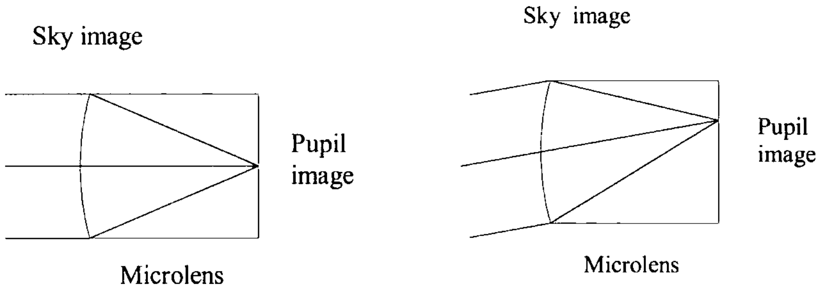

(a) Telecentric sky image. (b) Non-telecentric sky image

Figure 2-5. Non-telecentric sky image and pupil image shift. (a) Telecentric sky image and there is no pupil position shift. (b) Non-telecentric sky image which results in a shift of the pupil image position relative to the microlens optical axis. The thick lines are chief rays, which decide the pupil image central position on the microlens back surface. The thin lines are marginal rays, which decide the pupil image edge position on the microlens back surface.

The effect of non-telecentric sky image on the pupil position is shown in Fig. 2-5. In Fig. 2-5 (a), there is no pupil shift. This means that the centre of the pupil image is on the optical axis of the microlens, i.e. the pupil image is located on the centre of each microlens back surface. In Fig. 2-5 (b), the pupil is shifted a distance relative to the optical axis of each microlens. The amount of the shift is different for different positions in the telescope field of view and in the IFU field of view. In the centre of the telescope field, there is no pupil shift for the central microlens. However at the IFU field edge, a pupil shift will happen if the sky image is not telecentric. At the edge of telescope field, a pupil shift will happen everywhere in the IFU. Non-telecentricity will result in light loss when using fibres to collect the light if the fibre core is not oversized enough, or will result in low resolution and more stray light if the fibre core is oversized too much. When a deployable IFU moves from one position to another position in the telescope field, the pupil shift will change according to the position in the telescope field. This non-telecentric image cannot be corrected by the fore-optics. It makes the data reduction impossible to correct this non-uniform illumination in the fibre. It is obvious that non-telecentricity must be controlled.

Non-telecentricity may be introduced by the telescope fed sky image i.e. the chief ray has different angles at different positions on the field of view, or introduced by the IFU optics itself if the IFU fore-optics cannot image the telescope pupil at infinite distance, i.e. the IFU fore-optics is not a telecentric design. IFU optics which can ensure telecentricity was discussed in section 2.3.1. For a non-telecentric telescope sky image, from Fig. 2-5 (b), the relationship between telescope non-telecentric ray and pupil image shift on the microlens can be derived as

$$\Delta s = f_1 \cdot \tan(\frac{\beta}{M}) \qquad (2-13)$$

Where Δs is the amount of pupil shift. β is the non-telecentric angle on telescope focal plane. Given the allowed pupil shift, this equation can be used to calculate the allowed non-telecentric angle. The non-telecentric angle is small when the pupil is distant. Again, it is evident that for the same pupil shift, a high magnification of the fore-optics allows a large non-telecentric angle in the telescope focal plane.

As an example for FMOS IFU, the magnification is 20. The microlens has a focal length of 2.8mm. Given the allowed maximum pupil shift of 5 μm, the maximum allowed non-telecentric angle is 2.1° on the whole telescope field of view, compared with the maximum allowed non-telecentric angle of 0.115° for the same pupil shift without IFU fore-optics.

2.5 Light Coupling

Techniques for coupling light into and out fibre have been discussed by Nicia (1981) from the point of view of communication systems and first discussed by Hill and Angel (1983) for astronomical instruments. Nicia discussed coupling light from fibre to fibre (multimode) using different lenslets. Hill and Angel discussed using lenslets to couple light into fibres from the telescope and then using lenslets again to couple the light emerging from other end of fibres into the spectrometer. However, no mathematical calculations were given about the design for the coupling.

The coupling efficiency can be expressed by the product AΩ of the area of fibre core and the solid angle of emerging light. A guiding principle for using fibres is to minimise this product (Hill and Angel 1983, Brodie et al. 1988). The smaller this product, the easier it will be to make a spectrometer with good spectral resolution and throughput.

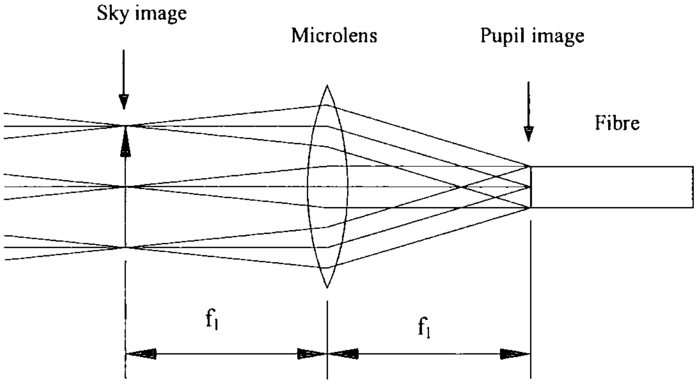

Figure 2- 6. Schematic that uses a microlens to couple the light into a fibre. In this arrangement, the chief rays of the pupil image are parallel to the optical axis everywhere on the fibre entrance and the AΩ Product has been exactly conserved.

Hill used a microlens to couple the light directly from a point source in the telescope focal plane to a fibre without using fore-optics. The configuration is shown in Fig. 2-6. A microlens is used to couple the light from the sky image onto the fibre. The distance between the sky image and the microlens is equal to the focal length of the microlens. The distance between the microlens and the fibre entrance is also arranged to be equal to its focal length. If the telescope exit pupil is at infinite or distant, the telescope exit pupil is imaged onto the fibre entrance by the microlens and the chief rays of the pupil image are parallel to the optical axis everywhere on the fibre entrance and so the AΩ product is exactly conserved. A reversed arrangement is used for the output end of IFU (Fig. 2-4) to ensure that the AΩ Product is exactly conserved. Other advantages are that the fibre can be fed at a fast focal ratio to reduce FRD. This method of coupling has the feature that the cone angle of the beam emerging from the fibre is not invariant, as in the simple coupling of bare fibres, but is sensitive to changes in telescope image quality. If the seeing improves, then Ω at the output gets small and from equation (2-12), the slit width becomes small and the resolution power increases. However, this feature is for a point source of the sky image. For an extended sky image, this feature does not exist.

Unfortunately, the configuration proposed by Hill cannot be used for IFU where the extended sky image needs to be sampled and each sampled element is fed into a fibre. For a microlens array, this configuration will introduce a blurred sky image on each microlens surface and cause cross-talk in the sampling process. A best method is to form the sky image on the curved surface of the microlens array. The aperture of each microlens can well sample the sky image and as the microlens array can have a ~100 % filling factor, no light is lost in the sampling process meanwhile each microlens can also image the telescope exit pupil onto its back surface.

Although this method appears to be good for IFU, at the input end, another problem appears. As the sky image is placed directly on the microlens surface, the chief rays of the pupil image are no longer parallel to the optical axis of each microlens. The angle between the chief ray and optical axis is variable. On the edge of the pupil image, one gets a maximum value which is

$$\theta_{\max} = \frac{1}{F_s} = \frac{1}{MF_{tel}} \qquad (2-14)$$

Where F_S is the focal ratio of the sky image after the fore-optics. M is the magnification of the fore-optics and F_{tel} is the telescope focal ratio.

Because the chief ray has an extra angle on the pupil image plane, when this light is fed to a fibre, it will introduce extra FRD. This is called geometrical FRD. From the above equation, for the IFU input microlens, this angle is only decided by the input focal ratio of the telescope sky image and fore-optics magnification. If the beam of the telescope sky image is slow or the fore-optics has a high magnification, the geometrical FRD will be very small and can be negligible. If there is no fore-optics and the microlens array is placed directly on the telescope focal plane to sample the sky image, F_S is equal to the telescope focal ratio of F_{tel}. For FMOS, F_{tel} is 2 and M is 20, so F_S is 40. This beam is very slow and the geometrical FRD can be negligible compared with the focal ratio 5 of the pupil image that is fed into the fibre. It is evident that a high magnification fore-optics can reduce the geometrical FRD.

2.6 Fibre Properties

The fibres used in astronomy are of step-index type (Parry 1998). Fibre FRD have been studied and measured by several authors (Gloge 1972, Gambling et al. 1975, Heacox 1986) from different points of view. Because FRD is difficult to measure accurately and changes from fibre to fibre and the measurement condition, these make the reliability of actual measurement and comparison a problem. Even the same fibre may have different FRD if the measurement is made by a different person or the fibre is from different batches. So in order to compare different fibres, measurements of FRD have been done extensively by many people. Only Heacox (1986) studied the fibre properties theoretically for the application of using bare fibre to couple the point source between telescope and spectrometer.

Microbending-induced beamspreading in optical fibres has been analyzed by Gloge (1972), who developed an equation to describe the distribution of optical power (P) in a fibre. This equation is solved by Gambling (1975) in the case of a collimated input beam at incident angle θ_0. An asymptotic form is given by Heacox (1986) and the output angular flux distribution in the far field is approximately given by

$$P(\theta\,|\,\theta_0) \propto \exp[-\frac{1}{2}(\frac{\theta-\theta_0}{\sigma_{BS}})^2\ ] \qquad (2-15)$$

Where

$$\sigma_{BS} = \frac{\lambda}{d_f}[\ \frac{1}{2n}\frac{L}{L_D}+0.19\ ]^{1/2} \qquad (2-16)$$

Where L is the fibre length. λ is the light wavelength. d_f is the fibre core diameter, n is the refractive index of the fibre core. L_D is a constant, called the modal diffusion length, which characterizes the microbending.

From this result, Heacox derived that the change in focal ratio of the input beam is given roughly by

$$\theta_{\max} \approx 2F^2\sigma_{BS} \qquad (2-17)$$

Where F is the focal ratio of the input beam.

Clearly, to reduce FRD, one must keep σ_{BS} and F small. There are some parameters which can affect σ_{BS}. (1) Short Fibre lengths are helpful to reduce FRD. (2) FRD will be more serious at long wavelength and for fibre with small core diameter. From equation (2-5) it is obvious that for the IFU, a fast beam will produce a small pupil size on the fibre entrance and thus need a small fibre core size. It needs to be noted that in the previous discussion, the fibre core is allowed to be oversized. This has a potential advantage to reduce the FRD.

Unfortunately many people don't consider the effect of above parameters on FRD when comparing the FRD of different fibres with different parameters (such as different core sizes). As a result, fibres with small core sizes are often identified as bad fibre because of the big FRD. These comparisons are limited by the fact that it is difficult to get fibres with the same geometrical parameters from different manufacturers. However, if the comparisons need to be carried out, one must at least scale the geometrical parameters to the same values and thus makes the comparisons more reliable.

2.7 Fibre Coupling Efficiency

In the previous discussions, the telescope pupil is imaged onto the fibre entrance and it is assumed that the fibre core is oversized to allow the pupil image to be fully coupled into the fibre. However when optical aberrations are present, a practical question is: how much the fibre core size should be needed and how much light can be coupled into the fibre? These questions will be discussed in this section.

2.7.1 Preliminary Mathematical Theory

In order to make the derivation feasible, the following assumptions are necessary.

(a) The point spread function of the optical system is space-invariant (independent of object point coordinates).

(b) The light from the object plane is incoherent.

For an optical system with a lateral magnification of 1, the irradiance at the image plane can be expressed by (Frank and Leno 1996)

$$I(X,Y) = \iint I_0(x,y)G(X-x,Y-y)dxdy \qquad (2-18)$$

Where I is the irradiance at the image plane. I_0 is irradiance at object plane. G is point spread function of the optical system.

For a linear optical system, from formula (2-18), one can get the irradiance at the image plane for an optical system with a lateral magnification of M

$$\begin{aligned} I(X,Y) &= \iint M\cdot I_0(x,y)G(X-x,Y-y)dxdy \\ &= \iint I_i(x,y)G(X-x,Y-y)dxdy \qquad (2-19) \end{aligned}$$

Where M is the lateral magnification of the optical system. I_i is the irradiance at the image plane when there is no optical aberration or diffraction, i.e. the ideal irradiance of the image.

The integral is 2-D convolution of the function I_i and G:

$$I = I_i \otimes G \qquad (2-20)$$

2.7.2 Mathematical Model of Multi-mode Fibre Coupling

For an IFU, a multimode optical fibre is used to collect the light from the telescope. The telescope pupil is projected by the microlens onto the fibre entrance. In this application, the scene of the telescope pupil is an extended image. This section will investigate how the optical aberration affects the coupling efficiency.

Optical aberrations contribute to the spreading of the optical image. It can be expressed by a Point Spread Function (PSF) as a 2-D circularly symmetrical Gaussian function (Jacobs 1999). The polar representation of this function is

$$G(r) = \frac{1}{2\pi\sigma^2}\exp(-\frac{r^2}{2\sigma^2}) \qquad (2-21)$$

Where σ is the standard deviation of the Gaussian function. $r=(x^2+y^2)^{1/2}$. The coefficient of $1/(2\pi\sigma^2)$ scales the function to produce a volume under the curve of unity.

Assume that the ideal pupil image has unit intensity over the whole field of the image. So, it can be expressed by a 2-D circularly symmetrical rectangular function. The polar representation of this function is

$$I_i(r)=\begin{cases}1, & |r|<\dfrac{d}{2}, \\ 0, & otherwise\end{cases} \qquad (2-22)$$

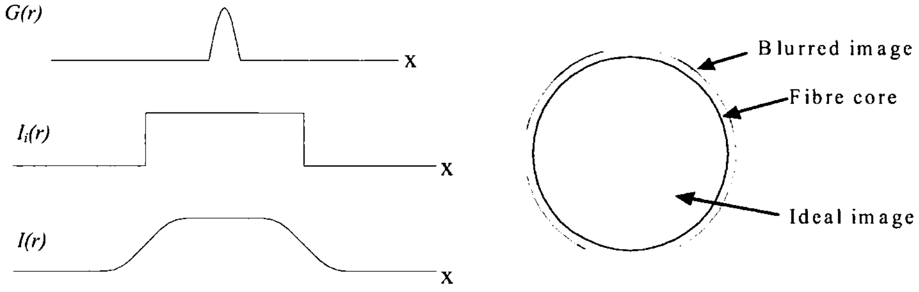

Figure 2-7. The schematic process of an image blurred by the optical aberrations. *G(r)* is the PSF of the optical system. *$I_i(r)$* is the ideal scene image (pupil image). *I(r)* is the blurred image.

The process by which an ideal scene image is blurred by the optical aberration is schematically shown in Figure 2-7. The convolution of the Gaussian function with the rectangular function yields the following analytic result for the burred image

$$\begin{aligned}I(r)&=I_i(r)\otimes G(r)\\&=\frac{1}{4\delta}\left(\frac{2}{\pi}\right)^{1/2}\left\{erf\left[\frac{d/2-r}{\sqrt{2}\delta}\right]-erf\left[\frac{-d/2-r}{\sqrt{2}\sigma}\right]\right\}\end{aligned} \qquad (2-23)$$

Again I(r) is also a circularly symmetrical function.

The error function erf(x) is expressed as

$$erf(x) = \frac{2}{\sqrt{\pi}} \int_0^x e^{-t^2} dt \qquad (2-24)$$

and erf($\propto$)=1.

The coupling efficiency is defined as the ratio of the collected flux of the light when the fibre core diameter is of finite size to that when the fibre core size is infinite. It is expressed as

$$\eta = \frac{F(R)}{F(\propto)} \qquad (2-25)$$

Where *F(R)* is the flux of light collected by the fibre when the fibre core radius is R. *F($\propto$)* is the flux of light collected by the fibre when the fibre core radius is infinite.

As the irradiance profile I(x) has circular symmetry, F(R) and F($\propto$) can be calculated as

$$F(R) = \int_0^R I(r) 2\pi r dr \qquad (2-26)$$

$$F(\propto) = \int_0^\propto I(r) 2\pi r dr \qquad (2-27)$$

So the coupling efficiency is

$$\eta = \frac{\int_0^R I(r) 2\pi r dr}{\int_0^\propto I(r) 2\pi r dr} \qquad (2-28)$$

Where *I(r)* can be calculated according to formulae (2-23). A simple way to calculate the coupling efficiency is using a numerical method. *F(R)* and *F($\propto$)* can be expressed as power series by integrating formulas (2-26) and (2-27). Here the numerical method is used to calculate the coupling efficiency and a computer C program was designed to calculate *I(r)* and the coupling efficiency. Some calculations and results will be discussed in the next subsection.

2.7.3 FMOS IFU Fibre Core Size

In this subsection, the formulas derived in the previous subsections are used to calculate the FMOS IFU pupil profile after it is blurred by the IFU fore-optics and microlens. The pupil image is formed on the back surface of each microlens and in ideal case will be with a diameter of 2x28 microns. As there is optical aberration for the IFU optical system, the pupil image is blurred. The optical aberration can be expressed by the RMS spot radius and the RMS radius is $\sigma=3.6$ microns over the whole field. The blurred image of the telescope pupil was calculated by formulae (2-23). Fig. 2-8 is the cross section profile of blurred pupil image of FMOS IFU. The coupling efficiency is calculated according to equation (2-28) and the result is shown in Fig. 2-9. The FWHM is almost unaffected by the blurring and is still 2x28 microns.

From the calculations, some general conclusions can be drawn. When fibre core size is the same as ideal scene, there is still some light that may not be collect by the fibre and will be lost. It is obvious that the fibre core needs to be oversized in order to collect more light. The above examples suggest that when the fibre core radius is oversized σ and 2σ, about 97% and 99% of the light can be collected by the fibre, respectively. The conclusions are summarized as

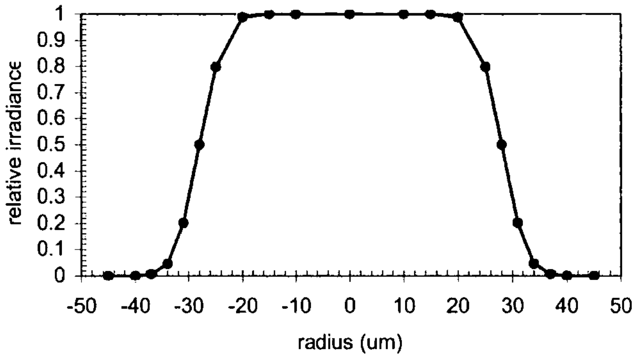

Figure 2-8. The cross section profile of the pupil image irradiance of FMOS IFU. The relative intensity is scaled to a unit. The pupil image size is 2x28 microns. The optical aberration has RMS radius $\sigma=3.6$ microns. The FWHM of the profile is still about 2x28 microns, the same as the ideal image.

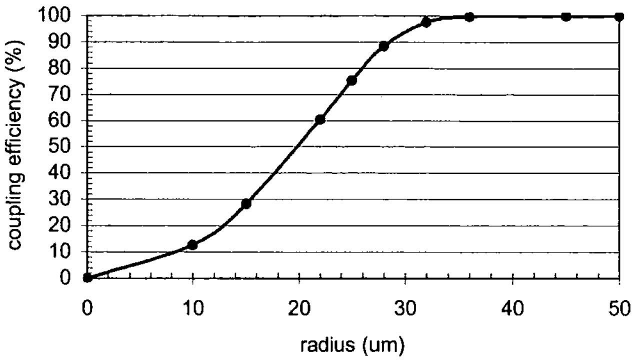

Figure 2-9. The coupling efficiency vs. fibre core radius curve for FMOS IFU. The coupling efficiency is 88.4% at radius 28 microns, 97.5 % at radius 32 microns ($\sim 28+\sigma$) and 99.8% at radius 36 microns ($\sim 28+2\sigma$).

1. It is suggested that the fibre core radius should be between $D/2 + \sigma$ and $D/2 + 2\sigma$. Where D is the ideal pupil image size.

2. When optical aberration is much smaller than the image size, FWHM is almost not changed after the scene is broadened by the optical aberrations.

In an actual instrument, there is a centering position error between the centre of microlens and fibre core. If this centering error needs to be considered, the fibre core size needs to be further oversized. In this case, the fibre core radius should be between $D/2 + \sigma +\ t \sim D/2 + 2\sigma +\ t$. Where t is the centering error.

2.8 Figure of Merit of the IFU

There are different methods to define the figure of merit for the system performance of the imaging spectrometer. A figure of merit, which is proposed by Allington-Smith et al. (1998), is given as $Q = N_{spatial} \cdot N_{spectral} \cdot$ efficiency. Where $N_{spatial}$ and $N_{spectral}$ are the numbers of independent samples in the spatial and spectral directions, respectively. Based on Jacquinot's method (1954), a figure of merit was given by Atherton (1983) as $Q = B \cdot \tau \cdot A \cdot \Omega \cdot R \cdot N_{\lambda}$. Where B is the source function, τ is the efficiency, A is the area of the collimated beam, Ω is the solid angle subtended by the entrance aperture, R is the resolution power, N_λ is number of parallel spectral channels, i.e. spectral multiples. Atherton used this figure of merit to compare the performances of the imaging long slit spectrograph, imaging Fabry Perot spectrometer and imaging Fourier Transform spectrometer.

However, for fibre IFU system, the situation is different. In principle, there is no limitation to the size of the field of view. The number of fibres and microlenses can be as larger as possible. From the discussions in the previous sections, the performances of the fibre IFU system are decided by fibre FRD, the actual fibre core size and so on. The optical aberrations and registration errors between fibre bundle and microlens array are included in the fibre oversizing constant K_{pup}. If fibres are not oversized, this will result in a light loss and so a low throughput. Therefore, the performance of a fibre IFU can be estimated according to a figure of merit, which is given as

$$Q = \sqrt{\frac{\Omega A}{\Omega_o A_o}}\ \eta \qquad (2-29)$$

Where η is the efficiency of the IFU system. It includes the reflection and transmission loss of the IFU optics and the light loss in the coupling process. Ω and A are the solid angle and area of a sample element at the telescope focal plane. The sample element is magnified by IFU fore-optics and sampled by a microlens and then coupled onto a fibre. After this sample element is outputted from IFU, i.e. at pseudo-slit, the sample element is represented as Ω_0 and A_0. An ideal IFU will have a figure of merit of 100%.

For lenslet +fibre +lenslet IFU, Ω A is the solid angle and the area of a sample element at the telescope focal plane. The sample element is coupled onto a fibre. However, at the IFU output end, i.e. at the spectrograph slit, from equations of (2-12) and (2-5), the solid angle and sample area are not conserved and they are given as

$$\Omega_0 A_0 = \Omega A(K_{pup} K_F)^2 \qquad (2-30)$$

So, the figure of merit for the IFU is

$$Q = \frac{1}{K_{pup} K_F} \eta \qquad (2-31)$$

One can derive that equation (2-31) is suitable for both lenslet +fibre +lenslet and lenslet +fibre IFU systems. Again from this equation, it is evident that compared with FRD, the oversizing of fibre core has the same effect to reduce the system performance of the IFU.

Clearly, for both lenslet+fibre+lenslet and lenslet+fibre IFU systems, in order to reduce K_{pup}, each fibre needs to be correctly centered to its microlens. As a microlens array is used to sample the telescope focal plane image (sky image), one needs a 2-D fibre bundle and each fibre in the fibre bundle needs to be accurately centered to the corresponding microlens. Currently microlens array can have a pitch accuracy of better than 1 micron, so the microlens-microlens position error can be negligible. Thus the fibre-fibre position on the fibre bundle is crucial to reduce to the coupling loss between microlenses and fibres. It is difficult to build a 2-D fibre bundle with small position error and this is a disadvantage of this IFU system.

Let us consider the example of the FMOS IFU. Here the microlens aperture diameter and the focal length are 500 μm and 2.8 mm respectively. The ideal pupil image size is about 67 μm and fibre core is oversized as 80μm, so K_{pup} is 1.19. The pupil image is fed to fibre at F/5 (defined by two opposite corners of the microlens) and emerges at F/4, so the fibre FRD factor K_F is 1.25. If we assume that there is no light loss in the coupling process because the fibre is oversized enough to accommodate the registration error and the optical aberration. This results in Q= 0.67η. The IFU performance is dominated by both the oversizing of the fibre core and the fibre FRD.

2.9 Summaries and Conclusions

In this chapter, the discussion is concentrated on lenslet +fibre+ lenslet and lenslet +fibre systems. The functions of IFU fore-optics are to magnify the telescope focal plane image to make it suitable for microlens sampling and create a telecentric sky image. The advantages of telecentric designs are demonstrated. It is also shown that high magnification fore-optics can reduce the non-telecentric angle on the fibre entrance.

For IFU systems, microlenses can be used to couple light onto the fibres. Demonstrated is how to design a microlens and fibre system which can maximize conservation of the AΩ product. It is evident that high magnification fore-optics can reduce geometrical FRD for the input microlenses. At the fibre output end, the AΩ product can be exactly conserved with a suitable arrangement of the output microlenses.

Fibre properties are also discussed. Fibre FRD is a function of fibre modal diffusion length, fibre core size, fibre length and wavelength. The oversizing of fibre core can reduce FRD in a sense. One must be careful and make sure that all the conditions are the same (or at least need to scale these parameters to be the same) when comparing the performances of different fibres.

A mathematical model is derived which can be used to calculate the optimized fibre core size according to the required coupling efficiency. Extreme oversizing of fibre core will reduce the IFU system performance. It is show that the fibre core radius should be between $D/2 + \sigma + \quad t \sim D/2 + 2\sigma + \quad t$ in order to avoid extreme oversizing and light loss because of optical aberration and alignment error between microlens and fibre.

A figure of merit for IFU system is derived, which can be used to compare and estimate the performance of the IFU system. It has shown that the oversizing of the fibre core and the fibre FRD have the same effect to reduce IFU system performance, i.e. both can linearly reduce the figure of merit of the IFU system. Finally, the IFU for FMOS project is used as a practical design example to show the applications of these theories.

Chapter 3

Highly Efficient All-reflective Spectrometer/Imager for UKIRT

ABSTRACT

In this chapter, the design of a Compact All-reflective near InfraRed (1-2.5 μm) Spectrograph and imager (CAIRS) is described. CAIRS is designed for the UK Infrared Telescope (UKIRT). CAIRS is designed to provide a comprehensive spectroscopic and imaging capability in the near infrared. It uses one slit or two slits for use with image slicers so that it can provide imaging spectroscopy over an extended field. It can also work with a fibre IFU and provide the imaging spectroscopy. Different gratings can be used in order to reach resolving powers up to 10,000.

As the instrument uses only mirrors, there is no chromatic aberration and all primary aberrations are almost completely eliminated over a large field of view. Details of CAIRS can also be found in a paper by Ren et al. (1997a).

3.1 Introduction

There are many spectrographs which are designed for working over the 1-2.5 μm wavelength range. In many cases, mirrors are desired for the spectrometer design considering the potential ability to work at an extremely broad wavelength range and the limit to the available size of the lens. Most of these existing spectrographs are dedicated for use with long slit or multi-slits and make use of the telescope Cassegrain hole in the beam to position on-axis fold mirror or detector within the un-illuminated central portion of the pupil. This simplifies the optical design and can avoid using off-axis optics. These instruments work well with the long slit or multi-slit model and no light is lost provided that the object and image between telescope and spectrograph is conjugated.

However, for an integral field spectrometer using fibres, the relationship of the conjugation between telescope and spectrometer does not exist. Since the hole will be filled by the coupling fibres, retrofit of such a spectrograph with a fibre coupler will entail a light loss due to shadowing (Heacox 1986). This is the case for SMIRFS, which provides a NIR IFS for UKIRT (Haynes 1998). The NIR fibre IFU can operate over 0.9-1.8 μm wavelength range without cooling. Examples of these instruments include FMOS (Maihara et al. 2000) for the Subaru 8-meter telescope, the AUSTRALIS design study (Taylor 1998) for VLT, AOIFU (Guérin 1998) for Canada-France-Hawaii Telescope, COHSI (Kenworthy et al. 1998). However, some work (Tecza and Thatte 1998, Haynes et al. 2000) shows that it may be possible for fibre IFU to be cooled and operated over 1-2.5 μm wavelength range. It is obvious that the no-obstruction design is necessary for the fibre IFU spectrograph.

The compact all-reflective near infrared spectrograph/imager is designed for UKIRT. It is designed to function over the J, H and K near-infrared bands covered by a ROCKWELL 1024x1024 HgCdTe HAWAII detector. CAIRS is designed to work with IFU and long slit or multi-slits. When working with fibre IFU, a microlens array at the fibre input entrances is used to sample the sky image. At the output ends of the fibres, linear microlens arrays are used to convert fibre output beam to a suitable F number (F/36) for CAIRS. In long slit or multi-slit mode, it can accept the F/36 beam directly from UKIRT through the slit mask. It can also work with the Advanced Image Slicer (AIS) (Content 1997). With IFU or AIS, CAIRS can provide the imaging spectroscopic ability. In this chapter, only the slit mode is discussed, as the IFU can be a late adding unit.

3.2 Instrument Specifications and Requirements

CAIRS has two modes, one is long slit spectroscopy (using one slit or two slits), the other is imaging. It uses all-reflective mirrors with no obstruction. The design requirement and goals include the following: (a) This instrument should be capable of obtaining both high spatial resolution (0.1 arcsec/pixel) to allow detailed studies of the composition of star forming regions and high quality direct imaging which is valuable to study the spatial structure and temperature distribution of particulate disks around young solar-type stars. (b) One slit and two-slits should be provided. Two slits are needed for use with image slicers. (c) High spectral resolutions are achievable by using high ruling density grating. The high spectral resolving power should be sufficient to measure the velocity dispersion in unresolved stellar systems such as galactic nuclei. (d) The instrument should show no vignetting until the anamorphic factor reaches 1.4. (e) An all-reflective mirror system with no obstruction is required to obtain high transmission and freedom from chromatic aberration. (f) The design should be compact to keep the whole instrument in a cryogenic dewar. The instrument specifications are summarised as follow:

- Grating. 300, 150, 75/mm ruling density.
- Diffraction order. Up to third order.
- Slit. Slit width 0.5 arcsec, or 0.25 arcsec. All slits are 1.8 arcmin length.

(a) For image slicers, two slits can be used, each 1.8 arcmin long, displaced by 512 pixels in the dispersion direction.

(b) In order to utilise long wavelength range, one slit can be used, with 1024 pixels long and dispersing 1024 pixels.

- Resolving power(R). The camera can accept anamorphic factor 1.4, with a maximum resolving power of 5000 (0.5 arcsec slit width) or 10,000 (0.25 arcsec slit width).
- Image scale. 0.1 arcsec / pixel high spatial resolution.
- An imaging mode which images the full field (1.8 arcmin by 1.8 arcmin) on to the detector if the grating is replaced by a flat mirror.
- Beam size. Pupil size of 50 mm.
- IR detector array. ROCKWELL 1024 x 1024 HgCdTe detector array with 18.5 μm x 18.5 μm pixel pitch.

3.3 Optical Design

CAIRS consists of three cryogenic parts: collimator, grating and camera. When the grating is replaced by a flat mirror, it works in the imaging mode , and the incident angle and reflected angle on the flat mirror is 22.5 degrees, respectively. Otherwise it works in the spectroscopic mode.

In spectroscopic mode, CAIRS can work with one or two slits. We envision that two slits will be useful with the Advanced Image Slicer (AIS). Two slit slicer was also used by other instrument (Murphy et al. 1999), where field of view is more important than spectral coverage. Together with the AIS, this will provide a compact system for imaging spectroscopy over a large field of vied. The optical layout of the CAIRS when working in two slits spectroscopic mode is shown in Fig. 1a and Fig. 1b. The two slits are on the telescope focal plane. Fig. 1b is rotated about the Z-axis by 90 degrees with respect to the Fig. 1a. It is evident that the design is very compact.

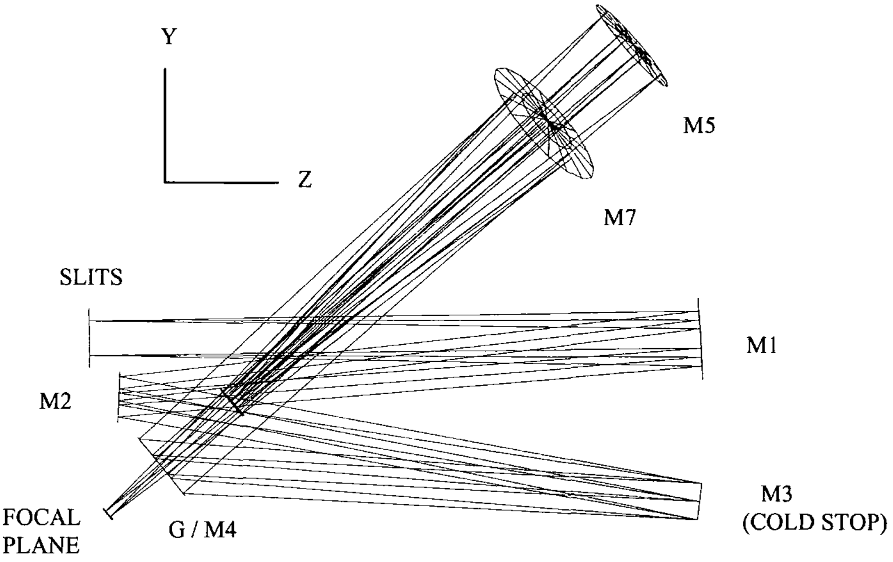

Figure 1a. The optical layout of the CAIRS (top view)

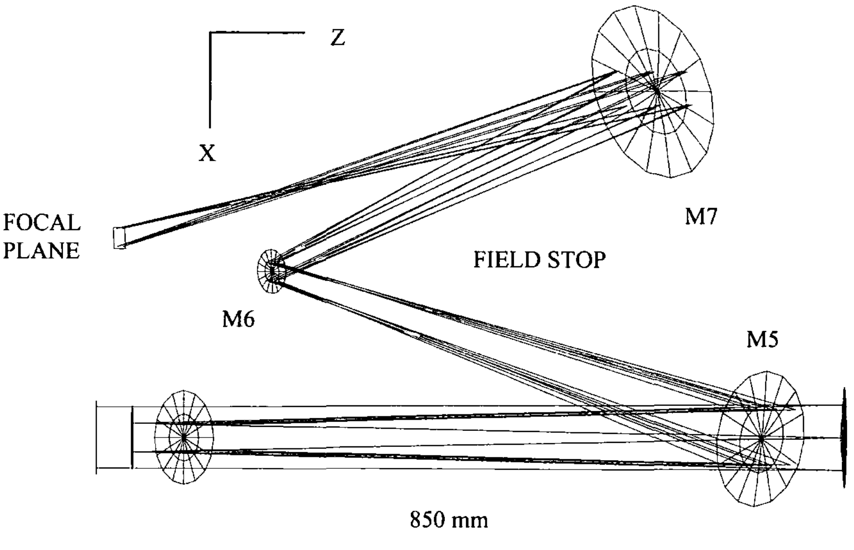

Figure 1b. The optical layout of the CAIRS (side view)

A folded design must be adopted to accommodate the required collimator focal length of 1750 mm in a compact cryogenic space. The collimator consists of three spherical mirrors M1, M2 and M3 which are on the same plane. The beam size on the grating is 50mm. Mirror M1 and M2 form an image of UKIRT exit pupil on the third mirror M3 which is the optical cold stop of the CAIRS. In a previous design, only one mirror was used for the collimator, but this design was excluded because the physical size was too big. We also tried to use a two mirror system for the collimator, but found that it is too difficult to image the exit pupil of UKIRT to a suitable place and at the same time to keep a good image quality.

Different gratings can be mounted to get different resolving powers. The grating can be replaced by a flat mirror which permits imaging of the whole field in undispersed light.

The camera consists of three mirrors of M5, M6, M7. M5 is an elliptical surface and is the only aspheric mirror in the design. The aspheric surface has no high order aspheric deformations and so is easy to fabricate. M6, M7 are convex and concave spherical surfaces, respectively. An intermediate image is formed after mirror M5 where a field stop can be erected. The three mirrors are tilted and decentered about the optical axis. However, they have a common optical axis and are symmetrical to the axis. This kind of three-mirror system was used for camera designs elsewhere (Torr et al. 1993, Dohlen 1996, Ren 1997b). When optical systems use rotationally symmetric components, coma and distortion are corrected to the first order by the symmetry of the system.

Two mirrors were considered for the camera but this was excluded because it needed all aspheric surfaces and the image quality requirements were not satisfied. The two mirror systems had been analysed with third-order aberration theory by Gelles (1975) and Wynne (1969). In some applications, it can be used instead of a three-mirror system. The solution consists of introducing additional variables: decentering and aspheric figuring of the individual elements, in addition to tilt. In fact, for an unobstructed imaging system, a minimum of three spherical mirrors is necessary to correct central coma and astigmatism in a system consisting of tilted, centred mirrors (Buchroeder 1970).

Table 3-1 summarises the optical technical data of the CAIRS.

Table 3-1. Optical Technical Data of CAIRS

Collimator	$f_1 = 1750$ mm, F/36, three spherical mirrors
Grating	75 gr/mm, 150 gr/mm, 300 gr/mm, or a flat mirror for imaging
Camera	$f_2 = 500$ mm, F/10, two spherical mirrors, one elliptical mirror

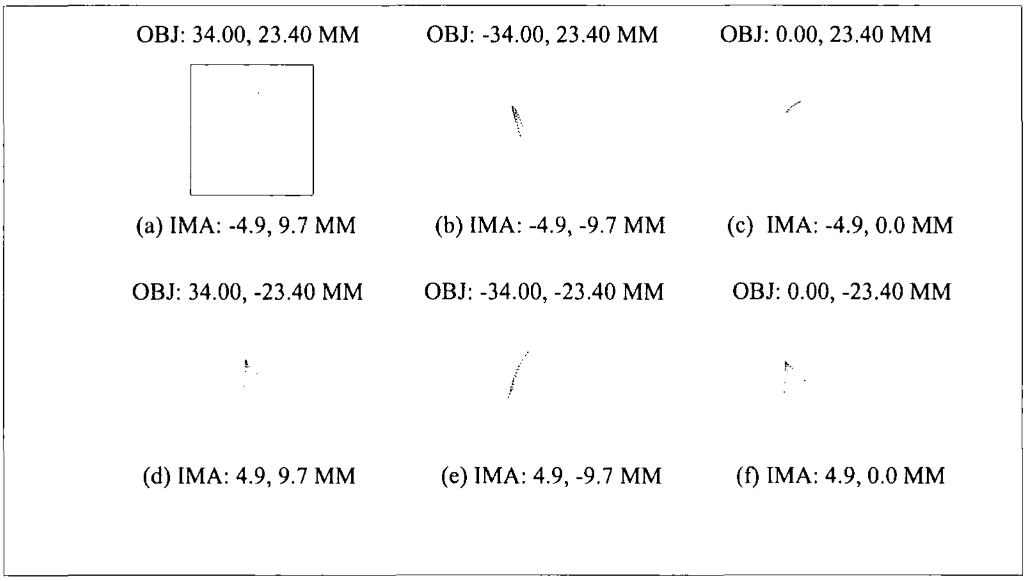

Figure 3-2. The spot diagrams for two-slit spectroscopic mode with wavelength 2.2 μm. The box represents one detector pixel size.

The whole optical system was optimised in the spectroscopic (with different gratings) and the imaging mode simultaneously. All the mirrors are silver coated and the average reflection is about 98% in the infrared for each surface. In order to show the imaging quality, one spectroscopic configuration from Table 3-2 is chosen. The central wavelength is 2.2μm and diffraction order number is 2. The grating is 150/mm. In this configuration, two slits are used and the two-slit distance is 2x23.40 mm on telescope focal plane. In this case, the anamorphic factor will reach 1.38. Fig. 3-2 is the spot diagram at 2.2μm wavelength for the two-slit spectroscopic mode with the 150/mm grating. Fig. 3-3 and Fig. 3-4 are the spot diagrams at wavelength of 2.17μm and 2.23μm, respectively. Fig. 3-5 shows how the spectra are laid on the detector in the two-slit mode for the case described above. Note that this may require the use of a band-pass filter to avoid overlaps between the spectra. The spectral positions on the detector focal plane and the correspondent image positions on Fig. 3-2, Fig. 3-3 and Fig. 3-4 are shown in Fig. 3-5. The box in the spot diagram represents one detector pixel size (18.5μm x 18.5μm). Ray trace diagrams show that over the whole field in different modes, the spots are all less than the size of one detector pixel and the Airy disk. Distortion is less than 1.5 per cent. Imaging quality is diffraction limited over the whole field of view.

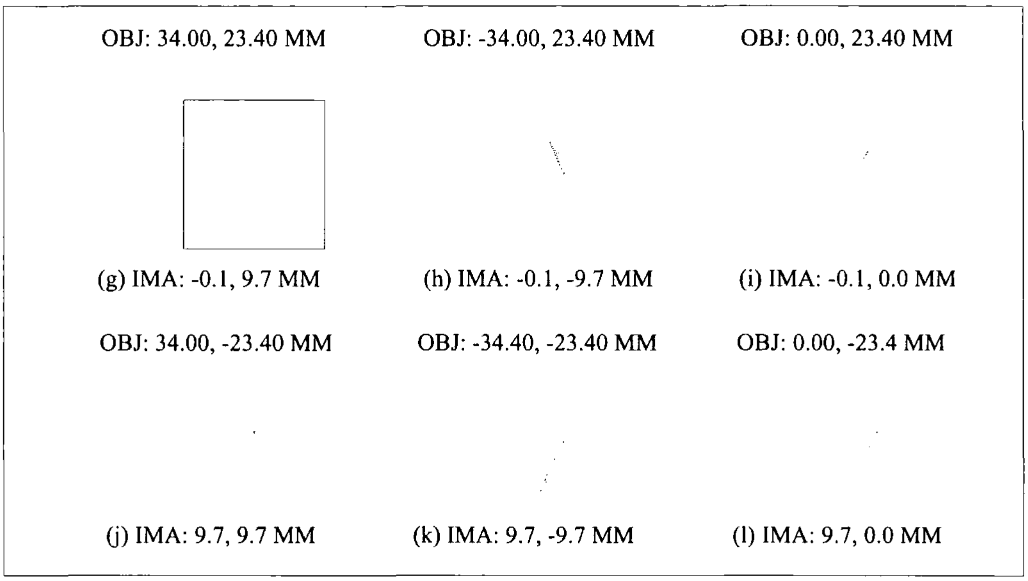

Figure 3-3. The spot diagrams for two-slit spectroscopic mode with wavelength 2.17 μm. The box represents one detector pixel size.

For CAIRS, as the collimator uses three spherical surfaces, the main contributor of the aberration is the collimator, and the aberration of the camera is very small compared with the collimator. Since CAIRS uses only mirrors, chromatic aberration is not a problem.

Stray light must be tightly controlled for infrared spectroscopic instruments. The philosophy for CAIRS is to suppress stray light through design. Systems requiring high stray light rejection almost always require a reimaging optical configuration (Philip 1983). This has the advantage of more opportunity for placement of additional baffling for the control of stray light. CAIRS has two stops, the field stop and Lyot cold stop, which are very useful in eliminating out-of-field radiation and diffracted radiation, respectively. The grating has the potential to diffract

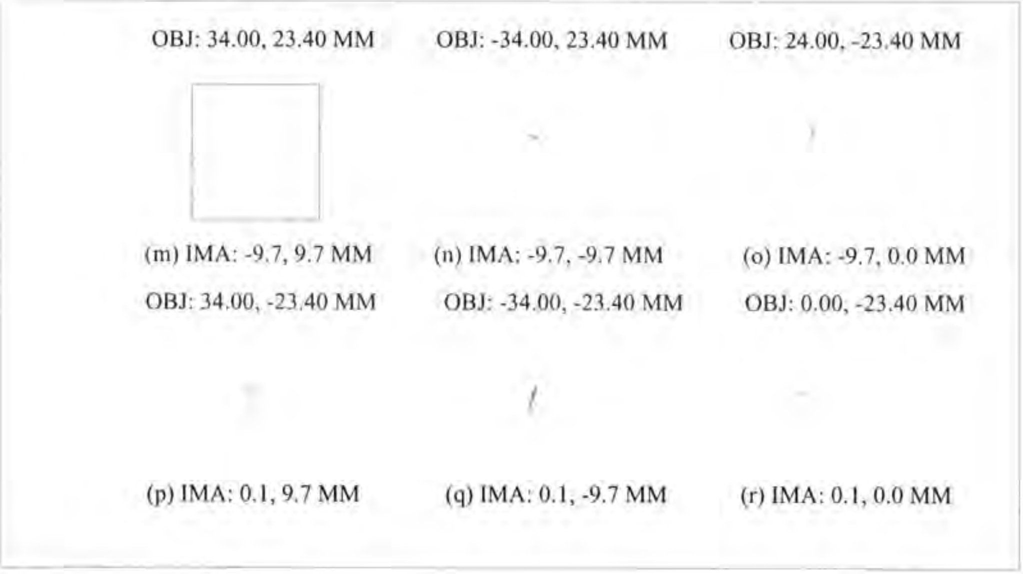

Figure 3-4. The spot diagrams for two-slit spectroscopic mode with wavelength 2.23 μm. The box represents one detector pixel size.

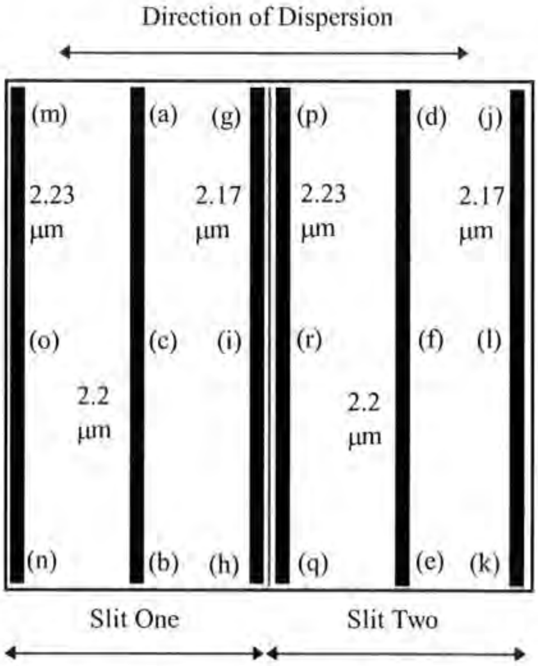

Figure 3-5. Illustration of the spectra on the detector focal plane for two-slit mode.

off-axis stray light. A field stop is placed at the intermediate focus after the grating and obstructs any imaged light that is outside the field of view. A cold stop is placed at the location of the image of the telescope pupil. Finally, since the components of the CAIRS may be emitting radiation in the infrared, the whole device of CAIRS is encased in a cold dewar to avoid infrared thermal radiation.

Different spectroscopic configurations have been calculated for CAIRS when the slit width is 0.5 arcsec. Some calculations are shown in Table 3-2.

Table 3-2. Some Possible Spectroscopic Configurations

Diffraction order	Ruling density (/mm)	Incident angle (deg)	Groove angle (deg)	Wavelength range		Anamorphic factor	Resolving power
				One slit (nm)	Two slits (nm)		
Central wavelength = 2200 nm (Blaze wavelength = 2200 nm in order specified)							
1	75	27.62	5.12	481	240.5	1.08	1011
2	75	32.79	10.29	246	123	1.16	2133
3	75	38.04	15.54	166	83	1.26	3415
1	150	32.79	10.29	246	123	1.16	2133
2	150	43.43	20.93	126	63	1.38	4938
3	150	54.90	32.4	83	41.5	1.71	9355
1	300	43.43	20.93	126	63	1.38	4938
2	300	68.09	45.59	58	29	2.47	19223
Central wavelength = 1560 nm (1st order blaze wavelength = 2200 nm)							
1	150	30.20	10.29	143	71.5	1.12	1556
2	150	38.04	10.29	125	62.5	1.26	3415
1	300	38.04	20.93	125	62.5	1.26	3415
2	300	54.90	20.93	62	31	1.71	9348
Central wavelength = 1250 nm (1st order blaze wavelength = 2200nm) (2nd order blaze wavelength = 1100nm)							
2	150	34.21	10.29	124	62	1.19	2464
2	300	46.45	20.93	63	31.5	1.45	5914

In Table 3-2, there is no vignetting when anamorphic factor is less than 1.38.

3. 4 Summaries and Conclusions

CAIRS uses an all reflective design. This results in good transmission and no chromatic aberration, which means that there is the potential to extend its working wavelength (for example, it can extend to 2.8-5.4 μm). Except for one elliptical mirror, all mirrors are spherical surfaces. The camera consists of three mirrors, which share the same axis and are thus easy to mount.

CAIRS can be used with one slit, two slits and works in spectroscopic or imaging mode. It has no vignetting until the anamorphic factor reaches 1.4. It can use different gratings (75/mm, 150/mm, 300/mm), and works at different wavelengths (J, H and K wave band). Image quality in the whole field of view is completely diffraction limited in both spectroscopic and imaging modes. As there is no light obstruction, it is suitable for working with fibre IFU.

Chapter 4

Apochromatic lenses for NIR Astronomical Instruments

Abstract

A method based on the Herzberger approach has been investigated for the selection of glasses for apochromatic correction over the near-IR wavelength range. The method avoids algebraic complexity and simplifies the glass selection processes. Doublet and triplet glass combinations can be chosen directly from the partial dispersion versus V number plot. Good combinations of NIR doublet and triplet are given. Design examples show that the method is practical and efficient.

Details of this chapter can also be found in a journal paper (Ren and Allington-Smith 1999).

4.1 Introduction

With the fast evolution of modern infrared arrays, there is an increased trend of using lenses in the 1-2.5 μm wavelength range for NIR astronomical instruments (Moorwood and Delabre 1990, Persson et al. 1992, Warren and Rudy 1994, Nadeau 1994, Willner 1994, Elston 1998, Pogge et al. 1998, Lenzen et al. 1998). Refractive systems are attractive for many applications because they can accommodate wide fields of view and fast focal ratios while permitting a compact and un-obscured optical design.

For refractive optical design, the first step is to choose potential optical glasses to correct chromatic aberration. The control of chromatic aberration through the selection of glasses is one of the most extensively studied subjects in the field of lens design (Robb and Mercado 1983, Buchdahl 1985, Lessing 1957, 1958, 1970, Stephens 1959, 1960, Mercado and Robb 1981, Sands 1971, Forbes 1984, Robb and Mercado 1983, Robb 1985, Sigler 1986, Herzberger and Salzberg 1962). Different glass selection methods have been investigated at visible wavelength that can yield apochromatic and superachromatic lens systems. The term apochromatic and superachromatic mean paraxial colour correction at three and four wavelengths, respectively.

One approach uses the Buchdahl glass dispersion equation to select glasses for systems of thin lenses that yield apochromatic and superachromatic colour correction. Robb (1985) and Buchdahl (1985) use this method to choose two kinds of materials for a doublet. Another approach uses Herzberger's relative partial dispersion and Abbe number equation, which can also yield apochromatic and superachromatic colour correction. Herzberger and Salzberg (1962) use this method to select glasses which can reach the same performance.

However, most of these studies were done at visible wavelengths. Little attention has been given to the Near Infrared (NIR) wavelengths (1 – 2.5 μm). The use of a doublet is often limited by the small number of available glasses and the inability of a doublet to achromatise over the whole NIR wavelength range. No paper has been found about the choice of glasses for a triplet for the NIR astronomical instruments. The Buchdahl glass dispersion equation is mathematically too complex for the selection of glasses for doublets. From the point of view of optical engineering applications, it is important to find a simple and practical method to choose glasses for the chromatic-aberration correction.

This chapter investigates a method that use Herzberger's approach to choose glasses to design doublet and triplet for apochromatic correction at the NIR wavelength range. Doublet glasses or triplet glasses can be chosen directly from the partial dispersion – V number plot, without algebraic complexity. Finally, two design examples are given.

4.2 Glass Partial Dispersion and V Number

For NIR glasses, Sellmeier and Herzberger dispersion formulas are used to calculate the index of refraction. The glass catalogues of various manufacturers, available in digital form, can be used to fit the index data and calculate the coefficients of the dispersion formulas. Then, the dispersion formulas can be used to calculate the optical index at any wavelength. The more data one enters, the more accurate will be the fit. The glass index data in this paper is from the infrared glass catalogue published with the Zemax optical design program (1998). These data are provided by Schott (Schott Spec Sheet, 1991) or compiled from published source (*Handbook of Optics,* 1995), and their accuracy has been confirmed by Feldman's measurement (Feldman 1979).

For infrared glasses, Herzberger dispersion formula (Herzberger 1962) is often used to calculate the glass index

$$n = A+BL+CL^2+D\lambda^2+E\lambda^4+F\lambda^6 \qquad (4-1)$$

Where $L=1/(\lambda^2-0.028)$. Schott uses the Herzberger formula to calculate its glasses for NIR. The three-term Sellmeier dispersion formula can also be used to calculate the index of infrared glass with adequate accuracy (Sutton 1961)

$$n^2 - 1= K_1\lambda^2/(\lambda^2 - L_1) + K_2\lambda^2/(\lambda^2 - L_2) + K_3\lambda^2/(\lambda^2 - L_3) \qquad (4\text{-}2)$$

As is the case for visible optical wavelength, for infrared wavelength the V-number and partial dispersion are defined for a stated spectral region $\lambda_1 < \lambda_2 < \lambda_3$ as:

$$V = \frac{n_2 - 1}{n_1 - n_3} \qquad (4-3)$$

$$P = \frac{n_2 - n_3}{n_1 - n_3} \qquad (4-4)$$

Where n_1, n_2 and n_3 are the indices of refraction at the short wavelength λ_1, central wavelength λ_2 and long wavelength λ_3, respectively. It is important to note that λ_1, λ_2 and λ_3 are also the wavelengths to be corrected for chromatic aberration.

The plot of partial dispersion versus V-number is extremely important in choosing glasses that will permit secondary colour correction. Unfortunately, many glass catalogues provided with computer design programs (such as Zemax) or by glass companies only provide the V-number and P data that are calculated at the F-d-C wavelengths. In fact, these data are useless for glass selection for NIR, as they will be different at visible and NIR wavelengths. Shannon (1996) has calculated V-number and P values of some visible optical glasses in different wavelength ranges. He also compared the V-number versus P plots of these glasses in the visible F-d-C and the infrared wavelength ranges, and found that the glass distributions change dramatically when the wavelength shifts to the infrared.

Herzberger (1962) calculated the partial dispersion P of some infrared glasses in the wavelength 1.5 – 5.0 μm. He used the index for 3.5 μm as the central wavelength λ_2. It is found that the distribution of glasses on the V-versus-P plot for differing short wavelength λ_1, central wavelength λ_2 and long wavelength λ_3 is also dramaticly different and this has generally been ignored. For example if λ_1, λ_2 and λ_3 are 1, 1.75 and 2.5 μm, respectively, the V-number and P of glass CaF2 is 54.6 and 0.488, respectively, compared with 91.5 and 0.591 when λ_1, λ_2 and λ_3 are 1.25, 1.65, and 2.2 μm, respectively. So the V-number and P data must be calculated according to the wavelengths at which one corrects for chromatic aberration.

NIR astronomical instruments work in the J, H and K bands, which are also standard atmospheric windows of transparency (Persson 1992). In order to avoid refocusing in the three bands, one chooses the infrared wavelengths as

$\lambda_1 = 1.25$ μm, $\lambda_2 = 1.65$ μm, $\lambda_3 = 2.2$ μm.

Using formulae (4-1), (4-2), (4-3) and (4-4), one can calculate glass indices, V number, and partial dispersion P of most used glasses in the NIR wavelength. The results are given in Table 4-1. All of these indices are for room temperature (20°C), and all of these glasses have high transmission.

Table 4-1. Refraction indices, V number, and partial dispersion of NIR glasses at 20 °C. The refraction indices of IRG2, IRG3, IRG7, IRG9 and ZnSe are calculated with Herzberger formula; the others glasses with Sellmeier formula.

Glass	n_2 (1.25μm)	n_2 (1.65μm)	n_3 (2.2 μm)	V number	P
Silica	1.44748	1.44280	1.43501	35.5110	0.6246
LiF	1.38512	1.38190	1.37659	44.7701	0.6217
MgF_2-O	1.37214	1.36995	1.36648	65.3879	0.6128
IRG9	1.47745	1.47461	1.47031	66.4437	0.6028
IRG7	1.54755	1.54279	1.53584	46.3737	0.5929
CaF_2	1.42746	1.42556	1.42280	91.4696	0.5907
MgO	1.71941	1.71449	1.70762	60.6185	0.5824
IRG11	1.66140	1.65675	1.65060	60.8103	0.5699
IRG3	1.81383	1.80709	1.79841	52.3309	0.5627
BaF_2	1.46719	1.46571	1.46396	144.4753	0.5412
IRG2	1.85741	1.85088	1.84321	59.9108	0.5400
$SrTiO_3$	2.29795	2.28014	2.26082	79.4784	0.5203
ZnS	2.27935	2.26973	2.26338	79.4784	0.3974
ZnSe	2.46802	2.45278	2.44368	59.7034	0.3739

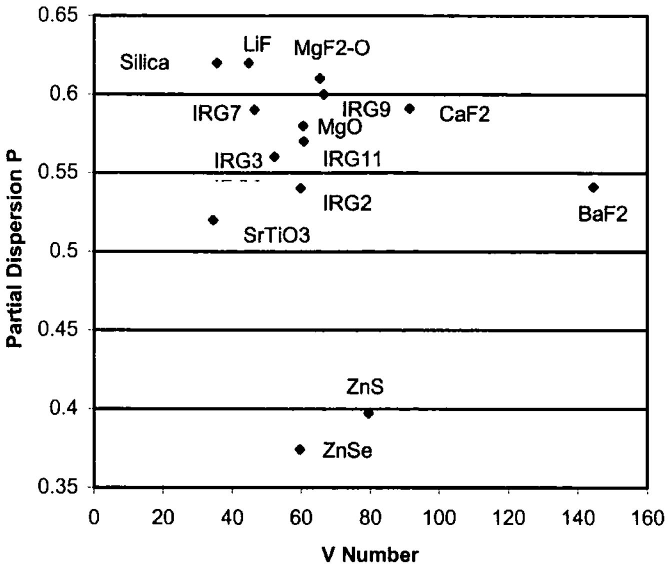

Figure 4-1. Plot of partial Dispersion P versus V number for NIR glasses at wavelengths 1.25, 1.65, and 2.2 μm at 20 °C.

A plot of V number versus partial dispersion at 20 °C is shown in Fig. 4-1. It can be seen that BaF2, ZnS and ZnSe glasses are far away from other glasses on the plot. This is an important character for glass choice, as will be shown in late sections. As NIR instrument are often operated at cryogenic temperature, we also calculate the partial dispersion and V number of all these glasses at temperature 77 K and find the relative values of these glasses are almost unchanged. So the V number versus partial dispersion plot at 20 °C can be used as a standard map for the glass choice at other temperatures

4.3 Glass Selection of Two-Material Doublet

For simplicity in application, only axial chromatic aberration will be considered. For thin lens doublets in close contact or with a small airspace, the conditions for three wavelengths colour correction are (Herzberger 1962)

$$\frac{\Phi_1}{V_1}+\frac{\Phi_2}{V_2}=0 \qquad (4-5)$$

$$\frac{\Phi_1}{V_1}P_1 + \frac{\Phi_2}{V_2}P_2 = 0 \qquad (4-6)$$

Where Φ_k is the optical power of lens k, Φ is the whole power of the two-lens doublet, V_k is the V number of lens k, and P_k is the partial dispersion of lens k.

Solving the above equations (5) and (6), we have $P_1 = P_2$. This means that for two glasses, they must have the same partial dispersion in order to correct the chromatic aberration at three wavelengths. From Table 4-1 and Fig. 4-1, it is clear that there are no two glasses that have the same partial dispersion value exactly. Thus, any two-glass doublet will have residual chromatic aberration. The secondary residual chromatic aberration for the two thin lenses can be expressed as (Kingslake 1978)

$$\Delta l = \frac{P_1 - P_2}{V_1 - V_2}\frac{1}{\Phi} \qquad (4-7)$$

On the P - V number plot, the slope of a line connecting the two points corresponding to these two glasses is proportional to the amount of secondary residual chromatic aberration. The amount of excess power that must be introduced in the element of the lens in using these glasses to achieve secondary colour correction is inversely proportional to the length of the line separating the two glass points. It is noticeable that from Fig. 4-1, in the direction of partial dispersion P, ZnS and ZnSe are far away from other glasses and this means that ZnS and ZnSe are not suitable to form doublets with other glasses. BaF_2 and CaF_2 are far away from other glasses in the V number direction and are very close in partial dispersion to some other glasses. This means that BaF_2 and CaF_2 can be used to form doublets with other glasses. BaF_2 is better than CaF_2 because of its larger V number. Oliva and Gennari (1995) confirmed that BaF_2/IRG2 has better performance than CaF_2/IRG7.

Table 4-2 lists some possible combinations for doublets and the residual chromatic aberration. The residual aberration is calculated per unit Φ. The smaller the residual chromatic aberration, the better the two-lens doublet for the correction of the chromatic aberration. In practical application, the two lenses can be separated slightly to facilitate cooling.

Table 4-2. Some possible combinations for two-glass doublets.

Combination	BaF_2/IRG2	$BaF_2/SrTiO_3$	BaF_2/IRG3	BaF_2/IRG11	BaF_2/MgO
$\nabla l\,(10^{-4})$	-0.1419	-1.900	2.333	3.430	4.913

combination	BaF_2/IRG7	BaF_2/Silica	BaF_2/LiF	BaF_2/MgF_2-O	CaF_2/MgO
$\nabla l\,(10^{-4})$	5.270	7.654	8.074	9.053	-2.690

combination	CaF_2/IRG9	CaF_2/IRG7	CaF_2/Silica	CaF_2/LiF	CaF_2/IRG11
$\nabla l\,(10^{-4})$	4.835	4.878	6.058	6.638	-6.784

combination	CaF_2/IRG3	MgF_2-O/Silica	MgF_2-O/LiF	MGO/IRG7	MGO/Silica
$\nabla l\,(10^{-4})$	7.154	6.058	6.638	-7.371	-16.807

4.4 Glass Selection of Three-Material Triplet

As we discuss above, the requirement for doublets is that the two glasses have the same partial dispersion. This limits the possible applications, as only few glasses have a close partial dispersion and small residual chromatic aberration. For a triplet in close contact or with small airspace, the conditions under which three lenses can be achromatised for three wavelengths are (Kingslake 1978)

$$\Phi_1 + \Phi_2 + \Phi_3 = \Phi \qquad (4-8)$$

$$\frac{\Phi_1}{V_1} + \frac{\Phi_2}{V_2} + \frac{\Phi_3}{V_3} = 0 \qquad (4-9)$$

$$\frac{\Phi_1}{V_1}P_1 + \frac{\Phi_2}{V_2}P_2 + \frac{\Phi_3}{V_3}P_3 = 0 \qquad (4-10)$$

Resolving these equations, one gets

$$\Phi_1 = -T_{23}\frac{1}{E_1}V_1\Phi \qquad (4-11)$$

$$\Phi_2 = -T_{31}\frac{1}{E_2}V_2\Phi \qquad (4-12)$$

$$\Phi_3 = -T_{12}\frac{1}{E_3}V_3\Phi \qquad (4-13)$$

Where Φ_k, V_k, and P_k are the power, V number, and partial dispersion of lens k, respectively and

$$E_1 = \frac{1}{V_2 - V_3}[V_1(P_2 - P_3) + V_2(P_3 - P_1) + V_3(P_1 - P_2)]$$

$$E_2 = \frac{1}{V_3 - V_1}[V_1(P_2 - P_3) + V_2(P_3 - P_1) + V_3(P_1 - P_2)]$$

$$E_3 = \frac{1}{V_1 - V_2}[V_1(P_2 - P_3) + V_2(P_3 - P_1) + V_3(P_1 - P_2)]$$

$$T_{12} = \frac{P_1 - P_2}{V_1 - V_2}, \qquad T_{23} = \frac{P_2 - P_3}{V_2 - V_3}, \qquad T_{31} = \frac{P_3 - P_1}{V_3 - V_1}$$

The meanings of E_1, E_2, E_3, T_{12}, T_{23} and T_{31} can be explained on a P – V number plot. For example, for a Silica/BaF2/ZnSe triplet, glass 1 is Silica, glass 2 is BaF_2, and glass 3 is ZnSe. If one plots the three chosen glasses on the P – V number plot shown in Fig. 4-2 and then join the three points to from a triangle, E_1 is the vertical distance of glass 1 to the line joining the other two glasses and is negative if glass 1 falls bellow the line. Similarly, E_2 is the vertical distance of the glass 2 to the line joining the other two glasses. E_3 is the vertical distance of the glass 3 to the line joining the other two. Only E_3 is shown in Fig. 4-2. T_{ij} is the slope of the line joining the glass i and glass j. All the three lenses will be as weak as possible if we select glass types having large E_1, E_2, E_3 and small T_{12}, T_{23} and T_{31}. If two glasses have the same or close V number values, the slope of the line will be infinite or larger, and this situation must be avoided when one chooses glasses. In general, a good triplet will have a large triangular area corresponding to the three glasses and will have a small power distribution on the three elements.

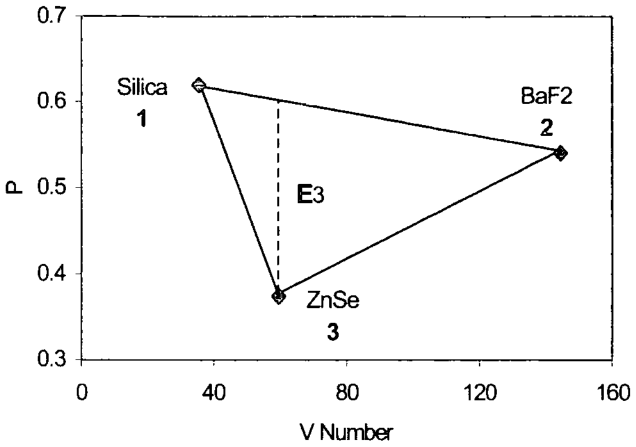

Figure 4-2. P – V number plot of the glasses used for a three-lens triplet.

The basic principle for glass selection is to obtain the minimum values of the optical powers Φ_1, Φ_2 , Φ_3 , since the smaller the optical power, the smaller the higher-order aberrations. Some possible combinations of three-lens triplet are listed in Table 4-3. All of the triplets in Table 4-3 have a reasonable power distribution except CaF2/BaF2/ZnSe, which has a larger power with the first and second elements and is listed just for comparison. The power of each thin lens is calculated with that of the triplet as the unit. The square root of the averaged and squared weighted refractive power Φ_k of all the lens elements can be used to evaluate the performance (Sasian and Descour 1998). The parameter has the advantage of being independent of lens scaling, aperture size, and field angle. It is termed W and for a triplet it can be expressed as

$$W = \left(\frac{1}{N}\sum\Phi_K^2\right)^{1/2} = \left[\frac{1}{3}(\Phi_1^2 + \Phi_2^2 + \Phi_3^2)\right]^{1/2} \qquad (4-14)$$

Where N is the number of the elements in the triplet. The triplets are listed according to their W values in Table 4-3.

The maximum paraxial rms spot radius (R_{max}) is also listed in Table 4-3. The paraxial rms spot radii were calculated at the three wavelengths of λ_1, λ_2 and λ_3 by using Zexam optical design program, allowing correction of spherical aberration and aphochromatism. For the calculation, all the triplets have a focal length 100mm at F/5 with the thickness of 5 mm for all the three elements. It is obvious that except CaF2/BaF2/ZnSe, all the triplets have a similar W, so they all have a similar R_{max} value. The CaF2/BaF2/ZnSe has a lager R_{max} than other triplets, because two of its elements (CaF2 and BaF2) have a larger optical power.

Table 4-3. Some possible combinations for three-lens triplet.

Combination	Φ_1	Φ_2	Φ_3	W	Rmax (μm)
$SrTiO_3/BaF_2/ZnSe$	-0.342936	1.228050	0.114886	0.739	0.792
$SrTiO_3/BaF_2/ZnS$	-0.346881	1.271849	0.075034	0.762	0.785
Silica/BaF_2/ZnSe	-0.234825	1.431636	-0.196811	0.846	0.801
LiF/BaF_2/ZnS	-0.317755	1.521649	-0.203894	0.905	0.765
IRG7/BaF_2/ZnSe	-0.373084	1.521516	-0.148432	0.908	0.755
Silica/BaF_2/ZnS	-0.242130	1.556429	-0.314299	0.926	0.763
IRG3/BaF_2/ZnSe	-0.507877	1.582340	-0.074463	0.960	0.807
IRG7/BaF_2/ZnS	-0.381774	1.617015	-0.235241	0.969	0.743
IRG3/BaF_2/ZnS	-0.509999	1.618521	-0.108523	0.981	0.754
$CaF_2/BaF_2/ZnSe$	-1.17137	2.397588	-0.226217	1.546	1.815

Once the glasses have been chosen, the actual lenses can be assembled in any order. Again, in practical application, the component lenses of the triplet can be separated slightly to facilitate use in a cryogenic instrument.

4.5 Design Examples

Using glasses from Tables 4-2 and Table 4-3, two camera designs for NIR spectrograph have been optimised to illustrate colour correction at 1.25, 1.65, and 2.2 μm. Both cameras have focal length 150 mm at f/2 and the aperture stops are a focal length (150 mm) before the first lens surface. The collimated beam sizes are 75 mm. The detector array is assumed to be a Rockwell 1024 x 1024 with 18.5-μm pixel size. The optical layouts are showed in Fig. 4-3. One camera is a detached triplet and a detached doublet, and the other comprises two detached triplets. The triplet is silica/BaF_2/ZnSe, and the doublet is silica/BaF_2. The last element in the two cameras is a ZnSe field lens. All the optical specifications for the two cameras are the same. The only difference is that the silica/BaF_2 doublet is replaced by a silica/BaF_2/ZnSe triplet in the triplet - triplet camera. Although some glass combinations have better performance, we only choose classical glasses in view of their good physical characteristics. Some glasses such as IRG2, IRG3, IRG7, IRG9 and IRG11 are avoided, as Schott will most probably stops the production of these little-used glasses. After silica/BaF2/ZnSe is chosen, the doublet silica/BaF2 is chosen in order to minimise the number of glasses. The design is optimised at the cryogenic temperature of 70 K.

Although the two cameras are only optimised at the wavelength of 1.25, 1.65 and 2.2 μm, the chromatic aberration is also well corrected at other wavelength between 1-2.5 μm. Fig. 4-4 shows spot diagrams of the two cameras. It is not surprising that the triplet - triplet camera has a better optical performance than the triplet - doublet camera. This is because the silica/BaF2/ZnSe triplet is better than the silica/BaF2 doublet for colour and other aberration corrections.

F/2 Camera: Triplet - Doublet

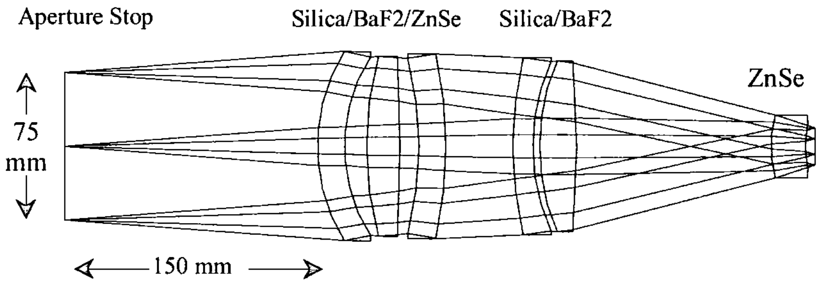

F/2 Camera: Triplet - Triplet

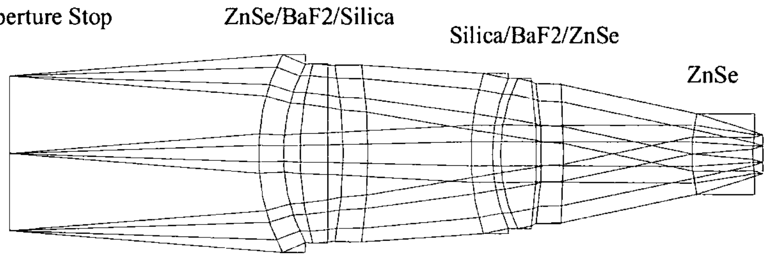

Figure 4-3. Optical layout of F/2 NIR camera. All Lens surfaces are spherical. Spot diagrams are displayed in Fig. 4-4.

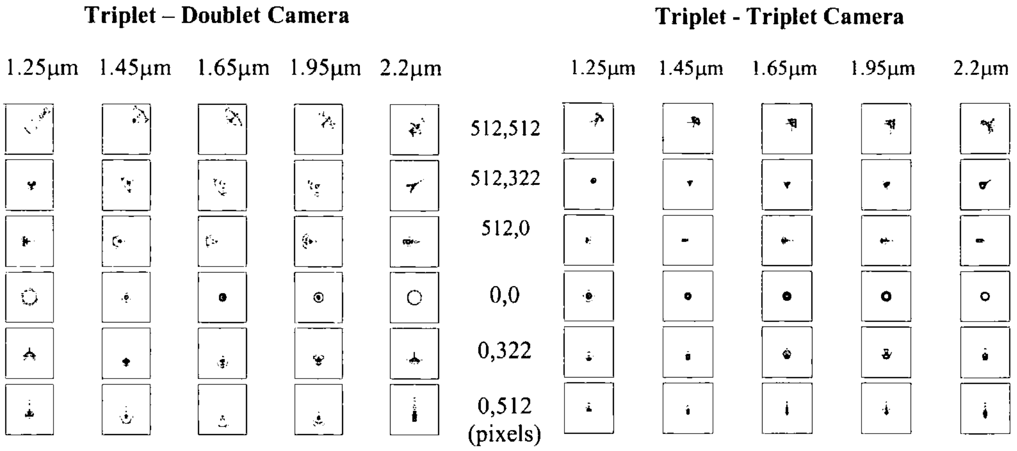

Figure 4-4. Spot diagrams at several wavelengths and field positions (expressed in pixel units) from the centre of detector array. The box size is equal to one detector pixel which is 18.5 μm.

4.6 Summaries and Conclusions

The choice of a doublet is limited by the fact that the two glasses must have the same partial dispersion. In principle, a doublet has residual chromatic aberration when the partial dispersions of the two glasses are not equal. For triplets, one has more freedom to choose glasses for apochromatic lens design. I have developed a simple procedure to identify suitable combination of glasses for use in NIR and have shown that some classical glasses, such as fused Silica, BaF2, ZnSe and LiF, can be used to form a high performance triplet. The design examples show that triplet – doublet or triplet – triplet combination can be used to design a faster camera, and the triplet has better performance than the doublet for apochromatic lens design.

Chapter 5

Design, fabrication and testing of microlens arrays for IFU spectrometers

Abstract

In this chapter, two types of microlens arrays, i.e. polymer and monolithic glass microlens arrays are described. The manufacture technologies are discussed. Design theories are derived. Different test methods and the experiment apparatuses are described. Finally, microlens arrays from different manufacturers are tested, and compared according to encircled energy by a mathematical model. The tests and analyses show that the microlens image quality is dominated by stray and scattered light, which results from wave aberration and surface roughness.

5.1 Introduction

Microlenses and microlens arrays were originally used in the telecommunication industry. The applications include beam collimation and coupling of the light from a laser diode into a single-mode fibre (Paek and Weaver 1975, Abarot et al. 1997). Microlenses were also used for connectors, directional couplers, attenuators, switches, wavelength-division multiplexers in fibre communication systems (Tomlinson 1980). For other applications, microlens arrays are used to collect the light onto two-dimensional CCD image sensors (Michael et al. 1997) or onto the detector of focal plane array (Motamedi et al. 1997)

An approach pioneered by Hill et al. (1983) is to use a microlens to image the telescope pupil onto the fibre core. In this case the microlens acts somewhat like a field lens. This microlens is referred to as the input microlens. If a similar microlens is place at the output end of the fibre, the pupil imaging optics will convert the effect of FRD in the fibre into an increased image size and this microlens is called the output microlens. The output microlens can also convert the F ratio from the fibre to any F ratio that can be accepted by a spectrometer.

Although microlenses are relatively new in applications for astronomical instrumentations, they are increasing used in integral field spectrographs (Allington-Smith et al. 1998, Felenbok 1998, Prieto et al. 1998, Herbst 1998). Microlens arrays are key elements for integral field units. As described in Chapter 2, microlens can be used for coupling light into optical fibre by imaging the telescope pupil onto the fibre core. Comparing IFU with bare fibre system which can provide a limited fill factor of 70%, microlens array + fibres system can provide a continuous spatial sampling on the sky image with almost 100% fill factor. Microlenses can be carefully chosen to feed the fibre at a faster beam of F/3-F/5 to reduce fibre FRD. However currently commercial microlens arrays are not perfect and all the advantages can only be obtained if the microlens arrays are of high quality.

There are two kinds of microlenses, refractive microlens and diffractive microlens. As the diffraction efficiency of diffractive microlens is wavelength dependent, it is not suitable for IFU spectrometers where a broad wavelength range is required. So in this chapter, only refractive microlenses are discussed.

In this chapter, the basic properties and fabrication of microlens array are described. The limitations for the design and fabrication of microlens for IFU spectrometer are also described. Finally, microlens arrays from different manufacturers are tested and compared.

5.2 Microlens Array Manufacture

Micro fabrication technologies such as photolithography and resist processing (reflow) were used to manufacture epoxy/polymer microlens. For the manufacture of monolithic glass microlens array, epoxy/polymer microlenses were transferred into fused silica by Reactive Ion Etching (RIE). Microlens array can also be replicated in polycarbonate and epoxy by embossing and casting techniques using a master microlens array.

5.2.1 Fabrication of Polymer/Epoxy Microlens Array

Many manufacturing techniques for refractive microlens arrays have been developed. A very promising and widely adopted technique is the reflow or resist-melting techniques (Popivic et al. 1988, Haselbeck et al. 1993).

The procedure of microlens array fabrication by controlled melting of a photoresist is quite simple. A thin base layer (about 1 μm thickness) of positive photoresist is coated on a glass substrate. The resist is then hardened by baking. A second layer (typical 1-100 μm) positive photoresist is coated on top of the base layer. A mask is set on the top of the second positive photoresist. A standard developing process of microlithography (such as UV light cure) is applied and the exposed photoresist is resolved. An array of photoresist cylinders is formed on the glass substrate. Next, the photoresist is melted at a temperature of about 150-200 °C. Surface tension forms the liquid into a spherical shape that can be used as a microlens. This process is shown in Fig. 5-1. The base layer is important in microlens manufacture. If there is no base layer, the actual shape depends on the critical angle between the substrate and the resist at the circumference of the lens. This angle is a material constant that depends only on three constants of surface tension between substrate, liquid and air. For high numerical aperture lens, the critical angle is quite large. When the critical angle is too large, fabrication error may occur: the surface is still steep at the rim, but the centre is flat. Microlens with a moderate numerical aperture cannot be easily fabricated by melting photoresist on a glass substrate. Haselbeck (1993) reported that a thin bottom layer (base layer) with a thickness of about 1 μm on top of the substrate could be used to decrease the critical angle. They had made spherical microlenses with diameters ranging from 150 to 400 μm and numerical aperture from 0.1 to 0.3. In fact, with the base layer, microlens can be manufactured on any substrate.

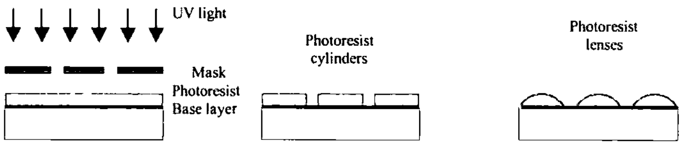

Figure 5-1. Fabrication of refractive microlens by photoresist-melting.

The lens shape error may be very small. However, it varies from manufacturer to manufacturer. Jay et al. (1994) used Preshaped Photoresist Refractive Optics by Melting (P^2ROM) to fabricate high-quality refractive microlens and an F/4.5 microlens with less than one wave aberration was achieved. Microlens with small spherical aberration was also reported by Haselbeck (1993). The spherical aberration was 0.11 waves for a 272 μm diameter lens with a 666 μm focal length.

5.2.2 Monolithic Glass Microlens Array

In the previous subsection, it was demonstrated that refractive polymer microlens can be made with good optical quality. However, their robustness and spectral range are limited (Stern 1994). Polymer/epoxy has spectral absorption in the infrared wavelength range. This property limits the applications of polymer/epoxy microlenses to the infrared. There is also a concern that polymer/epoxy microlens fabricated on glass substrate may be broken at cryogenic temperature. Comparing with polymer/epoxy microlens, the advantages of Monolithic glass microlenses are obvious. Monolithic glass microlenses have good physical and mechanical properties and can work at cryogenic temperature. These make them suitable for use in infrared IFU beyond the wavelength of 1.8 microns where the whole IFU may need to be cooled to cryogenic temperature. IR grade fused silica and other optical materials such as silicon can be chosen to fabricate the microlens array.

A very promising and widely adopted technique for the fabrication of monolithic glass microlens array is Reactive Ion Etching (RIE). The polymer/epoxy microlenses can be transferred into fused silica or other glasses by RIE. Other techniques, such as microlens arrays formed on a glass plate by use of a CO_2 laser (Wakaki 1998) are not discussed here as they are not the dominant techniques and some of them are not suitable to fabricate microlens arrays with high filling factor and good image quality for astronomical IFS.

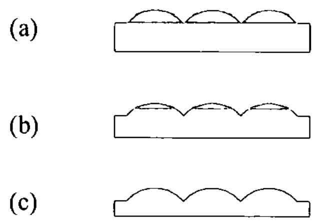

Figure 5-2. Principle of fabrication of monolithic microlens array by RIE process. (a) Before etching. (b) During etching. (c) Monolithic microlens array achieved after etching.

Monolithic microlenses are obtained by a two-step fabrication process (Erdmann 1997). The first step is to fabricate the polymer/epoxy microlens array on a glass substrate by photoresist-melting. This process has been discussed in the previous subsection. The second step is to transfer the lens shape into the glass substrate (such as silica or other glasses) by RIE, thus monolithic glass microlens array is obtained. This is a well-known smart technology (Popovic 1988). Fig. 5-2 shows the process of RIE which transfers the preshape into the glass substrate. Wave aberrations can be minimized by an appropriate choice of etching parameters, especially the etch ratio of RIE. Eister (1996) reported that the form of lenses can be controlled by changing the etch rate between resist and substrate.

The property of the two-step process may result in larger shape error for monolithic lenses than that for polymer/epoxy lenses. However, many high quality monolithic microlenses are reported to be obtained by RIE. Examples include Erdmann (1997), Mersereau (1992), Severi (1999). Silicon microlenses with a deviation from a sphere of less than λ/20 (λ=1.55 um) within the central 80% of the diameter have been fabricated. It was found that the rim region deviate strongly from a sphere (λ/2 wave length) because of an unstable plasma at the begin of the etching process. Surface roughness of less than 3 nm (RMS) was found for microlenses etched in fused silica (Nussbaum et al. 1997). Before RIE transfer, a deviation from a sphere of λ/20 (RMS) and λ/4 (p/v) was observed for the polymer/epoxy microlens. After RIE, the deviation was λ/8 (RMS) and 0.84λ (p/v). By carefully controlling the etch ratio of RIE, good microlenses with very small wave aberration were also achievable by Mersereau (1992). He reported fabrication of refractive monolithic fused silica microlens (100 μm diameter, F/2.8) with wavefront aberration less than λ/4. Analysis using commercial fringe analysis software showed less than one quarter wave (at 0.63μm) of third spherical aberration and less than one tenth-wave of coma and astigmatism for this lens. By careful control of fabrication parameters, especially the O_2 flow-rate, spherical aberration could be reduced and monolithic silica microlenses with λ/8 wavefront aberration were fabricated (Severi 1999).

5.3 Microlens Properties

In this section, microlens physical and optical properties are described. These properties, such as surface roughness, spherical aberration and wave aberration are important to control the image quality.

5.3.1 Paraxial Equations and Design Parameters

A plano-convex microlens is described by the lens diameter D, the radius of curvature R and sag height S as shown in Fig. 5-3.

The focal length f (in air) of a plano-convex refractive microlens is simply given by

$$f = \frac{R}{n-1} = \frac{S^2 + r^2}{2S(n-1)} \qquad (5-1)$$

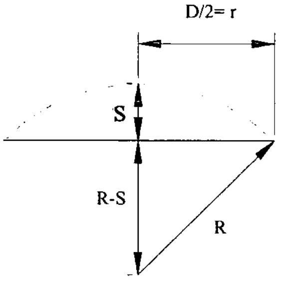

Figure 5-3. Plano-convex microlens

Where f is microlens focal length in air and r=D/2.

n is refractive index of lens material.

The sag height is given by

$$S = R - \sqrt{R^2 - r^2} = (n-1)f - \sqrt{[(n-1)f]^2 - r^2} \qquad (5-2)$$

Sag height is an important parameter and the curvature radius or focal length is controlled by the sag height in the manufacture. The sag height range is in 0.5 – 30 microns. Increasing the sag height (fast lens) outside this range may cause a big shape error and a surface deviation from the ideal spherical shape. This is because when manufacturing big microlens by melting photoresist, the inside of the microlens may still not be melted although the surface already flows thoroughly. In a later section, it will be shown that increasing the microlens diameter will also increase the optical aberration.

Lens diameter or pitch of microlens array is an important parameter for the IFU design as it decides the spatial sample resolution for the sky image. The diameter range of microlens is 10 – 1,000 microns. It needs to be noted that microlenses with diameter larger than 500 microns may have a risk of increased lens shape error.

5.3.2 Microlens Shape and Fill Factor

It is important for microlenses to be in the correct packing geometry to get the maximum fill factor. Low fill factor will results in the loss of light and thus low efficiency for IFU. Fig. 5-4 shows the possible packing geometries for different microlenses with different shapes to reach the maximum fill factor. In this figure, the lens-lens gap is assumed to be zero. For circular lens, the maximum fill factor can only reach 90.7 % (Nussbaum et al. 1997). For hexagonal lens in hexagonal package and rectangular lens in rectangular package, the maximum fill factor can be 100%.

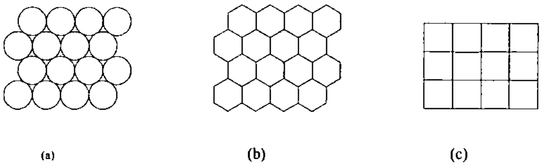

Figure 5-4. Microlens package. (a) Circular lens in hexagonal package. (b) Hexagonal lens in hexagonal package. (c) Rectangular lens in rectangular package. The maximum fill factor is 100% for (b) and (c) while it can only reaches 90.7 % for (a).

If there is lens-to-lens gap for microlens array, the fill factor will be reduced. Normally, the lens-to-lens gap is about 2 – 5 microns. If the lens-lens gap is fixed, microlens array with larger lens diameter will have a high fill factor. This is true in most cases. Monolithic microlens arrays normally have a lens-to-lens gap of 5 – 10 microns, while epoxy/polymer microlens arrays may have a very small lens-to-lens gap, which can be negligible.

5.3.3 Microlens Array Uniformity

Microlenses are typically of high uniformity from lens to lens within an array. Normally the uniformity of the focal length within an array is < 1% and from array to array it is typically within 3%. For deep lenses the sag is more difficult to accurately etch so it may be off by as much as 10%. A shallower sag etches in less time and can be held to tighter specifications.

5.3.4 Surface Roughness

Surface roughness is an important specification for microlenses. A rough surface will introduce scattered light. The scattered light is always a problem for microlenses (Lee 1998). It seems that polymer/epoxy microlens surfaces are rougher than that of monolithic microlens. It needs to be noted that most polymer/epoxy microlens arrays are fabricated by replication from a mater. It is very possible that the poor surface quality of polymer/epoxy microlens is introduced by the master. Monolithic microlenses have good surface quality although it is transferred from the polymer/epoxy microlens (two-step manufacture). Currently polymer/epoxy microlenses for astronomical instruments are not AR coated because of the problem of outgassing. Any surface imperfection will caused scattered light and thus results in the loss of light. Surface roughness can be measured using Atomic Force Microscope (Nussbaum et al. 1997). The total integrated scattered light (TIS) of an optical surface can be estimated from its RMS surface roughness δ by

$$TIS = (\frac{4\pi\delta}{\lambda})^2 \qquad (5-3)$$

The method for obtaining a value of RMS surface roughness from a measurement of TIS (equation (5-3)) forms the basis for a U.S. standard of effective surface roughness. Roughness measured by TIS correlates well with those measured by profiling techniques for surface roughness range in the 1-100 Å RMS range. The wavelength dependence of TIS predicted by equation (5-3) has been verified by experiment in the wavelength range from 0.25μm in the UV to 1.15 μm in the near IR (Mattsson 1989). When calculating scattered light from the RMS surface roughness measurement, an important condition is that scattered light is caused by micro-irregularities and not by dust or some other form of particulate contamination. Scattered light caused by particulate contamination may not correlate with roughness. Before making any scattered measurements the surface should be inspected by a microscope to be sure that it is free from particulates.

From formula (5-3), one can reach the conclusion that at the long wavelengths, i.e. at NIR wavelengths, the scattered light will not be so serious compared to that at visible wavelengths. Monolithic glass microlenses fabricated by MEMs Optical have a surface roughness of 4-6 nm

(Production Sheets, MEMs Optical). At the 0.63 microns testing wavelength, 5 nm RMS surface roughness corresponds to 1% TIS. This is very small and can be negligible. Epoxy/polymer microlenses have a high surface roughness which is about 13nm or larger which corresponds to 7% of TIS.

5.3.5 Optical Coating

It is very interesting to have the microlens and array AR coated to get the 4% gain in throughput in each microlens curved surface. The conversional thermal evaporation vacuum coating involves a high temperature heating process. An important parameter, which affects coating quality, is the kinetic energy of the atoms adsorbed on the substrate. If this energy is too low, the result is a porous layer which is both mechanically and chemically unstable. This problem may be partially overcome by heating the substrate to approximately 250°C as the coating is applied. Unfortunately this cannot be applied to microlens arrays which are heat sensitive.

Ion-Assisted Deposition (IAD) offers the solution to this problem. In this technique, the newly-deposited coating layer is subjected to a stream of ions. These ions transfer energy to the adsorbed surface atoms, thereby increasing their kinetic energy and resulting in a more compact, non-porous layer. In this process, no heating of the substrate is required, which enables this technique to be applied to sensitive material at temperatures well under 100°C, such as polymer and epoxy microlens array. More details about IAD can be found from the work of Martin et al. (1983) and Tsai et al. (1997). The process of IAD coating makes it suitable for coating on the structured surface of microlens arrays and should result in uniform coating of the array surface. IAD coating has been successfully used for SELFOC gradient index microlens (Kyogoku et al. 1990). Currently IAD has also been used for the GMOS IFU.

Another possible coating for microlens is Solgel antireflection coating. Traditional Solgel coatings are soft. Cleveland Crystals in Cleveland can make a hardened coating. The Solgel coating can be optimised at 0.45-1.8 micron wavelength range. This hardened coating have also been used for the FAST Spectrograph for the Tillinghast Telescope (Fabricant 1998).

For microlens array coating, one must ensure that the coating is uniform over the whole coated surface. If not, extra wave aberrations may be introduced. Besides getting an increase in throughput, it can be expected that the microlens surface roughness may be improved after coating, so the scattered light that is relevant to the surface roughness may also be reduced further.

5.3.6 Depth of Focus

Depth of focus is defined as the allowed shift of the image plane from the ideal focal plane for which no change of image quality is observed.

For a diffraction-limited microlens, the depth of focus can be expressed as

$$2\Delta z = \frac{4\lambda F_n^2}{n} = 4\lambda n F^2 \qquad (5-4)$$

Where λ is wavelength.

F_n is the microlens F number in medium with refractive index n.

F is microlens F number in air.

n is refractive index in image space.

Noted that the depth of focus is dependent on the refractive index n and F number. If the F number in air is fixed, the higher the refractive index of the microlens, the larger the allowed depth of focus.

Assuming that the wavelength is 0.4 microns, the depth of focus is +/- 10 microns, +/- 19 microns, +/- 29 microns and +/- 42 microns for a F/3, F/4, F/5 and F/6 microlens, respectively. As for IFU spectrometers, the microlens forms the telescope pupil image on its back surface, this requires that the microlens array thickness is tightly controlled and the thickness tolerance should be less or equal to the depth of focus. Normally the array thickness tolerance can reach +/- 20 microns (Private communication with MEMs Optical, Inc). It may be difficult to fabricate microlens array with thickness tolerance less than +/- 20 microns, or this microlens array may be expensive to fabricate. It is obvious that microlens F number should be slower or equal to F/4 in visible wavelength range considering the requirement for the thickness tolerance.

5.3.7 Spherical Aberration of Plano-convex Microlens.

Spherical aberration is the dominant aberration for microlenses. In Appendix A, third-order aberration theory is used for deriving an expression for the spherical aberration of microlens. The transverse (lateral) spherical aberration (TSA) of the plano-convex can be expressed as:

$$TSA = \frac{N.A^2 D}{4n_0^2(n_0-1)^2} = \frac{D}{16F^2 n_0^2 (n_0-1)^2} \qquad (5-5)$$

Where N.A is the numerical aperture.

F is the F number of the microlens.

D is lens diameter.

n_0 is the refractive index of the medium.

From formula (5-5), some conclusions can be drawn. (1) The relationship between spherical aberration and microlens size, i.e. microlens diameter, is linear. Increasing microlens size will increase the spherical aberration. (2) Spherical aberration is inversely proportional to the square of the F number. (3) High refractive index optical material is helpful to reduce the spherical aberration.

As an example, a fused silica microlens is used to focus collimated light into F/2, i.e. coupling the light into fibre core. The refractive index n_0 is 1.457 when wavelength is 0.630μm and the microlens aperture is 500μm. Thus TSA = 17.62 μm. According to Zemax ray tracing, the geometrical spot radius is 16.85 μm at the focal plane. This result is in good agreement with the third order approximation.

Note that the spherical aberration according to equation (5-5) is calculated at the paraxial focal plane. The spherical aberrations can be reduced further if they are at the optimised focal plane. Fig. 5-5 shows the chromatic-spherical aberration of an actual microlens optimised for the minimum chromatic-spherical aberration. The optical material is silica and the wavelength range is 0.45-0.9 microns.

In Fig. 5-5 (a), the F/5 silica microlens is scaled to different diameter (the F number is fixed). It is clear that the chromatic-spherical aberration increases linearly with the diameter of the microlens. For smaller microlens, the image quality is diffraction limited. When the diameter of the microlens is larger than 0.6 mm, the spherical aberration begins to dominate and the image quality is no longer diffraction limited. Continuing to increase the size of microlens will make the image quality unacceptable because of the geometrical optical aberrations. A reasonable size for this microlens is a diameter of about 0.5 mm.

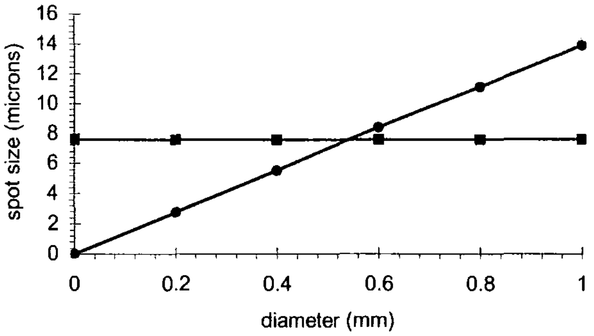

Figure 5-5 (a). Spot size versus diameter for a F/5 silica microlens at wavelength range 0.45 – 0.9 microns. Circles are chromatic-spherical aberration. Squares are Airy disk at 0.63 micron.

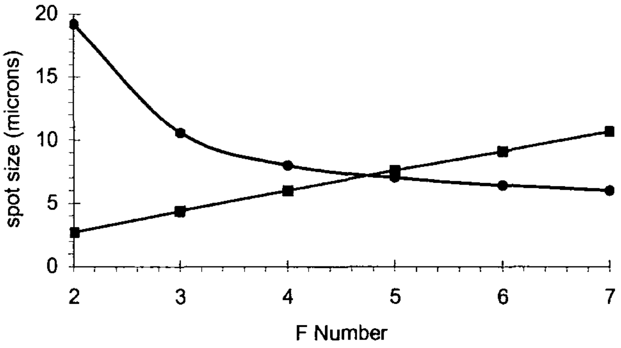

Figure 5-5 (b). Spot size versus F number for a 500 micron diameter silica microlens at wavelength range 0.45 – 0.9 microns. Circles are chromatic-spherical aberration. Squares are Airy disk at the primary wavelength of 0.63 microns.

In Fig. 5-5 (b), it can be seem that the relationship between chromatic-spherical aberration and F number is not linear. When the microlens is faster than F/3, the chromatic-spherical aberration increases very quickly. At about F/5, the geometrical aberration is equal to diffraction spot size. For a microlens slower than F/5, the image quality is diffraction limited. However, it is important to note that for a microlens with F number between F/3 – F/6, the geometrical aberration changes more slowly and the microlens is still closely diffraction limited.

Although the above analyses are carried out for silica microlens, these conclusions can be applied for epoxy/polymer and most glass microlenses that have similar refractive indexes to silica. For a few glasses, such as Schott SF5, the spherical aberration can be reduced because of the high refractive index, but the chromatic aberration will increase. It also needs to be noted that silica is a good glass for fabricating microlenses and the technique for the fabrication of silica microlens is well developed than other glasses (Production Sheets, MEMs Optical Inc.). As a general rule, the diameter of microlens is recommended to be less than 1 mm and the best value is about 0.5 mm. The optimised F number is between F/3 – F/6 and the best value is about F/5.

5.3.8 Wave Aberration and Image Quality

In the previous subsection, spherical aberration is discussed. However this is just the theoretical analysis and no fabrication error of the spherical shape is considered. In practice, the microlens may have bigger wave aberration than that of the theoretical calculation because of the fabrication error. For microlens, measurement shows that there is larger wave aberration outside the 80% central aperture, i.e. near the area of the edge and corners of the microlens. This is obviously caused by the manufacture of the microlens because the surface tension is different at the boundary of the microlens compared with that at the centre in the manufacture melting process.

These shape errors result in aberrated point-spread function and thus result in low encircled energy. The aberrated point-spread functions have been studied by several authors (Barakat 1964, Mahajan 1983). Mahajan studied the effect of fourth-, sixth-, and eighth-order balanced spherical aberrations on the incoherent point-spread function of the optical system with a circular pupil. They showed that the location of the first minimum remains practically unchanged. However, the aberrations reduce the irradiance distribution inside the Airy disk. The irradiance distribution decreases inside the Airy disk and increases in the bright ring around it. The central irradiance, i.e., the Strehl ratio, is determined by the phase aberration or wave aberration. For large wave aberrations, the Strehl ratio (SR) can be determined indirectly from the interferometric measurements (Bobroff and Rosenbluth 1992, Mahajan 1983)

$$SR \approx \exp(-4\pi^2 W_{rms}^2) \qquad (5-6)$$

Where W_{rms} is the RMS wave aberration at the measurement wavelength.

Mahajan (1983) studied the PSF, i.e. the irradiance distribution of the image of a point object and the encircled energy when wave aberrations are present. He found that at small radius the aberrated point spread function and encircled energy for a given aberration could be determined from the aberration-free results by multiplying them with the Strehl ratio.

For microlenses, the effects of the aberrated point-spread function on the image quality are twofold. First, it reduces the irradiance inside the Airy disk and increases the irradiance in the diffraction rings or wings. This is evident in the tests of microlenses (Section 5.6) where an increasing irradiance was found in the diffraction wings compared with an aberration-free ideal microlens. Secondly, the irradiance in the diffraction wings is scattered by the rough surface of microlens, resulting in scattered light from both diffraction wings and Airy disk. From equation (5-6), for a W_{rms} of 0.1, 0.2 and 0.4, the SR is 0.68, 0.21 and 0.002, respectively. For the 0.4 RMS wave aberration, the PSF and encircled energy in Airy disk are only 0.002 that of aberration free system. It is evident that the encircled energy drops dramatically with the increasing of RMS wave aberration. For microlenses, RMS wave aberration less than 0.1 is desirable and RMS wave aberration less than 0.2 is a necessary requirement and is also practically possible. As a rule of thumb, the peak-to-valley wave aberration is 3~5 times of RMS aberration (Mclean 1997). This requires that the peak-to-valley wave aberration must be less than 1 wavelength at the 0.63 μm measurement wavelength at the whole aperture of the microlens.

5.4 Design of Microlens Array

For IFU spectrometers, in most cases the in-stock microlens arrays are not suitable and a customized design is necessary. In order to get a good image quality, it is important to know how to specify the custom-designed microlens array.

The specifications must not be too difficult to fabricate considering the current techniques, but can still ensure good image quality. According to the discussions in the previous sections, the specifications of the microlens array may include the following. This list also serves as a summary of the previous discussion.

(1) Focal length and sag height

Sag height variation: +/- 2% in a single array, +/-3 % batch to batch. Optimised wavelength must be indicated when specifying the focal length.

(2) Pitch

When microlens gap is small, (e.g. < 5 μm), the pitch of microlens array decides the microlens size, i.e. microlens aperture diameter. The diameter should not be bigger than 1 mm and 0.5 mm is an optimised value.

(3) F number

The F number of the microlens also needs to be carefully chosen. It is decided by the focal length and pitch. The optimised value of the F number is F/4 – F/6. A fast light can reduce the FRD when feeding light onto the fibre.

(4) Gap between lenses

The lens-to-lens gap should be as small as possible. 5 microns or less is an acceptable value.

(5) Microlens shape

Microlens shapes can be Hexagonal or rectangular. Although circular shape is the best considering the curvature shape error in the fabrication, it is not suitable for IFU input array because of the poor fill factor. Hexagon is closer to a circular shape and has a smaller corner area which may introduces less wave aberration than rectangular shape microlens. So hexagonal microlens is preferred.

(6) Wave aberration

Although microlens wave aberration is very small and can be negligible at the central area, it may reach 2 wavelengths or bigger in the areas near edges and corners. Large wave aberration may reduce the irradiance distribution inside the Airy disk and increase irradiance in diffraction wings. More stray light in the diffraction wings will result in a low encircled energy even in a large radius. Considering the image quality requirement and the feasibility of fabrication, a reasonable value for wave aberration is less than 1 wavelength in peak-to-valley over the whole aperture of the microlens.

(7) Surface roughness

Surface roughness may introduce scattered light. For monolithic glass microlenses, the surface roughness may be very low and the scattered light may be negligible. For epoxy/polymer microlens, surface roughness may be very high and vary between different manufacturers. It may introduce about 10% scattered light. The surface roughness of epoxy/polymer microlens should be less than 13 nm RMS considering the feasibility of fabrication.

In many cases, it may be difficult to get the values of wave aberration and surface roughness from the manufacturer because they cannot do all of these tests. As an alternative, one can ask for a microlens sample from the manufacturer for testing and some information about optical image qualities can also be got by scaling the microlenses. This will be discussed in a later section.

5.5 Microlens Test Experiment

In this section, different methods are used to measure the PSF, encircled energy and wave aberration of microlenses. The purpose is to characterise microlens arrays, to identify what affects their image quality and how to choose high quality microlenses from different manufacturers.

5.5.1 Test of Microlens PSF and Encircled Energy

The measurement of microlens PSF and Encircled Energy (EE) is one of the most important tests for characterizing microlenses since as shown in a later section, comparisons of microlenses from different manufacturers and the performance estimation by scaling are all dependent on the measurement of encircled energy. PSF or EE measurement have be carried out by several authors (Lee 1998, Hutley 1991). Lee (1998) used a pinhole located before the testing microlens to measure its PSF and EE. For IFU spectrometers, microlens arrays are used to sample 2-D sky image and form the images of telescope pupil onto the fibre core entrances. For this application, it is important to know that how much light can be collected by the fibre and how much light is lost because of scattering.

The apparatus for testing PSF and encircled energy is showed in Fig. 5-6. A HeNe laser light with a wavelength of 632.8nm is used as light source. The laser is collimated by two sets of lenses. A spatial filter is used to remove the diffraction contamination. Two iris diaphragms with the same diameter are located in the collimated beam to remove any stray light further from the collimated light. A neutral density filter is used to adjust the intensity of the laser light to avoid saturation of the CCD detector. The microlens array under test is located on a X,Y,Z translation stage for accurate location and focusing. The imaging system is an Olympus microscope, which is composed of a microscope objective, an eyepiece and a camera lens. The objective can be selected to the desired magnification. It is important that the objective must be faster than the testing microlenses. The microlenses form their PSFs on the back surface of the array and the PSFs are collimated by the objective and eyepiece. The collimated PSFs are focused by the camera lens onto the CCD detector.

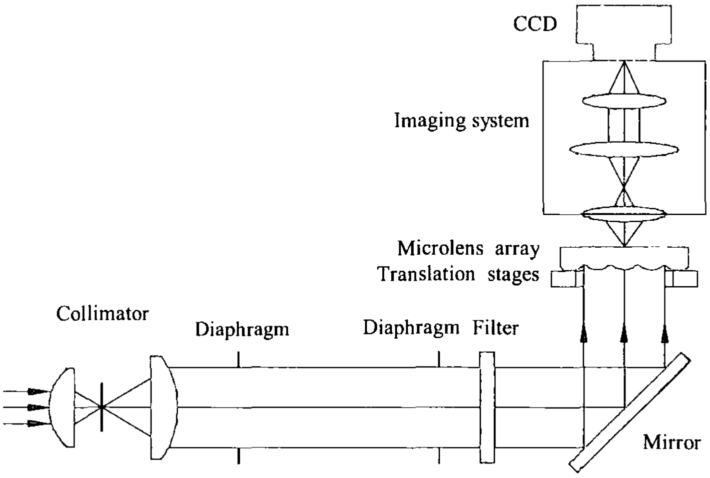

Figure 5-6. The schematic diagram of microlens PSF and encircled energy test.

It should be noted that no mask has been applied before the microlens. Several microlenses (only three are shown in this figure) are illuminated by the collimated light and only the central one is tested each time.

The CCD detector is a Pixtor 416 detector with 16 bits for data saving and transfer. This means the dynamic range is from 0 to 65,536. This was the highest dynamic range commercially available at that time.

The encircled energy is defined as the fraction of the total energy enclosed within a circle of radius centred on the PSF peak. Hutley et al. (1991) anticipated that there are two problems in the measurement of the encircled energy that need to be solved. The first problem is the dynamic range of the CCD detector which must be very high since the intensity in the spots will be several powers of ten greater than the background level and both have to be measured with comparable accuracy. The second problem is to define with sufficient accuracy, the boundaries of the area over which the total intensity is integrated. These boundaries should be drawn through a locus of minimum intensity. Because of these problems, Hutley didn't measure the encircled energy. For the first question, the key point is how to increase the signal-to-noise ratio.

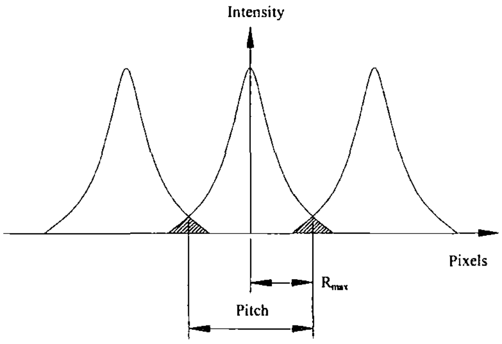

Figure 5-7. The cross-section intensity distributions of PSFs on CCD detector. Only three microlens PSFs are shown. R_{max} is the maximum radius that is equal to half pitch of the microlens array. The encircled energy is integrated over the whole area with a diameter of one pitch.

For the second problem that Hutley anticipated, the encircled energy is calculated and integrated in the whole area of one pitch diameter, i.e. the radius is from zero (the central position of the testing microlens) to the maximum radius that is equal to half pitch of the microlens array. This area corresponds to the whole encircled energy of the testing microlens although in principle the radius should be infinite for an individual lens if a mask is applied. Here, note again that no mask be applied in the test. As several microlenses are illuminated, in the area of one pitch diameter, the tested microlens gets some extra stray light from its neighbour lenses and because of the symmetry, the amount of the extra stray light is exactly equal to that of the light that is lost. This process is schematically shown in Fig. 5-7. In this way, although the measurement is the relative encircled energy, it actually equals the absolute encircled energy.

At first, it was found that the CCD detector has some noise that affected the measurement accuracy. There are two kinds of noises. One is high spatial frequency that exists in the same frame of exposure and changes from CCD pixel to pixel. The high spatial frequency may be caused by the non-uniformity of the CCD pixel sensitivity and detector readout electronics. The second is low frequency noise. It changes from frame to frame and may be caused by the CCD detector electronics or the electronic power supply unit because of the slow changes of the power voltage from time to time. Although the noise is very low, it is variable from frame to frame and affects the measurement accuracy of the encircled energy dramatically. These problems are solved by adopting a proper exposure procedure, in which the PSF exposure and the background exposure are taken alternately. For each test, ten PSF exposures and ten background exposures are taken. The ten PSF exposures and ten background exposures are stacked and averaged to get a master PSF frame and a master background frame, respectively. The high spatial frequency noise in the master frame will be about 1/3 that in the individual exposure. The PSF master frame is then subtracted by the background master frame and the low frequency noise is removed. Then, the PSF and encircled energy are analysed by a software package on STARLINK workstation. The procedures for the data reductions with different software are summarised as following

- *MAKEMOS* in *CCDPACK* package is used to stack, average the individual exposures and to get a master frame.
- *SUB* in *KAPPA* package is used to subtract the background frame from the PSF frame.
- *PSFMEASURE* or *PPROFILE* in *IRAF* package is used to analyse PSF and encircled energy.

The PSF and encircled energy is a function of measurement wavelength. In all the measurements, the wavelength is at 632.8nm unless otherwise stated. The tests at other wavelength were also carried out but not listed here.

5.5.2 The Measurement of Surface Profile

An accurate surface profile is sufficient to determine the lens focal length for a plano-convex microlens if one knows the material refractive index. Contact surface profilers were used to measure the microlenses (Mersereau 1992). However this measurement is experience dependent and measurement errors may be introduced. This method is also not considered here because of the risk of making dig and scratch on microlens surface.

Non-contact optical interferometric surface profilers are more useful and reliable for microlens measurement. This method is based on 3-dimensional data obtained optically. The data is processed by software to get the accurate curvature of the measured lens. Other informations, such as surface deviation and roughness, are also available.

Zygo NewView 100 surface profiler is based on scanning white-light interferometry and can generate a three-dimensional measured surface image. The NewView 100 was used to measure the microlens curvature radius and its surface roughness.

5.5.3 Wavefront Aberration Measurement

Although a lot of information can be got from the measurement of the surface profile, there are still some limits to it. The main problem is that it cannot get the information about microlens shape near the corners and edge. These areas are suspected to be one of the main contributors to the wave aberration and scattered light. It was therefore decided that an interferometer measurement is necessary to measure the wavefront aberrations of the microlens, especially to measure the wavefront aberration at microlens corner and edge.

It is very natural that a modified Twyman-Green interferometer is first considered because it is easy to carry out. A Twyman-Green interferometer allows the measurement of the deviation from a perfect sphere. After the test apparatus was set up and some measurements were carried out, it was found that the interferograms of the microlens were not clear enough. In this measurement, the light passes through the microlens and is reflected back by an adjustable mirror. The poor interferograms were because the light beam passes through the testing microlens twice. If the adjustable mirror is not used, the light is reflected back from the microlens curved surface directly, but the interferograms did not improve as the reflection is low for the transmitting glass surface and there are two surfaces which will reflect light back. One is the testing curved surface and another one is the flat surface on the other side of the microlens. The reflected light from the flat surface will contaminate the interferogram. Another drawback of using a Twyman-Green interferometer to measure the wave aberrations is that there are various of ways that light may be reflected back to generate a interferometrical fringe pattern as Hutley et al. (1991) pointed out (such as the reflections from front surface Cat's eye and the rear surface Cat's eye). This may cause superimposed fringe patterns which may distort the pattern under study and make it impossible to obtain a reliable quantitative interpretation.

Because of these problems, an alternative design of the interferometer seems necessary. The problems can be solved if light passes only once through the testing microlens. A modified Mach-Zehnder interferometer was used for the measurement. The Mach-Zehnder interferometer directly measures the wave aberrations which describes the deviation of the actual wavefront from a perfect wavefront. The schematic diagram of the modified Mach-Zehnder interferometer is shown in Fig. 5-8a. Collimated HeNe laser light with a wavelength of 632.8nm is divided in two by first cube beamsplitter 1. One beam is directed by a plane mirror 4 through the microlens array 5 and the light focussed by the testing microlens is collected and collimated by a microscope objective 6. The other beam is reflected by a plane mirror 3 and then combined with the first beam at the cube beam splitter to generate an interferogram at the CCD detector. A lens 8 with a suitable focal length is used to image the pupil, which is the testing microlens aperture, onto the CCD detector. A neutral density filter 2 is used to adjust the intensity of the laser light in one of the beam in order to ensure that interfering beams are of equal intensity and thereby to maximise the fringe contrast. Fig. 5-8b is the experimental set up of the modified Mach-Zehnder interferometer. The testing microlens array can be clearly seen located before the objective.

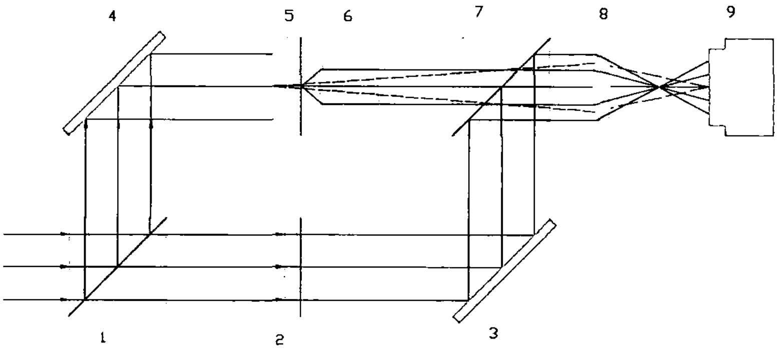

Figure 5-8a. Schematic of the Mach-Zehnder interferometer. 1— Cube beamsplitter. 2— Neutral density filter. 3— Plane mirror. 4— Plane mirror. 5— Testing microlens array. 6— Microscope objective. 7— Cube beamsplitter. 8— Pupil image lens. 9— CCD detector.

Figure 5-8b. The experiment setup of the modified Mach-Zehnder interferometer for the measurement of microlens wavefront aberrations.

It is important to take the photography of the interference pattern correctly. An aberrated wavefront continuously changes its shape as it travels. Only at the position of the pupil, can one get the required interferogram. For this purpose, two conditions have to be satisfied (Malacara 1978): (a) the interferogram at the pupil of the system must be representative of the wavefront distortions there, and (b) the photographic plate (or CCD) must be placed in a plane conjugate to the pupil of the measurement instrument.

5.6 The Tests of Microlenses

In the last section, different microlens test apparatus and methods have been described. In this section various microlens arrays will be tested with these apparatus and methods. The tests of LIMO microlenses are discussed in Chapter 9. Although many microlens arrays from different manufacturers were tested, only those with good qualities are presented here.

5.6.1 TEIFU Microlens Arrays

The microlens arrays for the Thousand Element Integral Field Unit (TEIFU) (Haynes et al. 1998) are manufactured by Adaptive Optics Associates (AOA). TEIFU has been used at

William Herschel Telescope. There are two kinds of microlens arrays for TEIFU. One is IFU input microlens array and the other is an output microlens array. Only the input array is discussed.

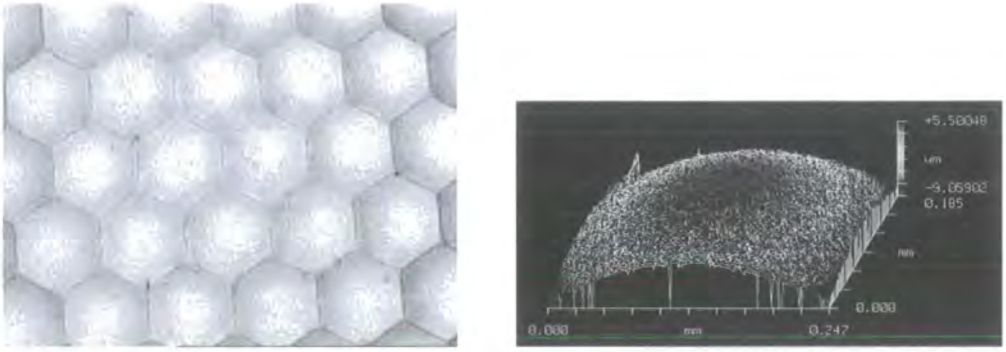

(a) (b)

Figure 5-9. Photograph of TEIFU input microlens array (a) and 3-D surface profile (b) after coating. The microlens surfaces have been damaged by over-bombardment during the coating. The radius is 940.82 microns and surface roughness Ra is 0.130 microns. Note that there is a peak on the left rear corner in figure (b) which is believed to be a dust. The microlens diameter is 0.3017mm and F number is F/5.6.

The input microlens array is composed of 31x20 microlenses fabricated on a rectangular fused silica substrate. The microlens material is epoxy. For TEIFU, the sky image is formed on the curved surface of the microlens and the image of telescope pupil is formed on the back flat surface. The flat side of the input microlens array is glued to an input fibre bundle to avoid light loss at the air-glass interface. The microlenses are hexagonal and hexagonally packed. Fig. 5-9 (a) is a microphotograph of the input microlens array. The fill factor is ~100%.

The microlens array was sent to Avimo Thin Film Technologies for an IAD low temperature coating using a 0.4-0.7 μm standard anti-reflection coating. The coating was not successful because of over-bombardment which resulted in a rough surface.

The transmission of the AR coated microlens was also measured using a Perkin-Elmer /UV/VIS/NIR Lambda 19 atomic absorption spectrophotometer at Durham University. The measurement is to compare the transmission before and after the AR coating. The measurement wavelength is from 0.45 to 0.8 microns and the coated and un-coated part of the array plate were measured for comparison. The measurement is showed in Fig. 5-10. It is clear that the coated part has lower transmission than that of the un-coated. This means that the coating was not done correctly.

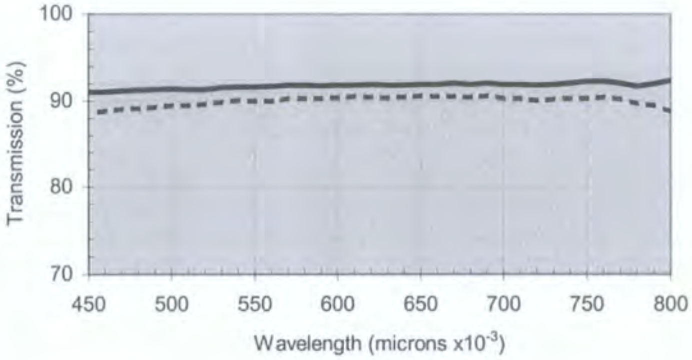

Figure 5-10. Transmission vs. wavelength of TEIFU input microlens before and after coating. The solid curve is for un-coated microlens and dashed curve is for coated microlens.

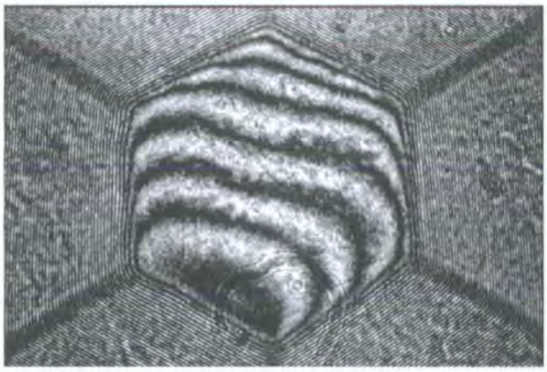

Figure 5-11. The interferogram of TEIFU input microlens (after AR coating). The peak-valley wavefront aberration is about 1.5 wavelength on the whole microlens aperture. The hexagonal shape can be seen clearly. At the area near the lens edge, the wavefront aberration increases quickly.

The wave aberration test was carried out by using the modified Mach-Zehnder interferometer (Fig. 5-8). The interferogram is shown in Fig. 5-11. The microlens array was carefully aligned.

Several microlenses were measured and no significant differences in the wave aberration were found. This confirms that the uniformity of the microlenses is very good. The measurement was also carried out on different days with individual alignment of the measurement system. Again no differences were found and this confirmed that the alignment of the measurement system was accurate. The measurement accuracy for peak-valley wave aberration is estimated to be better than $\lambda/4$ wavelength.

The peak-valley wave aberration of the microlens was 1.5 wavelengths over the whole microlens aperture at 0.63 μm. Note that for Mach-Zehnder interferometer, one fringe corresponds to one wavelength difference in wave aberration. It is clear that at the centre part of the microlens (80% of the full aperture), the wave aberration is small. However at the edge and corners, the wave aberration increases more rapidly than that at the central part. This big wave aberration at the edge may be caused by the fabrication process: the boundary conditions are different which results in the different tensions between the photoresist and the substrate, thus results in different surface curvatures.

The PSF of the input microlens is showed in Fig. 5-12. The test apparatus is shown in Fig. 5-6. The irradiance of the PSF is on logarithmic scale in order to clearly show the scattered light. The diffraction disk is clear and the PSF is uniform on the focal plane for different microlenses. It is clear that there is some stray light around the Airy disk and in the diffraction wings. This is caused by wave aberration. The encircled energy obtained by integrating the flux of PSF over the full aperture is shown in Fig. 5-13 for the microlens before coating. At small radius, the encircled energy is dominated by optical aberration. At large radius (after about 50 μm), the encircled energy increases slowly and the scattered light begins to dominate. There is 90% encircled energy at radius 57 μm and the encircled energy is very low compared with theoretical calculation because of the big wave aberration and surface roughness. The surface RMS roughness is estimated to be 0.013 microns, the same as for Epigem microlenses (see next subsection) for un-coated microlenses and contributes about 7% scattered light. The PSF and encircled energy were measured before coating. However, there is no significant difference in the encircled energy before and after AR coating. The reason is not clear and it needs to be noted that the equation (5-3) for scattered light calculation is no longer suitable because the roughness is outside the eligible range. Although the coating surface is rougher than before coating, it is still very uniform and the microlens is still in good shape and can focus light correctly. This implies that IAD coating may be suitable for microlens array AR coating if applied correctly.

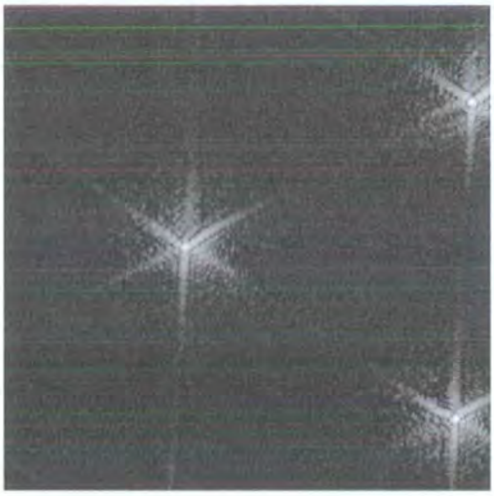

Figure 5-12. The PSF image of TEIFU input microlenses before coating. The intensity scale is logarithmic. The PSFs of three microlenses are shown in the figure. The diffraction disk can been clearly seen. The microlens array has good uniformity in image quality and focal length.

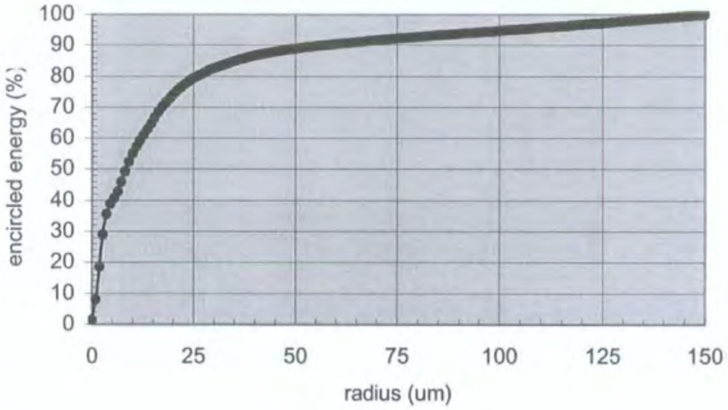

Figure 5-13. Encircled energy curve of TEIFU input microlens before coating. The maximum radius is 150 μm, which is pitch/2 of the microlens array. There is 90% encircled energy at the radius of 57 μm.

5.6.2 GMOS Microlens Arrays

The GEMINI Multi-Object Spectrographs (GMOS) (Allington-Smith 2000) microlens array is composed of 30x44 microlenses fabricated on a circular fused silica substrate with fill factor of

~100%. It is also fabricated by AOA with the same techniques for TEUFU microlens array. Although the IAD coating for TEIFU microlens array is not successful, it is still believed that considering the low temperature and uniform of the coating, IAD is the best technique for microlens array. For GMOS microlens array, the IAD coating was done by Siltint Industries Limited. Siltint was chosen because its experiences on plastic AR coating. The photograph of the input microlens array is shown in Fig. 5-14.

The surface roughness was not measured but it is expected to be similar to TEIFU microlens array as both use the same manufacture techniques. From Fig. 5-14 (a), it can be seen that the surfaces are not smooth. The PSFs are shown in Fig. 5-15. The PSFs are very similar to that for TEIFU input microlens array in Fig. 5-12. The encircled energy of the microlens is shown in Fig. 5-16. There is 90% encircled energy in the radius of 54 μm for un-coated microlens. Compared with the encircled energy of TEIFU input microlens (90% encircled energy at radius 57 μm), the GMOS input microlens is almost the same optical quality.

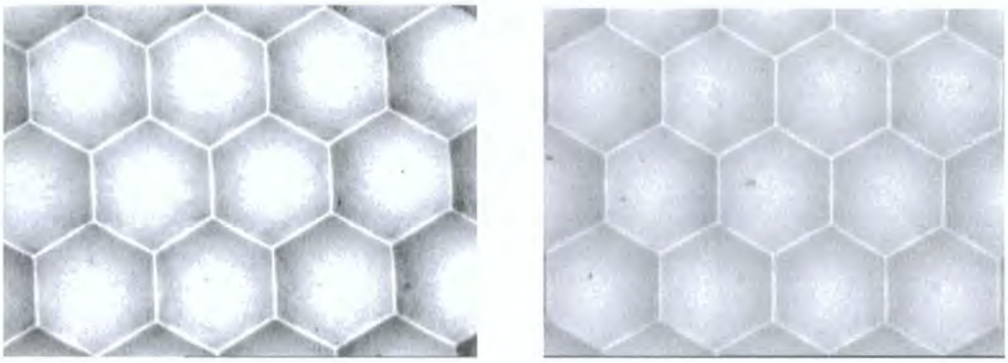

(a) (b)

Figure 5-14. The photograph of GMOS input microlens array before (a) and after coating (b) for the same array. The un-coating array photograph is brighter than the coated array. The hexagonal lenses are hexagonally packed. The microlens diameter is 0.406 mm and F number is F/4.85. The array is composed of 30x44 lenslets with 28x42 lenslets for clear apertures

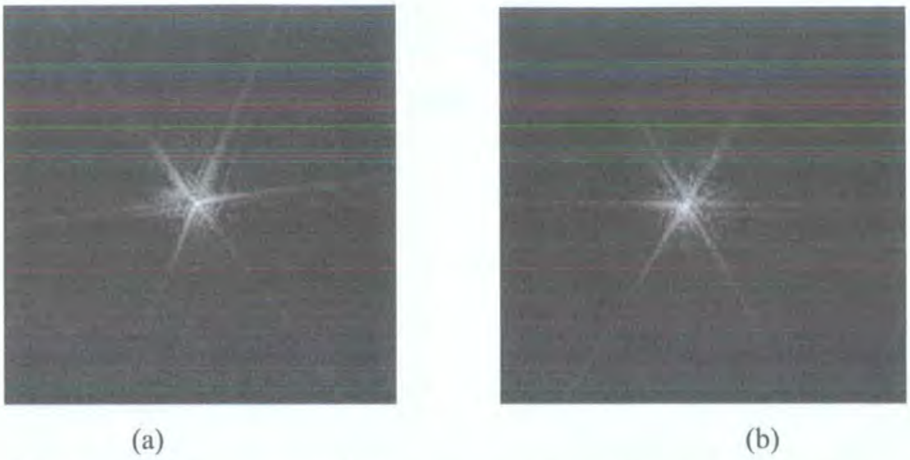
(a) (b)

Figure 5-15. The PSF image of GMOS input microlenes before coating (a) and after IAD coating (b). The intensity scale is logarithmic. The diffraction disk can be clearly seen.

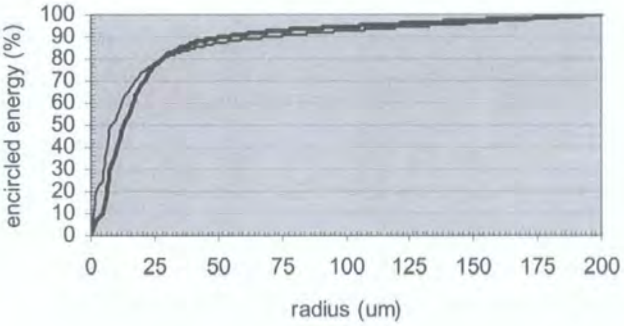

Figure 5-16. The encircled energy of GMOS input microlens. Thin curve is for coated microlens and thick curve is un-coated. There is 90% encircled energy in the radius of 54 μm and 71 μm for the un-coated and coated microlens, respectively. The Airy disk is 7.5 μm.

The PSFs for GMOS coated and un-coated microlenses are shown in Fig. 5-15. The PFSs are very similar before and after coating. The encircled energies are shown in Fig. 5-16. At small radius, the coated microlens is better than the un-coated according to the encircled energy. However, at bigger radius, i.e. when the radius is bigger than 30 μm, the coated microlens is slightly worse than the un-coated. The difference is about 2% in encircled energy. As a net result, the microlens array is almost the same quality after IAD coating. It is possible that the coating slightly changes the shape of the curved surface of the microlens. It is also noted that the microlens array was not clean and some dust and grains were still left on the microlens surface after coating. This situation may be improved for monolithic microlens array as cleaning this kind of microlens array will not be a problem.

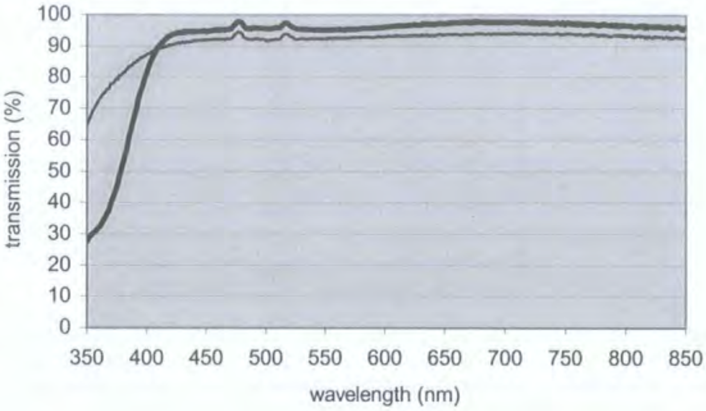

Figure 5-17. GMOS microlens transmission curves. The thin curve is for the un-coated and the thick curve is the coated microlens. The transmission is 92.8% and 95.9% for un-coated and coated surfaces, respectively at 0.85 μm. There is about 3% gaining in transmission after coating.

The spectral transmissions of the coated and un-coated arrays were measured at the blank area of the microlens array with the Perkin-Elmer /UV/VIS/NIR Lambda 19 spectrophotometer and are shown in Fig. 5-17. It is clear that the transmission is improved and there is about 3% gain in transmission after coating. The measurement is consistent with the specification of Siltint's catalogue that there is less than 0.4% reflection in the standard wavelength range (Multilayer Specification Sheet 2000).

5.6.3 Epigem Microlens Array

The sample was manufactured by Epigem Limited. The material of the microlens array is PMMA (polymethyl Methacrylate). The microphotograph is shown in Fig. 5-18(a). The microlenses are close packad with almost 100 % filling factor. The 3-D surface profile was measured with the NewView 100 surface profiler and is shown in Fig. 5-18 (b). The curvature radius is 272.29 microns. The surface roughness Ra is 0.013 microns, which introduces about 7 % scattered light according to equation (5-3).

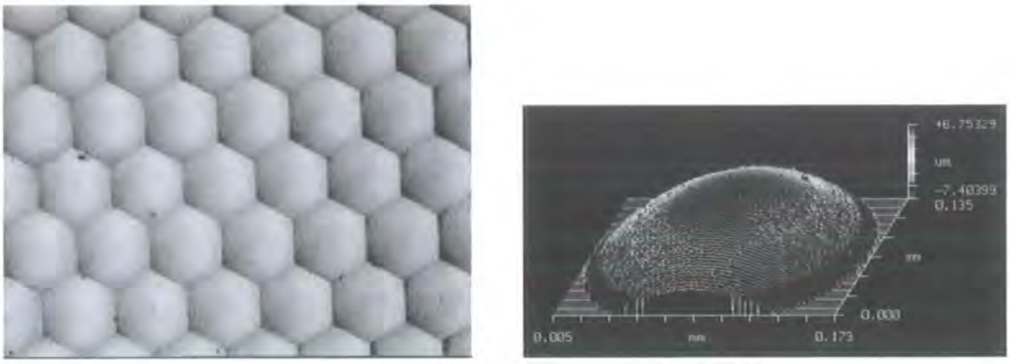

(a) (b)

Figure 5-18. Photograph of EPIGEM hexagonal microlens array (a) and 3-D surface profile (b). The hexagonal microlenses are hexagonally packed. The microlens diameter is 0.250 mm and F number is F/2.2.

The wave aberration is shown in Fig. 5-19(a). The peak-valley wave aberration of the microlens was 0.5 wavelengths over the whole microlens aperture at 0.63 μm. The wave aberration is very small even though the microlens is very fast (F/2.2). The 0.5 wavelength aberration corresponds to 0.69 μm curvature error, which is 2.3% of the sag height.

The PSFs are shown in Fig. 5-19(b). The stray light around the Airy disk and diffraction wings is very low compared with both of TEIFU and GMOS input arrays. This is because the wave aberration is very small and thus most light is concentrated in or near the Airy disk. The encircled energy of the microlens is shown in Fig. 5-20. There is 90% encircled energy in the radius of 20.1 μm and the image quality is excellent. It is clear that the other 10% encircled energy is contributed mostly by the scattered light, which is introduced by the surface roughness.

The spectral transmission of the PMMA was also measured using a blank area of the microlens array because of the concern about spectral absorption. The measurement is shown in Fig. 5-21. There is no spectral absorption over the visible wavelength range. However at near infrared there is strong absorption around 1.7 μm. This implies that this microlens can be used in the visible with no loss due to absorption. If this microlens is used for the near infrared, it will be necessary to fabricate the microlens on glass substrate. In this case, because the microlens thickness, i.e. the sag height is small (below 50 microns), the spectral absorption will be very low and can be negligible.

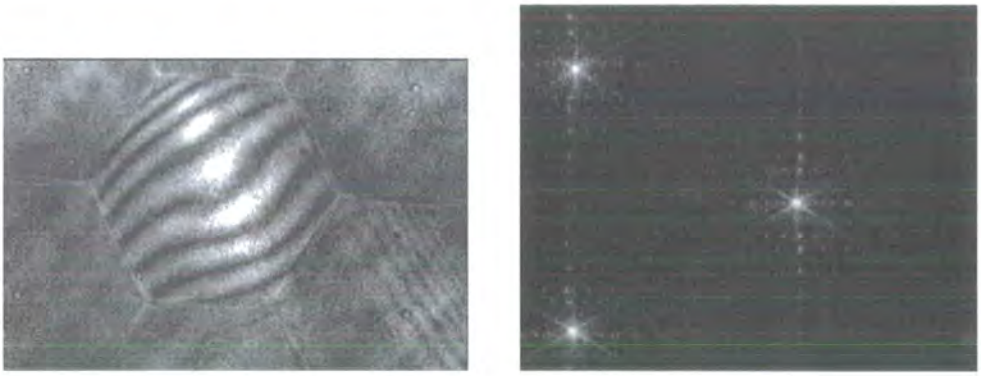
(a) (b)

Figure 5-19. Interferogram of Epigem hexagonal microlens (a) and PSFs (b). The peak-valley wavefront aberration is about 0.5 wavelength on the whole lens aperture. The hexagonal shapes can be seen clearly. In figure (b), the intensity scale is logarithmic and the stray light is very low.

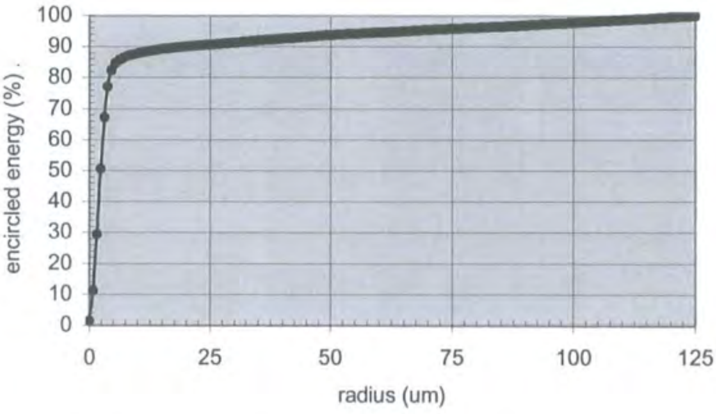

Figure.5-20. Encircled energy curve of the Epigem microlens. The maximum radius is 125 μm which is pitch/2 of the microlens array. There is 90% encircled energy at radius 20.1 μm. The diameter of Airy disk is 3.4 μm.

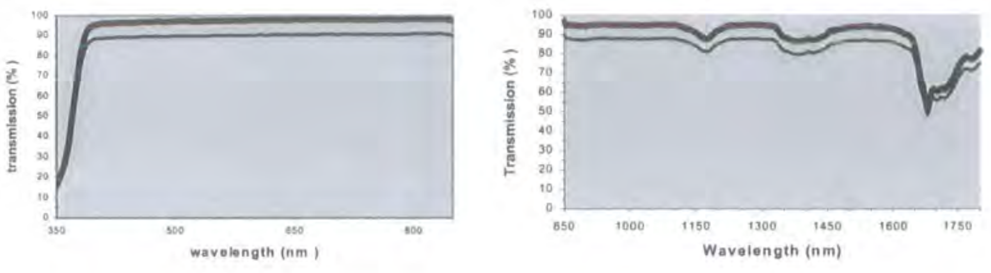

(a) (b)

Figure 5-21. The PMMA Transmission curves at visible wavelengths of 350-850nm (a) and near infrared wavelengths of 850-1800nm (b). The PMMA is 1mm thickness. The thin curve is the transmission including reflection loss of two PMMA-air interfaces. The thick curve is the internal transmission after the PMMA-air interface reflections are removed. Note that there is a discontinuity at 850nm because of changing detector.

5.6.4 AMS Microlens Array

The AMS microlens array is fabricated by monolithic silica using special RIE technique. Silica microlenses have better optical and physical properties than polymer microlenses. Fig. 5-22 (a) is a photograph of the AMS hexagonal microlens array. It can be clearly seen that there is a lens-to-lens gap, which is about 10-15 microns according to the measurement. The accuracy of the measurement is limited by the resolution of the translation stage of the microscope, which is 5 microns. The 15 micron gap will introduces about 6% scattered light if the microlens is uniformly illuminated. Note that the photograph is not clear. This is because the microlens has a small sag height and good surface quality.

The surface quality is excellent and the surface profile is shown in Fig. 5-22 (b). Curvature radius is 4666.52 and RMS surface roughness is 0.003 microns. The surface roughness introduces only about 0.4% scattered light at the measurement wavelength of 0.63 microns. The scattered light is very low and can be negligible.

The interferogram of AMS hexagonal microlens is shown in Fig. 5-23. The wave aberration is too small to observe. Note that the microlens is very slow with a F number of F/21. The slow microlens has a small sag height, which is 6.2 microns. It is not surprising that the small sag height introduces small wave aberration.

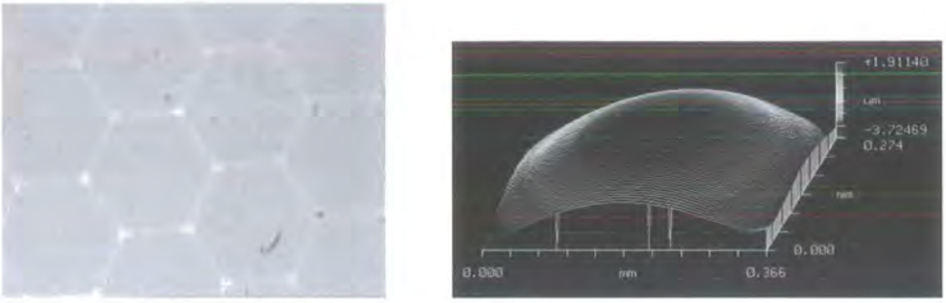

(a) (b)

Figure 5-22. The photograph of AMS hexagonal microlens array (a) and 3-D surface profile (b). The radius is 4666.52 microns and surface roughness is 0.003 microns. The microlens diameter is 0.480 mm and F number is F/21.

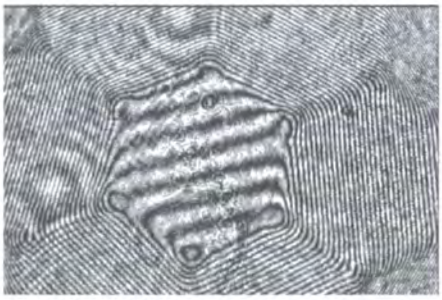

Figure 5-23. The interferogram of AMS hexagonal microlens. No significant wavefront aberration can be observed. The peak-valley wavefront aberration is very small over the whole microlens aperture.

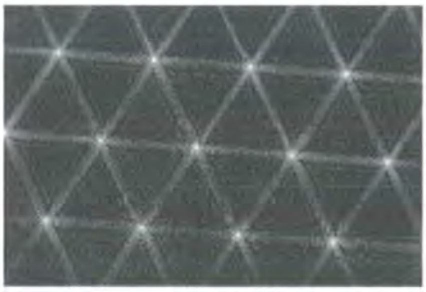

Figure 5-24. PSF images of AMS microlenses. The intensity is on a logarithmic scale. Diffraction disk can be clearly seen. There is some scattered light in the diffraction wings. The uniformity of the focal lengths is excellent.

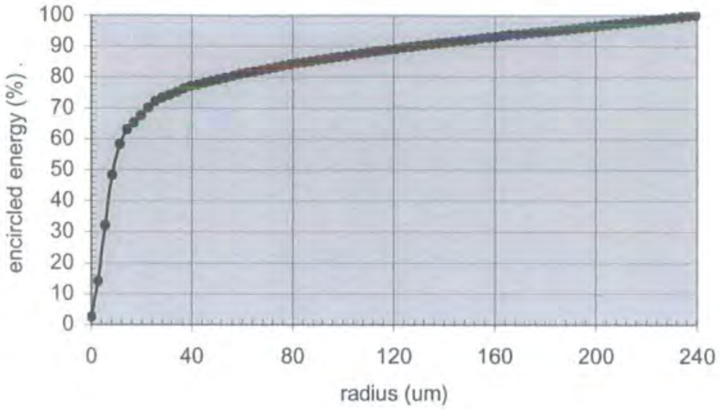

Figure. 5-25. The encircled energy curve of an AMS silica monolithic microlens. There is 90% encircled energy at radius 123 μm. The measurement wavelength is 0.6328 μm and the Airy disk is 32.3 μm.

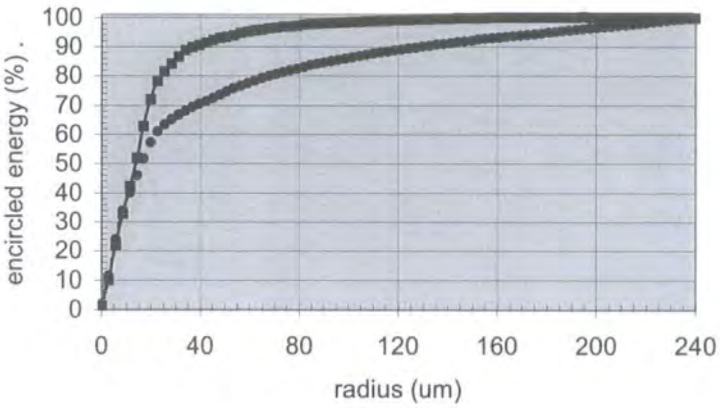

Figure. 5-26. The encircled energy curves of an AMS silica monolithic microlens. The upper curve is the measurement with 400 μm pinhole mask. The lower curve is the measurement without pinhole mask. There is 90% encircled energy at radius 130 and 37 μm for the microlenses without and with mask, respectively. The measurement wavelength is 0.5435 μm.

The PSFs of the microlens array is shown in Fig. 5-24. It is clear that the PSFs are very uniform and so the focal lengths are uniform for the microlens array. There is some scattered light in the diffraction wings. This may be because there is a large lens-to-lens gap and there are some shape errors at the microlens aperture edges. Both will certainly introduce scattered light.

The encircled energy of the AMS microlens is shown in Fig. 5-25. There is 90% encircled energy in the radius of 123 μm. At first glance, the encircled energy is low, but the microlens is very slow and after scaled to F/5, the encircled energy will increase. This will be discussed in the next section.

Fig. 5-26 is the encircled energy of another AMS microlens. In this figure, one curve is for the microlens without a pinhole and another one is for the microlens with a 400 microns pinhole placed before it to block the microlens edge, corner and the microlens-to-microlens gap in the measurement. It confirms that the microlens edge area or lens-lens gap makes a great contribution to the scattered light. So for this microlens array, encircled energy is dominated by the gap between microlenses. Note also that the measurement wavelength is 0.5435 μm whereas the other measurements presented previously are at 633nm. Since scattered light is worse and wave aberration is big at shorter wavelength, this makes the encircled energy curve looks worse at short wavelength. Comparing the measurement of without mask at long wavelength (Fig. 5-25), the scattered light is more serious at short wavelength. This is consistent with equation (5-3) for the TIS calculation.

5.7 Comparison of Microlenses According to Encircled Energy

In this section, a mathematical formula is derived to scale microlenses with different specifications (i.e. different diameter and F number) to the same specifications, so that a comparison between different microlenses can be made. This formula can also be used to estimate the image quality of a microlens which has different specifications with the tested one. This is useful if one will purchase a custom-design microlens array from one company but only has information on a tested array of different specifications. The estimation is done by scaling the specifications of the tested microlens to that of the custom-design. Note that the comparison and estimation are for uncoated microlenses.

5.7.1 Mathematical Theory

A practical way to compare the image quality of microlenses is to scale different microlenses with different sizes and F number to the same specifications, i.e. the same aperture diameter and F number, so that the comparison according to encircled energy is feasible.

A formula which can be used to calculate the encircled energy for arbitrary aperture shapes was derived by Clark et al. (1984). It only considers the diffraction and is expressed as

$$E(r_0) \approx 1 - \frac{\lambda f}{2\pi^2 r_0} R \tag{5-9}$$

Where λ=wavelength,

f=effective focal length,

r_0=radius on the focal plane,

R=aperture perimeter-to-area ratio, and

E=normalized encircled energy—fraction of the energy transmitted by the aperture that falls within the circle of radius r_0 about the irradiant centre of the PSF.

For a lens with circular shape, R is

$$R = \frac{4}{D} \tag{5-10}$$

Where D is the diameter of the circular lens. For a lens with a square shape, D is the side length of the square lens. For a lens with a hexagonal shape, D is the diameter of the inner tangent circle of the hexagon. For close packed hexagonal or square lenses, D is also equal to the array pitch.

From formula (5-10), Clark's equation (5-9) become

$$E(r_0) \approx 1 - \frac{2\lambda F^{\#}}{\pi^2 r_0} \tag{5-11}$$

So, the relative encircled energy, i.e. the fraction of light compared with that within the lens diameter is

$$E_{rel}(r_o)=\frac{E(r_o)}{E(\frac{D}{2})}=\frac{1-\frac{2\lambda F^{\#}}{\pi^2 r_o}}{1-\frac{4\lambda F^{\#}}{\pi^2 D}} \tag{5-12}$$

Formula (5-12) is a function of $F^{\#}$ and D. The comparison in fact is to scale the microlenses with different $F^{\#}$ and different diameter D to the same $F^{\#}$ and same diameter D. If the relative encircled energy is fixed (such as 90% encircled energy) when a lens is scaled to another $F^{\#}$ and diameter, from formulae (5-12) one has the relationship

$$\frac{1-\frac{2\lambda_1 F_1^{\#}}{\pi^2 r_{o1}}}{1-\frac{2\lambda_1 F_1^{\#}}{\pi^2 D_1}}=\frac{1-\frac{2\lambda_2 F_2^{\#}}{\pi^2 r_{o2}}}{1-\frac{2\lambda_2 F_2^{\#}}{\pi^2 D_2}} \tag{5-13}$$

It needs to be noted that the equation also allows the measurement wavelength to be scaled. The meaning for formula (5-13) is that for the same encircled energy (such as 90%), after the lens is scaled from $F_1^{\#}$, D_1 and r_{o1} to $F_2^{\#}$, D_2 and r_{o2}, the encircled energy in radius r_{o1} and r_{o2} is the same before and after scaling. So, formula (5-13) can be used to estimate the encircled energy in radius r_{o2} for a new microlens with diameter D_2 and F number $F_2^{\#}$, according to a measurement data of the encircled energy from a lens with D_1, $F_1^{\#}$; Another application of formula (5-13) is to compare different microlenses manufactured by different companies. After all are scaled to the same aperture diameter and $F^{\#}$, it is obvious that for the same encircled energy the lens with smaller radius will be better than that with bigger radius after scaling, i.e., the smaller the radius, the better the microlens is.

Although equation (5-13) is derived from Clark's equation (5-9) which only consider aberration-free optical systems, the results have more general validity. Mahajan (1979) and Barakat and Houston (1963) have shown that to the first order the behaviour of encircled energy function is independent of aberrations. As a result, equation (5-13) is valid for large radius even when aberrations are present. The influence of aberrations is to increase the minimum value of the radius for which the equation is valid. Furthermore, it has been stated in section 5.3.7 that small aberrations only cause a change of irradiance distribution within the PSF. In this case, the shapes and positions of Airy disk and diffraction wrings are not affected by the aberrations. This has been confirmed by the PSF photographs shown in section 5.6. In these photographs, the Airy disk is clearly seen, the scattered or stray light is in the diffraction pattern outside the Airy disk and along the diffraction spikes. In the area that is far away the Airy disk, the scattered or stray light is exactly along the diffraction wings (for hexagonal microlens there are 6 wings). This means that in this case the scattered or stray light can also be scaled according to diffraction without causing significant error. In the next section, it will be shown that equation (5-13) is only used to scale microlenses at 80% and 90% encircled energy. It is obvious that the encircled radii at 80% and 90% encircled energy are far away from the Airy disk and in this case the influence of the aberration is negligible.

5.7.2 Comparisons According to the Measurement Data

The comparisons are carried out by scaling different microlenses manufactured by different companies to the same diameter and $F^{\#}$, at the encircled energy of 80% and 90%, respectively. As all the microlenses have the same diameter and $F^{\#}$ after scaling, the smaller the radius which has 80% or 90% encircled energy (EE), the better the microlens is. At large radius, the EE is mainly decided by diffraction and scattering. The comparison is more relevant to the scattered light and diffraction because this includes most of the encircled energy and the encircled energy curve is relatively flat and far away from the Airy disk.

Note that all the microlenses in the comparisons have hexagonal shape and are hexagonally packed. This ensures that all the lenses have the same conditions for comparisons. It is not appropriate to compare circular microlens with hexagonal microlens because circular microlens cannot be close-packed with 100% fill factor.

The calculations according to the measurement data discussed in the previous subsections are shown in Table 5-1. From Table 5-1, it is clear that Epigem microlens is the best in image quality. AOA microlenses are worse than that of Epigem and AMS. AOA microlens for GMOS and AOA microlens for TEIFU have almost the same performance at 90% encircled energy, but AOA microlens for TEIFU has a better performance at 80% encircled energy and this means that this lens has a relatively small aberration. Also at 80% encircled energy, the radius for Epigem microlens is only 9.1 microns, much less than the other microlenses, this is because its wave aberration is very small.

Table 5-1. Comparison of microlens performance according to scaling of encircled energy.

	Before scaling		After scaling to: F/5, D=500 um	
Lens	Radius r_{01} with 80% EE	Radius r_{01} with 90% EE	Radius r_{02} with 80% EE	Radius r_{02} with 90% EE
Epigem: F/2.2, D=250um	4 um	20 um	9.1 um	44.5 um
AMS: F/21, D=480um	54 um	127 um	15.4 um	50.8 um
AOA/GMOS: F/4.85, D=406um	30.9 um	54 um	32.7 um	58.2 um
AOA/TEIFU: F/5.6, D=301.7um	26 um	57 um	25.2 um	61.5 um

5.7.3 Performance Estimation According to the Measurement Data

In most cases, the in-stock microlens array that one can obtain from a manufacturer may not be similar to the required specifications for an actual IFU spectrometer. But these in-stock microlens arrays are inexpensive and in some cases one can obtain a free sample for test purposes. The cost of a custom-designed microlens array will be about 10 times that of the in-stock. This is the case for the FMOS IFU. One interesting question is how to estimate the performance of a microlens using the measurement data of a microlens which has different specifications but is manufactured by the same company. For example, suppose that one had measured a microlens with the specification of F/3 and diameter 300 microns and this is an in-stock microlens array, what would be the performance of a custom-design microlens array with the specifications of F/5 and diameter 500 microns?

Here the Epigem F/2.2, D=250 μm microlens was used to scale to different $F^{\#}$ but with the diameter of 500 μm. For the microlens array for FMOS IFU, the specifications are F/5, D=500 μm. It is interesting to know how the encircled energy changes for microlenses with different $F^{\#}$. Again formula (5-13) is used to scale the Epigem microlens to different $F^{\#}$. All of the Epigem microlenses before and after scaling have the same image quality because all of them are scaled from the same lens of F/2.2, d=500 μm that is listed in Table 5-1. The results are listed on Table 5-2.

Table 5-2. The scaling of Epigem to different $F^{\#}$ at 500 μm diameter.

F/3, D=500 μm		F/4, D=500 μm		F/5, D=500 μm		F/6, D=500 μm	
r_{02} with 80% EE	r_{02} with 90% EE	r_{02} with 80% EE	r_{02} with 90% EE	r_{02} with 80% EE	r_{02} with 90% EE	r_{02} with 80% EE	r_{02} with 90% EE
5.5 μm	28.7 μm	7.3 μm	36.9 μm	9.1 μm	44.5 μm	10.8 μm	51.6 μm

From Table 5-2, it can be seem that a fast lens can collect more light than a slow one. The radius for the same encircled energy is proportional to the $F^{\#}$. It can be seem that the radius r_{02} with 80% encircled energy increases more quickly than the radius with 90% encircled energy. But the difference is not obvious. From F/6 to F/3, the radius with 90% encircled energy at F/6 is 1.8 times that at F/3, compared with 1.96 times with 80% encircled energy.

5.8 Summary & Conclusions

Two kinds of refractive microlenses were discussed in this chapter. Their properties are summarised as follows

- Polymer/epoxy microlens can be fabricated with high surface shape accuracy, i.e. with small wave aberration. An example is Epigem microlens, which has 0.5 peak-valley wavelength aberration which corresponds to 2.3% sag height error.
- The surface roughness of Polymer/epoxy microlens is about 0.013 μm, which introduces about 7 % scattered light. It is difficult to reduce the roughness below this value with current techniques. Note that all the tested polymer/epoxy microlenses are fabricated by replication from a master.
- Monolithic glass microlens can have a very low surface roughness and the scattered light introduced by the surface roughness can be negligible. An example is AMS

microlens, which has a surface roughness of 0.003 μm which introduces only 0.4% scattered light at the measurement wavelength of 0.63 μm.

- Monolithic microlens may have big wave aberrations because of the Two-Step manufacture process. Care needs to be taken to control the wave aberration which may be caused by the RIE transfer process.
- For all microlenses, it is desirable that the peak-valley wave aberration is less than one wavelength if good image quality is required.

A mathematical model is also derived to allow a comparison between different microlenses. The image qualities of Epigem and AMS microlenses are better than that of TEIFU and GMOS microlenses. This is because TEIFU and GMOS microlenses have big wave aberrations. Finally, it was demonstrated that IAD is suitable for microlens AR coating.

Chapter 6

FMOS project

Abstract

In this chapter, the scientific cases and FMOS instrument concepts are described. The requirements and specifications for these instruments are discussed and these will be used as design guides for the following chapters. Most of this chapter is taken from the FMOS design document (Dalton et al. 1999).

6.1 Introduction

FMOS project is an international cooperation between UK, Australia and Japan. Some of the work of FMOS will be carried out at Durham. These include the Multiple IFUs (M-IFUs), fibre connectors, and the optical spectrographs. The M-IFUs and optical spectrographs are options for FMOS. In this chapter, the scientific cases are described first, then is the FMOS instrument concept. Finally, the design requirements and specifications for M-IFUs, fibre connectors and the optical spectrographs are given. This chapter includes a brief description of the instrument design requirements which will be designed or built at Durham. More details about other instruments can be found in FMOS design documents (Dalton et al. 1999, Maihara et al. 2000).

6.2 Scientific Cases of FMOS Project

FMOS is a conceptual design for a versatile optical and near-infrared fibre spectroscopic facility for the prime focus of the 8-m Subaru telescope. FMOS will provide the visible (0.4μm~0.9μm) and NIR (0.9μm~1.8μm) spectroscopic ability. The NIR will be useful to study redshifted galaxies, cool objects and those regions which are optically hidden by dust. The scientific cases were discussed in detail in the FMOS design document (Dalton et al. 1999). These are summarized in Table 6-1.

Table 6-1. Scientific cases for FMOS instrument (From FMOS design document)

Scientific Cases	Wavelength Ranges (μm)	FMOS Mode	Number of objects /field
Brown dwarfs	0.6 –1.8	MOS	≥300
Young stellar objects	1.0 –1.8	IFU	~50
Galactic structure	0.4 –1.0	MOS	≥100
Stellar abundances	0.4 –0.9	HDMOS	~5
Planetary nebulae	0.4 –0.9	MOS	≥200
Galaxy evolution	0.4 –1.8	MOS/IFU	>400
XMM fellow up	0.4 –1.8	MOS/IFU	~400
High-z QSQs	0.4 –1.8	MOS	≥200
QAL systems	0.4 –0.9	HDMOS	≥10

Some of the scientific cases have been discussed in Chapter 1. It is clear that most of the scientific cases require the optical and NIR spectroscopy simultaneously over the wavelength range 0.4 –1.8 μm. Extending the wavelength coverage beyond 1.8 μm is unlikely to be productive due to the instrumental thermal background and the requirement to cool cryogenically the whole instrument. It is also impractical to work at wavelength shorter than 0.4 μm because of the low transmission of the glasses, the difficulty of coating and chromatic aberration. Non-cryogenic spectrograph have been studied by several people (Dallier and Cuby 1998, Joyce et al 1998). A general conclusion is that the sky emission above 1.8 μm (H band) is essentially limited by the thermal emission, while below this limit, the OH airglow emission dominates. As the sky is not thermal emission dominated in the wavelength range of 0.4 –1.8 μm, this makes a non-cooled instrument feasible.

6.3 The Principles of FMOS Instrumentation

The configuration of the FMOS instrument is shown in Fig. 6-1. At the top, the beam from the Subaru telescope is corrected by the Prime Focus (PF) Corrector, which is used to provide adequate image quality over the full 30′ FOV. The PF corrector has the following specifications:

- Wavelength range: 0.45 – 1.8 μm.
- Field of View: 30′ diameter.

- Image quality: 80% encircled energy within 0.4″ diameter and 90% encircled energy within 0.5″.
- Output focal ratio: 2.07.
- Telecentricity: telecentric images desired for a flat focal plane.

At the PF end, two different fibre modules are installed to give a Multi-Object Spectroscopic (MOS) mode using the "Echidna" positioner and an integral field spectroscopic mode (M-IFU) which includes a small number of fibres fed to an existing High Dispersion Spectrograph (HDS). The integral field module consists of about 15 individual modules, which are deployed within the prime focus plane. Each integral field mode consists of about 200 fibre elements covering a contiguous field. The spectrographs are located on the floor of the telescope dome. The fibre connectors are used to provide a break in the fibre train so that the prime focus instrument can be stowed in the instrument storage room. The fibre connectors also split the optical and NIR components of the light from each fibre into two separated sets of fibres which feed the optical and NIR spectrographs, respectively.

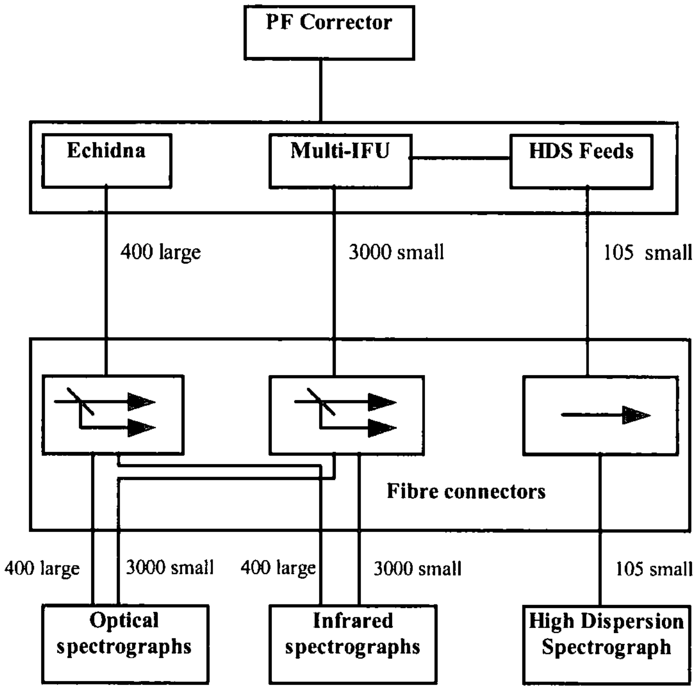

Figure 6-1. The basic concept of FMOS instrument.

400 large fibres from the Echidna positioner are split into two sets of fibres by a fibre connector. One set is for the visible wavelengths and is fed to the optical spectrographs. The other set is for the NIR wavelengths and is fed to the NIR spectrographs. Each set of fibres contains 400 large fibres. Similarly, 3000 small fibres from the M-IFU are also split into two sets of fibres. One set is fed to the optical spectrographs and other set is fed to the NIR spectrographs. Each set of the small fibre contains 3000 fibres. Also 105 extra small fibres that are from the M-IFU are fed to the existing high dispersion spectrograph. There are two optical spectrographs and two infrared spectrographs.

Note that the baseline system contains only the MOS Mode (Echidna) and the NIR channel, i.e. the NIR fibre connector and NIR spectrographs. The baseline system is being designed and built currently. The other parts are upgrade options and are for future consideration.

6.4 FMOS IFU

FMOS will provide about 15 deployable Integral Field spectroscopic Units enabling two-dimensional spectroscopy within the 30' diameter field. The specifications and constraints are given as:

- Accessible total field: 30′ diameter.
- Input focal ratio: F/2.07
- Output focal ratio: F/5
- Working wavelength range: 0.45 – 1.8 μm.
- Number of positionable modules: 15-20.
- Sampling increment: 0.3″
- Diameter of module field: 5.1″
- Field Geometry: hexagonal or square
- Number of fibres /module: 200-150
- Fibre center spacing at slit: 3 pixels.
- Total slit length: 6000 pixels.

There are about 15-20 positionable IFU modules needed to be deployed on the 30′ telescope field. This requires that the optical design of the IFU must be as simple as possible. A simple optical design means a compact IFU which can ensure that at least 15 IFU modules can be deployed on the telescope field. A configuration is shown in Fig. 6-2 in which 15 IFUs can be deployed on the telescope field. The IFU consist of a fore-optics and a microlens array and fibre bundle assembly. The fore-optics provides a magnified telescope sky image on the microlens array surface and the microlens array images the telescope pupil onto the back surface of each microlens which is also the entrance of each fibre. The PSF of the sky image is sampled by about two microlenses. The optical aberrations of the fore-optics need to be carefully corrected, especially the chromatic aberration because the IFU needs to work simultaneously at the visible and near infrared (0.45 –1.8 μm). All the IFU optical components are mounted in a tube. The tube has an outside diameter of about 16mm. However the head of the tube is smaller, with a diameter of less than 13mm. Note that at the head of the IFU tube, a prism is used to fold the light into the tube.

Figure 6-2. A configuration of 15 IFUs deployed within the 30′ diameter telescope field. The circle represents the diameter of the telescope field, which is about 140mm.

Each IFU module will have about 200 "pixels" (spatial elements), each of which consists of a small optical fibre fed by a microlens. The telescope sky images are magnified about 20 times by the fore-optics of the IFU to make it suitable to be sampled by the microlenses. A microlens array is then used to sample the sky image while projecting the telescope's pupil image onto the fibre cores. The IFU field geometry can be hexagonal if a hexagonal microlens array is used to sample the sky image or square if a square microlens array is used. The microlens array is accurately aligned and glued to a fibre bundle. At the other ends of the fibre bundles, the fibres are connected to a Fibre Connector, which splits the light into optical and NIR wavelengths and then feeds the fibres to the slits of the spectrographs.

6.5 FMOS Fibre Connecter

The environment of the Subaru telescope prime focus requires that the instrument modules can be automatically removed from the telescope and stored in the prime focus instrument storage room. The upper limit to the weight of the instrument and considerations of the flexure stability require the spectrographs to be located on the floor of the telescope dome. It is therefore necessary to employ a long fibre train. This fibre train ends in a connector box which accepts the MOS and IFS fibres from the instrument via a mechanical/optical connection which must be disconnected each time the instrument is removed from the telescope. The presence of a break in the fibre train provides a natural location for a set of dichroics which splits the light from the focal plane into visible and NIR wavebands to feed the spectrographs. The use of dichroics at the break point allows wavelength-optimized fibres to be used for the long fibre train to the spectrographs, and also allows for the possibility of visible and NIR spectroscopy simultaneously. The fibre connector also needs to convert the focal ratio to make it suitable to feed the spectrograph, which decided that lenses must be employed. Other advantages of using lenses for the connector will be discussed in Chapter 10.

There are 3000 small fibres, which are from the IFS system. The specifications for the IFS fibre connector are

Input focal ratio: F/5
Output focal ratio: F/5
Input fibre (source fibre) core diameter: 65 μm.
Output fibre (receiving fibre) core diameter: 65 μm.
Input wavelength range: 0.4 μm – 1.8 μm.
Output wavelength range (visible): 0.4 μm – 0.9 μm.
Output wavelength range (NIR): 0.9 μm – 1.8 μm.
Coupling efficiency: 95%.

The IFS fibre connector has an input and an output focal ratio of F/5. The optical designs for these connectors must minimize the effects of the optical aberrations in order to maximize the coupling efficiency due to the extended nature of the fibre source. The optical layout is shown in Fig 6-3 for a connector. The beam from the source fibres is collimated by the collimating lens. The visible light is transmitted to visible receiving fibres while the infrared is reflected by the beam splitter (dichroic) to the infrared receiving fibres. The collimating lens consists of a SK2/CaF2 doublet and the focusing lens consists of a SK2/F6 doublet for both the visible and near infrared channels. All the lens surfaces are spherical surface. Both the source and receiving fibres can be glued on the flat surfaces of the doublets to reduce the Fresnel reflection loss. The imaging quality is diffraction-limited over a 0.64 mm diameter field for the source fibres at the primary wavelength of 0.9 μm. Several fibres can be coupled for each connector.

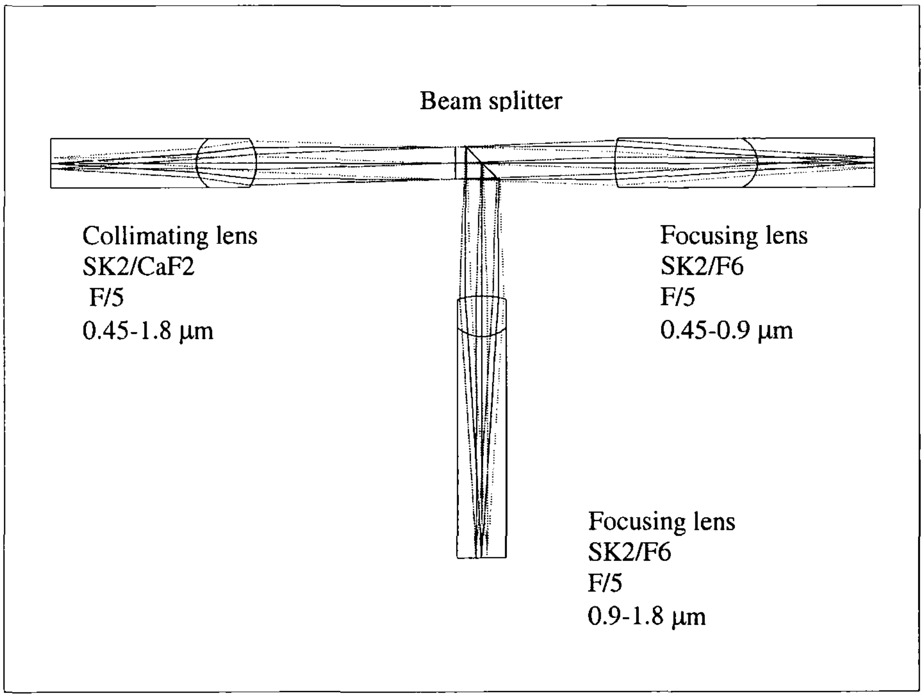

Figure 6-3. The optical layout of the IFS fibre connector.

A key specification for the fibre connectors is the coupling efficiency. The 95% coupling efficiency is an acceptable value for the FMOS committee. To calculate the coupling efficiency, one needs to understand the principle of the coupling process between the source fibre and receiving fibre. The working principle is shown in Fig. 6-3. The light from the source fibre is first collimated by a collimating lens and then focused on the other end of a focusing lens where the receiving fibre is located. The image of the source fibre is projected onto the receiving fibre.

However the image of the source fibre will be broadened by optical aberration. The optical aberrations of the fibre connectors are ~ 3 μm RMS in radius (diffraction limited at 0.9 μm), and this results in a coupling efficiency of about 66% for the IFS fibre connectors. The efficiency is much lower than the required specification. If high coupling efficiency is needed, it is necessary to oversize the core size of the receiving fibre. The oversizing has two functions: one is to accommodate the image of the source fibre on the receiving fibre entrance, which has been broaden by the optical aberration; Another function is to compensate the position shift of the image of the source fibre on the receiving fibre entrance. The position shift may be caused by the position alignment errors of the fibres and lenses. If the output fibre core diameter is oversized as 70 μm, the coupling efficiency will be ~97% for the IFS fibre connector. These are just theoretical estimations. If the alignment or assembly errors of the fibre connector are considered, the receiving fibre size needs to be further oversized.

The coupling efficiency for the fibre connectors in Fig. 6-3 are not sensitive to the alignment error on the lateral and axial directions because of the nature of expanded collimated light. However, the position of the source fibre image on the focusing lens end is very sensitive to the alignment error of the tilt angle between the collimated lens and focusing lens. These fibre image positions are a function of the tilt angle error and focal length of the receiving lens. The bigger the focal length of the receiving lens, the bigger the image position error. Small lens also have a small axial aberrations. The lenses for the fibre connectors need to be as small as possible if the manufacture is not a problem. In actual design, each lens can be used to couple one or several fibres. A disadvantage of the design in Fig. 6-3 is that doublets will have a big size and it will be difficult to align the fibre position accurately. Another option for the design of the IFS fibre connector which uses Selfoc microlenses is investigated and the detail is presented in Appendix B.

For MOS fibre connector, there are 400 fibres and the specifications are

Input focal ratio: F/2
Output focal ratio: F/5
Input fibre (source fibre) core diameter: 85 μm.
Output fibre (receiving fibre) core diameter: 195 μm.
Input wavelength range: 0.4 μm – 1.8 μm.
Output wavelength range (visible): 0.4 μm – 0.9 μm.
Output wavelength range (NIR): 0.9 μm – 1.8 μm.

Coupling efficiency: 95%.

The MOS fibre connector can be done in a similar way as the IFS fibre connector. A more detail discussion about the MOS fibre connector will be presented in Chapter 10.

6.6 Optical Spectrograph

The spectrographs accept the light which are fed from the IFS fibre connectors. The spectrographs are required to accept F/4.5 beam at slits because of the fibre FRD.

The specifications for the optical spectrographs are summarized below:

Wavelength range (μm): 0.45-0.90
Desired wavelength range (μm): 0.40-0.90
Input collimator focal ratio: F/4.5
Final camera focal ratio: F/1.46
Collimated beam diameter (mm): 150
Detector format /spectrograph: 3K x 3K
Detector pixel size (μm): 15
Slit length of spectrograph: 140mm
Required image quality: 50% enclosed energy in 1.2 pixels
Reference wavelength (μm): 0.675
Reference maximum grating ruling (lines/mm): 1,800
Maximum R for small fibres: 17,800
Maximum R for large fibres: 5,500

The maximum spectral resolution is decided by the scientific cases and the feasibility of the grating size and ruling density. High spectral resolution will also be useful to remove OH lines. The required image quality ensures that the PSF of the spectrograph is optimally sampled by about two detector pixels.

The spectrographs need to be optimized for maximum throughput. This implies that the number of optical elements should be as small as possible. The camera focal ratio is F/1.45 which is very fast. Also A 3K x 3K detector is used and this decides that the camera needs to work at a large field angle. The optical aberrations need to be tightly controlled so that they don't broaden the spectral image and reduce the spectral resolution too much. All of these mean that the camera design is critical to achieve the requirements for the optical image quality.

6.7 Summary and Conclusions

In this chapter, the FMOS instrument concepts are described. The instrument specifications and requirements will be used as the guides for the design and constructions in the late chapters. However, it needs to be noted that when these specifications were originally developed, much of the design work was not completed. So it is possible that some of the specifications will need to be adjusted according to the final designs and constructions of these instrumentations.

Chapter 7

FMOS project: The Design of Optical Spectrograph

Abstract

In this chapter, designs for FMOS optical spectrograph are described. These include the designs of a collimator and a camera. The collimator is a Schmidt type optical system with chromatic aberration well corrected over the wavelength range of 0.45 –0.9 μm. The F/1.46 optical camera consists of 10 elements in four groups with all spherical surfaces. The optical aberrations are well corrected for both collimator and camera and this results in good image quality for the spectrograph. The spectrograph performance is estimated in spectral and spatial directions. It is shown that the spectrograph meets the requirements for the FMOS project. Other questions, such as the optical component manufacture, are also discussed.

7.1 Introduction

Two kinds of spectrographs are required for the FMOS project. One is the near infrared spectrograph which is designed at Cambridge and is not discussed here. The optical spectrograph is designed by the University of Durham and it is planned that two of these will be built. The optical spectrograph will accept two kinds of fibres at the slit, i.e. large and small fibres. The two spectrographs will be fed by 3000 small fibres with core diameter of about 80 μm. The fibres are placed side-by-side with no gap at the slit. So for this fibre, no cross disperser is needed and the spectrograph works only in a single dispersion order. The spectrograph can also be fed by 400 large fibres with core diameter of about 250 μm, cross dispersion is also not needed if all the 400 larger fibres are fed to one spectrograph as the fibre-to-fibre gap is less than two fibre core sizes. However if the 400 large fibres are fed to two spectrographs simultaneously, cross disperser can be adopted.

The optical specifications for the optical collimator, camera and spectrograph were discussed at Chapter 6. In this chapter, the collimator design is first discussed, followed by the camera design. Then the spectrograph design is presented. Finally the manufacture of the optical components and estimated performance are described.

7.2 Collimator Design

According to the FMOS design document (Dalton et al. 1998), the slit length is 140mm, the beam size is 150mm, and the input focal ratio is 4.5. This implies that the focal length of the collimator is 675mm.

The collimator is a Schmidt type system. It consists of a primary mirror, a secondary mirror, two identical correctors and a grating. The optical layout of the collimator is shown in Fig. 7-1. The collimator design, including the Zemax design file, was initially proposed by Ian Parry for a near infrared spectrograph for FMOS (Dalton et al. 1998). For the FMOS optical spectrograph, it was found that some modifications are necessary. For a Schmidt system, the glass corrector introduces chromatic variation of spherical aberration. Further improvement can be obtained by achromatizing the corrector with two glasses of different dispersions (Bass et al. 1995, Schroeder 1987). The silica corrector plate is replaced by a new one which consists of two materials: CAF2 and F5. The spherical primary mirror is replaced by an aspheric mirror. The corrector plate consists of two glasses with aspheric surface on each of the outside surfaces. The primary mirror aspheric surface has an 8th order term of aspheric constant. A filter (not shown) can also be located in the optical path before the second corrector to avoid the overlap of the spectrum between different orders. An ideal lens (paraxial surface in Zemax) is used as the camera for optimization of the collimator design. The ideal lens has a focal length of 220mm which is the same as that of the real camera.

In Fig. 7-1, the fibre slit is decentered -72mm in Y direction. The beam from the fibre slit is reflected by the primary mirror and passes through the first corrector plate. The grating is tilted about X axis in YZ plane (dispersion plane). The dispersion direction on the grating is in the Y direction. The beam is then dispersed by the grating. The beam passes through the first corrector plate for the second time and is reflected by the primary mirror again to form an intermediate spectrum image on the secondary mirror. After striking the primary mirror a third time, the beam passes through the second corrector and a spectrum image is formed on the focal plane of the camera lens. The intermediate spectrum image can be used to remove the OH contamination from the sky by hardware (a mask which blocks light at the known wavelengths of the OH lines). The design is not optimized for this because this would result in degradation in the image quality on the focal plane.

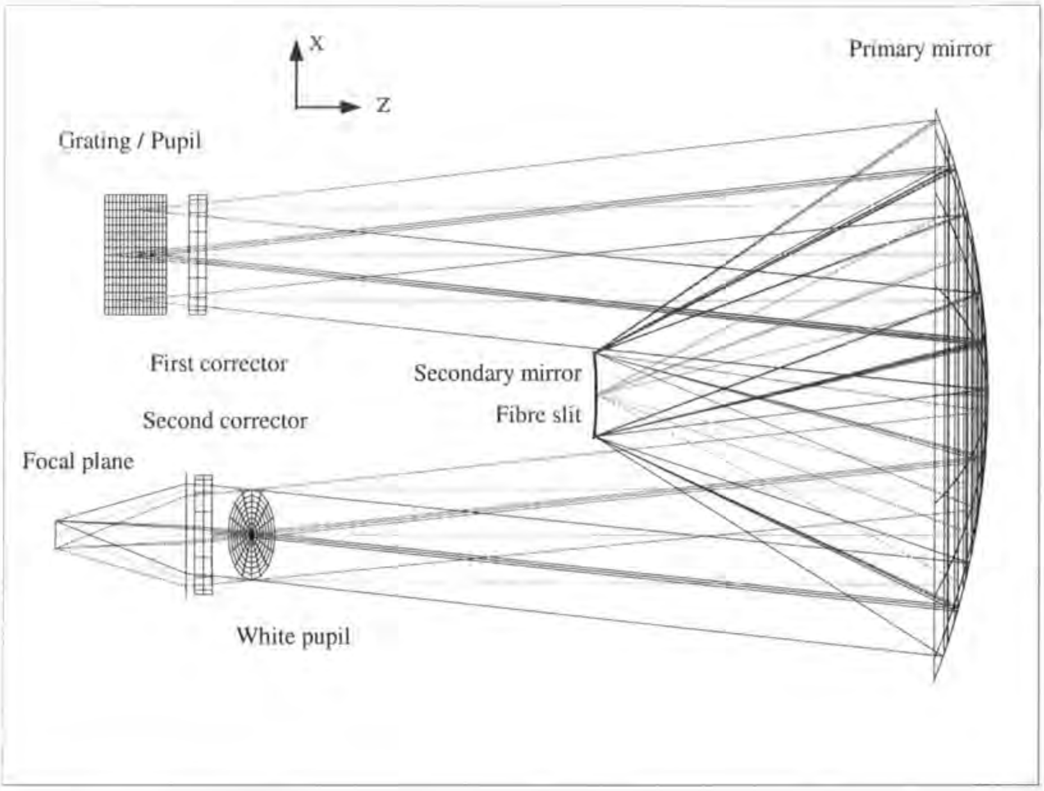

Figure 7-1. Layout of FMOS optical collimator. Two identical corrector plates are use in the design. The grating serves as an aperture stop which is imaged as a white pupil by the mirrors. The grating and white pupil is tilted 31° about X axis in YZ plane.

The spectrograph works at near Littrow mode. Different gratings with different ruling densities can be used to achieve different spectral resolutions, but the angle between incident and diffracting beam in the dispersion plane on the grating is fixed as 6.168° for all gratings for the central diffraction wavelength. For a 1870 lines/mm grating and 0.5 μm central wavelength, the grating is tilted 31° about X axis in dispersion plane when works at first diffraction order. The 31° tilted angle corresponds to an anamorphic factor of 1.2. The current design can accept the anamorphic factor up to 1.2 without vignetting. Note that the anomorphic factor is a function of the grating tilt angle and the grating tilt angle is equal to the diffraction angle at the central wavelength.

The optical aberrations need to be well controlled for the collimator because some aberrations, such as astigmatism, cannot be balanced or cancelled by a transmissive camera. The two mirrors and the two-corrector plates share the common optical axis which is defined by the centers of the primary mirror and the secondary mirror. All the optical components are in symmetry. As discussed in chapter 3, low order optical aberration can be corrected by the symmetry (Ren, Allington-Smith et al. 1997). The high order aberration is well corrected by the two corrector plates and the aspheric primary mirror. The chromatic aberration which is introduced by the two corrector plates is also corrected by using two kind glasses (CAF2/F5).

Two gratings are used to optimize the design of the collimator. One is 1870 lines/mm and the other is 1130 lines/mm. The wavelength range for each grating is carefully chosen to cover the whole field of view of the CCD detectors. The two gratings cover the two extreme ends of the wavelength range of 0.45 – 0.90 μm. This ensures that the chromatic aberration is well corrected over the whole 0.45 – 0.90 μm wavelength range. The spot diagram of the optical aberrations is shown in Fig. 7-2. It is evident that astigmatism is the dominant aberration. Over the whole field of the collimator image plane, the geometrical spots are within two detector pixels in both x and y directions. This implies that encircled energy is better than 95% in two detector pixels including the effect of both diffraction and optical aberrations.

The position of the aperture stop (pupil) is a trade-off between the grating size and camera design. The aperture stop is located on the grating and this makes the grating size small. An image of the grating is formed before the second corrector plate and the image is a white pupil. It is desired that the white pupil is located as close as possible to the camera lens, i.e. close to the second corrector plate. This can reduce the size of the camera lenses and the optical aberration of a real camera. The position of the white pupil is a trade-off between the optical aberrations of the collimator and the camera. As the white pupil is located after the grating, all the light rays with different wavelengths will pass through it with the same aperture diameter, so the white pupil design can reduce the size of the camera lens.

The curvature radius of the fibre slit is also optimized to reduce the optical aberration and field curvature. The fibre slit has a spherical curvature radius of 737.6481 mm and the fibre slit is decentered -72mm in y direction. The fibres need to be carefully aligned to point to the aperture stop or white pupil, i.e. the chief rays from each fibre must pass through the center of the aperture stop or the center of the white pupil (see Fig. 7-1 and Fig. 7-3). Any alignment error will introduce vignetting for the light from the fibre. A diaphragm is located at the position of the white pupil to reject stray light and serves for the alignment. Fig 7-3b is the footprints on the grating and white pupil.

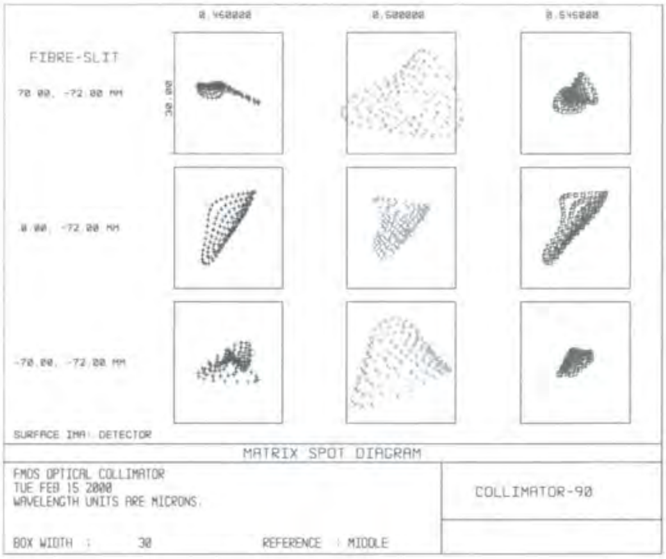

Figure 7-2a Spot diagram of optical aberration. There points (70mm,-72mm), (0mm,-72mm) and (-70mm,-72mm) on the slit are imaged onto the detector at three wavelengths. The side of the box is 30μm, which is equal to two detector pixels. The grating is 1870 lines/mm and the wavelength range is 0.4-0.545μm.

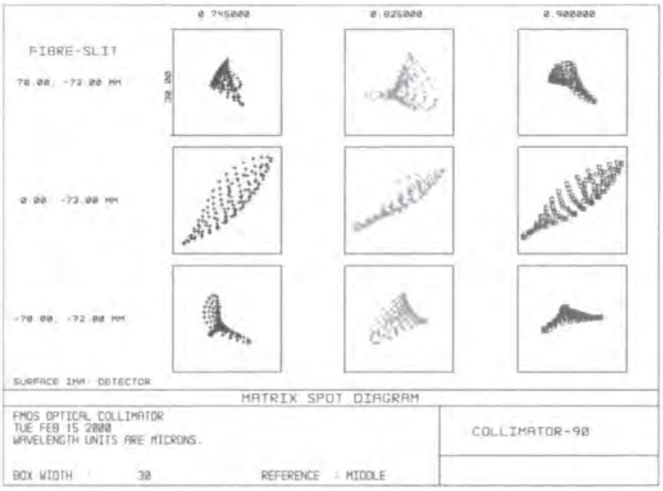

Figure 7-2b Same as Fig. 7-2a. The grating is 1130 lines/mm and wavelength range is 0.745-0.90μm.

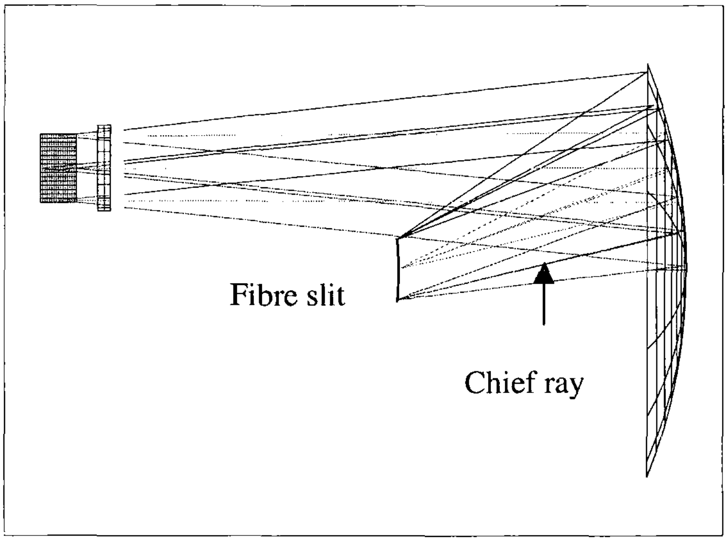

Figure 7-3a. Schematic of the alignment for fibre slit. The fibres need to be aligned to point to the center of the pupil which is the grating or white pupil. In this figure, three chief rays from three points on the fibre slit are shown. It is clear that each fibre needs to be tilted to avoid vignetting.

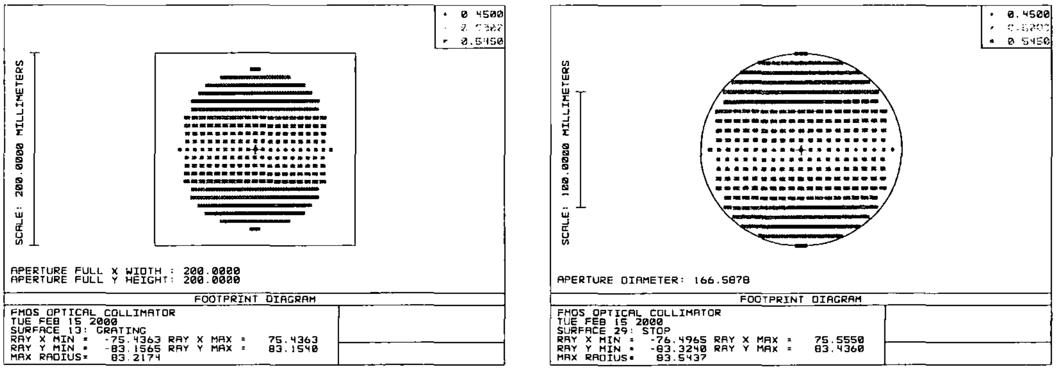

(a) (b)

Figure 7-3b. Footprint on Grating (a) and white pupil (b). The white pupil diameter is 152mm. It is tilted 31° and located 1239.6624 behind the primary mirror.

The distortion needs to be carefully checked for any optical system that uses off-axis mirrors. When a mirror is used at off-axis, besides introducing astigmatism, it may also introduce a distortion of the image because of the geometrical asymmetry in the meridional and sagittal planes. Unfortunately, in some case Zemax can't calculate the distortion correctly for optical system with coordinate breaks. The distortion can be worked out from ray tracing on the spot diagrams. The distortions in dispersion and spatial directions are different. The distortion is 7.4% in the spatial direction, but is only 0.6% in the dispersion direction. The distortion in the spatial direction causes only a shift of the spectrum on CCD detector which is not a problem for a spectrograph. However, the distortion in the dispersion direction needs to be controlled, otherwise the spectra near the detector edges may partly lie outside the detector. The footprints of the slit are shown in Fig. 7-4 for three wavelengths which correspond to the slit images on left edge, center and right edge on the detector.

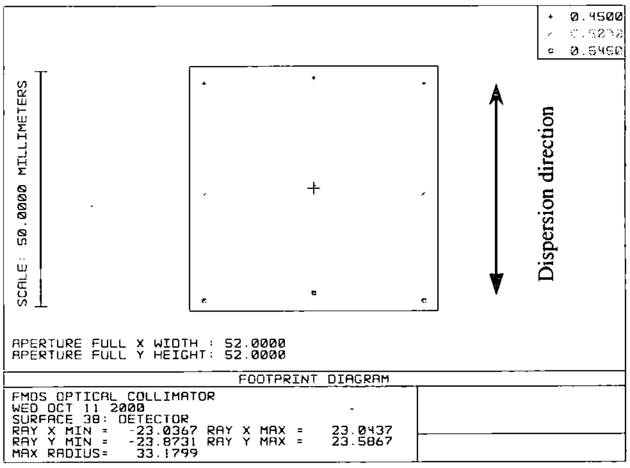

Figure 7-4. Footprint diagram of slit at wavelength 0.70μm, 0.733μm and 0.844μm which correspond the slit image on the detector left edge, center and right edge. The square represents the CCD detector. The corresponding spot diagram of optical aberration is shown in Fig. 7-2.

Finally, the specifications of the components of the collimator are as follows:

Fibre slit:

Spherical curvature radius =737.6481.

Decenter = -72mm, slit length =140mm

Grating /Aperture stop:

Beam diameter =167x151mm. Tilt angle =31° (This corresponds to anamorphic factor of 1.2).

White pupil:

Pupil diameter =167x151mm. Tilt angle =31°. Position: 1239.6624mm behind primary mirror.

Primary mirror:

Curvature radius=1331.3173 mm, 8th aspheric coefficient= -1.720E-023.

Clear aperture size =923.5x441mm.

Secondary mirror:

Curvature radius= 672.9824mm, Clear aperture size=142x142mm.

First and second corrector (internal surface is flat and external surfaces are aspheric):

Glasses: CAF2/F5, Thickness =15mm for both CAF2 and F5. Clear aperture diameter=183mm.

Table 7-1. Aspheric coefficients of corrector plate.

	CAF2	F5
2th aspheric order term	-4.8190E-005	-1.6763E-005
4th aspheric order term	5.1646E-10	2.04209E-010
6th aspheric order term	-1.6320E-015	-1.2746E-015
8th aspheric order term	9.3722E-021	6.31682E-021

7.3 Optical Camera Design

The camera for the spectrograph is fundamentally different from a commercial camera lens. The difference is that nearly all commercial camera lenses contain an internal stop where an iris is often placed. By contrast, the entrance pupil of the spectrograph camera is located roughly one focal length ahead of the first element of the camera. This results in the need for relatively large lens diameters and presents a unique aberration-control challenge (Oke et al. 1995). This problem is more serious for the design of a fast camera. Fortunately, the collimator that was discussed in the previous section can create a white pupil that is located closely to the camera.

Much work has been done by many people to design a fast camera with large field of view for astronomical spectrographs (e.g. Oke et al.1995, Kells et al. 1998, Rodgers and McCarthy 1994, Garth et al. 1994). A F/1.25 camera for the Keck II Telescope (Garth et al. 1994) was designed by Harland Epps. It uses 9 elements in 5 groups with 2 aspheric surfaces and three elements are CAF2. This camera delivers an image quality of 15.3 μm rms spot radius and 59.74 μm geometrical spot radius in the worst case over the field angle of 11.4 degrees and the wavelength range of 0.44-1.1 μm. Similar cameras with aspheric surfaces designed by Epps were also used for other projects (Oke et al. 1995, Kells et al. 1998). Rodgers and McCarthy explored a F/2 camera design using spherical and aspheric lenses at the wavelength range of 0.31 – 0.55 μm with a field angle of 8 degrees. For all spherical lenses, it uses 11 elements of CaF2, Silica and Ultran 30 to deliver an image quality of 80% encircled energy in a diameter of 20 μm in the worst case. It seems that 11 spherical lenses are reasonable for a fast camera with a large field of view.

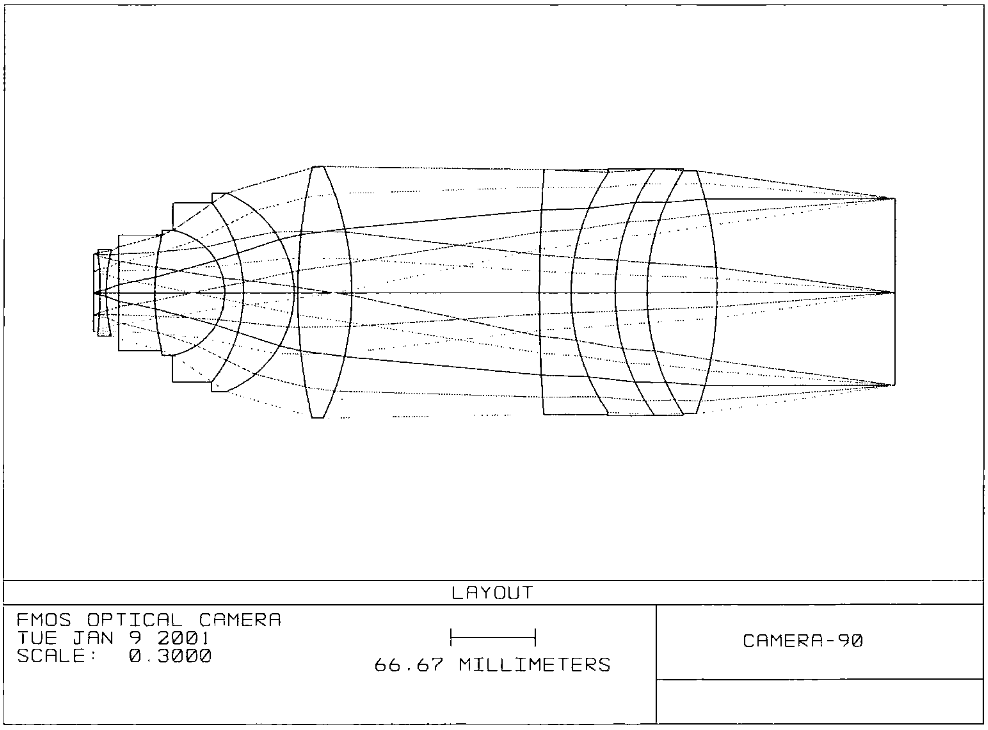

Figure 7-5. The optical layout of FMOS F/1.46 camera. The camera consists of 10 spherical lenses in four groups. The focal length is 220mm and the beam size is 150mm. The aperture stop is 140mm before the first lens surface.

The optical layout of the FMOS F/1.46 camera is shown in Fig. 7-5. The camera focal length is 220mm. The camera field radius is 8.5 degrees. The camera is composed of four lens groups. The first group consists of four lenses. The second one is a CaF2 singlet. The third one has four lenses. The last one is a LaK10 singlet and serves primarily to reduce the Petzval sum and thus reduce the field curvature. It also serves as the detector window. All the glasses have a high internal transmission over the wavelength range of 0.4 – 0.9 microns. Note that all the lens surfaces are spherical. The aperture stop is located 140 mm before the first lens surface of the first lens group. This is a trade-off between collimator and camera image quality. No vignetting exists in the whole field. The optical aberrations are well corrected in the whole wavelength range and the spot diagrams are shown in Fig. 7-6 over the whole field and wavelength range. Almost all the light is located in two detector pixels. The maximum rms spot radius of the optical aberration is less than 7.0 microns in the whole field. Note that the spot diagrams are just for the camera itself and don't include the aberrations of the collimator.

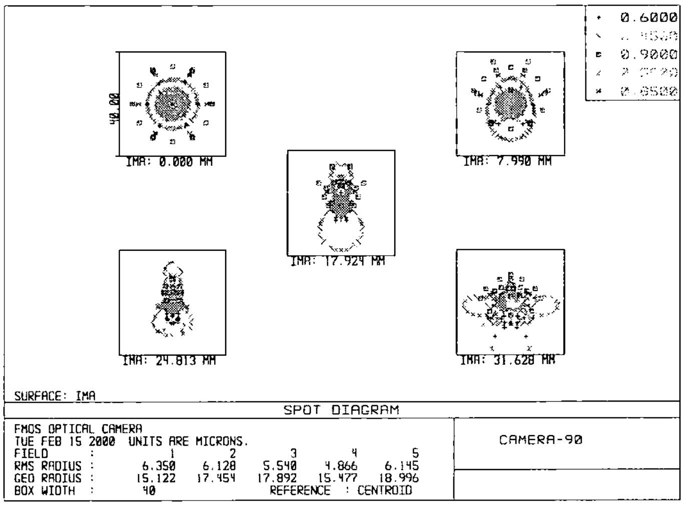

```
FMOS OPTICAL CAMERA
TUE FEB 15 2000  UNITS ARE MICRONS.
FIELD       :        1       2       3       4       5
RMS RADIUS  :    6.350   6.128   5.540   4.866   6.145
GEO RADIUS  :   15.122  17.454  17.892  15.477  18.996
BOX WIDTH   :      40          REFERENCE  : CENTROID
```

Figure 7-6. Spot diagram of the optical camera. Chromatic aberration is well corrected in 0.45-0.9μm. The box width is 40 μm. The field radius is 31.628mm on the camera focal plane.

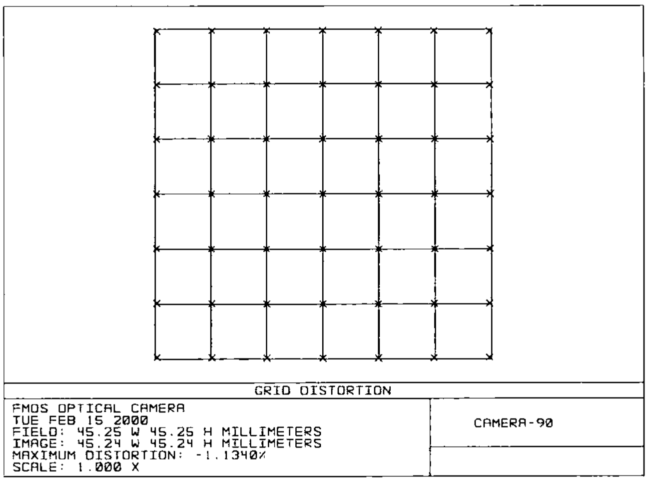

```
FMOS OPTICAL CAMERA
TUE FEB 15 2000
FIELD: 45.25 W 45.25 H MILLIMETERS
IMAGE: 45.24 W 45.24 H MILLIMETERS
MAXIMUM DISTORTION: -1.1340%
SCALE: 1.000 X
```

Figure 7-7. Distortion diagram of the optical camera. The maximum distortion is about 1.134% over the whole field of view.

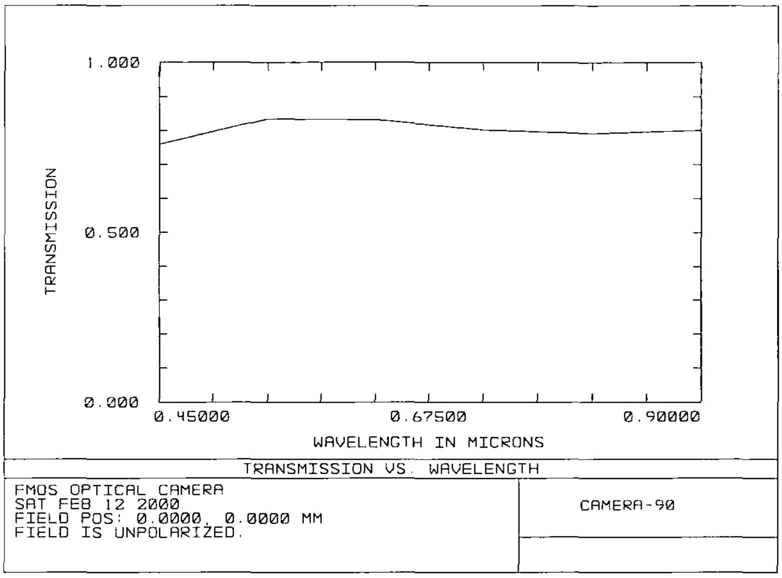

Figure 7-8. Transmission curve over wavelength range of 0.45 – 0.9 μm. Assuming that the AR coating allows 99% transmission. Transmission curve includes the reflection loss after AR coating. The average transmission is 80%.

The aperture stop can also locate one focal length (220mm) before the first surface of the camera, but this may cause a degradation of the image quality and is not necessary for this spectrograph as the collimator can produce a white pupil which is close to the camera.

The image focal plane is flat. The distortion of the camera is about 1% over the whole field. The distortion map is shown in Fig. 7-7. The beam size is 150 mm which is also the diameter of the aperture stop in the design. The lens size is decided by the aperture stop diameter and the distance from the first surface to the aperture stop. The clear apertures for all the lenses are less than 200 mm. The details of the lens data are listed in Table 7-2. The transmission is calculated and is shown in Fig. 7-8.

Table 7-2. Lens data of the optical camera (Units are mm)

Surface	Comment	Radius of curvature	Thickness	Glass	Clear Aperture
OBJ	Object	Infinity	Infinity		
1 STO	Stop	Infinity	-140.00		150.00 ∅
2	Lens 1	-300.5754	-55.00	PK51A	196.3 ∅
3	Lens 2	183.2923	-25.00	SF6	195.7 ∅
4	Lens 3	174.4704	-35.00	SILICA	199.0 ∅
5	Lens 4	173.5561	-25.00	LAK10	193.3 ∅
6	-	1394.2276	-148.2078		196.2 ∅
7	Lens 5	-236.68	-43.00	CAF2	203.0 ∅
8	-	463.1415	-3.00		200.6 ∅
9	Lens 7	-86.5297	-40.00	CAF2	160.4 ∅
10	Lens 8	-116.0973	-15.00	LAK10	144.7 ∅
11	Lens 9	-51.5126	-55.00	CAF2	100.8 ∅
12	Lens 10	297.9588	-28.3837	SF6	93.6 ∅
13	-	-2921.0344	-10.00		74.3 ∅
14	Lens 11	145.4746	-5.00	LAK10	68.4 ∅
15	-	-360.8593	-5.00		64.9 ∅
IMA	Image	Infinity			63.54 ∅

Finally, the image quality of the optical camera can be further improved if vignetting is allowed at the corners of the CCD detector. In this case, the size of each lens for the camera can also be further reduced.

7.4 FMOS Optical Spectrograph

The spectrograph design is done by replacing the ideal paraxial lens (see Fig. 7-1) with the real camera which is discussed in section 7-3. As the camera aperture stop is located about 140mm before the first surface of the camera in both the collimator and camera design, the camera and spectrograph don't need to be re-optimized again after the ideal paraxial lens is replaced by the real camera. The optical layout of the spectrograph is shown in Fig. 7-8. Note that a band pass filter can be placed near the white pupil where the beam is collimated and the beam size is small (about 150mm diameter). Note that as the beam is collimated and the filter has no optical power, it doesn't add chromatic aberration to the spectrograph. As mentioned previously, if the spectrograph is fed by the small fibres with 80 μm core size, cross disperser is not needed. However if it is fed by the large fibres with 250 μm core size, a cross disperser may be needed and it may also be located near the white pupil. Again as the beam is collimated, the insertion of the disperser does not introduce significant optical aberrations.

The image quality of the spectrograph is shown in Fig. 7-9a and 7-9b, respectively. Almost all the light is located in the box of two-pixel width. The maximum rms radius is less than 10 microns over the whole field and the whole wavelength range.

The distortion is similar to that of the collimator alone. The distortion is 7% in spatial direction and 0.2% in the dispersion direction. This is not surprising as the camera has a small distortion and thus has almost no contribution to the distortion of the spectrograph.

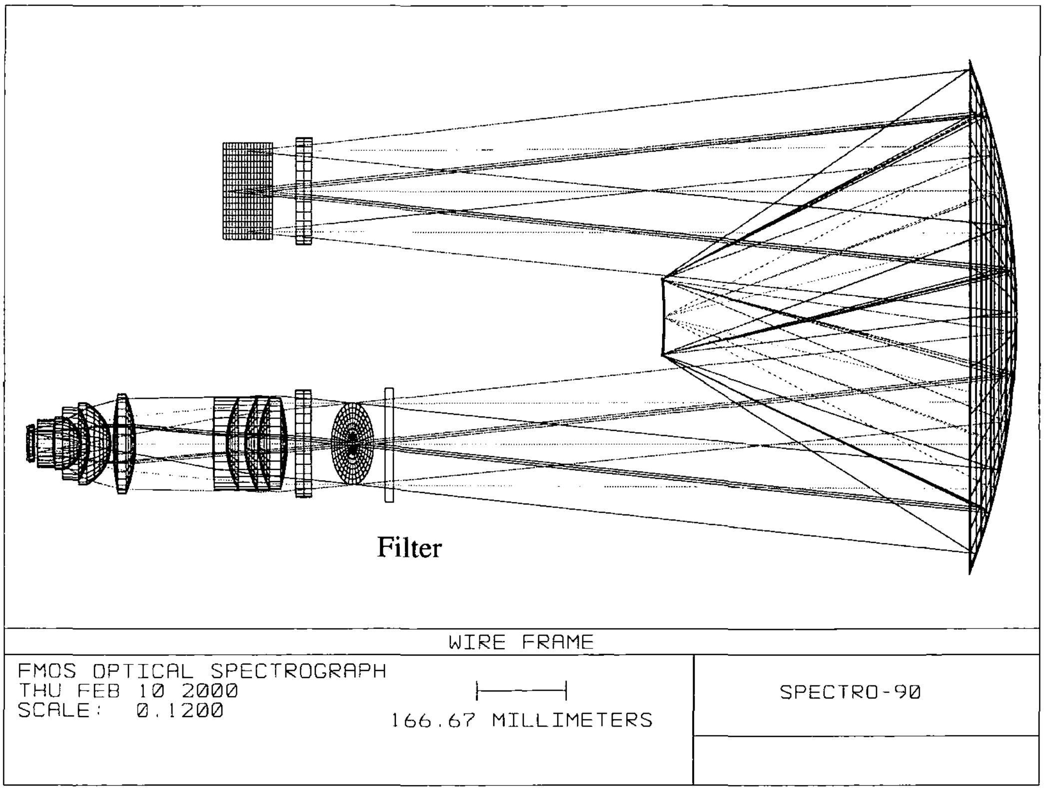

Figure 7-8. Layout of the optical spectrograph. The ideal paraxial lens (see Fig. 7-1) is replaced by the real camera. A band filter is located before the second corrector and near the white pupil.

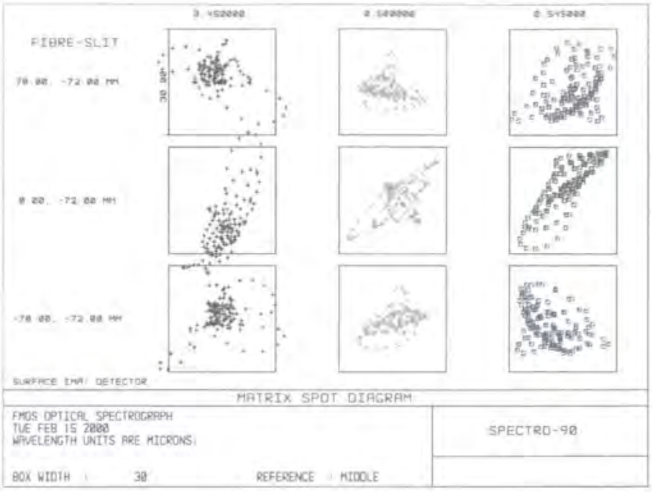

Figure 7-9a. Spot diagram of the optical spectrograph at wavelength 0.45-0.545 μm. The maximum RMS radius is less than 10 μm.

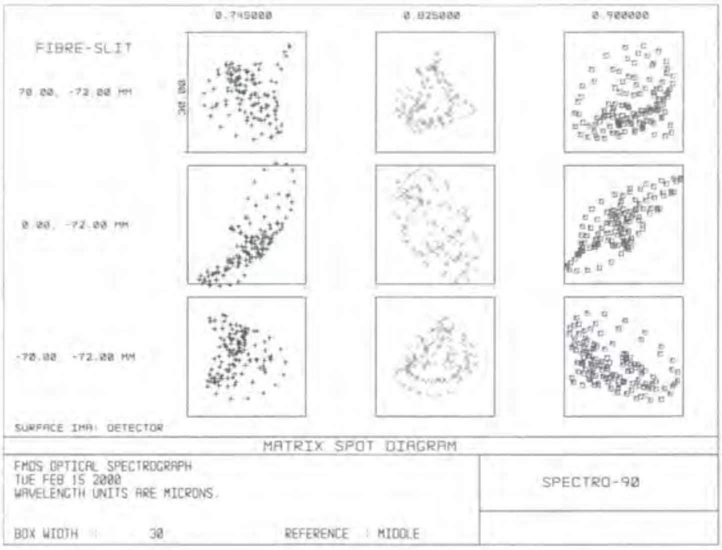

Figure 7-9b Spot diagram of optical spectrograph at wavelength 0.745-0.9 μm. The maximum RMS radius is less than 10 μm over the whole field of view.

As the grating is tilted 31° with the X axis in the YZ plane, this means that the grating reflection angle is 31°. The incident angle can be calculated according to the grating equation and it is 24.8°. The angle between incident and reflection angle is 6.2°. Therefore the anamorphic factor is 1.23.

7.5 Optical Manufacture

For the collimator, the aspheric primary mirror can be made of aluminum and can be manufactured by diamond-turning. The CAF2 element in the CAF2/F5 corrector plate may also be manufactured by diamond turning. Both aluminum and CAF2 are diamond-turnable materials (Rhorer and Evans 1995). The aspheric coefficients of the finishing surface profile can be measured by using the form and contour measurement device of Form Talysurf Series 2 (Taylor Hobson Precision catalogue 2000). The F5 is glass and is not diamond-turnable, however conversional technique can be used for the manufacture of the glass corrector plate (Buchroeder 1972).

The manufacture for the camera should not be a problem as all the lens surfaces are spherical. The maximum size is less than 200 mm of clear diameter and this is not a problem for the availability for both CAF2 and optical glass. For CAF2, the availability of the material can be up to 250 mm in diameter (catalogue of Crystran Ltd 2000).

The two mirrors in the collimator can be coated with silver. The reflectivity of the silver is better than 98% in the specified wavelength range (Melles Griot Catalogue, 2000). All other transmitting optics in the collimator and camera can be multi-layer coated which can deliver a transmission better than 99% (Kells et al. 1998). These include the two correctors in the collimator, band filters and all glass-air surfaces in the camera. Sol-Gel AR coating can also be considered.

7.6 Spectrograph Performance Estimations

7.6.1 Optical Aberrations and Spectral Resolution

Optical aberration will broaden the slit image on the CCD detector and thus reduce the resolving power of the spectrograph. In chapter 2 for the IFU fore-optics, the ideal image of fibre is presented by a symmetrical rectangular function and the optical aberration is presented by a symmetrical Gaussian function. Note that the problems are 2-dimensional although they can be presented by the symmetrical functions. The broadened fibre image is the convolution of the optical aberration and the ideal image of the fibre. The broadened fibre image is still a 2-

dimensional function, however it is symmetrical. For a spectrograph, one only needs to consider the slit image in spectral or dispersion direction when calculating the spectral resolution, so the discussion is a one-dimensional problem. The optical aberration of the spectrograph can be expressed by a one-dimensional Gaussian function. The fibre slit is presented by a one-dimensional rectangular function. So formula (2-23) can still be used to calculate the broadened fibre slit image on the CCD detector, the difference is only that for a spectrograph, this formula is a one-dimensional (in spectral direction) problem. The irradiance of the broaden (fibre) slit for a spectrograph is expressed as

$$I(r)=\frac{1}{4\delta}(\frac{2}{\pi})^{1/2}\left\{erf\left[\frac{d/2-r}{\sqrt{2}\delta}\right]-erf\left[\frac{-d/2-r}{\sqrt{2}\delta}\right]\right\} \qquad (7-1)$$

Where r is the distance from the slit center in the spectral or dispersion direction on the CCD detector. δ is the RMS spot radius of the optical aberration of the spectrograph. d is the slit image size projected onto the CCD detector. For FMOS, assume that anamorphic factor is 1 for simplification. Thus, the image size is d=26 μm on the CCD detector for a fibre with 80 μm core size. The RMS radius of the optical aberration is well less than 9 μm on the whole CCD detector in most cases and only in worst is 10 μm. So, we take δ =10 μm. The profile of the irradiance distribution is calculated with a computer C program and the result is shown in Fig. 7-10.

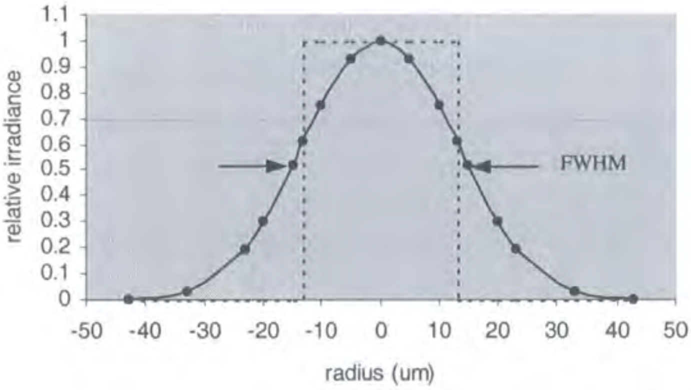

Figure 7-10. The profile of the slit image on the CCD detector. The dashed curve is the ideal slit image which is 26 μm. The solid curve is the simulated slit image which is broadened by the optical aberration of the spectrograph and the FWHM is 30 μm.

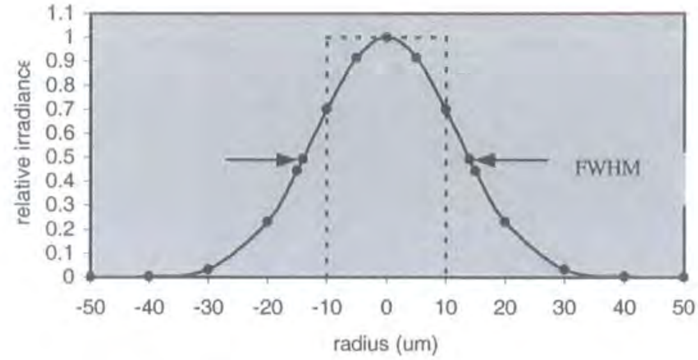

Figure 7-11. Same as Fig. 7-10 except that the ideal slit image size is 20 μm. The FWHM is 28 μm in this case. Compared with Fig. 7-10, the ideal slit image is broadened more by optical aberration.

From Fig. 7-10, it is clear that the slit image is broadened by the optical aberration of the spectrograph. The broadened slit image is well represented by a Gaussian function and the FWHM is 30 μm. Compared with the ideal slit image which is 26 μm, the slit image is 1.15 time wide because of the optical aberration. Note that the FWHM is a function of the optical aberration and the ideal slit image size. The broadening of the slit image can be reduced by reduction of optical aberration or increase of the slit size. If the optical aberration is fixed as δ=10 μm, further reduction of the fibre core size in fact can't increase the spectral resolution too much because of the broadening of the slit image. For example, if the ideal slit image size is reduced to 20 μm which corresponds to a fibre core size of about 60 μm on the slit, as the ideal slit image is broadened more by optical aberration, the FWHM is 28 μm and so the effective slit width is not much reduced. This case is shown in Fig. 7-11.

The spectral resolution for the slit limited case is (Schroeder 1987)

$$R = \frac{Wm\lambda\rho}{\Phi D} \qquad (7-2)$$

Where W is the illuminated width of the grating. m is diffraction order. λ is the wavelength. ρ is grating ruling density. D is telescope aperture. Φ is the angular width of the slit projected onto the sky.

The slit width on the camera focal plane, i.e. on the detector is given as

$$w' = \Phi D F_2 / r \qquad (7-3)$$

Where F_2 is camera focal ratio. r is the anamorphic factor and is defined as the ratio of diffraction beam diameter and incident beam diameter on the grating.

From equations (7-2) and (7-3), one has

$$Rw' = \frac{WF_2 m\lambda\rho}{r} \qquad (7-4)$$

Note that the right side of the equation is constant after the grating and spectrograph are decided. This means that the spectral resolution R is determined by the projected slit width w′ on the detector. Assume that R_0 and $w_0^{'}$ are the nominal spectral resolution and slit width at ideal case respectively, and R and w′ are the actual spectral resolution and slit width respectively when optical aberrations are present. From equation (7-4), one has

$$R_0 \cdot w_0^{'} = R \cdot w^{'} \qquad (7-5)$$

The actual spectral resolution R is determined by the actual slit width w′ by

$$R = R_0 \cdot \frac{w_0^{'}}{w^{'}} \qquad (7-6)$$

It is evident that the actual spectral resolution will be reduced by the broadened slit width. The broadened slit width is represented by the FWHM. For FMOS optical spectrograph, $w_0^{'}$=26μm. The actual slit width is w′=30 μm (see Fig. 7-10). So the actual spectral resolution is

$$\mathrm{R} = 0.87\mathrm{R}_0 \qquad (7-7)$$

The actual spectral resolution is 87% that of the nominal value in the worst case because of the optical aberration. In most cases, the image quality will be better than in the worst case. On the average, the actual spectral resolution will be better than 90% that of the theory. Note that the actual slit width of 30μm is sampled exactly by two detector pixels and so is critically sampled.

7.6.2 Spatial Image Quality

The requirement for the spatial image quality is that 50% encircled energy in 1.2 pixels which is 18 μm. Fig. 7-12 shows the encircled energy in the worst case over the whole field of view and whole wavelength range. It is evident that in the 1.2 pixels (9μm in radius), the encircled energy is much better than 50%. Almost all the light is located in the one pixel radius. Note that the encircled energy curves have been scaled by the diffraction.

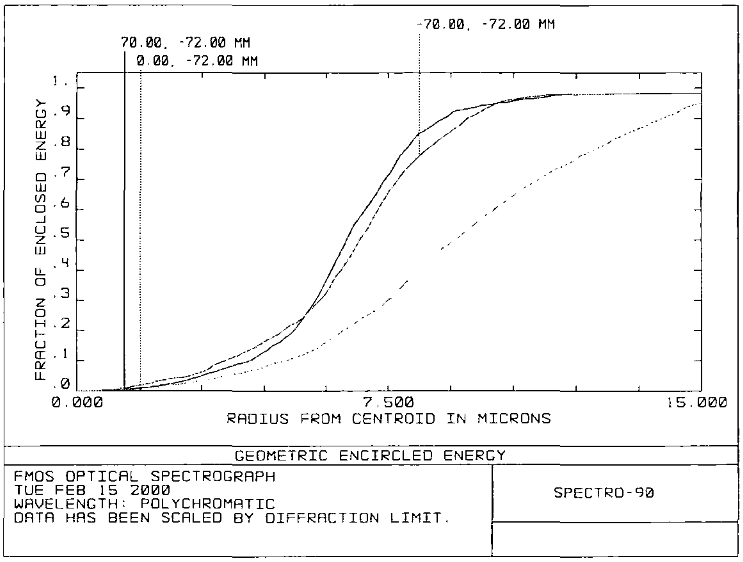

Figure 7-12. Encircled energy in the worst case. The radius of 9 μm corresponds to 1.2 detector pixels. Note that the curve has been scaled by diffraction.

7.6.3 Optical throughput

The transmission of the camera has been discussed in a previous section and its average transmission is 80%. The collimator mirrors are assumed silver coated with 98% average reflection at each mirror. The corrector plates and filter are AR coated with a transmission of 99% at each air-glass interface. This results in a throughput of 85% for the collimator if the grating is not included. The efficiency of the grating varies from grating to grating. Assume that a Volume-Phase Holographic (VPH) grating is adopted. The principle and performance of the VPH grating has been described by several people (Kogelnik 1969, Owen et al. 1995, Barden 1998). The efficiency of this grating is assumed to be 85% at peak wavelength. The efficiencies of the collimator, camera and the spectrograph are listed in Table 7-3.

Table 7-3. Estimated throughput

Camera	80%
Collimator (no grating)	85%
Collimator (with grating)*	72%
Spectrograph (no grating)	68%
Spectrograph (with grating)*	58%

* At blaze (maximum throughput)

7.7 Summaries and Conclusions

The collimator, camera and spectrograph design are discussed which meet the specific requirements for the FMOS project. The collimator delivers very good image quality and it consists of two mirrors and two identical corrector plates. The throughput is estimated to be 85% when the grating is not included. The risks or challenges for the manufacture of the primary mirror and the corrector plates are also described. The camera consists of 10 elements in four groups and the image quality is excellent. The few air-glass interfaces in the camera result in a high throughput which is about 80%. All the camera lenses are spherical and the manufacture is not a problem. The optical aberration is 10 μm rms spot radius in the worst case for the spectrograph. The current design can accept an anamorphic factor 1.23 without vignetting. Further increase of anamorphic factor is possible but may introduce vignetting.

A mathematical model is used to calculate the slit profile broadened by optical aberrations. The spectrograph performance is estimated. In the dispersion direction, the spectral resolution is about 90% of the nominal value because of the optical aberration. In the spatial direction, almost all the light is located in two pixels even in the worst case. The throughput of the whole spectrograph is about 68% when the grating is not included. This performance meets the specific requirements for the FMOS project.

Chapter 8

The design of FMOS IFU

Abstract

This chapter discusses the optical design of an IFU prototype for the FMOS. A simple and compact fore-optics design is presented. The manufacture tolerances of the lenses of the fore-optics are described. The design of the microlens arrays and fibre bundle for the IFU is also presented.

8.1 Introduction

As described in chapter 6, the deployable IFU will provide the integral field ability for the FMOS optical and near infrared spectrographs. For efficient use of the telescope time, it is required that the IFU can work at optical and near infrared simultaneously. Currently the IFU is an upgrade option for the FMOS project. The design of the IFU prototype is discussed in this chapter.

8.2 Instrument Concept and Requirements

The sky image is fed to the IFU from the telescope after correction by the Prime Focus (PF) Corrector. The function of the IFU fore-optics is to magnify the telescope focal plane image, i.e. magnify the sky image to a suitable size to be sampled by the microlenses. The microlens array forms the image of the telescope pupil onto the back surfaces of the microlenses, where the fibre entrances are located.

The image quality requirements for the IFU optics weren't stated in the FMOS document. But it is obvious that the requirements cover two aspects. One is for the magnified sky image. The other is for the pupil image. The magnified sky image is formed on the microlens array surface. The seeing disk is sampled by two microlenses. According to sampling theory, this requires that the spot size of the PSF is less than two microlenses. The IFU pupil image is formed on the fibre entrance. The pupil image quality must be tightly controlled. If not, the blurred pupil image may lie outside the fibre core and results in light loss, or reduce the resolution of the IFU spectrometer if the fibre core is oversized too much to accommodate the blurred pupil image. In principle, a diffraction-limited or nearly diffraction-limited image is desired. Also the magnified sky image must be telecentric to avoid a shift of the pupil image on the microlens back surface.

Other requirements for the FMOS IFU are: The optical design should not be so complex as to increase the cost. The optical system must be as compact as possible to employ as many IFUs as possible in the telescope focal plane. The length of the IFU probe (from the pickoff prism to the fibre bundle) must be larger than about 100mm to allow access to any part of the 140mm diameter telescope field.

8.3 Fore-optics

8.3.1 The Design Principle

The basic design principles of the IFU have been discussed in Chapter 2. These are used for the IFU design in this Chapter. For clarification, some equations are listed in this section again for the specific applications of the FMOS IFU.

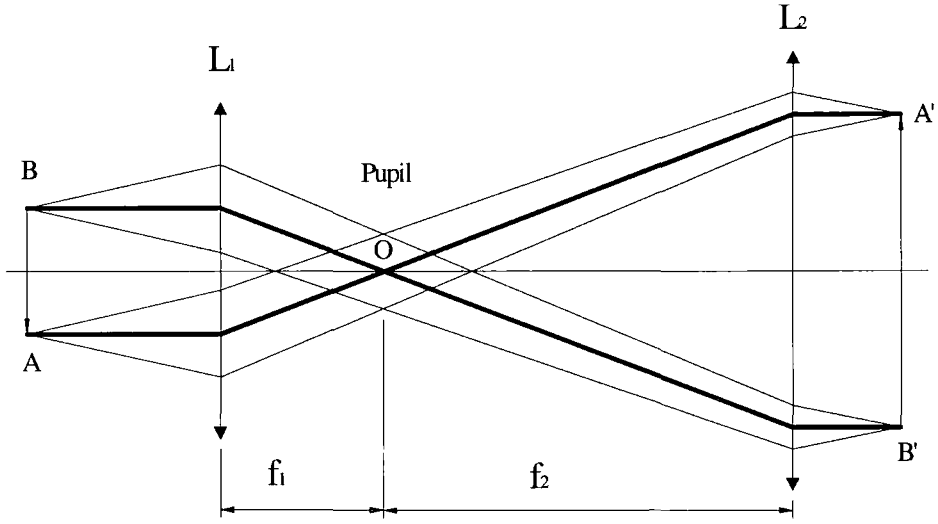

Figure 8-1 Schematic diagram of the IFU optical principle. The IFU optics is composed of positive lenses of L_1 and L_2. Lens L_1 and L_2 have the same focus point O. AB is the sky image on the telescope focal plane, which is magnified by the IFU optics to get an enlarged sky image A′B′. The thick lines are chief rays.

The IFU optics is schematically shown in Fig. 8-1. The IFU optics is composed of two groups of lenses. The first group is represented by a positive thin lens L_1 and the second group is represented by a positive thin lens L_2. L_1 and L_2 have the same focus point O. AB is the sky image on the telescope focal plane (after the PF Corrector). In this figure, AB is a real image. The rays are re-imaged by lens L_1 and lens L_2 to form a real image A′B′. The real image A′B′ can then be sampled by the microlens array. The chief rays form a real image at L_1's focus point O by lens L_1. As O is also the L_2's focus point, the chief rays are collimated again by lens L_2. The chief rays of the magnified image A′B′ are parallel to the optical axis, so the image is telecentric. In fact, the IFU optics is an inverse Keplerian telescope. However, the actual IFU will be more complex as it needs to image both the sky image on the microlens surface and the telescope exit pupil at a infinite distance, i.e. the IFU sky image must be telecentric on the whole field of view. In Fig. 8-1, I assume that the telescope exit pupil is at infinity or very distant and this is generally true for Subaru and other telescopes. Note that an intermediate pupil image is formed at point O.

It is obvious from Fig. 8-1 that the lateral magnification M can be expressed as

$$M = \frac{A'B'}{AB} = \frac{f_2}{f_1} \qquad (8-1)$$

Where f_1 and f_2 are the focal lengths of lens L_1 and L_2, respectively.

For FMOS IFU, assume that the microlens diameter is 500μm, which corresponds to a sampling increment of 0.3″ and this sampling increment is 0.0246 mm on the telescope focal plane. According to the definition of the magnification in equation (8-1), the magnification M is 20.3.

The telescope pupil is imaged onto the back surface of each microlens. According to equation 2-5, the pupil image size on the microlens back surface can be expressed as

$$D_{pup} = \frac{f_1}{F_{tel} M} \qquad (8-2)$$

Where f_l is the microlens focal length. F_{tel} is the telescope F ratio on telescope focal plane. M is the image magnification.

8.3.2 Non-telecentric Image

Non-telecentricity has been discussed in Chapter 2. It may be introduced by a telescope fed-sky image. For telescope non-telecentricity, the relationship between the telescope non-telecentric ray and pupil image shift on the microlens is discussed in Chapter 2 and is given as

$$\Delta s = f \cdot \tan(\frac{\beta}{M}) \qquad (8-3)$$

Where Δs is the amount of pupil shift. f is the microlens focal length. M is the (lateral) magnification of IFU. β is the non-telecentric angle on the telescope focal plane.

For FMOS IFU, the magnification is 20.3. The F/5 microlens has a focal length of 2.8 mm. Given the allowed maximum pupil shift of 3 μm, the maximum non-telecentric angle is 1.2° on the whole telescope field of view.

8.3.3 The Detail Design of the Fore-optics

Two sets of fore optics were designed. The first one used CAF2 glass. The CAF2 material was found to be expensive and difficult to manufacture for a lens with small size. The second fore-optics was redesigned based on the first one with some improvement. It uses only common optical glasses and CAF2 is no long used. Only the second design is discussed in the thesis.

The optical layout is shown in Fig. 8-2. The design is optimised for the optical (0.45-0.9μm) and near infrared (0.9-1.8 μm) simultaneously. The fore-optics consists of a prism lens, a doublet and a telecentric lens. The design is very simple and uses the minimum number of lenses. The prism lens consists of a precision BK7 prism (12.7 x12.7 mm) and a SK2 lens. One surface of the SK2 lens is flat which can be glued to the BK7 prism. The doublet consists of a F5 and a SK2 lenses. The telecentric lens is fused silica with a flat surface for simplicity of manufacture. All the lens surfaces are spherical or flat.

The FMOS IFU works at F/2.07. For a fast optical system, stray light may be a problem because of the large cone angle at which the light may come into the optical system. The fore-optics has a long optical path between the prism and the microlens array so a long tube is needed to mount all the optical components (see Fig. 8-6). Multiple reflections may occur if much stray light comes into the tube. After several reflections, the stray light will arrive the other end of the tube where the microlens array is located. The long and slim tube in fact is a good guide for the stray light and almost all the stray light will arrive the microlens array although it is attenuated by the multiple reflections. An important aim of the design is to suppress the stray light in the design. The fore-optics has the ability to eliminate the stray light which may be caused by the mechanical mountings, i.e. the multiple reflections of the inner wall of the tube. The design principle is shown in Fig. 8-3 for details. The sky image is located near the interface between the prism and SK2 lens. A pinhole can be sandwiched between them to serve as a field stop to block the stray light from the outside field. An intermediate pupil is formed just before the doublet where a diaphragm (aperture stop) can be located to serve as a Lyot stop to remove any stray light that is faster than F/2.07. Both the field stop and the aperture stop are slightly oversized to avoid blocking the useful light. The oversizing may introduce slight stray light and which can be suppressed by the use of a special paint on the inner wall of the IFU tube.

The spot diagram of the fore-optics is shown in Fig. 8-4. The image quality is diffraction-limited for both the magnified sky image and the pupil image. Assume that Limo square microlenses are used and each microlens has a square aperture. The pitch of the microlens array is 400 μm and the focal ratio is F/5 which is defined by the two opposite corners of the microlens. The microlens will be discussed in more detail in a later section. The good image quality will make the fore-optics more tolerant to errors which may be caused by the lens manufacture and alignment processes.

Fig. 8-5 shows the simulation of the pupil image on the microlens back surface where the fibre entrance is located. The simulation is done by ray tracing using Zemax. The fibre core diameter is assumed to be 80μm. The diameter of the telescope pupil image on the microlens back surface is 73.32 μm on the centre of the field. The pupil image is broadened by optical aberration. The dominant aberration is chromatic which may cause a shift of the pupil position at different wavelength. However, the shift is significantly less than 3 μm RMS because the PSF of the pupil image is diffraction-limited.

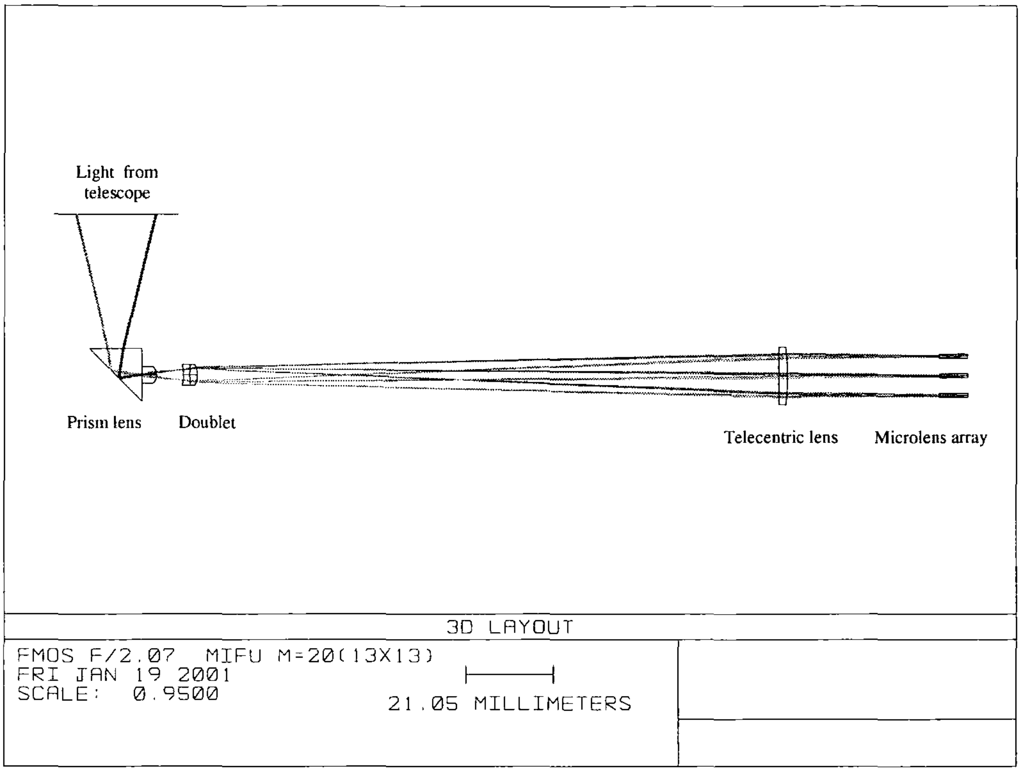

Figure 8-2. The optical layout of the FMOS IFU fore-optics. The magnified sky image is formed on the curved surface of the Limo microlens array.

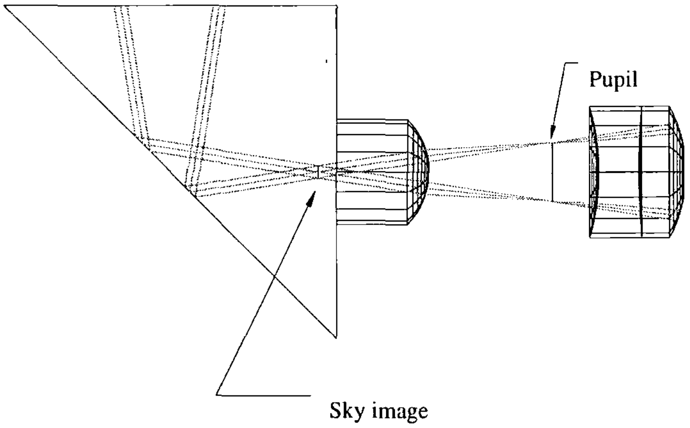

Figure 8-3. The design principle of stray light suppression. The fore-optics has a real sky image and an intermediate pupil image which can be used to suppress the stray light.

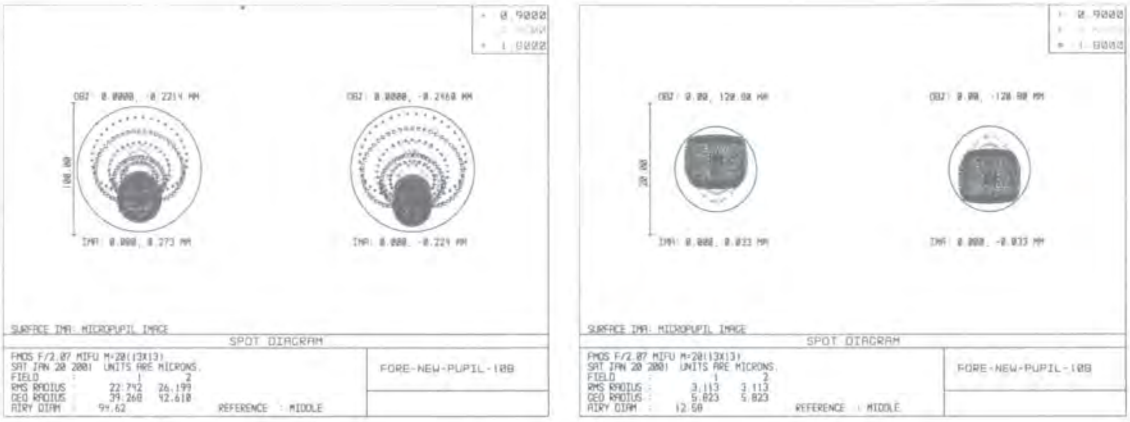

(a) (b)

Figure 8-4. Spot diagraphs of the magnified sky image (a) on the field edge and the pupil image (b) on the microlens back surface. The circles are the Airy diameter. The image qualities are diffraction-limited for both (a) and (b).

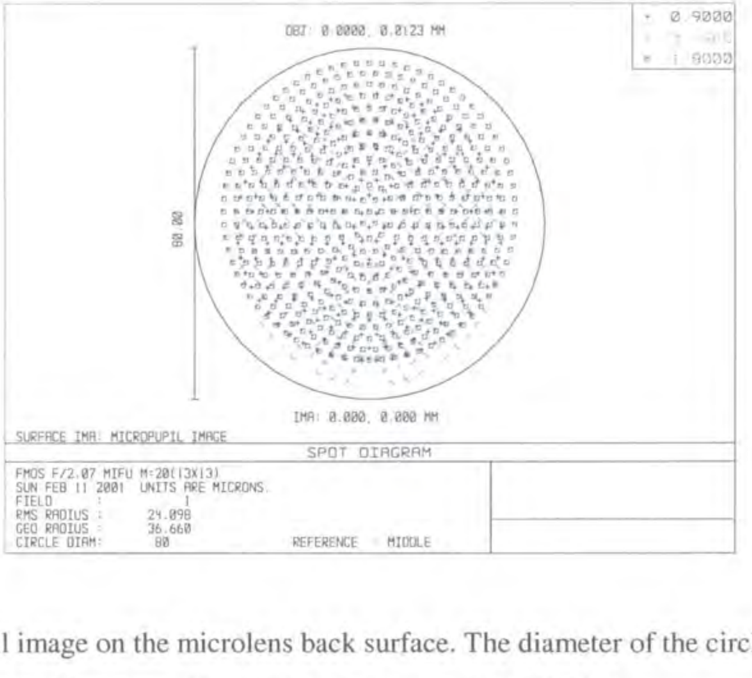

Figure 8-5. Pupil image on the microlens back surface. The diameter of the circle is 80 μm which represents the fibre core. The pupil image diameter is 73.32 μm.

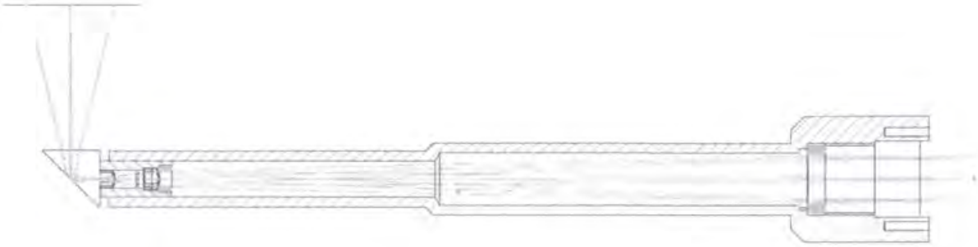

Figure 8-6. The mechanical assembly of the fore-optics (Designed by George Dodsworth).

The BK7 prism was an in-stock product and was purchased from Melles Griot. The hypotenuse was coated with silver. The silver coating delivers an average reflection of better than 98% over the 0.45 – 1.8 μm range (private communication with Melles Griot 1999). The SK2 lens, the F5/SK2 doublet and the silica lens were manufactured by Knight Optical.

The mechanical mounts were designed by George Dodsworth and the mechanical drawing is shown in Fig. 8-6. The prism lens is glued on a short tube mount. The doublet is then fixed on the mount from the other side by a screw. The prism lens and the doublet form a sub-assembly. The sub-assembly can insert into the IFU tube and slide into it for +/- 2mm for the axial adjustment which is necessary to ensure that the magnified sky image is telecentric. As discussed at the beginning of this chapter (see Fig. 8-1), the IFU consists of lenses L_1 and L_2. Lenses L_1 and L_2 need to have the consistent focal point O to ensure that the magnified sky image is telecentic. However manufacture error may result in an inconsistent focal points for these two lenses after assembly. This requires a fine adjustment in the axial direction and this can be done by moving the sub-assembly in the IFU tube (see Fig. 8-6). Two screw holes on the IFU tube can be used to quickly fix the prism lens and doublet sub-assembly as soon as the adjustment is confirmed. The fibre bundle and microlens assembly can be connected to the IFU tube at the other end. The design is very compact and the IFU head diameter is about 13mm. This ensures that more than 15 IFUs can be deployed on the telescope focal plane.

The inner wall of the IFU tube was coated with Nextel which attenuates 95% of the light for each reflection.

8.3.4 Fore-optics Fabrication and Tolerances

The lens design tolerances have a close relationship with the methods by which these lenses will be aligned and assembled. One method involves no alignment. For this method, all the lens tolerances are tightly controlled in the design and manufacture. The tolerances are very small and thus have very little effect on the image quality. The precision of the lens position is obtained by its mechanical mounting. For the FMOS IFU optics shown in Fig. 8-2, this requires that the tolerances of lens thickness are +/- 0.02mm which is not achievable.

Another method can have loose tolerances for the manufacture. But this needs adjustment and alignment of the positions of some lenses, such as the axial position alignment of the sub-assembly which was discussed in the previous section, to compensate for the deviation of the lens from its ideal position because of the manufacture errors. For this method, the thickness tolerances of the prism doublet and the singlet are +/- 0.1mm. The telecentric lens is +/- 0.2mm. These tolerances are more reasonable and this method is adopted.

For manufacture, the spherical shapes of all of these lenses needed to be specified. The wave aberration is less than ¼ wavelength at 0.63 microns. This ensures that the manufacture error has almost no effect on the image quality of the IFU system.

Finally, the singlet, doublet, and the telecentric lens were fabricated by Knight optical Ltd., because of its low price and good quality. The prism was purchased directly from Melles Griot.

8.4 Microlens Design

The microlens array is a key element for the IFU. Most microlenses are not perfect and suffer from low encircled energy because of the poor image quality. The characterizations of microlens array have been discussed in Chapter 5. Two kinds of microlens have been considered for the FMOS IFU: hexagonal microlens and square microlens.

8.4.1 Hexagonal Microlens Array

Fused silica hexagonal microlenses have been considered for the IFU. In this case, the microlens is optimised for collimated light (object is at infinity) and this is consistent with the situation for the IFU where the pupil is at infinity due to the telecentric design of the IFU fore-optics. In the wavelength range of 0.4 ~ 1.8 μm, chromatic and spherical aberration is not a problem for a small silica microlens. When the diameter increases, chromatic and spherical aberration will begin to dominate and this has been discussed in Chapter 5. Fig. 8-7 gives the design details of a fused silica microlens and the spot diagram of the optical aberration. The design wavelength is 900μm. This is necessary for the manufacture as the microlens curvature and focal length, i.e., the microlens thickness needs to be specified at a monochromatic wavelength. It can be seem that although the design wavelength is at 900 μm, the image quality of the microlens is diffraction-limited over the whole wavelength range of 0.45-1.8 μm.

Fig. 8-8 shows the configuration of the microlens array. The 500 μm microlens diameter is defined as the distance between the opposite faces of each hexagonal microlens. The 217 hexagonal microlenses are hexagonally packed to form an array. The enclosed circle of the array defines the field of each IFU.

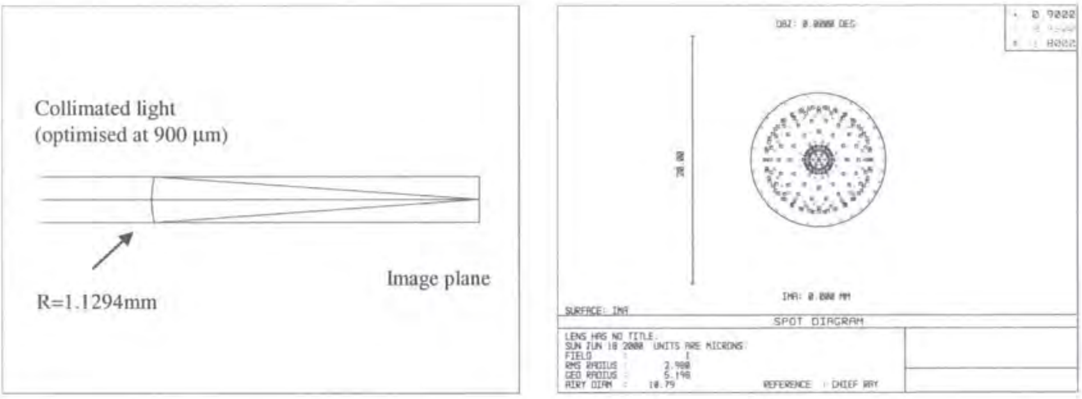

(a) (b)

Figure 8-7. A F/5 fused silica microlens with a diameter of 500 μm (a). The design wavelength is 900 μm. The spot diagram is shown in figure (b) and the circle is the Airy disk.

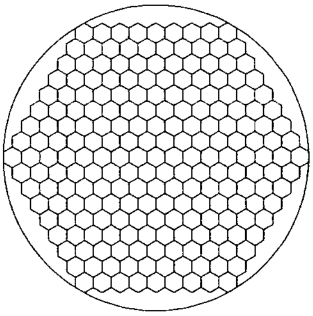

Figure 8-8. Layout of a sample IFU field containing 217 hexagonal microlenses. The 0.3 arcsec sample increment (500μm) is defined as the distance between opposite faces of each hexagonal microlens. The diameter of the enclosing circle is 5.1 arcsec (8.5mm).

The hexagonal microlens array is made from monolithic fused silica. To ensure good quality of the microlens array, some requirements must be met. The lens-lens gap must be less than 5 μm. Wave aberration of microlens must be less than 1 wavelength at 0.63 μm on the whole aperture (or at least at 90% of the aperture). Surface roughness is required to be less than 0.006 μm. The techniques for the manufacture of monolithic silica microlenses arrays are well developed and hexagonal monolithic microlens array can be manufactured by MEMs Optical or AMS. MEMs Optical can also provide anti-reflection coating (MEMs Optical catalogue 2000). However, according to a measurement (Ren 2000a), MEMs microlenses have much stray or scattered light, which results in a very low encircled energy. The stray light is believed to be caused by large wave aberration and lens-lens gap. MEMs cannot guarantee that the wave aberration is less than one wavelength at 0.63 μm on the whole aperture of the microlens. It seems that AMS microlens is the only choice for monolithic hexagonal microlens array. AMS microlens array has been used by the PMAS integral field spectrograph and the image quality is claimed to be excellent (Roth et al. 2000). It needs to be noted that Epigem can manufacture high quality PMMA hexagonal microlens array. Although PMMA has strong spectral absorption at near infrared, the transmission will not be a problem if the PMMA microlenses are manufactured on a glass substrate.

8.4.2 Square Microlens Array

Another option is to use square microlens array. LIMO microlens array have been used for some IFU spectrographs (Prieto et al. 1998, Sugai et al. 2000). A main reason to use LIMO microlens array for the FMOS IFU is its low cost. A custom-designed microlens array is needed. The square microlens array consists of two pieces of cylindrical lens arrays. Normally, the two pieces of cylindrical lenses need to have different curvatures because there is a gap between them and all the microlenses on the two pieces need to focus on the same focal plane. A novel custom-design is derived which uses the same curvature for the two pieces of cylindrical microlenses, however with different glasses to ensure that the two pieces of microlenses have the same focal plane. In this method, the cost for the tooling is only half of the conversional LIMO microlens array. The optical layout and spot diagram of the microlens is shown in Fig. 8-9a and Fig. 8-9b, respectively. The first cylindrical lens is Schott LAK9 glass with a thickness of 2mm and the second one is Schott LAK10 glass with a thickness of 4.8mm. Both lenses have a curvature radius of 2mm. The gap between the two pieces of arrays is 81.6 μm. The square microlens pitch is 400μm and the focal length is 2.8mm. This corresponds a focal ratio of F/5 at the corner of each square microlens and this ensures that almost no light is lost due to vignetting when a F/4.5 spectrograph is fed by the IFU. The image quality is diffraction limited over the 0.45 – 1.8 μm wavelength range.

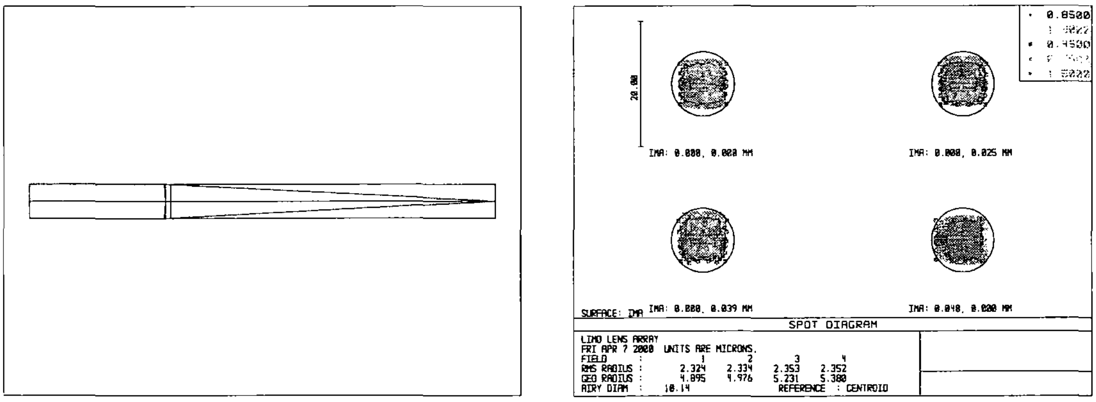

(a) (b)

Figugre 8-9. The optical layout (a) and spot diagraph (b) of the custom-designed LIMO microlens. The circles are Airy disk. The microlenses on the two pieces of arrays have the same curvature radius.

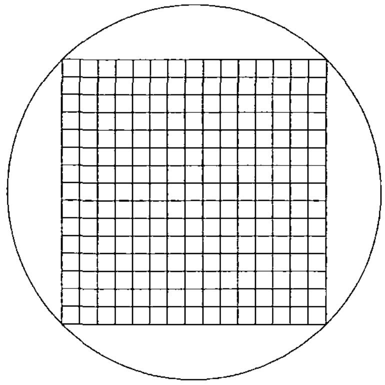

Figure 8-10. The layout of a sample IFU field containing 15x15=225 square microlenses. The distance (400μm) between opposite faces of each square microlens defined a 0.24 arcsec sampling increment. The diameter of the enclosing circle is 5.1 arcsec (8.5mm). There is some vignetting for the four microlenses at the four corners if the IFU field of view is the same as that in Fig. 8-8 for the hexagonal microlens array.

The microlenses are closely packed to form an array. Each array contains 225 square microlenses and has a pitch of 400μm. In fact the square microlens array is composed of two pieces of LIMO cylindrical arrays. Fig. 8-10 shows the configuration of the microlens array. Note that the distance between the opposite faces of each square microlens is 400 μm, which defines a 0.24 arcsec sampling increment. The enclosed circle of the array defines the field of each IFU, which is 5.1 arcsec (8.5mm) and is the same as that in Fig. 8-8 for a hexagonal microlens array.

The square microlens array was manufactured by Limo GmbH. The specifications for the manufacture are listed in Table 8-1. Note that λ_d is equal to 0.5892 μm. The specifications are necessary to ensure a high quality microlens array.

Comparing Fig. 8-8 with 8-10, for the same IFU field of view of 5.1 arcsec (8.5 mm) diameter, the hexagonal microlens array occupies more field area than that of the square microlens array, so can provide more useful field of view. It is evident that the hexagonal microlens array can make better use of the IFU field of view.

Table- 8-1. The main manufacture specifications of LIMO microlens array

Surface	Spherical: R=2.0mm
Maximum Filling (P/A)	>95%
Surface accuracy	$\lambda_D/5$
Surface quality	MIL 40-20
Aperture	400 +/- 0.01mm
Pitch	400 +/- 0.001 mm
Thickness tolerance	+/- 0.02 mm

8.5 Elastic Deflection of FMOS IFU Tube

The IFU will be movable in the telescope field via a "Fishing-Rod" mechanism and all the optical components are assembled in a aluminium IFU tube. In two extreme cases, each IFU can be located at the telescope field edge and centre, respectively. The IFU tube can be represented as a cantilever. When the IFU tube is located at the edge of the telescope field, there is almost no deformation. However, when the IFU is located at the centre of the telescope field, the aluminium tube will suffer maximum deformation. Two kinds of load apply on the tube. One is concentration load which is applied by the optical components and their mounts. Another one is the uniform load which is applied by the tube's gravity. These two kinds of loads are schematically shown in Fig. 8-11, which presents the case when the IFU tube is located at the centre of the telescope field. The whole deformation of the IFU tube needs to be tightly controlled and the maximum must be less than the allowed deformation. The allowed deformation is the maximum allowed tolerance for the distance between the telescope focal plane and the IFU. According to tray tracing, the maximum allowed deformation is 6 μm which will result in no significant degradation of the IFU image quality.

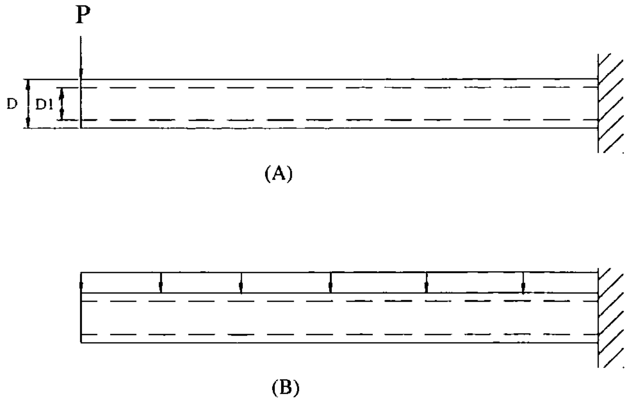

Figure 8-11. The Schematics of IFU tube mathematical model. (A) For cantilever beam with concentration load at the free end. (B) Cantilever beam with uniform load.

For a cantilever beam with concentrated load at the free end (Fig. 8-11 (A)), the maximum deflection happens at the free end and can be expressed as (Kutz 1998)

$$y_1 = \frac{Pl^3}{3EI} \qquad (8-4)$$

Where y_1 is the maximum deflection. *P* is the concentrated load. *l* is the length of the beam. *E* is modulus of elasticity. *I* is moment of inertia.

For hollow with circular cross-section beam, the moment of inertia *I* is

$$I = \frac{\pi(D^4 - D_1^4)}{64} = 0.0491(D^4 - D_1^4) \qquad (8-5)$$

Where D is the outer diameter of the hollow circle beam. D_1 is the inner diameter of the hollow circle beam.

For the FMOS IFU tube, l=0.125 m, D=12 x10^{-3} m and D_1 = 8 x10^{-3}. So, I=817 x10^{-12} m^4.

And for cantilever beam deflection under uniform load, the maximum deflection also happens at the free end and can be expressed as (Kutz 1998)

$$y_2 = \frac{Wl^3}{8EI} \qquad (8-6)$$

Where W is the total uniform load on the beam (N). And W=wl where w is uniform load per unit of length.

So, the total deformation under the concentrated load and gravity is

$$y = y_1 + y_2 = \frac{Pl^3}{3EI} + \frac{Wl^3}{8EI} \qquad (8-7)$$

For the IFU optical lenses, the prism has a size of 13 x 13 x 13 mm and the typical optical density is ρ=3.7gcm^{-3} =3.7 x10^{4} kgm^{-3}. The weight of the prism is 2.46 x 10^{-3} kg. Assume that the doublet and the singlet has the same weight as the prism, the total optical lenses weight is 7.38 x 10^{-3} kg. Assume again that the weight of optical mounts for these lenses is twice the weight of the lenses. So the concentrated load and deformation are

P=22.2 x 10^{-3} kg =0.217 N and y_1 =2 x 10^{-6} m.

For aluminium alloy, the modulus of elasticity is E=70 x10^{9} Nm^{-2} and the density is ρ=2700 kgm^{-3} =26460 Nm^{-3} (Carvill 1993). The tube weight is 0.0212 kg =0.21 N. Therefore, the deformation due to the self-weight of the tube is

y_2=0.9 x10^{-6} m.

Thus, the total maximum deformation is

$y=y_1 + y_2$ = 2.9 x10^{-6} m = 2.9 μm

The maximum deformation is estimated to be less than the allowed value of 6 μm.

8.6 The Design and Construction of the Fibre Bundle

In this section, possible techniques for the constructions of the fibre bundles are discussed first. Following is the technique for the construction of FMOS fibre bundle.

8.6.1 Fibre Bundle Techniques

The fibre bundle is a key element for the fibre IFU. The light from microlens array is coupled into the fibres. This requires that the fibre-to-fibre position of the fibre bundle must be accurate if the coupling loss is to be minimised. The geometry of the fibre bundle is decided by the microlens array, i.e. a square microlens array need a square packed fibre bundle.

Optical fibre bundle arrays are simple to conceptualise, but their fabrication has proven to be difficult when high-precision positioning is required (Sasian et al. 1994). Fibre bundles were first developed and used for switching systems which utilize macroscopic optical elements such as optical fibre bundle arrays, holograms, grating, lens, and mirrors as their basic hardware building block. In these systems information is carried by light beam arrays that are collimated, manipulated, and focused onto spatial light modulator in a stage-by-stage fashion. The applications of high precision fibre bundles for astronomical instruments occurred recently, since the realization of microlens array + fibre bundle IFU. There are some existing techniques that are suitable to build the fibre bundle.

A. The Construction of fibre bundle by stacking

This method uses an array of tubes. The construction of the tube array is schematically shown in Fig. 8-12. The tubes are stacked in a holder which has a rectangular inner shape. By closely packing these circle tubes, a hexagonal fibre bundle is achievable. Note that the outer diameter of the fibre ferrule needs to be custom-made to match the pitch of the microlens array. The holder may be made of stainless steel or glass. After the tube array is built, the fibres are inserted in the tubes and the whole array is immersed in epoxy adhesive. The fibres are cured and then the fibre bundle face is polished. The accuracy of the centre-to-centre positions of the tubes is decided by the accuracy of the outer diameter of each tube and the assembly of the tubes. The tolerances of the holder also need to be tightly controlled. If the size of the holder is too small, it may not be possible to fit all the tubes. If it is too big, there may be gap which will affect the position accuracy of the tubes.

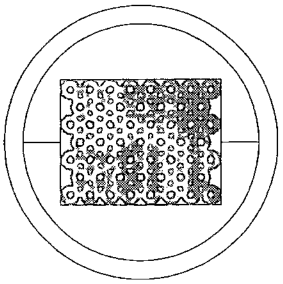

Figure 8-12. Schematic of a 2-D fibre array constructed by using tubes. The ferrule outer diameter is custom-designed to match the pitch of the microlens array.

Tubes designed for medical applications are used to build the fibre array. Almost all of the these tubes are made of stainless steel. They are manufactured by drawing and produce in a series of standard Gauges. Each standard Gauge corresponds a specific inner and outer diameter. The size varies between different drawings or batches and the difference may reach about +/- 40 microns for sizes suitable to hold fibres, although the variation may be small within the same drawing. The big variation between batches cannot be tolerated for the IFU fibre bundle since high position accuracy is required. The metal tube also has a different thermal coefficient with the fibre, which may introduce stress on the fibre when temperature changes and thus causes FRD. Examples of the use of such tubes include the fibre bundles for the TEIFU and GMOS IFU. The fibre-to-fibre position accuracy is about 8 μm RMS according to actual measurement for TEIFU. Disadvantage of the use of the medical tubes is that the pitch of the microlens array must be decided according to the actual measured pitch of the fibre bundle after it has been completed because of variation of the tube sizes from batch to batch.

For this tube array, the accumulation of tolerance may happen in the two stacking directions. A method to reduce this tolerance accumulation is to use high accuracy tubes. Fibre ferrules can be used to replace the medical tube for the construction of the fibre bundle and they are produced by a precision drawing process and can be made of metal or glass. The inner diameter can be accurate to a tolerance of +/- 1 microns for both metal (Nippon Tokushukan MFG .Co. Ltd 2000) and glass (Becton Dickinson 2000). There are several advantages of using glass fibre ferrule. These include their tight tolerance and similar polishing characteristics with quartz fibres. Borosilicate glass has a similar thermal coefficient with quartz fibres. Funnelled ends are available, which can provide a quick insertion of the fibre and provide stress relief at the end face.

Polishing the end of the fibre is crucial and can greatly impact the quality of the installation. A mirror-finished end of the fibre bundle is desired and this will reduce the light loss at the interface. If fibre and ferrule do not have the similar polishing characteristics, undercutting may happen. Undercutting happens with materials that polish at different rates resulting in the end of the fibre polishing to a depth below the end of the ferrule. Borosilicate glass ferrule and the glass from which fibres are constructed polish at similar rates. Therefore, the finished end of the glass and the fibre end are smooth with minimum undercutting. This can result in superior polishing.

B. The Construction of fibre bundle by wafers

An array of holes made from wafers can also be used to build the fibre bundle. The process is schematically shown in Fig. 8-13. The fibre position accuracy is mainly decided by the accuracy of the hole position within the wafer. The wafer material can be polymide which can be machined by using an excimer laser. The high photon energies associated with these ultraviolet lasers enable direct material removal in the polymeric substrate. The substrate of the wafer can also be silicon so that the array of the holes can be made by the well-established technique of silicon chemical etching. Normally the thickness of the wafer is less than 1mm, so two wafers are needed to accurately hold the fibres. The fibres are inserted into the holes in the wafer and then glued by epoxy adhesive. This wafer technique was used by Kopf et al. (1984) and Proudley et al. (1994). The accuracy of the mean fibre position error is reported to be ~6.3 μm RMS for an array of 16 fibres (Proudley et al.1994).

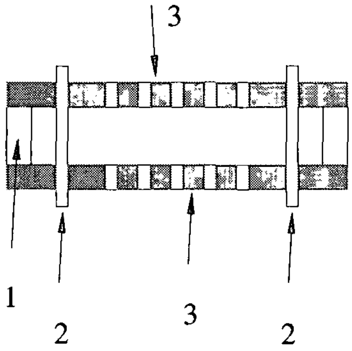

Figure 8-13. Section view of a 5x5 capillary array constructed by two pieces of wafers. 1 is the spacer for supporting the two wafers. 2 is the aligning fibre. 3 is the wafer.

A different technique using one plate of hole array but with active alignment for each fibre gives a position accuracy of 1.5 μm for a 4x8 fibre array. However the drawbacks of this method are the long time required to assemble large arrays and the possibility that only one broken fibre may ruin an entire array (Sasian et al. 1994).

C. The Construction of fibre bundle by V grooves.

V grooves are a traditional way to mount linear array of fibres and are formed by etching (Bostock et al. 1998). Fibres can be accurately held in the V-shape grooves by gluing. Typically V grooves are used for linear array but 2-D array can also be formed by stacking the linear arrays (Fig. 8-14; see Miller 1975). Silicon is a well-developed material suitable for etching V grooves. Silicon V groove can achieve high accuracy with a centre-to-centre position tolerances < 1 μm. An example is the silicon V groove manufactured by Wave Optics, Inc. The position tolerances can be as small as ±0.25 microns for a 250 microns centre-to-centre spacing. MicroDevices, Inc. can fabricate 2-D fibre array using the V groove technique. In principle, this 2-D array has high position accuracy in the linear V groove direction which is decided by the fabrication. But in the stacking direction, the position error may be large because of the accumulation of the tolerances of each linear V groove array. Recently, the maximum positioning error is reported to be 10 μm for a fibre bundle made by Danzer et al. (1992).

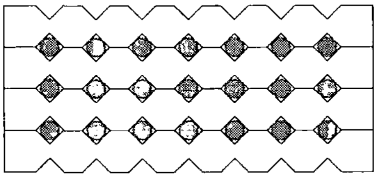

Figure 8-14. 2-D fibre bundle constructed by stacking of linear V grooves. The dark circles are fibres. The 3x7 capillary array is formed by four pieces of linear arrays of V grooves. Each piece is a linear array with 7 v-grooves on each side.

8.6.2 The Construction of FMOS IFU Fibre Bundle

There are some requirements for the fibre for the FMOS IFU. The fibre must have a good transmission over the 0.45 – 1.8 μm wavelength range. The fibre must have a small FRD which may be introduced by the fibre itself in the manufacture process. The fibre also needs to have good mechanical properties (i.e. not break).

Table 8-2. The fibre specifications

	Nominal value	Measured value
Core diameter	80 +/- 2 μm	80 - 82 μm
Cladding diameter	112 +/- 5μm	113-115 μm
Buffer diameter	205 +/- 10 μm	208-210 μm
NA	0.22+/-.02	
Product code	FIA 080112205	

The fibre was purchased from Polymicro Technologies LLC, considering its good reputation and the above requirements. Low OH core fibre has a good transmission over the 0.45-1.8 μm wavelength range. The materials are silica, doped silica and acrylate for the fibre core, cladding and buffer, respectively. The attenuation is less than 10 dB/km. The specifications are listed in Table 8-2

The fibre bundle was made by AndaOptec Inc according to the required specifications for the FMOS IFU. AndaOptec had successfully made an 80x80 square fibre bundle for VIMOS and the fibre position error was 17 μm RMS for the fibre bundle and 11 μm RMS for the fibre bundle and microlens array assembly (Prieto et al. 2000). The position error of the fibre bundle and microlens array assembly is slight smaller than that of the fibre bundle alone because the fibre bundle and microlens array can be best fit each other in the assembly process. As Limo square microlens array is used for FMOS IFU, the fibre array must be in square package. The square fibre array consists of 15x15 fibres. Normally, stacking technique can only be used for hexagonal fibre arrays. By using precision rods, square fibre array can be built by stacking technique. The fibre head of the bundle is schematically shown in Fig. 8-15. For construction of the fibre bundle, the buffer of each fibre is removed and only the cladding is left because the diameter of the cladding is more accurate than that of the buffer. The stripped length is about 20mm for each fibre. The stripped fibres are then stacked with the precision rods in a precision square holder which consists of two halves. The holder together with the fibres is then inserted into a tube. The end face of the fibres bundle head is polished after gluing and curing.

The main specification for the fibre bundle is the maximum fibre position error which should be less than +/- 8 μm (see Fig. 8-15). This implies that the fibre position error is less than about +/- 3 μm RMS. Another important specification is the FRD for the fibre bundle which may be caused by the adhesive or mounting when building the fibre bundle. Unfortunately, fibre FRD is not considered to be a problem in fibre communication systems, and AndaOptec Inc cannot guarantee the FRD for the fibre bundle.

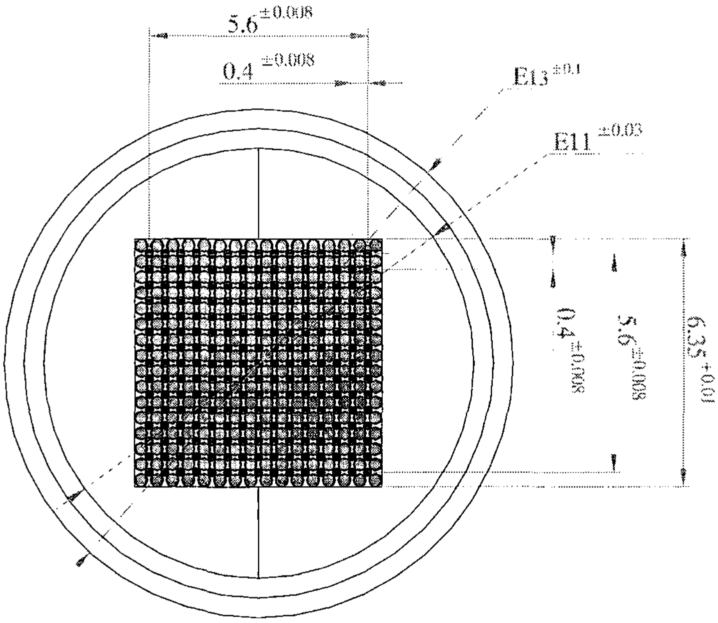

Figure 8-15. The end face of the FMOS IFU fibre bundle head (Courtesy of AndaOptec).

The configuration of the fibre bundle is schematically shown in Fig. 8-16. The 15x15 fibres are arranged in 15 sub-slits at the other end of the fibre bundle. Each sub-slit corresponds to one row on the bundle head. At present there is no specification for the configuration at the sub-slit ends. The fibres are arranged in the sub-slit side by side with no gap between them. In order to reduce the cost of the fibre bundle, the position accuracy of the fibres in each sub-slit is not subject to a specification. However, the arrangement of sub-slits will allow the IFU to be used with an existing spectrograph for tests. All the fibres are protected in jackets and the jackets are protected by PVC tubes which limit the bend radius.

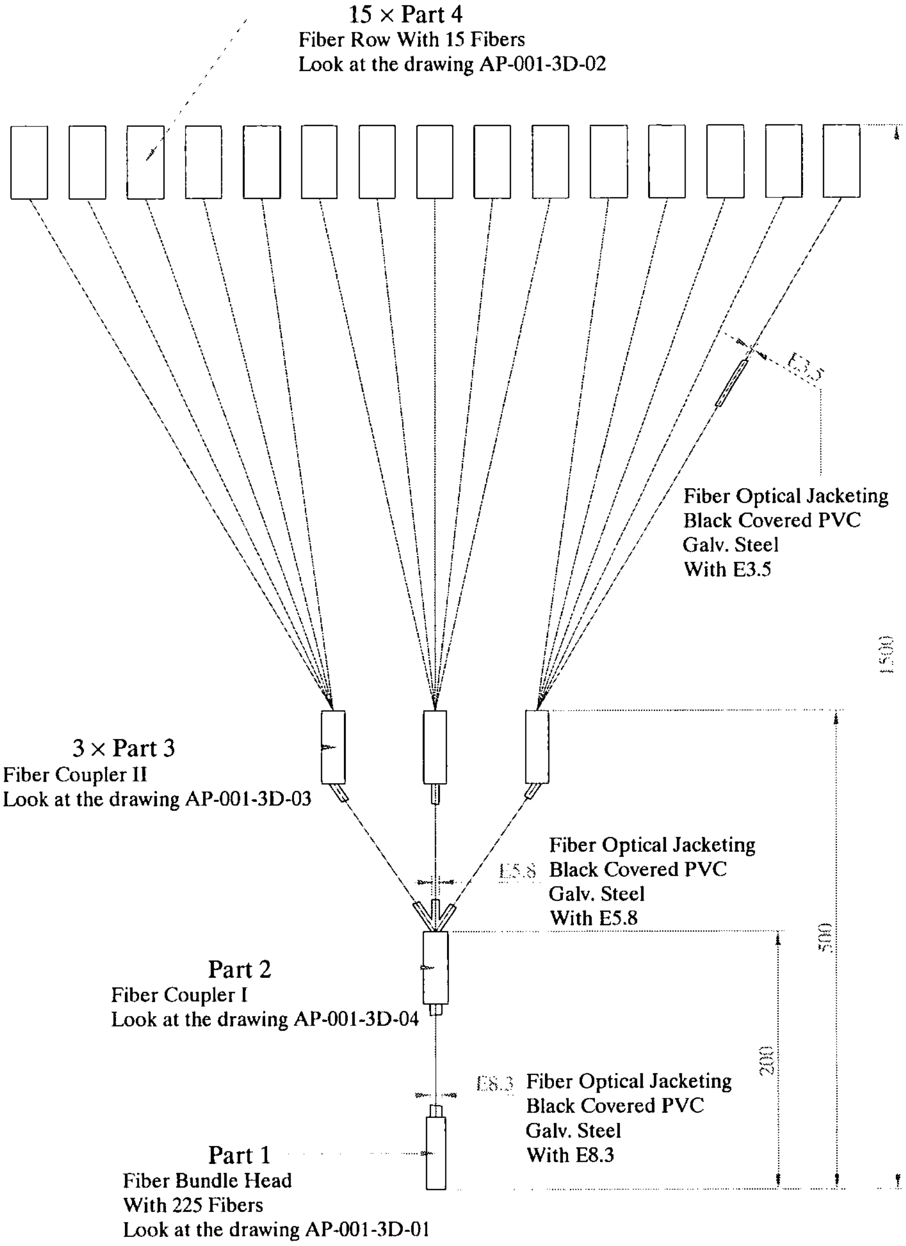

Figure 8-16. The configuration of the IFU fibre bundle (Courtesy of AndaOptec).

8.7 Estimated Performances

The focal length of the Limo microlens is 2.828mm and the magnification of the IFU is 20.3. The diameter of the telescope pupil image is 67.3 μm according equation to (8-2). This is a theoretical calculation when no optical aberration is present.

The telescope pupil image and fibre core size are listed in Table 8-3. Compared with the ideal telescope pupil image size which is 67.3 μm, the actual telescope pupil image diameter is 73.3 μm (see Fig. 8-5) due to broadening by optical aberration in the IFU optical system. The fibre core diameter is 80 μm which is oversized by about 7 μm compared with the actual broadened pupil image size. The oversizing of the fibre core is necessary to accommodate the broadened pupil image and to avoid light loss in the coupling process between the microlens array and the fibre bundle. There should be no significant light loss in the coupling process if the alignment error between microlens and fibre is less than 3.5 μm RMS.

Table 8-3. Pupil image size and fibre core size

Ideal pupil image size	67.3 μm diameter
Broadened pupil image size	73.3 μm diameter
Fibre core size	80 μm diameter
Allowed alignment error	3.5 μm RMS

The assembly of the microlens array and fibre bundle can be done by using back illumination, which will be discussed in the next chapter. Assume that the position registration accuracy between the microlens array and fibre bundle is better than 3.5 μm RMS. This is possible because the position error of the microlens array and fibre bundle may be partly compensated by the best fitting in the assembly process. This has been confirmed by VIMOS (Prieto et al. 2000) where the position error is 17 μm RMS for the fibre bundle alone and the position error is only 11 μm RMS for the microlens array + fibre bundle assembly.

For the FMOS IFU, the position accuracies of the Limo lens array and fibre bundle require better than 2 μm RMS and 3 μm RMS, respectively. It is reasonable to assume that the alignment error between microlens array and fibre bundle is less than 3.5 μm RMS so it does not cause any significant light loss in the coupling process. The performance of the IFU can be estimated by equation (2-32) according to a figure of merit

$$Q = \frac{1}{K_{pup}K_F}\eta \qquad (8-8)$$

As discussed in chapter 2, for FMOS IFU, K_{pup}= 1.19 and K_F = 1.25. This results in Q=0.67η. The IFU efficiency η includes the microlenses and other optics of the IFU. The estimated performances are listed in Table 8-4. The IFU optical efficiency includes the reflection losses at each lens and fibre surface. Assume that the average reflection loss is 2% at each surface over the 0.45 – 1.8 μm wavelength range after coating. The microlens is a key element for IFU and the main problem is scattered or stray light which has been discussed in Chapter 5. It is assumed that microlens efficiency is 80% and this is a reasonable value for the current techniques.

Table 8-4. Estimated performances of the FMOS IFU

IFU optics efficiency η (not include microlenses)	88.5%
Microlens efficiency	80%
IFU optics efficiency η (includes microlenses)	70.8%
Figure of merit (Q)	47%

It is obvious that the IFU efficiency is mainly determined by the microlens efficiency.

8.8 Summary & Conclusions

The design of the FMOS IFU has been discussed. This design ensures that the magnified sky image on the microlens surface is telecentric. The requirement of the telecentricity is necessary to eliminate any shift of the pupil image on the microlens array. The PSF of the sky image is diffraction-limited and much less than one microlens, which is the sampling element. The PSF of the pupil image is also diffraction-limited at most wavelengths and is almost diffraction limited at 0.45μm. The optical design of the fore-optics meets the FMOS requirements.

The alignment methods for the IFU optics are also considered in the design phase. The manufacture errors of the fore-optics lenses can be compensated by the alignment. To ensure telecentricity, the sub-assembly of lenses needs to be adjusted by moving along the optical axis in the IFU tube to compensate for the manufacture errors of the lenses. The magnified sky image needs to be formed on the microlens curved surface which can be done by adjusting the distance between the IFU and telescope focal plane.

The designs of microlens arrays are presented. The possible microlens arrays considered for FMOS are AMS and Epigem for hexagonal microlenses, and LIMO for square microlenses. The LIMO square microlens array is used for the FMOS IFU because of its lower cost and high specifications. The design shows that the image qualities of the microlenses are diffraction-limited.

Methods for making the fibre bundle are also described. The fibre bundle for the FMOS IFU is manufactured by AndaOptec according to the specifications required for the IFU. The maximum fibre position error is required to be less than +/- 8μm. The position error is estimated to be less than 3 μm RMS, which will have a little effect on the coupling process between the microlens array and fibre bundle.

The performance of the IFU system is also estimated. This will be compared with the actual measured performance which will be discussed in the next Chapter.

Chapter 9

The construction and testing of FMOS IFU

Abstract

In this chapter, the tests and measurements of the IFU key components are first described. These include tests of the Limo microlenses, the fore-optics and the fibre bundle. These tests and measurements are very important to ensure high performance of the whole IFU system. The construction of the IFU is also described. The IFU system performance is compared with that of the theoretical estimation and further possible improvements are suggested.

9.1 Introduction

The design and theoretical performance of the FMOS IFU are discussed in Chapter 8. A general question is, however, is this performance achievable? This question will be answered in this chapter. The system performance of the IFU is determined by some key components due to the limitation of the current techniques. These include the IFU fore-optics, microlenses and fibre bundle.

The diameter of the smallest IFU lens is only 4 mm and so the mechanical assembly error is critical. The IFU needs to deliver a telecentric sky image to the microlens and at the same time project the telescope pupil image onto the microlens back surfaces. According to ray tracing simulation, in order to maintain telecentricity, a mechanical alignment is necessary to account for the manufacture errors in the lenses and mechanical mounts. The FWHM of the PSF of the sky image needs to be less than the size of two microlenses. The optical aberration for the pupil image needs to be as small as possible because any aberration of the pupil image will results in a light loss in the coupling between the microlens array and fibre bundle.

There is a limitation on the quality of microlens arrays for the current techniques, which is discussed in detail in Chapter 5. The main problems are fill factor, wavefront aberration and surface roughness, which will introduce scattered or stray light and thus result in a low encircled energy. This means that poor microlenses will result in light loss.

For the fibre bundle, the main concerns are the fibre position-to-position error and the fibre FRD. An error in fibre position on the input face of the fibre bundle may result in a light loss in the coupling between the microlens array and fibre bundle because the pupil image may be located outside the fibre core. Fibre FRD may be introduced by the manufacture process of the fibre bundle if a large stress is applied on the fibres. This may result in low throughput of the whole spectroscopic instrument because some light may be lost due to vignetting inside the spectrograph.

In this chapter, tests and measurements of the Limo microlens array, fore-optics and fibre bundle are presented. The performance of the IFU system is also compared with that of the theoretical estimation and further possible improvement is suggested.

9.2 The Test of Limo Microlens Array

The tests of Limo microlenses were carried out after the microlens array was received. Because of concern about the quality of the microlenses, which may greatly affect the performance of the IFU system, a lot of tests were done in order to accurately characterize the Limo microlenses.

The first test was to check the position accuracy of the focal plane of the Limo microlens array. The Limo microlens array consists of two cylindrical microlens arrays (Fig. 9-1 (a)). The first is a LAK9 cylindrical lens array with a thickness of 2 +/- 0.1 mm. The second one is a LAK10 cylindrical lens array with a thickness of 4.8 +/- 0.02 mm. The gap between the two cylindrical arrays is 81.6 μm. If the manufacture error of the LAK10 array is bigger than the allowed tolerance of 0.02mm, or there is an assembly error for the two pieces of the cylindrical arrays, the PSF may not correctly form on the focal plane (i.e. the back surface) of the Limo microlens array. This may result in an extra optical aberration when projecting the telescope pupil image onto the fibres and thus cause a low coupling efficiency between the microlens array and the fibre bundle.

The Limo microlens array is illuminated by collimated HeNe laser light. The PSF must be located on the back surface of the microlens array. In order to get a clear image, the back surface is also illuminated by a white light. The PSF is shown in Fig. 9-1 (b). Dust on the back surface can be clearly seen. It is evident that the PSF is correctly formed on the back surface of the microlens array. This test confirmed that the thickness of the LAK10 cylindrical array and the assembly of the two cylindrical arrays are very accurate and meet the requirement for the IFU.

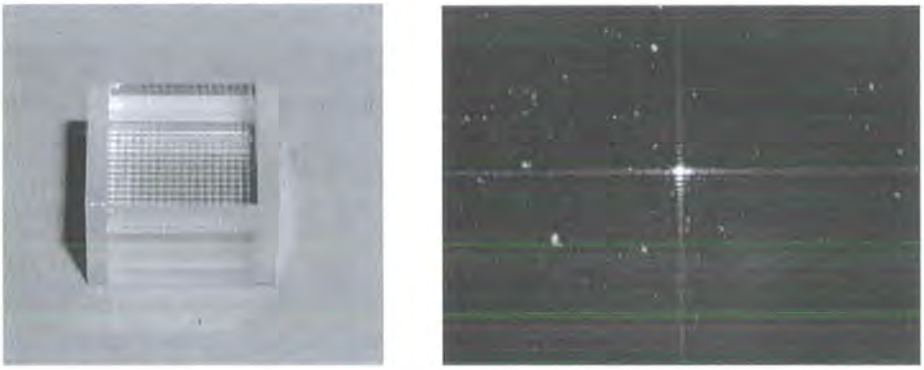

(a) (b)

Figure 9-1. Photograph of the Limo microlens array (a) and the PSF of one microlens (b). In (b), the focus point (PSF) is accurately formed on the back surface.

The measurement methods of the microlens PSF and enclosed energy were discussed in detail in Chapter 5. Fig. 9-2 is the measured PSFs of the Limo microlenses. The diffraction wings within the fifth peak or so is similar to that of the theoretical estimation. There are, however, significant components outside that and there is some stray light located in the diffraction wings. The stray light is believed to come from the lens-lens gap areas. These areas may have a surface curvature that deviates from the ideal shape. The enclosed energy is shown in Fig. 9-3. There is about 65% enclosed energy in the PSF central area (20μm radius). There is 35% light lost outside the central area. The loss may be introduced by the surface curvature deviation, scattered light and multiple-reflections of the microlens surfaces. The tested Limo microlens is not AR coated and there are four surfaces that can contribute to multi-reflections. Sugai et al. (2000) measured the surface profile of a 1.54mm pitch Limo microlens. He reported that there is about 100 μm width of the surface deviation between two lenses which introduces about 15% light loss for the encircled energy.

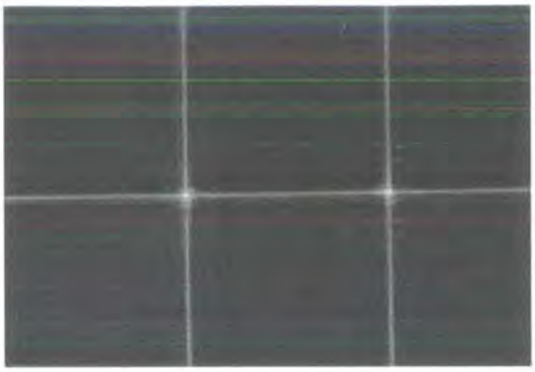

Figure 9-2. PSF of the LIMO microlenses. The intensity is on logarithmic scale. There is some stray light in the four diffraction wings of each microlens.

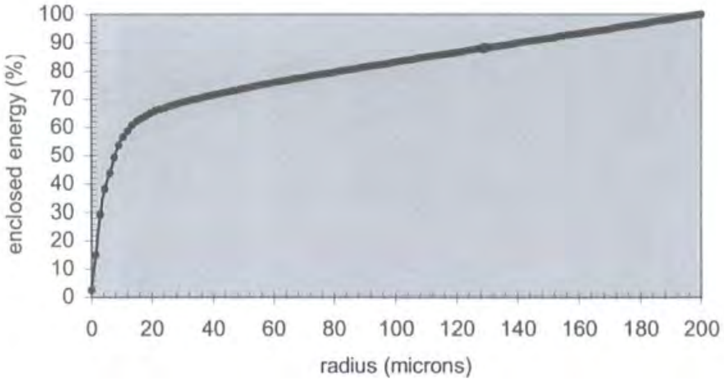

Figure 9-3. Encircled energy of the LIMO microlens. In a radius of 40 microns, there is 71 % encircled energy. It is obvious that the enclosed energy increases very slowly after a radius of 20μm.

In order to know exactly how much light can be coupled into the fibres, a test which simulated the pupil image on the microlens array back surface was also carried out. The experiment setup is schematically shown in Fig. 9-4. A screen is illuminated by a white light source. The screen is imaged onto the back surface of the microlens array where the fibres will be located for the real IFU. The iris diaphragms are used to adjust the pupil image size. The size of the pupil images was adjusted until it is exactly equal to 70 μm which is the actual pupil image size for the IFU. The light source, the screen and one of the iris diaphragms is located in a light sealed box to reduce stray light which may contaminate the measurement result. The second iris diaphragm is used to further remove stray light. The pupil images are imaged onto a SBIG ST7 16-bit CCD detector. The measurement wavelength range is 0.4 – 1.0 µm, which is limited by the detector's sensitive wavelengths. The measured pupil images are shown in Fig. 9-5. It is evident that the Limo microlens can form a sharp image (Fig. 9-5 left) due to its good PSF at the central area. However there is much stray light (Fig 9-5 right) between microlenses along the four diffraction wings of each microlens. The encircled energy of one of the pupil image is shown in Fig. 9-6. There is 61% encircled energy at the radius of 40 µm which represents the fibre core size. Because the curve is relatively flat after radius 40 µm, further increasing the fibre core size cannot collect much more light.

In order to further investigate the quality of Limo microlenses, a Zygo 5000 interferometer was used to measure the surface profiles of the microlenses. An in-stock Limo silica cylindrical lens array was purchased for the measurement to identify the quality of the Limo microlens since it was not possible to test the array used for the prototype without destroying it. The nominal surface radius of curvature and pitch are 1.0 mm and 0.4 mm respectively. The surface profile and interferogram of the measurement are shown in Fig. 9-7. The measured curvature radius of the cylinder is 1.052 mm. Compared with the nominal value of 1.0 mm, the error of the radius is about 5%. The surface roughness is 0.007 µm, which introduces about 2.5 % scattered light for each curved surface according to equation (5-3).

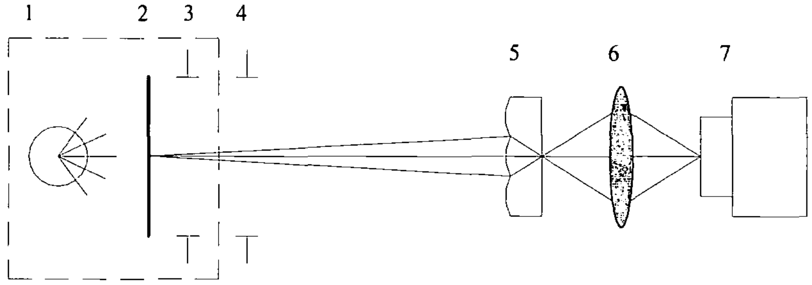

Figure 9-4. Schematic of the experiment setup for the test of the pupil image simulation: 1 – white light source. 2 – screen. 3 and 4 – iris diaphragms. 5 – test microlens array. 6 – image optics and 7 – CCD detector.

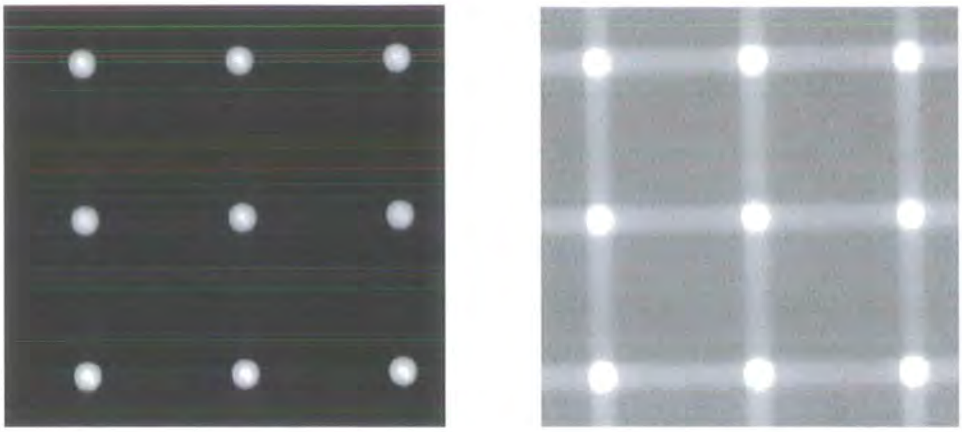

Figure 9-5. Measured pupil image. The intensity is on linear (left) and logarithmic (right) scale. The Limo microlens array can form a sharp image (see left figure), however it suffers from stray light (see right figure) which results in a low encircled energy.

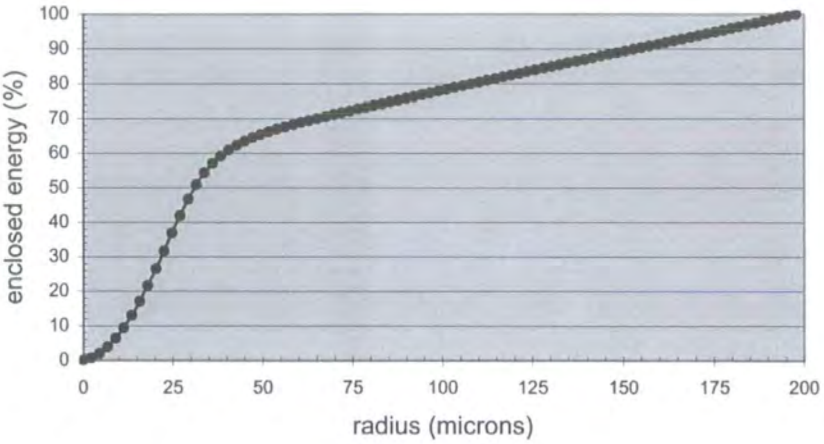

Figure 9-6. Encircled energy vs. radius of the pupil image. There is 61% encircled energy at the radius of 40 μm which represents the fibre core size.

The surface deviation was found to be a function of the measured aperture size. A measurement was carried out on the central part of the cylindrical lens, with different aperture widths and the measured results are shown in Fig. 9-8. For an aperture width of 150 μm, the surface deviations are 0.009 μm RMS and 0.051 μm PV (peak-valley), which correspond to wavefront aberrations of 0.006 RMS and 0.036 PV wavelengths at 0.63 μm, respectively. However, for an aperture of 300 μm, the surface deviations increased to 0.082 μm RMS and 0.35 μm PV, which correspond to the wavefront aberrations of 0.06 RMS and 0.25 PV wavelengths at 0.63 μm, respectively. It is obvious that at the central part of the Limo cylindrical microlens the wave aberration is very small. However, when the aperture size increases, the wave aberration increases rapidly compared with that at the central part. Unfortunately, The Zygo interferometer couldn't measure the 400 μm whole aperture due to the limitation of its numerical aperture of the objective.

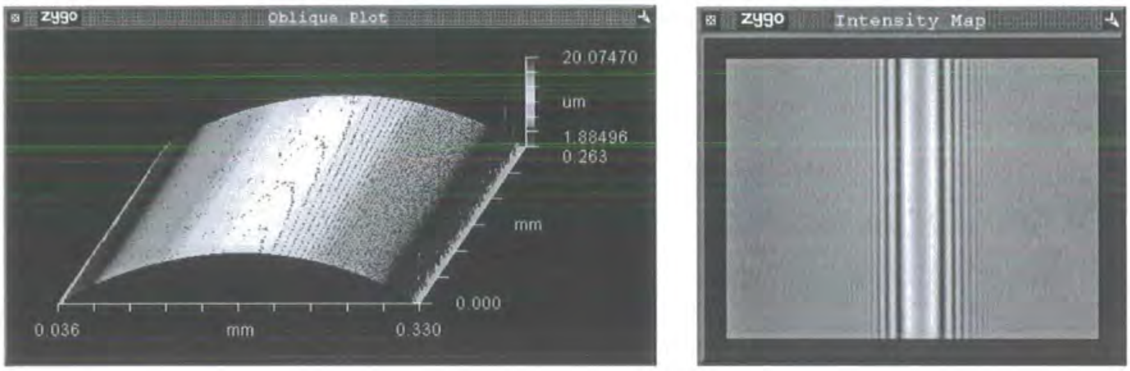

Figure 9-7. The surface profile (left) and interferogram (right) of a Limo cylindrical lens at the central part. The measured radius of curvature is 1.052 mm.

PV 0.051 um
Ra 0.007 um
rms 0.009 um
RadCrv 0.334167 m

PV 0.767 um
Ra 0.050 um
rms 0.082 um
RadCrv 0.170192 m

Figure 9-8. Surface deviation at different aperture sizes. Left: 150 μm aperture. Right: 300 μm aperture. Note that the vertical scale on the right is 10 times that on the left.

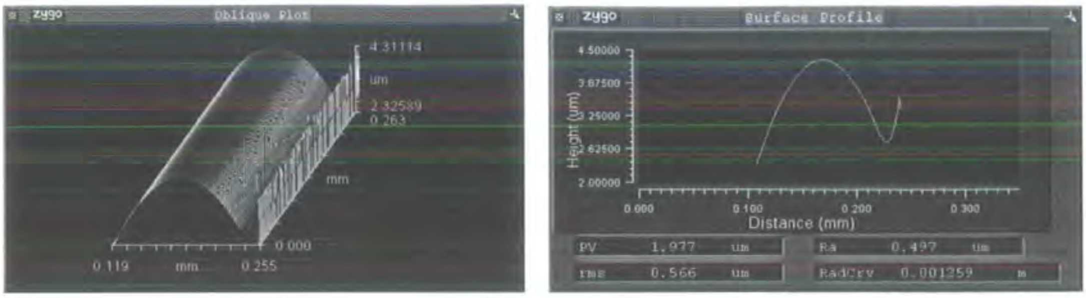

PV 1.977 um
Ra 0.497 um
rms 0.566 um
RadCrv 0.001259 m

Figure 9-9. Surface profiles at the edge of the Limo cylindrical microlens.

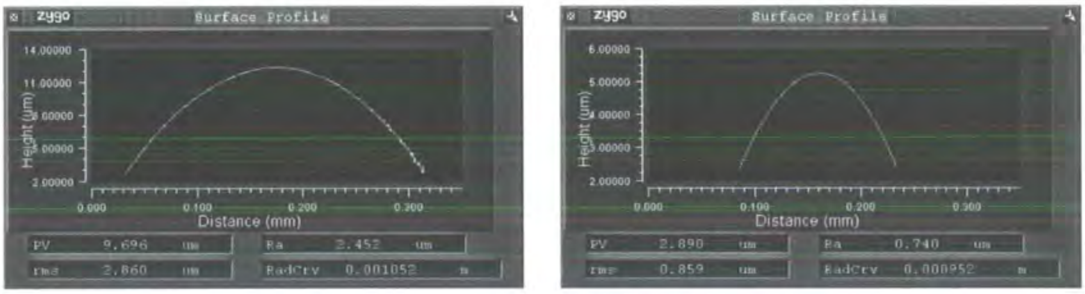

PV 9.696 um
Ra 2.452 um
rms 2.860 um
RadCrv 0.001052 m

PV 2.890 um
Ra 0.740 um
rms 0.859 um
RadCrv 0.000952 m

Figure 9-10. Surface section profiles at the centre (left) and edge (right) of the same Limo cylindrical microlens.

The fill factor is also an important issue, which may also result in low encircled energy. The surface profile at the edge of a Limo cylindrical lens was measured and the results are shown in Fig. 9-9. It can be seen that the lens-to-lens gap is about 10 μm and this is consistent with a previous measurement by microscope. The RMS and PV surface profiles don't have significant differences compared with that at the central part. However, a shift of the mean value of the curvature radius was found. The curvature radius is 0.952 mm for the same microlens at the edge, compared with 1.052 mm at the centre (see Fig. 9-10). The difference corresponds to the wavefront aberration of about 71 wavelengths at 0.63 μm.

Obviously, the surface profile accuracy between the lens-lens edge area is not consistent with Limo's quotation that the surface accuracy is $<\lambda_D/5$ and the fill factor is 92%. The measurement report was sent to Limo Gmbh and Limo agreed to re-optimise their techniques for fill factor. A second microlens array with the same specifications for the IFU was manufactured again. The encircled energy was measured again after it was received and unfortunately there was no improvement.

As a summary for the Limo microlens array, there is much stray light distributed in the diffraction wings. In Fig. 9-3, it can be see that there is about 35% stray and scattered light outside the 20 μm radius central area. The surface finishing is very good with a surface roughness of 0.007 μm, which introduces about 5 % scattered light for the two curved surfaces of the array. The lens-to-lens gap is about 10 μm, which introduces about 5% stray light. The Limo microlens array consists of 2 pieces of cylindrical arrays and the lenses are not anti-reflection coated. This introduces a stray light which is well less than 10% due to the multiple reflections between the glass-air interfaces. The rest of the lost light is caused by the aberrations due to the surface profile error and amounts to 15% -20% of the total.

9.3 IFU Fore-optics Test

9.3.1 The IFU Fore-optics Alignment and Test

To avoid significant degradation of the image quality, the IFU lenses need to be accurately aligned. Existing techniques for centring single lenses may be classified as interferometric or non interferometeric. Techniques using interferometry obtain a centring precision of up to 0.5 arcsec, but typical require sophisticated or expensive equipment (Carnell et al. 1974). Non-interferometric techniques have been reported with a centring precision of up to 5 arcsec (Khlebnikov and Salbut 1989). Jaramillo-Núñez et al. (1996) presented an apparatus which can align a doublet by using the reflected light from the alignment lens surfaces and involves the use of complex optical components.

In order to align the IFU fore-optics, a simpler apparatus based on Jaramillo-Núñez's method was derived, which uses two beams to align the lenses. The principle of the alignment apparatus is shown in Fig. 9-11. The beam from a HeNe laser is partially transmitted and partially reflected by a beamsplitter. The transmitted beam travels to a reference mirror. Part of the beam from the reference mirror is reflected toward the screen. The reference mirror is mounted on a tilt stage and adjusted until the beam is exactly reflected back to the iris diaphragm. Then the beam from the reference mirror can be used as an indication of the correction position on the screen. The reflected beam from the beamsplitter travels towards the alignment/test lens. The reflected beams from the two surfaces of the test lens are combined to form a diffraction pattern on the screen. The test lens is careful adjusted for its lateral direction and tilt angle until the reflected beams from the reference mirror and the centre of diffraction pattern are as close as possible on the screen and the distance between the reference beam and the diffraction pattern then can be used as an indication of the decentre of the two surfaces of the test lens and the tilt angle can be calculated according to the geometry of the triangle. A neutral density filter can be used to adjust the light intensity from the reference mirror. After the first alignment lens is finished, more lenses can also be added into the optical path for alignment.

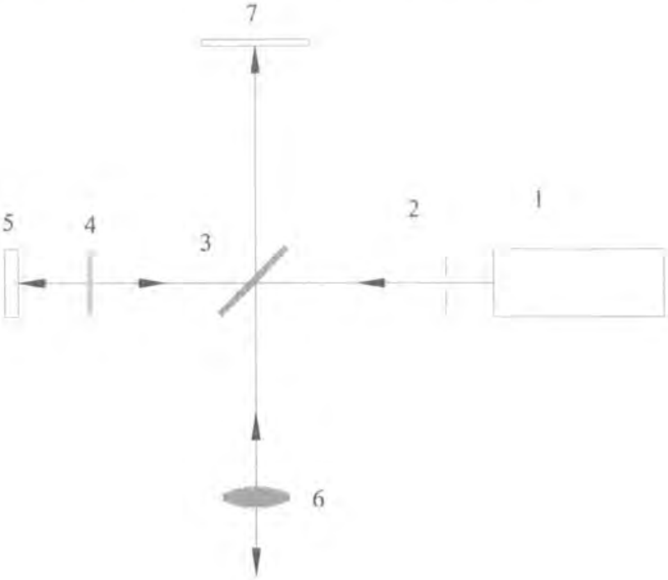

Figure 9-11. The schematic of optical lens alignment apparatus: 1 – HeNe laser light source. 2 – iris diaphragm. 3 - Beam splitter. 4 – neutral density filter. 5 – reference mirror. 6 – alignment lens. 7 – screen.

The fore-optics lenses were first mounted on individual translation and tilt stages to test the manufacture accuracy of the lens and the image quality of the fore-optics. The IFU alignment procedure is as following. First the telecentric lens was added into the optical path for alignment. The test lens was aligned by adjusting its lateral positions and tilt angle until the centres of the diffraction pattern from the test lens surfaces and the beam from the reference mirror were as close as possible on the screen and the diffraction ring was symmetrical (Fig. 9-12(a)). Then the doublet was added into the optical path behind the telecentric lens and was aligned in the same way. Finally the prism/lens assembly was aligned until the centres of the diffraction pattern formed by the reflected light from each surface were as close as possible (Fig. 9-12 (b)). The tilt angle error can be worked out from the distance between the diffraction pattern centres. At the centre of the diffraction pattern, there are two small bright spots which are reflected from the doublet and prism lens, respectively. The tilt angle between the lenses was thus measured to be about 5 arcsec, which is also at the limitation of this test apparatus. This is very close to the allowed manufacture error of each lens which is 3 arcsec, so the lens manufacture quality is considered to be good. Fig. 9-13 shows the alignment apparatus. The beamsplitter can be clearly seen.

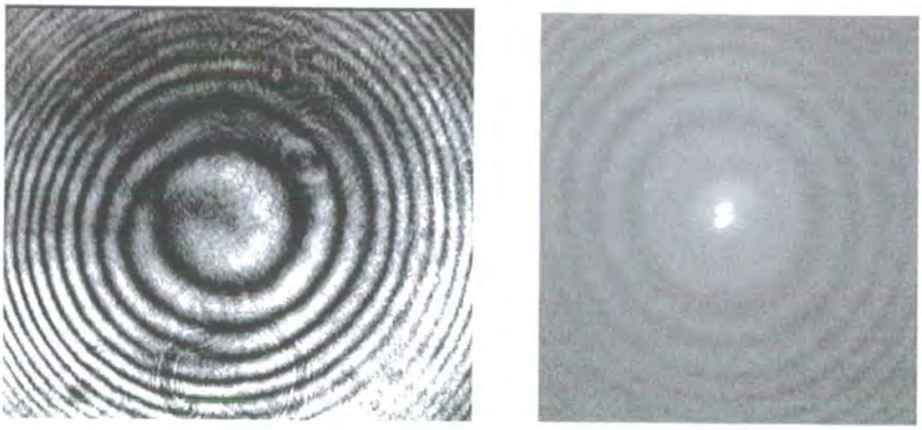
(a) (b)

Figure 9-12. Diffraction pattern formed by the two surfaces of the telecentric lens (a) and diffraction pattern from the whole fore-optics lenses (b).

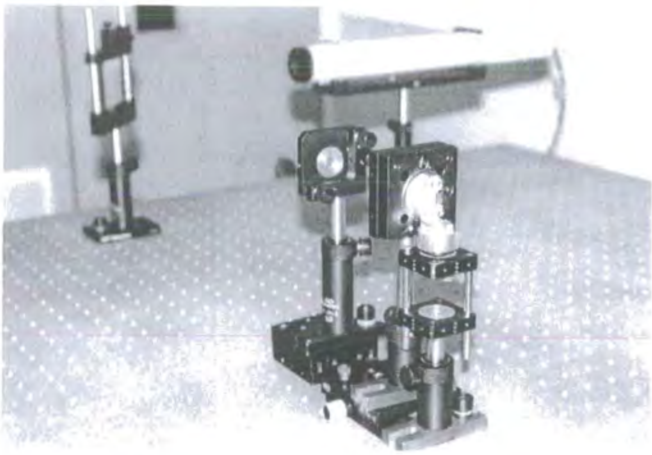

Figure 9-13. The experiment set-up for IFU lens alignment. The reference mirror is at the left, outside the picture.

After finishing the fore-optics alignment, the sky image PSF and pupil image PSF of the fore-optics were measured and compared with the theoretical tray tracing and no inconsistency was found. More details about how to test the sky image and pupil image qualities will be discussed in the next subsection.

9.3.2 The Construction and Test of the Fore-optics

For the IFU fore-optics, the prism and SK2 lens need to be glued together with a pinhole sandwiched between them. The SK2 flat surface was first applied with a drop of Norland 61 UV-curable adhesive. The pinhole was then located on the SK2 flat surface. The position of the pinhole on the SK2 lens surface was checked on the X-Y translation stage of a microscope until the alignment error was less than +/-0.1mm in lateral direction. The SK2 lens and pinhole were cured by exposure to UV light. Extra adhesive was removed by acetone. The SK2 and pinhole were then glued with the prism right angle face by using Norland 61 again. The prism and SK2 were carefully aligned on the microscope until the central position accuracy of the SK2 lens on the prism was better than +/- 0.1mm. The prism and SK2 interface were also carefully checked using the microscope to make sure that there was no air bubble and then the optimum position was fixed by exposing the adhesive to the UV light.

After the prism lens was made, it was glued to a short tube using Norland 61 adhesive. The SK2/F5 doublet was mounted to the short tube from the other end by a screw. There is an aperture stop in the short tube (see Fig. 8-6), which can reject any light that is faster than F/2. The photograph of the sub-assembly is shown in Fig. 9-14.

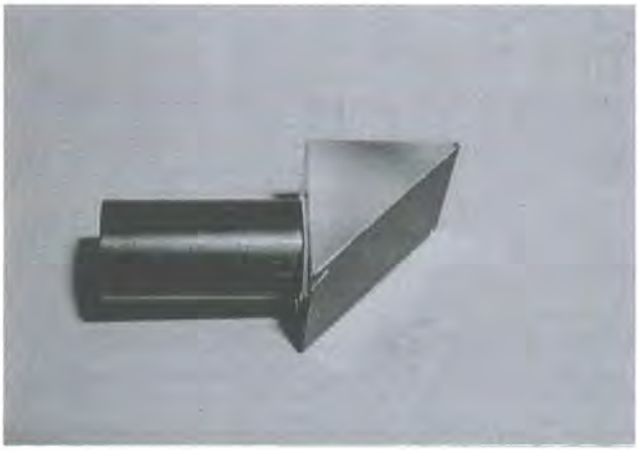

Figure 9-14. The sub-assembly of prism lens and doublet.

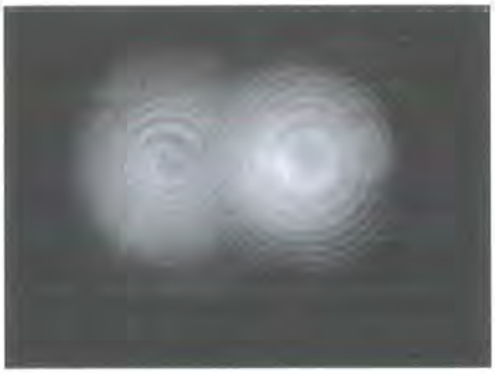

Figure 9-15. Diffraction rings of the sub-assembly. The tilt angle error is about 34 arc minutes.

The tilt angle error was measured using the same method discussed in the previous subsection. The diffraction patterns from the doublet and prism lens surfaces are shown in Fig. 9-15. The distance between the two diffraction rings is about 40mm and the distance between the measured lenses and the screen is about 4000mm. The tilt angle error therefore is 34 arc minutes. Compared with the measured results of the previous subsection, this tilt angle is obviously caused by the mechanical manufacture error of the short tube. However, the 34 arc minutes tilt error is still acceptable because according to tray tracing, the image quality of the IFU fore-optics is still diffraction-limited in this case. The tilt angle error of the telecentric lens does not need to be measured as tray tracing shows that the fore-optics image quality is not sensitive to the alignment error of this lens, and the image is still diffraction-limited even if the alignment error is as large as 5 degrees.

All fore-optics lenses are installed in a long aluminium black tube (see Fig. 8-6 for the drawing). In order to ensure that the sky image is telecentric, the IFU fore-optics needs to be aligned after all the optical lenses (not including microlens array) are assembled in the tube. The alignment principle is schematically shown in Fig. 9-16. The input collimated laser beam is fed to the prism lens. The output light emitted from the telecentric lens should be collimated if the fore-optics is telecentric. The principle of how to ensure telecentricity was discussed in Chapter 8 in detail. The key point is to ensure the two groups of lens L1 and L2 have the same focal point in Fig. 8-1. For the actual IFU fore-optics, this can be done by adjusting the axial position of the sub-assembly which consists of the prism lens and the doublet. The sub-assembly was mounted in a short tube which could be slid in the long fore-optics tube until the output light was also collimated for a collimated input light. The short tube was then fixed by two screws in the long tube. The non-telecentricity is less than 1.7 arc-minutes after the alignment, which corresponds to a pupil position shift of less than 1.4 μm. The finished fore-optics is shown in Fig. 9-17.

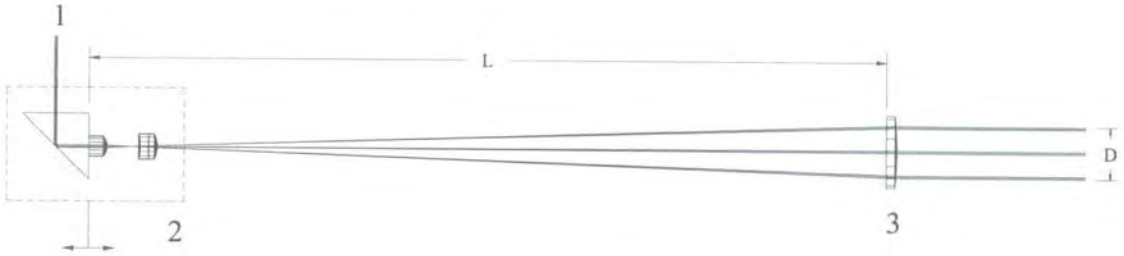

Figure 9-16. Schematic of the fore-optics alignment principle. 1- input collimated HeNe laser light. 2- sub-assembly. 3- telecentric lens. The sub-assembly can be slide along optical axis to ensure the output beam is telecentric.

Figure 9-17. The finished IFU fore-optics assembly. The short tube of the sub-assembly was fixed by two screws.

The fore-optics image quality test was done after the fore-optics was aligned. The PSF of the pupil image was measured using the Limo microlens array which was designed and manufactured for the IFU. The principle to test the PSF of the fore-optics pupil image is shown in Fig. 9-18. Collimated laser light is input on the prism and the PSF of the pupil image is formed on the back surface of the microlens array. The PSF is then collimated by a travelling microscope and focused onto a CCD detector by an imaging lens. Figure 9-19 shows the PSF of the pupil image at the fore-optics field edge. The test was done on the whole field and no difference was found. It is clear that the PSF of fore-optics pupil image is diffraction limited over the whole field.

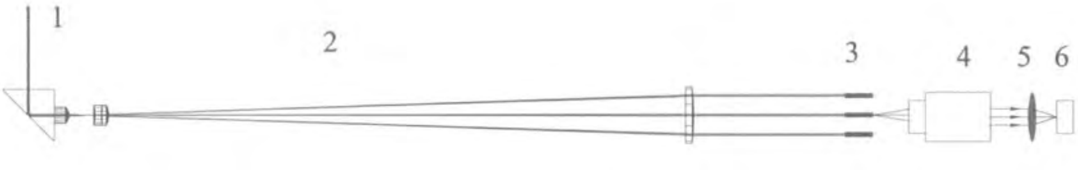

Figure 9-18. Schematic of the apparatus to test the PSF of the pupil image. 1- collimated HeNe laser light. 2- fore-optics. 3- microlens array. 4- travelling microscope. 5- imaging lens. 6- CCD detector.

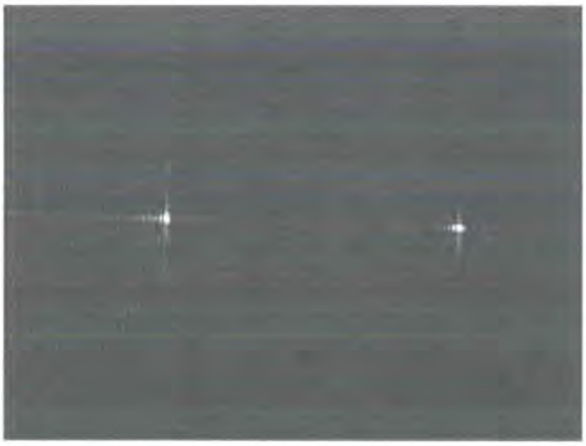

Figure 9-19. The PSFs of pupil image near the fore-optics field edge. The image is diffraction-limited.

Figure 9-20. Schematic of IFU sky image test. 1- Collimated HeNe laser light. 2- microscope objective. 3- IFU fore-optics. 4- Limo microlens array (only one lenslet is shown). 5 –travelling microscope. 6- imaging lens. 7- CCD detector.

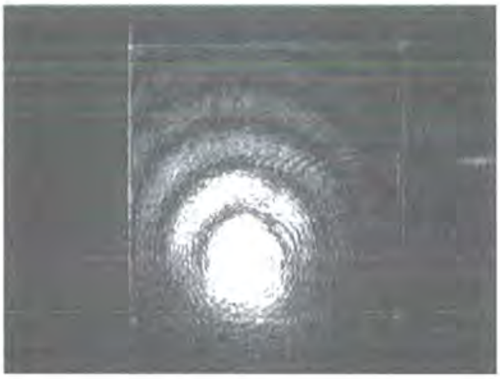

Figure 9-21. The PSF of the sky image formed on the curved surface of the Limo microlens array. The PSF is over exposed in order to clearly shown the square aperture of the microlens.

The test for the sky image is to compare the theoretical and actual image quality. The test apparatus is schematically shown in Fig. 9-20. The telescope sky image was simulated by using a high quality microscope objective. The telescope PSF was then magnified by the fore-optics and the PSF was formed on the microlens input curved surface. The microscope objective can only simulates a F/3 telescope image rather than the corrector F/2 of Subaru. The telescope focal plane is about 10mm below the prism. In this case, the image quality should be diffraction-limited. The measured IFU fore-optics PSF is shown in Fig. 9-21. The test image is close to diffraction-limited and the diffraction wings can be seen. The actual PSF of the sky image is close to the theoretical simulation. Considering we require that two microlenses sample the PSF of the sky image, the image quality of the fore-optics is good enough.

9.4 The Construction and Test of the Fibre Bundle

The fibre bundle is a key component of the IFU. The positions of the fibres on the input face of the bundle are decided by the microlens array. The fibres are packed in a square pattern. There are 15 rows each containing 15 fibres. The pitch is 400 μm. Each row is terminated to a sub-slit containing 15 fibres. There was no specific requirement for the slit end at the time when the IFU was constructed. So we did not require that the sub-slits could be assembled into a complete slit. For this reason the sub-slit assemblies are quite long.

The fibre bundle was made by AndaOptec Inc according to our requirements. The measurement for fibre position was carried out after the fibre bundle was received. The photograph of the fibre bundle is shown in Fig. 9-22 and the finish quality is excellent. The fibre position measurement was done by back illumination of the sub-slits by HeNe laser light. The bundle input was mounted on the translation stage of a microscope. The image of the end face of the bundle input can be visually observed on the eyepiece. The position of each fibre on the end face can be read out with the help of the translation stage and reticule. The distributions of the position error were measured and the result is shown in Table 9-1. Compared with the required specification of 8 μm maximum position error, it is obvious that the fibre bundle meets the requirement.

Figure 9-22. The photograph of the fibre bundle.

Table 9-1. The fibre position error distribution on the input face of the fibre bundle.

	Error: 0 μm	Error: 1 μm	Error: 2 μm	Error: 3 μm	Error: 4 μm	Error: 5 μm	Error: 6 μm	Error: 7 μm	Error: 8 μm
Row1: Number	0	4	5	2	2	1	0	0	0
Row2: Number	1	3	1	3	5	0	0	1	0
Row3: Number	1	1	4	2	4	1	1	0	0
Row4: Number	2	1	4	1	0	3	1	2	0
Row5: Number	0	4	3	2	2	2	1	0	0
Row6: Number	1	3	4	2	1	1	1	1	0
Row7: Number	2	4	2	1	2	1	1	1	0
Row8: Number	2	2	2	5	1	1	0	1	0
Row9: Number	2	2	4	1	0	2	0	2	1
Row10: Number	1	0	1	5	3	1	3	0	0
Row11: Number	0	3	3	1	3	4	0	0	0
Row12: Number	1	6	2	3	1	1	0	0	0
Row13: Number	3	1	3	3	2	2	0	0	0
Row14: Number	1	3	4	2	1	1	0	1	1
Row15: Number	1	2	6	2	2	1	0	0	0
Total: Number	18	39	48	35	29	22	8	9	2
RMS error	3.4 μm								

The fibre FRD is a concern, since AndaOptec cannot guarantee it. Fibre FRD was not measured for VIMOS fibre bundle, which was also manufactured by AndaOptec (Prieto et al. 2000). A test to measure the FRD of the fibre bundle is therefore necessary. To measure the FRD properties of a fibre it is necessary to illuminate the test fibre with an input beam of known focal ratio. The output beam can then be measured to determine the amount of the focal ratio degradation produced by the test fibre. The experiment setup is shown in Fig. 9-23. The collimated HeNe laser light is focused by a camera lens. The focused light is coupled onto an individual fibre on the input face of the fibre bundle which is installed on a XYZ and tilt stage for the fine adjustment. An iris diaphragm placed in the collimated beam is used to define the input focal ratio (here it is F/5). At the output end of the test fibre, a SBIG ST7 CCD detector is used to record the far field image of the test fibre. The output end of the test fibre is located on the window of the CCD detector. The relationship between the displacement on the detector and F ratio can be calibrated by locating the detector window on the focal point of the input F/5 beam, i.e. on the focal plane of the camera lens, after the input fibre is removed. A re-imaging system which consists of a re-imaging lens and microscope produces a magnified image of the input face fibre, which allows the input beam to be accurately positioned with respect to the test fibre by means of observation on the microscope. The re-imaging is also necessary for accurately locating the detector window on the focal point of the input beam for the calibration. A background exposure is also taken for subtraction from the test exposure to remove background stray light and detector noise.

As the fibre bundle is fed by the F/5 input beam, the FRD test measures how much encircled energy there is at output focal ratio of F/5 and F/4.5. The far field image of the output fibre end is shown in Fig. 9-24 when the focal ratio of the input beam is F/5, and the plot of encircled energy versus output focal ratio is shown in Fig 9-25. There is 80% and 90% at the F/5 and F/4.5 cone angle at the output end, respectively, which is an acceptable value.

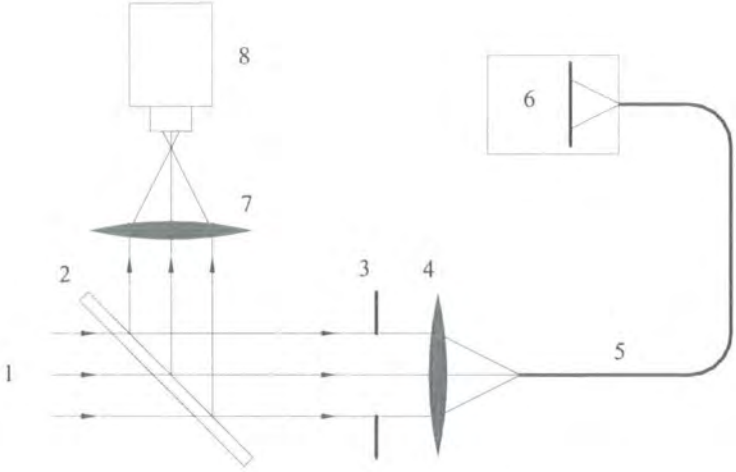

Figure 9-23. Schematic of experiment apparatus used for the measurement of the fibre FRD. 1- collimated HeNe laser light. 2- beam splitter. 3- iris diaphragm. 4-camera lens. 5- test fibre. 6- CCD detector. 7- re-imaging lens. 8- travelling microscope.

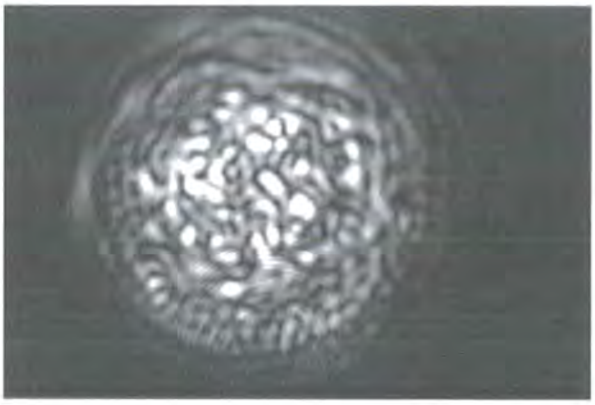

Figure 9-24. Far field image of the fibre output end, measured with a F/5 input beam.

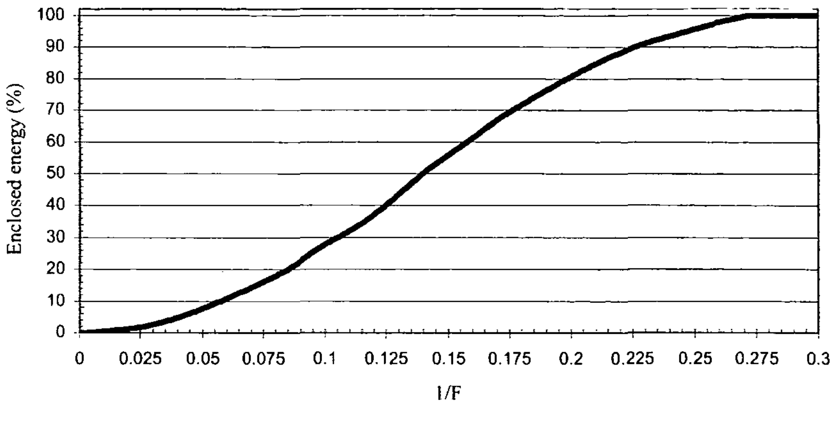

Figure 9-25. Plot of encircled energy vs. output focal ratio. The input beam is F/5. There is 80% and 90% at the F/5 and F/4.5 cone angle at the output end, respectively.

9.5 The Assembly of Microlens Array and Fibre Bundle

In order to avoid light loss due to misalignment and Fresnel reflection, the Limo microlens array and fibre bundle need to be careful aligned and glued together by adhesive. The assembly accuracy of microlens array and fibre bundle is very important to avoid light loss in the coupling between microlenses and fibres. As discussed in Chapter 8, to avoid light loss, the allowed alignment error between the microlens array and fibre bundle must be less than 3.5 μm RMS. An alignment method was introduced by Kenworthy and Parry (2001), which illuminates the back end of the fibre bundle. The light emitted from the fibre bundle input can be used for the alignment.

A modification based on the above method was used for the alignment of the IFU and the optical principle is schematically shown in Fig. 9-26. The fibres are illuminated by white light from the back end (sub-slit end). The images of the fibres on the fibre bundle input face are magnified and imaged onto the focal plane of a CCD camera by an imaging lens. The fibre images are overlapped on the CCD focal plane and form a common image if the microlens array and fibre bundle are well aligned. Any alignment error between microlens and fibre will be presented as a shift of the fibre image position relative to that of other fibres on the CCD focal plane and therefore can be used as an indication of the alignment error. The magnification of the image is decided by the ratio of the focal length of the imaging lens and that of the microlens. The focal length of the imaging lens is 25 mm and the focal length of the microlens is 2.8 mm, which yields a magnification of 8.9. Therefore the image size is 0.7 mm for the 80 μm fibre core and this is a suitable size to be recorded by the CCD. The CCD image is displayed on a monitor and is used as an indication for the alignment.

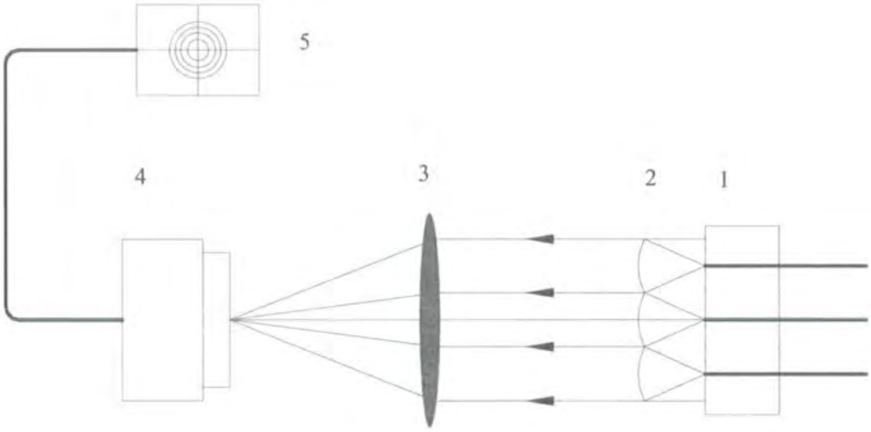

Figure 9-26. Schematic of the optical system for the alignment of microlens array and fibre bundle: 1- fibre bundle. 2- microlens array. 3- imaging lens. 4- video CCD camera. 5- monitor.

Figure 9-27. Fibre pupil image which is used to defined the optical axis of the fibre bundle.

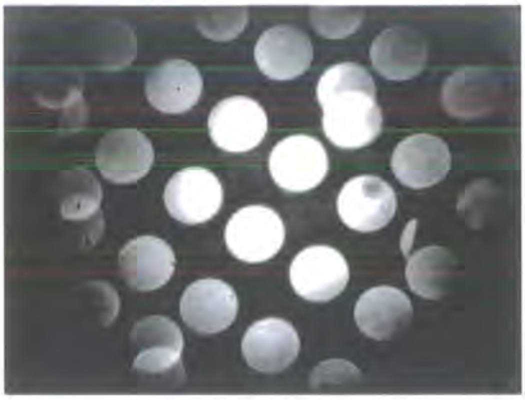

Figure 9-28. Photograph of the fibre images on the CCD before alignment. Note that each image size corresponds to 80 μm of the fibre core on the input face of the fibre bundle.

The first step of the alignment process is to define the optical axis of the fibre bundle, which is of great importance because all the fibre images need to be aligned to the optical axis in the alignment process. The microlens array is removed from the optical path in Fig. 9-26. One row of the fibres in the centre of the fibre bundle input face is back illuminated because other fibres located on the edge of the fibre bundle may introduce vignetting on the imaging lens. The image lens brings all the light of the illuminated fibres of this row onto the focal plane where the pupil of the test imaging system is located. The fibre pupil image is recorded by the CCD camera and is shown in Fig. 9-27. The centre of the fibre pupil image defines the optical axis of the fibre bundle. A transparent film with crosshair graticule on it is glued on the monitor. The centre of the graticule is located on the centre of the fibre pupil image and therefore can serve as the optical axis for the alignment.

After the optical axis is defined, a drop of Norland 61 is applied to the face of the fibre bundle input face. The face of the fibre bundle is held horizontally facing upward, and the Limo microlens array is placed on it for the manual alignment (Fig. 9-26). Only two rows of the fibres at the two edges of the fibre bundle face are back-illuminated at first. Before alignment, the images of the illuminated fibres do not overlap, as shown in Fig 9-28. The microlens array is carefully tilted and laterally moved until all the images overlap to form a common image and the centre of the common image is on the optical axis of the fibre bundle, which is also the centre of the graticule. Then each row of fibres is back illuminated separately to check the fibre image position until the image position error is less than that of the requirement. The microlens array and fibre bundle assembly is then cured by exposure to UV light. Fig. 9-29 is the common image of the two rows of fibres after alignment. The size of the fibre image is 12 divisions on the crosshair, which corresponds to 80 μm of the fibre core, so each division corresponds to an alignment error of about 7 μm between microlens and fibre and the alignment error can be read out from the shift of each fibre image to the optical axis on the crosshair. The maximum alignment error is about 7 μm which implies that the alignment error is less than 3.5 μm RMS. The photograph of the finished microlens array and fibre bundle assembly is shown in Fig. 9-30.

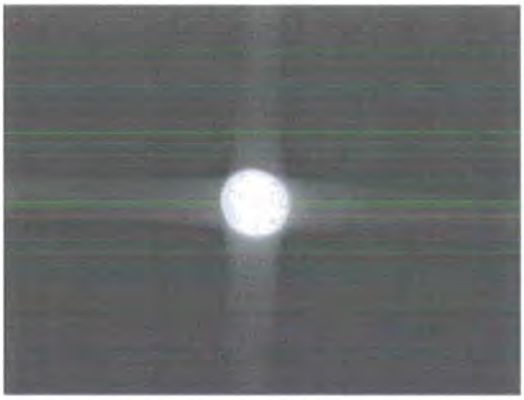

Figure 9-29. Photograph of the fibre images on the CCD after well alignment. All the fibre images are overlapped to form a common image.

Figure 9-30. Photograph of the finished microlens array and fibre bundle assembly.

Further improvement can be achieved if a specially designed XY and tilt mechanism is used for the accurate position control in the alignment process and if software is used to fit the central position of the fibre pupil image. These are not considered in this test because of the limitation of time.

9.6 IFU System Performance

The reflection loss is assumed to be 98% for each microlens or fibre surface. From Fig. 9-6, the Limo microlens can couple 61% enclosed energy onto the fibre with 80 µm core diameter and this results in a coupling efficiency of 57.4% for the microlens and fibre assembly if the assembly error of the microlens array and fibre bundle is assumed to have no effect on the coupling efficiency. Because the assembly error is less than 3.5 µm RMS and the fibre core is oversized compared with the pupil image, the microlens array and fibre bundle assembly error will therefore have no significant effect on the coupling efficiency.

The estimated performance of the IFU based on the measurement of its components is listed in Table 9-2 and the optical surfaces of the fore-optics are assumed to be anti-reflection coated. Compared with the theoretical estimation of the IFU system performance (see Table 8-4), the only difference of the measurement performance is the efficiency of the microlens array and fibre bundle assembly and this is due to the low quality of the microlens array. The IFU efficiency is therefore dominated by the quality of the microlens array.

Table 9-2. Measurement performances of the IFU

IFU optics efficiency (not include microlenses)	88.5%
Microlens array and fibre bundle efficiency	57.4%
IFU efficiency η	50.7%
Figure of merit (Q)	34%

High quality microlens arrays are available and an interesting question is to replace the Limo microlens array with a high quality microlens array, such as Epigem microlens array. The Epigem microlens array was discussed in Chapter 5. It is possible that an Epigem microlens array and fibre bundle assembly will deliver an efficiency of 85%. In this case, the IFU efficiency (or throughput) may be as high as up to 70%.

9.7 Summary & Conclusions

In this chapter, tests of the fore-optics, microlenses and fibre bundle were discussed. The qualities of these key elements are very important for the performance of the whole IFU system.

The image quality of the fore-optics is consistent with ray tracing. The sky image is nearly diffraction-limited and the pupil image is diffraction-limited. Non-telecentricity is less than 1.7 arc-minutes which corresponds to a pupil position shift of less than 1.4 μm.

The performance of the IFU is dominated by the image quality of the Limo microlens array. Many tests were done to characterise the microlenses. The poor quality of the microlens is mainly caused by the surface shape deviation near the edge area of each microlens.

Measurements for the position accuracy and the FRD of the fibre bundle were also carried out. The position accuracy is excellent, with a position error of 3.4 μm RMS. The fibre FRD is acceptable, with 80% encircled energy at F5 on the output end for a F/5 input beam.

A method for the alignment of microlens array and fibre bundle assembly was also described. This can ensure an assembly position accuracy of 3.5 μm RMS.

Finally, the IFU system performance was also estimated using the measurements described above and was compared to that of the theoretical estimation. The measured performance is worse than that of the theoretical estimation due to the poor image quality of the Limo microlens array. The IFU efficiency (or throughput) is 50.7%. However, the IFU performance can be improved by the use of a high quality microlens array and the efficiency may reach 70% if an Epigem microlens array is used.

Chapter 10

Design and Construction of FMOS Fibre Bundle Connector

Abstract

A prototype of a fibre bundle connector for FMOS project is described. The fibre bundle connector provides the function of connection and disconnection in the fibre trains. It also provides a more important function of converting the focal ratio from F/2 to F/5 because F/2 is too fast either for good transmission of light along a substantial length of fibre, or for the FMOS spectrographs. The fibre bundle connector consists of 100 coupling fibres. It works over the full 0.9 – 1.8μm wavelength range and the chromatic aberration is well corrected in the design. The design principle and the construction of the fibre bundle connector are discussed. The measured coupling efficiency is up to 88%. The coupling efficiency is compared with that of the theoretical estimation and good agreement is achieved. Finally, further possible improvement is also discussed.

10.1 Introduction

The fibre connector was first used for optical fibre communication system (Tomlinson 1980) where the connector only works at monochromatic wavelength or over a narrow wavelength band. The connector losses range from 10 % - 40 % depending on the techniques (Lacy 1982). Normally, each connector consists of a source fibre and a receiving fibre (Szostak 1987, Kurata et al. 1987). These techniques are limited to build 2-D fibre bundle connector which needs to couple a large number of fibres simultaneously. V-groove techniques (Chang et al. 1987, Sammueller 1984) were also used to build linear multi-fibre connectors, however the coupling efficiency is not known. Most of these connectors only use bare fibre and no lenses are employed so cannot convert the focal ratios to the required value at the receiving fibre.

There is very little published work on the use of fibre connectors for astronomical instrumentation. A fibre connector was developed at the Anglo-Australian Observatory, which couples the light from one source fibre to 7 receiving fibres and delivers 45% throughput (Lee and Taylor 2000).

FMOS is a fibre-fed spectroscopic facility for the 8m SUBARU telescope. The first phase of this system will consist of a multi-object fibre positioner (Echidna), a fibre bundle connector and two near infrared (NIR) spectrographs. At the SUBARU F/2 prime focus, the Echidna positioner will provide a multi-object mode for 400 fibres. The spectrographs are located off the telescope, since the whole system would be too large for a prime focus instrument, and will be located on the observing floor. This necessitates a break in the fibre train so that the prime focus instrument can be stowed in the instrument storage room when the system is not in use. Another important function of the fibre connector is to convert the focal ratio from F/2 to F/5 because the F/2 is too fast either for good transmission of light along a substantial length of fibre, or for the spectrographs. There are 400 fibres needed to be coupled so 4 fibre bundle connectors are needed if each one couples 100 fibres. A more detailed description of FMOS can be found in Dalton et al. (1999) and Maihara et al. (2000).

In this chapter, a prototype of the fibre bundle connector, which consists of 100 coupling fibres, is described. The optical design of the fibre bundle connector is discussed first, then the coupling efficiency is analysed when optical aberration and alignment error are present. The construction of the fibre bundle connector is then described. Finally the measurement of the coupling efficiency is carried out and compared with the theoretical estimation and further possible improvements are indicated.

10.2 The Design Philosophy of the Fibre Connector

Techniques for coupling light from a source fibre to a receiving fibre have been discussed by Nicia (1981) for the applications of communication system. The light from the source fibre is first collimated by a collimating lens, and then focused onto the receiving fibre by a focusing lens. In Nicia's discussion, the collimating lens and the focusing lens are of the same focal length, so the light is coupled onto the receiving fibre at an image magnification of 1 and the focal ratios are the same for both the source and receiving fibres. Different lenses, i.e. planar-curvature microlens, ball lens and gradient refractive index lenslet can be used. However, no discussion about fibre Focal Ratio Degradation (FRD) or non-conservation of the $A\Omega$ (the area and angle product) is included in Nicia's paper.

For an astronomical spectrometer, the non-conservation of AΩ product will result in either a low spectral resolution, or light vignetting loss because of the large output cone angle when the light is fed to a spectrometer.

Based on Nicia's method, a method is presented, which can be used to couple light from the source fibre to the receiving fibre and convert the focal ratio to the required value. At the same time, the AΩ product is conserved everywhere at the fibre end face. The principle is shown schematically in Fig. 10-1. The foci of the collimating lens and focusing lens are coincident. The focal ratio conversion is achieved by choosing different focal lengths for the collimating lens and focusing lens, respectively. Note that the chief rays which are parallel to the optical axis on the source fibre end face are still parallel to the optical axis after being coupled onto the receiving fibre end face, so the AΩ product is exactly conserved everywhere on the fibre entrance face. This means that no extra FRD is introduced in the coupling process.

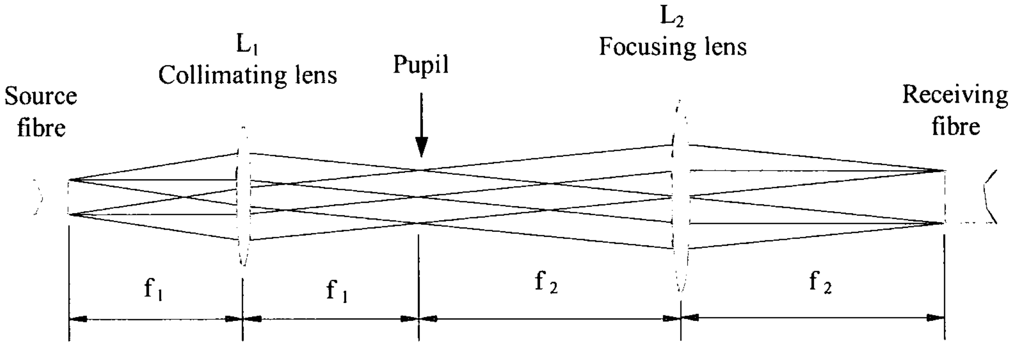

Figure 10-1 Schematic of fibre coupling by lenses. The light from source fibre is collimated by lens L_1 (collimating lens) and focused by L_2 (focusing lens) onto the receiving fibre. The AΩ product is exactly conserved everywhere on the receiving fibre entrance end face.

From Fig. 1, the magnification M is given by

$$M = \frac{D_2}{D_1} = \frac{F_1}{F_2} = \frac{f_2}{f_1} \qquad (10-1)$$

Where D_1, F_1 and f_1 are the source fibre diameter, focal ratio and focal length of the collimating lens, respectively. D_2, F_2 and f_2 are the receiving fibre diameter, focal ratio and focal length of the focusing lens, respectively.

For FMOS, as F_1=2.0 and F_2=5.0, so this requires M=2.50, i.e., $f_2=2.5f_1$.

10.3 Optical Design

Selfoc lenses were chosen for the FMOS fibre bundle connector due to their low cost and high image quality when working in a fast beam (F/2). The Selfoc lens is a radial gradient index lens. The fabrication process of Selfoc lens has been described by Miyazawa et al. (1980). Other lenses, such as conventional spherical lenses were also investigated and were excluded because of their poor image quality at F/2. Ball lenses are not acceptable because they introduce more air-glass interfaces in the connector, which will result in a low coupling efficiency because of the losses due to Fresnel reflection. Selfoc lenses have been used to couple light to multi-mode fibre for the applications of communication (Tomlinson 1980, Palais 1980, Sakamoto 1986). According to the Selfoc product sheet, the transmission can reach 99.5% depending on coating for a 5 mm thickness blank in the wavelength range 400-2000nm. A 0.25 pitch is chosen because these can be used as collimating and focussing lenses and the fibres can be glued on one of the lens faces. For a 0.25 pitch lens, the focal length can be expressed as

$$f = \frac{1}{N_0\sqrt{A}} \qquad (10-2)$$

Where, A=squared gradient constant. N_0=on-axis refractive index.

Obviously, the focal length of the Selfoc lens is decided by the gradient index material. By careful choices, it is found that the combinations of a Selfoc SLW 1.0 0.25 gradient-index lens and a Selfoc SLS 2.0 0.25 gradient-index lens can yield a ratio of focal length that is equal to 2.50. For SLS 2.0 0.25 lens, $\sqrt{A}$=0.243 and N_0=1.5569, which yields a focal length f_2=2.643mm at 0.83μm. For SLW 1.0 0.25 lens, $\sqrt{A}$=0.601 and N_0=1.5986, which yields a focal length f_1=1.0408mm at 0.83μm.

Figure 10-2 The optical layout of the FMOS fibre bundle connector (only one pair of coupling lenses is shown). The collimating lens is a SELFOC SLW 1.0 0.25 gradient-index lens. The focusing lens is a SELFOC SLS 2.0 0.25 gradient-index lens. The gap between the two lenses is about 0.4mm.

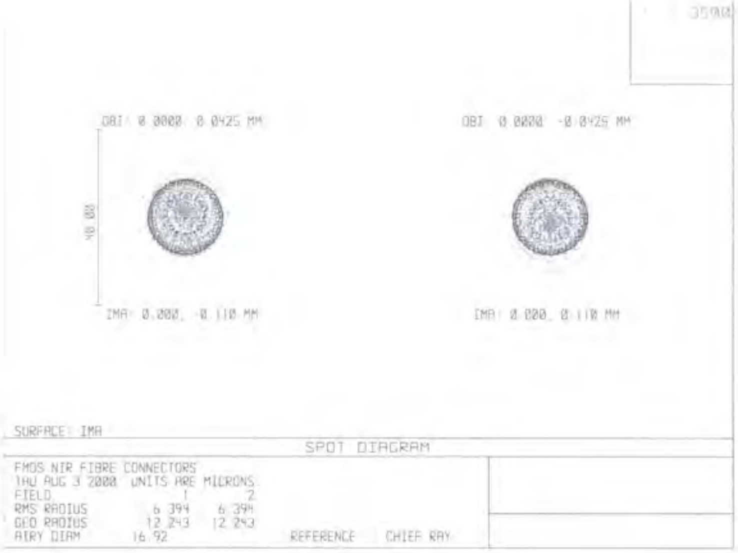

Figure 10-3 Ray-traced spot diagram of the fibre bundle connector. The image quality is diffraction or nearly diffraction limited over the whole wavelength range. The RMS spot radius is about 6.5 μm.

The optical layout of the fibre connector is shown in Fig. 10-2. The pupil is located on the back end face of the focussing lens and with a diameter of about 500 μm. To reduce the losses due to Fresnel reflections, the source and receiving fibres can be glued on the flat end face of the collimating and focussing lenses, respectively. There are two air-glass interfaces between the collimating and focusing lenses, with a gap of 0.4mm between the two lenses. The spot diagram of the optical aberration is shown in Fig. 10-3. The design is optimised in the wavelength range of 0.9 –1.8 μm. The Selfoc lenses have strong chromatic aberration in visible wavelengths, but this is not so serious in NIR. This has been confirmed by ray tracing. The 0.25 pitch Selfoc lenses have different lengths, which correspond to different optimised working wavelengths. The optimisation in the NIR wavelength range for the fibre bundle connector is therefore to choose a suitable combination of the collimating and focusing lenses. From Fig. 10-3, it is clear that the image quality of this system is very uniform in the 0.9-1.8 μm wavelengths with only a slight degradation at the blue end.

Summary of the lens specifications (form Selfoc lens catalogue):

Collimating lens: SELFOC SLW 1.0 0.25 0.83 gradient-index lens:
Lens diameter 1.0 +/- 0.010mm.
Focal length: 1.041mm.
Lens length 2.612 +/- 2.5 %.

Focusing lens: SELFOC SLS 2.0 0.25 0.83 gradient-index lens;
Lens diameter 2.0 +/- 0.010mm.
Focal length: 2.589mm.
Lens length 6.466 +/- 2.5 %.

Image magnification: The image is magnified 2.50 (F/2 -/F5).

Where the 0.83 designation means that the lens is optimised at 0.83 μm wavelength.

An actual measurement shows that the tolerances of the lenses are much smaller than that given in the catalogue: The actual variations of the lens diameter are about 6 μm. The small tolerance makes it possible to use a high precision sleeve to centre the lens and fibre accurately. Compared with conventional lenses, the ease of alignment due to the cylindrical shape of the lens is an important advantage of the Selfoc system. Any alignment error will result in a low coupling efficiency, as will be discussed in a later section.

10.4 The Choice of the Receiving Fibre Core Size

The fibre bundle connector may suffer from a low coupling efficiency because of optical aberration. For the FOMS fibre bundle connector, the source fibre core size is 85 microns.

According to ray tracing, the ideal image size of this fibre core diameter is 220 microns on the back end face of the focussing lens. The maximum RMS spot radius due to optical aberration is σ=6.5 μm (see Fig. 10-3). The ideal image of the source fibre will be broadened by the optical aberration. If we assume that the optical aberration is a symmetrical Gaussian function and that the ideal image of the source fibre is a symmetrical rectangular function. According to the discussion in chapter 2, the broadened image profile of the irradiance is also a symmetrical function and can be expressed as a convolution of the symmetrical rectangular function with the symmetrical Gaussian function

$$\begin{aligned} I(r) &= I_i(r) \otimes G(r) \\ &= \frac{1}{4\delta}\left(\frac{2}{\pi}\right)^{1/2}\left\{ erf\left[\frac{d/2-r}{\sqrt{2}\delta}\right] - erf\left[\frac{-d/2-r}{\sqrt{2}\sigma}\right]\right\} \end{aligned} \qquad (10-3)$$

Where erf(x) is the error function. $I_i(r)$ is the polar representation of the ideal image of the source fibre on the receiving lens end face. This treatment assumes that the ideal image is uniform in intensity over the whole area, which represents the worst case in the coupling efficiency calculation since this makes the coupling efficiency very sensitive to optical aberrations. G(r) is the polar representation of a Gaussian function, which represents the optical aberrations of the connector system. $I_i(r)$ and G(r) are given as

$$I_i(r) = \begin{cases} 1, & |r| < \dfrac{d}{2}, \\ 0, & otherwise \end{cases} \qquad (10-4)$$

Where d is the diameter of the ideal image of the source fibre. r is the radius distance from the centre of the image.

$$G(r) = \frac{1}{2\pi\sigma^2}\exp\left(-\frac{r^2}{2\sigma^2}\right) \qquad (10-5)$$

Where σ is the standard deviation of the Gaussian function. The coefficient of $1/(2\pi\sigma^2)$ normalises the function to unit volume.

When optical aberration is presented, the coupling efficiency can be calculated as

$$\eta = \frac{\int_0^R I(r)2\pi r dr}{\int_0^\infty I(r)2\pi r dr} \qquad (10-6)$$

Where R is the core radius of the receiving fibre. The broadened image irradiance I(r) can be calculated by equation (10-3). The broadened image irradiance section profile and the coupling efficiency are calculated numerically, with the results illustrated in Fig.10-4 and Fig. 10-5, respectively.

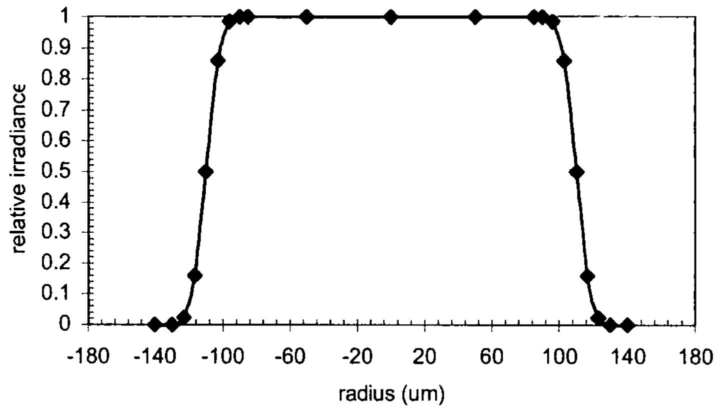

Figure 10-4 The section profile of the source fibre image irradiance of the FMOS fibre bundle connector at the focusing lens back end face.

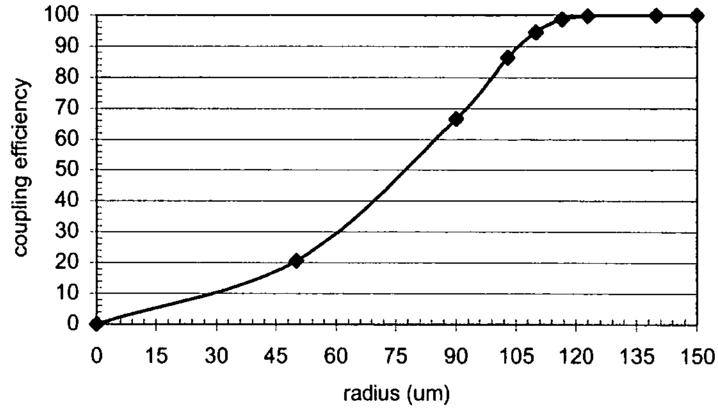

Figure 10-5 Coupling efficiency vs. receiving fibre core radius curve for FMOS fibre bundle connector. The coupling efficiency is 94.6% at radius 110 microns (D/2), 98.6 % at radius 116.5 microns (D/2 +σ) and 99.8% at radius 123 (D/2 +2σ) microns.

It is obvious that the receiving fibre needs to be oversized if high coupling efficiency is required. If the receiving fibre diameter is 246 μm, almost no light is lost because of the optical aberration. The actual receiving fibre core diameter is chosen as 250 μm because this is the size of an in-stock fibre.

10.5 Coupling Efficiency and Fibre Alignment Error

For the optical system in Fig. 10-1, the following alignment errors exist: position alignment error between the centre of the source fibre and the optical axis of the collimating lens, position alignment error between the centre of the receiving fibre and the optical axis of the focusing lens, and the angle alignment error which is caused by the tilt of the optical axis of the collimating lens with respect to that of the focusing lens. All of the alignment errors will result in an error in position of the image on the end face of the receiving lens, causing a position error between the image of the source fibre core and the receiving fibre core, which will result in a loss of light in the coupling process. It must be noted that a shift of the source fibre and collimating lens sub-assembly in the vertical plane perpendicular to the optical axis does not change the position of the source fibre image on the surface of the receiving fibre, and so this shift has no effect on the coupling efficiency. This is a fundamental advantage for this collimated light coupling system, which makes it possible to build the fibre bundle connector consisting of 100 pairs of coupling fibres.

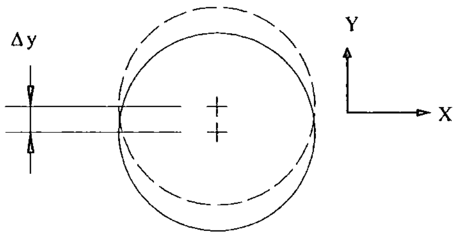

Figure 10-6 Schematic of fibre alignment error. The solid circle is the image of the source fibre core on the focusing lens end face where the receiving fibre is located. The dashed circle is the actual receiving fibre core. The alignment error is Δy.

The position error caused by the fibre alignment error on the receiving fibre end face is schematically shown in Fig. 10-6. Here the image of the source fibre core is shifted by Δy corresponding to the position of the receiving fibre core. In an ideal case, the image of the source fibre will be located exactly on the centre of the receiving fibre and thus Δy is zero. If an alignment error exists, Δy will not be zero and some light will be lost outside the receiving fibre core, resulting in a low coupling efficiency. In Fig. 10-6, it is assumed that the size of the receiving fibre is exactly the same as that of the image of the source fibre. Oversizing of the receiving fibre allows it to accept more light and thus increase the coupling efficiency, as discussed in the previous section. Note as mentioned previously that any source of alignment error will cause a position error between the image of the source fibre and the receiving fibre core on the focusing lens end face. So the alignment errors can always be expressed as a position error on the focusing lens end face.

The position error on the focusing lens end face caused by the alignment error between the source fibre and the collimating lens can be expressed as

$$\Delta y_a = M \cdot \Delta y_1 \qquad (10-7)$$

For the FMOS fibre connector, M is 2.5. The source fibre alignment error will be magnified 2.5 times and this means that this alignment error needs to be tightly controlled.

The position error caused by the alignment error between the receiving fibre and the focussing lens can be directly expressed as

$$\Delta y_b = \Delta y_2 \qquad (10-8)$$

The position error caused by the angle alignment error between the optical axis of the collimating lens and the optical axis of the focusing lens is a tilt error, and is given by

$$\Delta y_c = f_2 \cdot \tan\theta \qquad (10-9)$$

Where θ is the tilt error between the collimating and focussing lenses.

Finally on the receiving fibre input entrance, i.e. the end face of the focusing lens, the position error caused by all the alignment errors is just the sum of all the position errors and is given as

$$\Delta y = \Delta y_a + \Delta y_b + \Delta y_c = M \cdot \Delta y_1 + \Delta y_2 + f_2 \cdot \tan\theta \qquad (10-10)$$

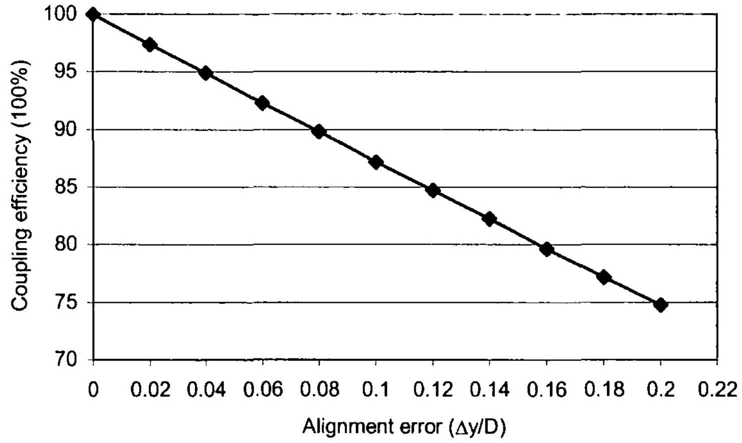

Figure 10-7 Coupling efficiency and fibre alignment error. The unit of the alignment error is Δy/D. Where D is the diameter of the receiving fibre.

The coupling efficiency is defined as the fraction of the light power of the source fibre that can be coupled onto the receiving fibre. From Fig. 10-6, the coupling efficiency when misalignment or alignment errors are present can be given as

$$\eta = \frac{\int_A I \cdot ds}{\int_{A_0} I \cdot ds} \qquad (10-11)$$

Where A is the intersection area of the source fibre image and the receiving fibre on the receiving fibre input entrance. A_0 is the area of the image of the source fibre. I is the irradiance of the image of source fibre and can be calculated according to Eq. (10-3).

The coupling efficiency is calculated by a numerical method and the result is shown in Fig. 10-7. For a diameter D of the image of the source fibre and the alignment error Δy, the coupling efficiency is a function of the alignment error $\Delta y/D$ and is almost linearly reduced with the alignment error if the optical aberration is fixed. For 95% and 90% coupling efficiency, it is required that the alignment errors are less than 0.04D and 0.08D, respectively. Note that no reflection loss is considered in the calculation.

If the required coupling efficiency is 95%, this requires that Δy is less or equal to 0.04D. Here we assume that the total alignment error is composed of three equal sources of error, i.e., $\Delta y_1=\Delta y_2=\Delta y_c$. For D=250 microns receiving fibre, from equations (10-8), (10-9), (10-10) and (10-11), one can get the allowed alignment error for each part is $\Delta y_1= \Delta y_2= 0.009D=2.2$ μm and $\theta=0.05°$. Table 10-1 lists some results of the calculations.

Table 10-1. Alignment errors and coupling efficiency

Coupling efficiency	Δy_1 (μm)	Δy_2 (μm)	θ (Arc degree)	Δy (μm)
95%	2.2	2.2	0.05	10
90%	4.4	4.4	0.1	20
85%	6.6	6.6	0.15	30

10.6 The Tests of the Selfoc Lenses

In order to reduce the risks and uncertainties, some measurements and tests were carried out before the construction of the fibre bundle connector. These included the measurement of the image quality of the Selfoc lenses, the magnification of the fibre bundle connector and the spectral transmission of the Selfoc lenses over the 0.9 – 1.8 μm wavelength range.

10.6.1 PSF and Encircled Energy

The Selfoc microlenses are key elements for the fibre connector. Most microlenses suffer from low encircled energy because of the wavefront aberration and surface roughness. The wavefront aberration pushes a substantial fraction of the light into the wings of the Point Spread Function

(PSF). The surface roughness may introduce scattered light. The PSF and encircled energy measurements for the Selfoc collimating and focusing lenses are shown in Fig. 10-8 and Fig. 10-9, respectively. Both lenses have been shown to provide excellent images, with very little scattered light. Both lenses are found to be diffraction limited when measured at 0.63um wavelength.

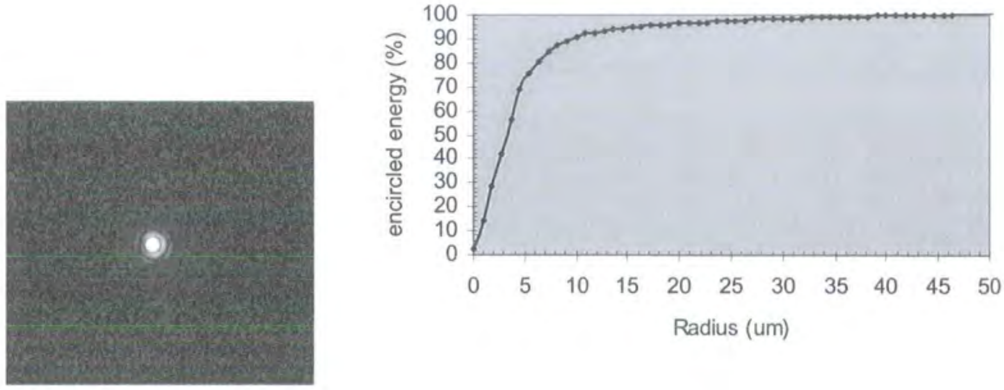

(a) (b)

Figure 10-8 The measured PSF (a) and encircled energy (b) of the Selfoc SLS 2.0 lens. No scattered light is found. The FWHM (Full Width at Half Maximum) is 3.66 μm. The measurement is made at F/5.

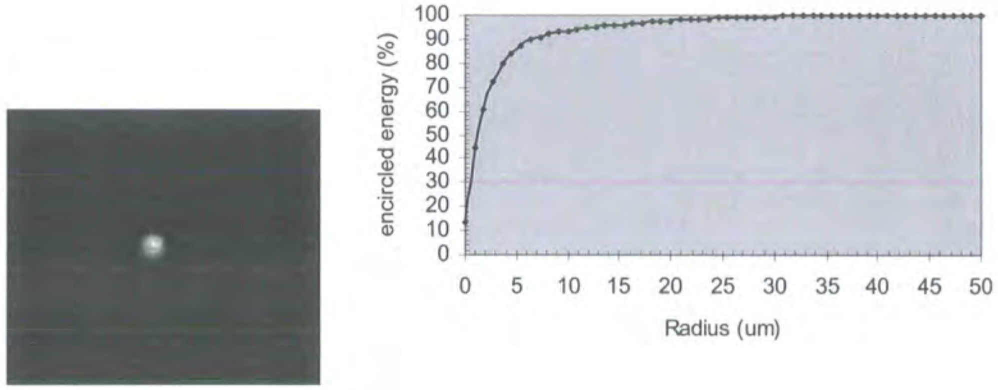

Figure 10-9 The measured PSF (a) and encircled energy (b) of the Selfoc SLW 1.0 lens. The FWHM is 1.85 μm. The measurement is made at F/2.

10.6.2 Magnification

The magnification M is a key specification for the fibre bundle connector. Too small a magnification may result in an output beam that is too fast for the spectrograph; Too large a magnification would result in an image of the source fibre which is larger than the receiving fibre core at the entrance face, giving a low coupling efficiency. A large magnification may also result in a focal ratio slower than F/5 for the receiving fibre, which would give rise to the FRD problem in the receiving fibre. The required magnification is given by the ratio of the focal lengths of the collimating and focusing lenses. A combination of the two lenses that meet the design specification must therefore give a magnification of 2.5. The magnification was measured by imaging a pinhole onto the back surface of the focusing lens, using an optical layout similar to that of Fig. 10-1, but the source fibre is replaced by a pinhole with a diameter of 100 microns. The pinhole is imaged onto the back end face of the focusing lens where the receiving fibre will be located. The measured image size of the pinhole can be used to work out the magnification of the connector. The measurement was made using a microscope and the pinhole image size was read using a translation stage. The pinhole image is shown in Fig. 10-10. This measurement confirms that the magnification is 2.5 with an accuracy of ± 2%. The test also confirms that the source fibre (here it is replaced as the pinhole) can be accurately imaged onto the back end face of the focusing lens where the receiving fibre will be located.

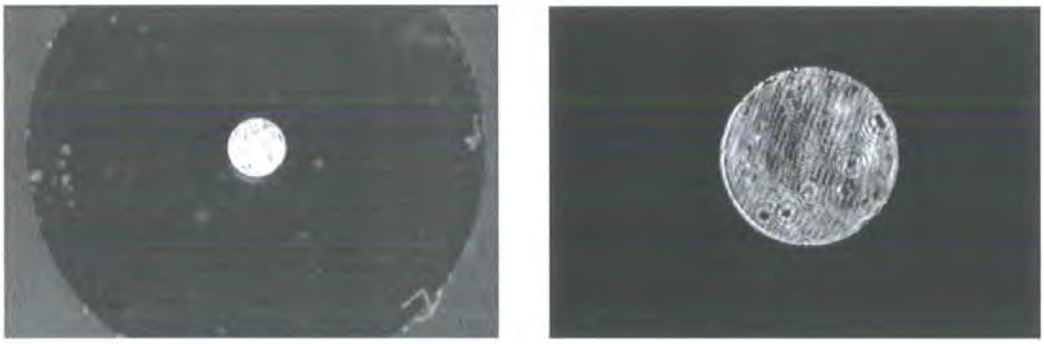

(a) (b)

Figure 10-10 The photograph of the image of a 100 μm pinhole on the back end face of the focusing lens. The lens back end face can be clearly seen (a). Note that there are some dust spots on the lens surface. The pinhole image is imaged onto a CCD detector by a 3.5x microscope objective (a) and a 10x objective (b), respectively. Note that the pinhole is correctly imaged onto the back end face of the focusing lens (a) and the sharp image (b).

10.6.3 Transmission

The Selfoc lenses are made from oxide glass. Some of these materials may have strong absorption at the wavelengths around 1.3 µm, which will result in a low transmission. A spectral transmission measurement is necessary to check the spectral absorption characteristics of the Selfoc lens although the manufacturer claims a minimum transmission of 89% for non-coated lenses with a 5 mm thickness over the wavelengths of 380- 2000nm (SELFOC Product Guide 2000). The spectral transmission measurement was made using two SLS 2.0 Selfoc lenses, which combined to form an afocal optical system. As the measurement is to check whether there is significant spectral absorption over the 0.9 –1.8 µm wavelength range, only relative transmission was measured. A Perkin-Elmer /UV/VIS/NIR Lambda 19 atomic absorption spectrophotometer was used for the measurement. The measurement result, confirming that there is no significant absorption feature in the near infrared, is shown in Fig. 10-11.

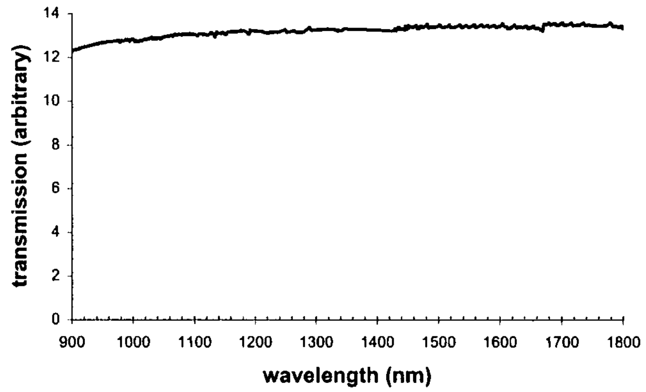

Figure 10-11 Transmission of a SLS 2.0 Selfoc microlens (see text).

10.7 The Construction of the Fibre Bundle Connector

The fibre, ferrule, Selfoc lens were assembled into a sleeve to form a sub-assembly. The fibre was first inserted into a fibre ferrule and glued with epoxy adhesive. The epoxy was carefully chosen to minimize the shrinkage when curing. This constraint is necessary to reduce the FRD of the fibre, which may be introduced by the stress due to the adhesive. The adhesive also has good polishing characteristics so that a high quality finish could be achieved. The ferrule and fibre were polished together until mirror-finishing surface was achieved. The Selfoc lens and the polished ferrule/fibre were then inserted into the sleeve, and glued in place using Norland 61 UV cured adhesive. The interfaces of the Selfoc lens, fibre and fibre ferrule were also glued together in this process. The Norland 61 adhesive was used because of its good transmission in the near infrared. The sub-assembly is schematically shown in Fig. 10-12 for both source fibre and receiving fibre. The source fibre, its ferrule, Selfoc lens and sleeve consist of a collimating sub-assembly, with a focusing sub-assembly for the receiving fibre (Fig. 10-13). The sleeve of the collimating sub-assembly is made of borosilicate glass and the source fibre and ferrule can be clearly seen inside the sleeve, while the sleeve of the focussing sub-assembly is made of stainless steel. The ferrule-sleeve assembly serves to provide accurate centring of the fibre-lens pairing. The individual sub-assemblies were inserted into a metal plate and glued by epoxy. Each metal plate (one for half of the connector) has 100 holes to accommodate these sub-assemblies. The two plates were manufactured by precision grinding the two mating surfaces. The two plates were then dowelled and clamped together. Custom-made reamers were employed to produce accurately bored holes through both components simultaneously so as to ensure precise alignment and eliminate the tilt alignment error between the collimating and focusing lenses. The mechanical drawing of the fibre bundle connector assembly is shown in Fig. 10-14.

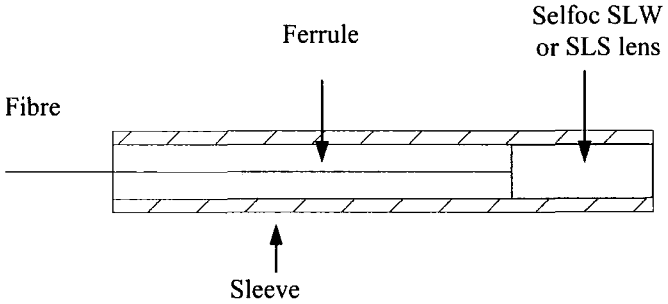

Figure 10-12 Schematic of the collimating sub-assembly or focussing sub-assembly.

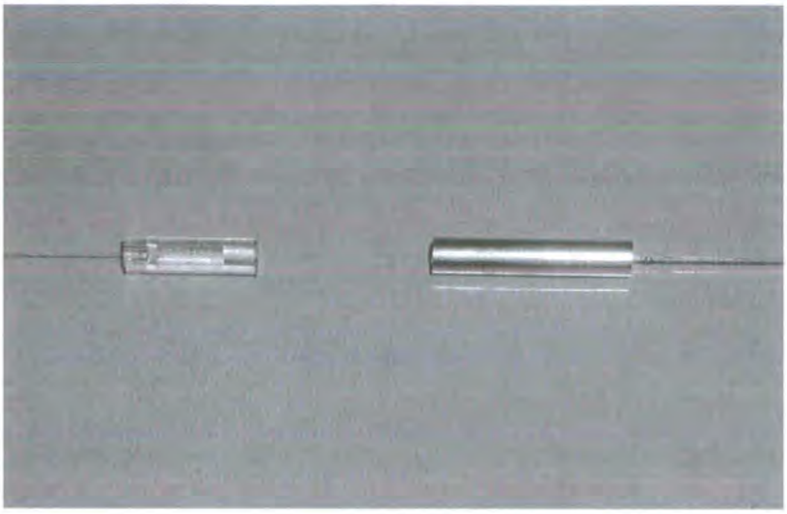

Figure 10-13 Photograph of the collimating sub-assembly (left) and focussing sub-assembly (right).

The two parts of the fibre bundle connector can be connected or disconnected quickly. In use, a central locating pin locates the two plates together, with a second pin providing radial alignment. The prototype fibre bundle connector uses capscrews to secure the two plates together, but it is envisaged that the final design may use a bayonet connection, with the two plates held together using a spring force. The photograph of the finished prototype of the fibre bundle connector is shown in Fig. 10-15.

The fibre ferrule is produced by precision draw process, and could be made from metal or glass. The inside diameter can be accurate to within a tolerance of +/- 1 μm for both metal (Nippon Tokushukan MFG .Co. Ltd 2000) and glass ferrule .

The source fibre used was CeramOptec WF 84/100/107P low OH fibre. The fibre core was 84 μm and the actual buffer diameter was 109 μm. The ferrules for the source fibres were purchased from InnovaQuarts Inc. This is an in-stock product with 126 +2/-0 μm ID (Inner Diameter), 990+/-10 μm OD (outside diameter) and 5mm Length. The in-stock ferrule is used because of its low cost. The sleeves were custom-designed to match the ferrule and the lens sizes, and were manufactured by Vitrocom Inc.

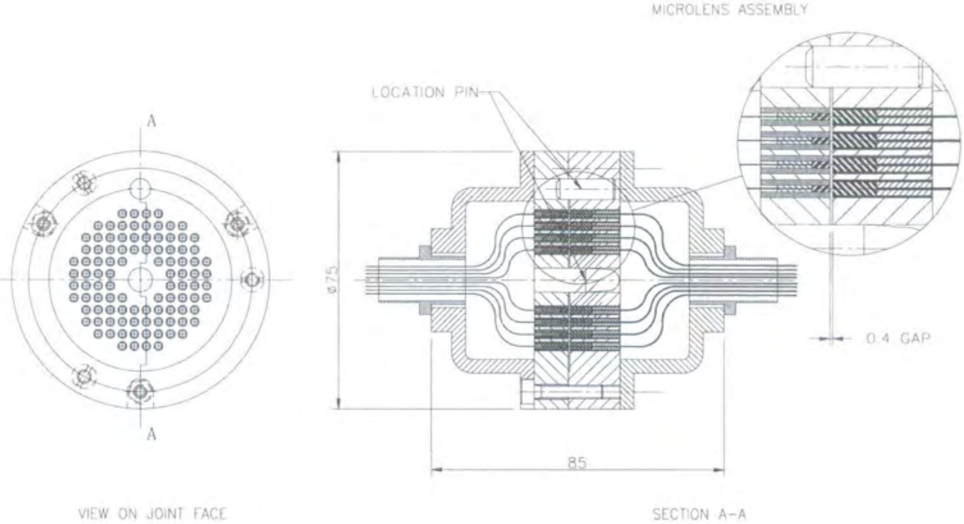

Figure 10-14 Mechanical assembly drawing of the FMOS fibre bundle connector (Designed by George Dodsworth). There are 100 source fibres coupled to 100 receiving fibres and the focal ratio is converted from F/2 to F/5.

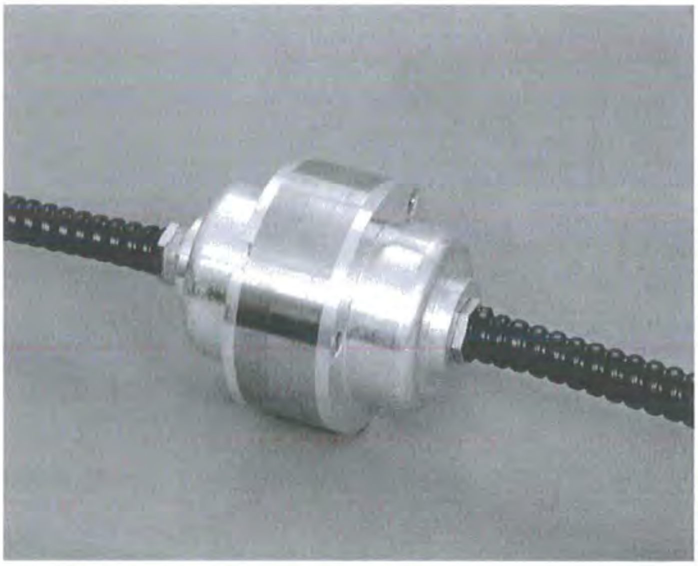

Figure 10-15 The completed prototype of the fibre bundle connector.

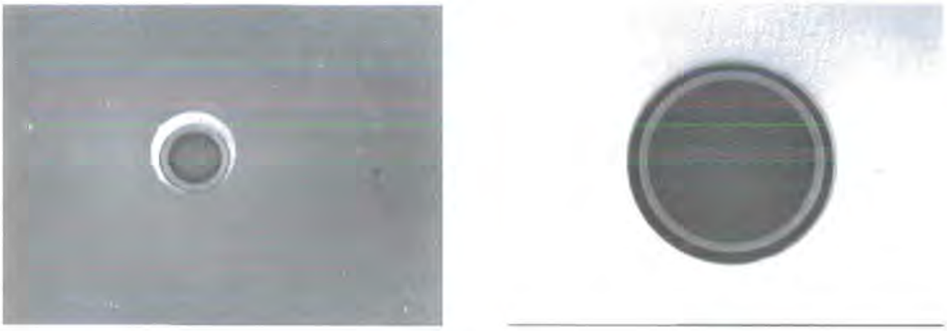

(a) (b)

Figure 10-16 Microphotographs of fibres in fibre ferrules. (a) is the F/2 source fibre and ferrule assembly. (b) is F/5 receiving fibre and ferrule assembly. Note that the source fibre is not accurately centred as the ferrule is not custom-designed. The receiving fibre is accurately centred in the custom-designed ferrule.

The receiving fibre used was Polymicro technologies FIP250275305 low OH fibre. The fibre core was 250 μm and the actual buffer diameter is 305 – 307 μm. The ferrules for the receiving fibres were custom-designed and were manufactured by Microlap Technologies, Inc. The stainless steel sleeves were purchased from CNW Coopers Needle Works Ltd.

Polishing the end of the fibre is a critical aspect of the construction and can greatly impact on the quality of the finishing product. A mirror-finished end of the fibre and ferrule assembly surface is desired, as this can reduce the light loss at the interface if the surface is clean. The microphotographs of fibres in fibre ferrules after polishing are shown in Fig. 10-16 (a) and (b) for source and receiving fibres, respectively. Note that there is a de-centre alignment error for the source fibre in Fig. 10-16 (a) because the source fibre ferrule was not custom-designed and there is a large gap between the fibre OD and the ferrule ID. The decentre is in estimation and is about 8 μm. The ferrule for the receiving fibre in Fig. 10-16 (b) was custom-designed and the fibre is accurately centred in the ferrule.

10.8 The Measurement of the Coupling Efficiency

The apparatus used to measure the coupling efficiency is schematically shown in Fig. 10-17. A pinhole is illuminated by a lamp. The image of the pinhole is projected onto the 84μm fibre entrance end face at F/2 by lens 3 and lens 6. The image size of the pinhole is 20μm. The fibre entrance end is installed on a XYZ translation and tilt stage to align the pinhole image accurately with the fibre core. The F/2 beam is achieved by adjusting the size of aperture 5. A narrowband filter 4 is located in the collimated light between lens 3 and 6 to allow only the specific wavelength to be measured. The F/5 output beam at the other fibre end face of the fibre bundle connector is imaged onto the CCD detector 9 by an image system 8. The CCD detector is sensitive over the wavelength range of 0.4 - 1.0μm. The image of the fibre output end is recorded by the CCD and is shown in Fig. 10-18b. The flux is integrated over an area slightly larger than the fibre image after subtracting a background exposure. The Selfoc focusing lens and receiving fibre are then removed to leave only the input fibre and Selfoc collimating lens 10. The Selfoc collimating output end face, which is also the pupil of the fibre connector, is imaged onto the CCD (Fig. 10-18a). Again the flux is integrated over an area slightly larger than the Selfoc lens after a background exposure is subtracted. The coupling efficiency of the fibre connector is the ratio of the integrated fluxes at the fibre connector output end and the Selfoc collimating lens output end face.

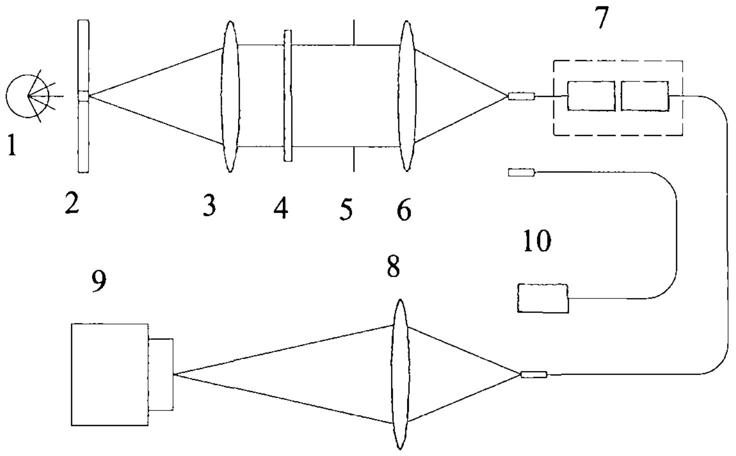

Figure 10-17. Schematic of coupling efficiency measurement of the FMOS fibre bundle connector. 1- lamp. 2- 50-μm pinhole. 3- lens 1. 4- narrowband filter. 5- aperture. 6- lens 2. 7- fibre bundle connector. 8- imaging system. 9- CCD detector. 10- source fibre and collimating lens (collimating sub-assembly).

(a) (b)

Figure 10-18 Microphotographs at the collimating lens output end face (a) and at the fibre output end of the connecter (b). From Figure (a) and (b), the coupling efficiency is 81.25 %. The pupil has a diameter of about 500 μm and is in good agreement with the result obtained from a tray tracing simulation.

The measurement is made at 0.905 μm and the coupling efficiency is 81.25 %. This includes the Fresnel reflection losses at two air-glass interfaces. The Selfoc lenses and the fibre ends are not AR-coated currently. The coupling efficiency is about 88% if the losses in the two air-glass interfaces are removed. The coupling efficiency at other wavelengths in the 0.9 –1.8μm range is expected to be similar or slightly better than that at 0.905 μm as the optical aberration is almost the same over the whole wavelength range, with slight degradation at 0.9 μm (see Fig. 10-3). The 8 μm decentre of the source fibre in the ferrule (see Fig. 10-16a) introduces 20 μm decentre on the receiving fibre entrance according to Eq. (10-7). The 20 μm alignment error results in about 10 % losses in the coupling efficiency (see Table 10-1). The measurement is in good agreement with the theoretical estimation.

The measurement has an accuracy of 1 % and the variation of coupling efficiency from fibre to fibre is less than 3% and this includes the variation that may be caused by the lamp light source.

10.9 Further Improvement

Further improvement can be made to increase the coupling efficiency. These include AR coating for the Selfoc lenses. The material of Selfoc lens is doped silica which can be AR coated by conventional thermal evaporation vacuum coating. Single-layer MgF_2 AR coated Selfoc lenses can be purchased from Melles Griot. Ion-Assisted Deposition (IAD) can also be considered: this technique has been applied to sensitive material at temperatures well under

100°C, such as epoxy microlens arrays. The IAD coating can be applied on the two interfaces of the fibre bundle connector so that 100 lenses can be coated simultaneously after the fibre bundle connector is built. It is estimated that about 5% gain in coupling efficiency can be achieved after AR coating. Further gain in coupling efficiency can be achieved by using custom-designed fibre ferrule for the source fibre to reduce the alignment error since this is the dominant source of the light loss in the coupling. Currently this alignment error introduces 10% coupling efficiency loss and it is estimated that about 5 – 7 % increase in coupling efficiency may be achieved by using a custom-designed ferrule. These improvements will be done in the next phase and it is estimated that the coupling efficiency of the fibre bundle connector may be better than 90 %.

10.10 Summaries and Conclusions

The design, theory and construction for FMOS fibre bundle connector have been present. Good agreement between theoretical estimation and actual measurement has been achieved. The coupling efficiency is up to about 88% if the losses in two air-glass interfaces are not included. The coupling efficiency of the prototype is dominated by the alignment error of the source fibre and ferrule assembly, as this ferrule is an in-stock product and not specifically custom-designed. Further improvement is also discussed. The coupling efficiency is estimated to be better than 90% if the in-stock fibre ferrule is replaced by a custom-designed ferrule.

Chapter 11

Thesis Summary

Abstract

This chapter summarizes the work presented in the thesis. Conclusions are achieved from the work discussed in the previous chapters. Future possible developments for the IFU techniques are also discussed.

11.1 FMOS Multiple IFU

Multiple-integral-field spectroscopy combines the advantages of the integral field spectroscopy (IFS) with those of the multiple-object spectroscopy and enables two-dimensional spectroscopy of multiple targets over an extended field. In order to make efficient use of large modern telescopes, the Multiple Integral Field Unit (M-IFU) for the FMOS project needs to work at visible (0.45-.9 μm) and near infrared (0.9 –1.8 μm) wavelength ranges simultaneously. The output light from the M-IFU can feed the optical and infrared spectrographs simultaneously via a fibre connector. In order to achieve high spatial and spectral resolution, the M-IFU must deliver a sub-arcsec image to the spectrographs. There are some crucial requirements for the design. These include the correction of chromatic aberration in the visible and near infrared simultaneously, the requirements of good optical image quality and the maximum efficiency. Also in order to deploy at least 15 IFUs on the telescope field, it is important to minimize the size of the IFU which requires that the optical design of the fore-optics must as simple and compact as possible.

A prototype M-IFU module was made. The design theory leading to the construction of the FMOS IFU was first discussed. The FMOS IFU fore-optics design, microlens design and fibre bundle techniques were presented and it was shown that the design meets the requirements of the FMOS project. The fore-optics image quality was tested and good agreement between theoretical estimation and actual measurement was achieved. The fibre bundle was manufacture by AndaOptec according to the design and requirements for the IFU. The measurements showed that the fibre bundle met the requirements. The technique for the assembly of fibre bundle and microlens array was also discussed and the assembly was successful.

The performance of the FMOS IFU is mainly determined by the quality of the microlens array. The actual measured IFU performance is worst than that of the theoretical estimation because the Limo microlens array did not reach its specifications. A lot of tests were carried out to identify the problems of the Limo microlens array. It needs to be noted that according to the discussion in chapter 5, although Epigem microlens arrays were found to be the best in image quality, they were not used because they are too expensive for a prototype and need a long time for manufacture. Further improvement of the IFU performance is possible by using high quality microlenses, such as Epigem microlenses.

The work for the prototype was successful. The Astronomical Research Group at University of Durham is on the way to build the M-IFU. The experiences and lessons learnt from the prototype give us enough confidence to build a high quality M-IFU at any time in the near future for a real project.

11.2 FMOS Fibre Bundle Connector

Although fibre connector is simple in concept, it is always a problem to design and construct a fibre connector with high coupling efficiency. This has been confirmed by a lot of work already carried out in the communication system. There are unique requirements for the FMOS fibre connector: (1) The fibre connector must convert the focal ratio from F/2 to F/5; (2) the fibre connector must couple 100 pairs of fibres simultaneously. These requirements decide that microlenses must be used to convert the focal ratio and the conventional microlenses cannot be used because of the F/2 fast beam. A unique method must be found to couple 100 pairs of fibres simultaneously, where in communication systems the fibre connector only couples a pair of fibre in most cases.

The building of a prototype is therefore needed to investigate the problems in the design and construction of the fibre bundle connector. A mathematical model to calculate the coupling efficiency when optical aberrations and alignment errors are present was derived. Selfoc gradient index microlenses were used, which can minimize both the optical aberration and alignment errors. The optical design, theoretical calculation of coupling efficiency and tests were carried out. The fibre bundle connector delivers high coupling efficiency and meets the requirement for FMOS project. Good agreement between theoretical estimation and actual measurement was achieved. The accuracy of the mathematical model for the calculation of the coupling efficiency was also confirmed by the measurement.

Further work is also needed on the mechanical design to provide protection for the fibre bundle. This work will be done in the next phase.

11.3 Other Work

Most modern large telescopes are optimized for optical and infrared observations and this provides an exciting opportunity to explore the distant universe. This means that there is an increasing need for near infrared astronomical instrumentation. A practical question is how to design an infrared instrument with the chromatic aberration well corrected? A simple method is to use only mirrors in the design as mirrors don't introduce chromatic aberration. Another method is the use of lenses which have many advantages compared with mirrors. The use of lenses in the infrared is limited by the availability of infrared transmission materials. Both of these method of using mirrors and lenses are demonstrated in the thesis.

Microlenses are the key element for the IFU system and the performance of the IFU system is mainly determined by the optical quality of the microlens array. The work of characterizing the performance of microlens arrays is therefore very important. The design and test of microlens array were discussed. A mathematical model was also derived which can be used to compare the image performance of microlens arrays with different specifications. High quality microlens arrays which meet the requirements for the IFU instrument were identified.

The design of an optical spectrometer is also presented, which is an upgrade option for FMOS. The design meets the specific requirements for FMOS. Further exploration of the possibility of simplifying the design or improving the optical performance is worthwhile.

11.4 Future Developments

There are two IFU technologies which are suitable to build highly efficient M-IFU: lenslet fibre bundle and image slicer. Although image slicing is the most efficient method in principle, there are important cases where the other technique is more practical. An example is the FMOS M-IFU for Subaru telescope where only the lenslet fibre bundle M-IFU can be used. Note that currently image slicer based IFUs can only be realized for the infrared where both the input and output beams for the IFU are slow since these make the use of the small off-axis mirrors possible. For visible spectrometers, the beam is generally fast and it is impractical to use the off-axis mirrors in a fast beam, since this introduces large optical aberrations.

The Astronomical Research Group at Durham are exploring both of these M-IFU techniques. An image slicer based IFU for GNIRS is being built in Durham. An image slicer IFU instrument for GIRMOS has also been studied. Many lenslet fibre and image slicer M-IFU instruments are also being built around the world. It can be expected that these two techniques will be more dominant in the near future.

Efforts are being made to extend the use of image slicer from the infrared to the visible while lenslet fibre bundle IFU to the cryogenic infrared. Cryogenic fibres have been tested at both the Anglo-Australian Observatory and Durham. Although the fibres and fibre bundles can survive at cryogenic temperature with almost no degradation of fibre FRD, there is still some work needed to do to ensure that the fibres can survive in the long term (i.e. can survive after one or two years of intensive use).

We are certainly in an exciting era when many large telescopes are being built. This presents exciting challenges for the design and construction of astronomical instruments.

Appendix A

Microlens Spherical Aberration

The conjugate points for a single refracting spherical interface with third-order approximation can be expressed as (Hecht 1998)

$$\frac{n_1}{s_0}+\frac{n_2}{s_i}=\frac{n_2-n_1}{R}+h^2\left[\frac{n_1}{2s_0}\left(\frac{1}{s_0}+\frac{1}{R}\right)^2+\frac{n_2}{2s_i}\left(\frac{1}{R}-\frac{1}{s_i}\right)^2\right]$$

Where n_1 and n_2 is the refractive index in the object space and image space, respectively. R is the radius of the curvature of the lens. S_0 is the object distance and s_i is the image distance. h is the beam height at the lens surface (marginal ray height).

When the object is at infinity, $s_0=\infty$. Considering $n_1=1$ and $n_2=n$, one obtains

$$s_i=f'-\frac{h^2}{2f'(n-1)^2}$$

Where f' is the focal length in the medium. Thus the longitudinal spherical aberration is

$$\begin{aligned}LAS&=\left|\ S_i-f'\ \right|\\&=\frac{N.A^2f}{2n(n-1)^2}\end{aligned}$$

And the transverse spherical aberration is

$$\begin{aligned}TAS&=LAS\bullet tgU'\\&=\frac{N.A^2D}{4n^2(n-1)^2}\end{aligned}$$

Where D is the lens aperture diameter. U' is the marginal ray angle in image space.

Appendix B

Design of a Fibre Connector for the FMOS IFS Mode

B.1. Introduction

The IFS fibre connector provides two functions. It needs to be connected and disconnected in the fibre train; A dichroic beam splitter is also required so that the 0.45 – 1.9 μm light can be split as optical (0.45 – 0.9 μm) and infrared (0.9 – 1.8 μm) and the IFU can feed the optical and infrared spectrographs simultaneously. The fibre connector consists of two parts and is schematically shown in Fig. B-1. The function of the fibre bundle coupler is to provide a connection and disconnection in the fibre train. The second function is provided by the dichroic beam splitter.

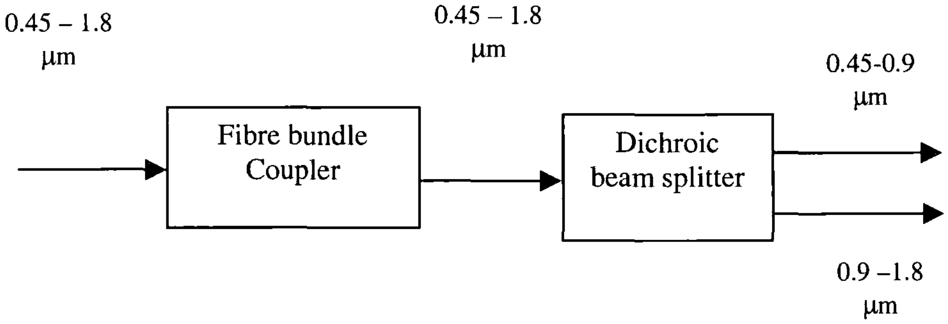

Figure B-1. Schematic of fibre connector.

B.2. Fibre Bundle Coupler

A coupler consists of two lenses. One is collimating lens and another is focusing lens. The collimating lens and focusing lens are two identical Selfoc SLW 1.0 0.25 0.63 microlenses. The source fibre is glued to the first end face of the collimating lens. The light from the F/5 source fibre is first collimated by the collimating lens and them focused by the focusing lens. The image of the source fibre is projected onto the receiving fibre at F/5. The receiving fibre is glued to the end face of the focusing lens. The optical layout and spot diagraph of the coupler are shown in Fig. B-2 and Fig. B-3, respectively. The optical aberration is corrected over 0.45 – 1.8 μm wavelength range and the image quality is nearly diffraction limited for wavelength longer than 0.5 μm. If the fibre core diameter of the source is D (= 80 μm) and the RMS spot radius of the optical aberration is σ (= 6.3 μm), the coupling efficiency is about 97 % and 99% for a receiving fibre core radius of $D/2 + \sigma$ and $D/2 + 2\sigma$, respectively in the case that there is no alignment errors. The relationship of the coupling efficiency and alignment errors is analyzed in Chapter 10.

Table B-1. The specifications of the fibre bundle coupler

Source fibre diameter	Receiving fibre diameter	Wavelength length range	Number of coupling fibres
80 μm	90 μm	0.45-1.8 μm	100 fibres /bundle

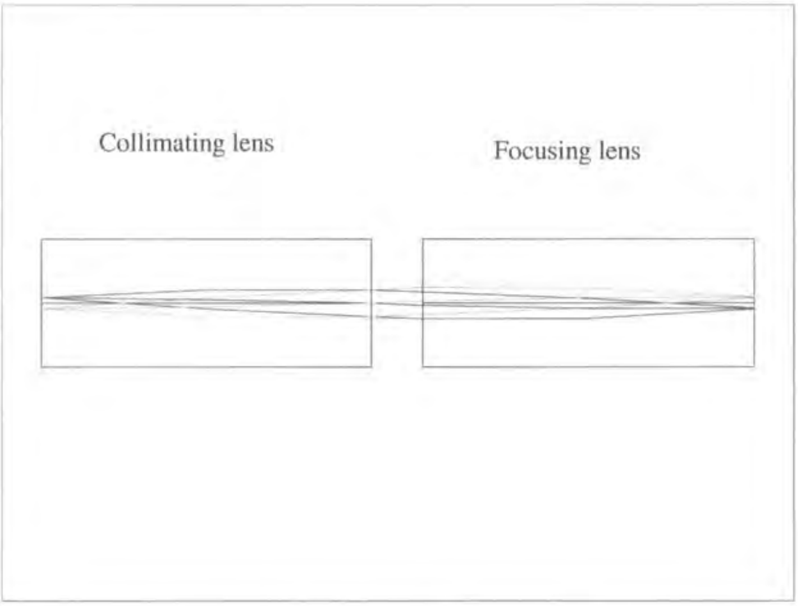

Figure B-2. The optical layout of F/5 – F/5 fibre coupler. Two identical Selfoc microlenses (SLW 1.0 0.25 0.63) are used to couple the light from F/5 fibre onto F/5 fibre. The lens to lens gap is 0.4 mm.

If the source fibre diameter is 80 μm, the receiving diameter is oversized as 90 μm to accommodate optical aberrations and alignment error. The source and receiving fibres are centered to the collimating lens and focusing lens by precision ferrules, respectively. A fibre coupling bundle consists of 100 coupling fibres and can be built with the same techniques described in Chapter 10. The specifications are listed in Table B-1.

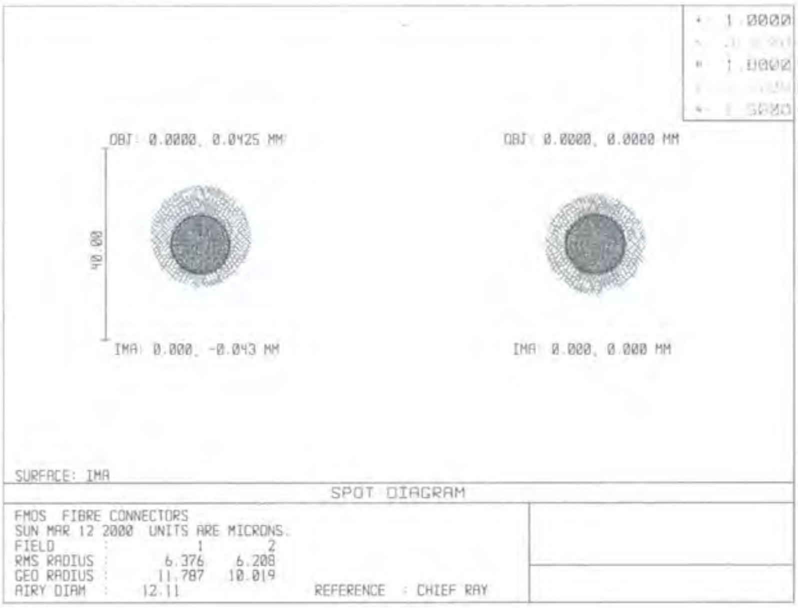

Figure B-3. Spot diagram of fibre connector. The chromatic aberration is corrected over the 0.45 – 1.8 μm wavelength range and the image quality is nearly diffraction limited after 0.5 μm wavelength. The maximum RMS radius is about 6.3 μm.

B-3. Dichroic Beam splitter

The function of the dichroic beam splitter is to split the 0.45 – 1.8 μm light into visible (0.45 – 1.8 μm) and NIR (0.9 – 1.8 μm) so that it allows visible and NIR spectroscopy simultaneously.

The optical layout of the dichroic beam splitter is show in Fig. B-4. Two identical Selfoc microlenses (SLW 1.0 0.25 0.63) are used as the collimating lens and focusing lens, respectively. The 0.45 – 1.8 μm light from the source fibre is first collimated by the collimating lens. The collimated VIS (visible) light is reflected by the beamsplitter film that is coated on the end face of the collimating lens and focused onto the first end face of the collimating lens while the collimated NIR light goes through the film and focused onto the end face of the focusing lens. The spot diagram is shown in Fig. B-5. The receiving fibre is expected to be 10 μm oversized and thus the core diameter is 100 μm.

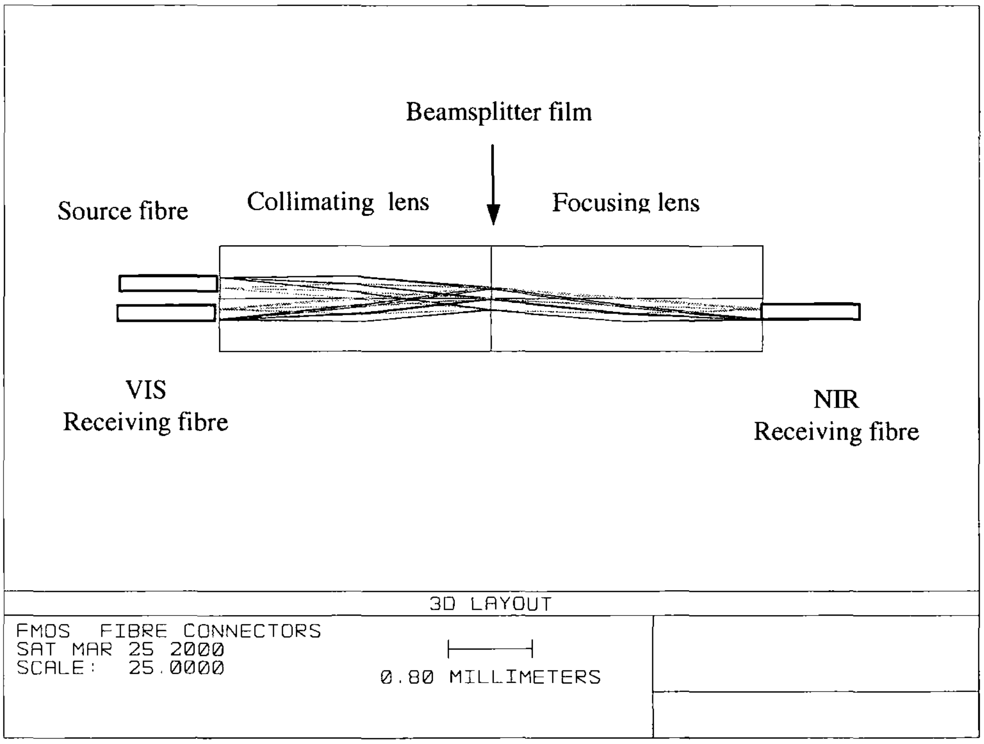

Figure B-4. The optical layout of the F/5 – F/5 Beamsplitter. Two identical Selfoc microlenses (SLW 1.0 0.25 0.63) are used. The fibre outside diameter is assumed to be 200 μm. The receiving fibres are oversized 10 μm.

Both of the source fibre and receiving fibres are accurately positioned with the lenses by fibre ferrules. The fibres are first inserted into the ferrules and glued by epoxy adhesive. After the epoxy is cured, the fibre and ferrule are polished and a fibre / ferrule assembly is formed. The source fibre and VIS receiving fibre are assembled in one ferrule and the NIR receiving fibre is assembled in another ferrule. The fibre / ferrule assemblies, the collimating and focusing lenses are then inserted into a precision sleeve and glued by Norland 61 UV cured adhesive. The whole assembly of the dichroic beam splitter is schematically shown in Fig. B-6. Note that there is one spare fibre on the NIR receiving fibre end (right side) and it is used for alignment.

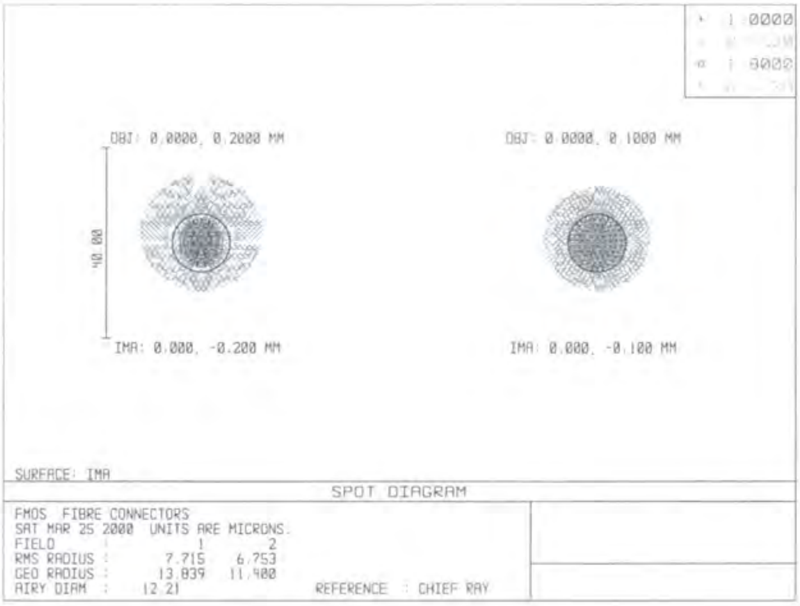

```
FMOS  FIBRE CONNECTORS
SAT MAR 25 2000  UNITS ARE MICRONS.
FIELD      :        1        2
RMS RADIUS :    7.715    6.753
GEO RADIUS :   13.839   11.400
AIRY DIAM  :    12.21                 REFERENCE  : CHIEF RAY
```

Figure B-5. The spot diagram of the F/5 – F/5 Beamsplitter. The maximum RMS radius is about 7.7 μm. The image quality is closely diffraction limited after 0.5 μm wavelength.

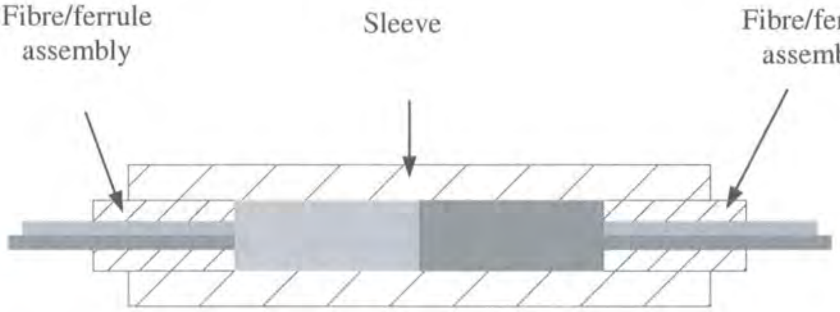

Figure B-6. The assembly of the dichroic beam splitter. Note that one spare fibre on the NIR receiving fibre end (right side) is used for alignment.

B-4. Estimated Coupling Efficiency

The coupling efficiency of the fibre connector is a function of optical aberration of the coupling lenses, the fibre size, the oversizing of the receiving fibre and the alignment errors. It is estimated that the actual achievable coupling efficiency is about 90% for the fibre coupler and dichroic beam splitter, respectively. Therefore, the whole coupling efficiency of the fibre connector is about 81%.

Bibliography

Allington-Smith, J. et al, "Integral field spectroscopy with the GEMINI Multiobject Spectrographs," *Proc. SPIE* **4008** (2000)

Allington-Smith, J. R. and Content, R., "Sample and background subtraction in fibre-lenslet integral field spectrograph," *PASP* **110** 1216-1234 (1998)

Allington-Smith, J., Haynes, R. and content, R., "Integral-Field spectroscopy with the GEMINI multi-object spectrographs," *Fiber Optics in Astronomy III*, ASP Conference Series, **152** 213-219 (1998a)

Allington-Smith, J.R et al. "A Low-Dispersion Survey Spectrograph (LDSS-2) for the William Herschel Telescope," *PASP* **106** 983-991 (1994)

Allington-Smith, J.R et al. "A faint object spectrograph for William Herschel telescope," *Mon. Not. R. A. S.* **238** 603-619 (1989)

Anandarao, B.G. et al., "A scanning metallic-mesh Fabry-Perot interferometer for airborne far infared astronomy," *Proc. SPIE* **445** 42-46 (1983)

Angel, J.R.P. et al., *Astrophysical Journal* **218** 776 (1977)

Arribas, S., et al., "INTEGRAL: An Optical-Fiber system for 2-D Spectroscopy at the 4.2-m William Herschal Telescope," Fiber optics in Astronomy III Vol. **152** 213-219 (1998)

Atherton, P.D., "Imaging Spectrometer in Optical Astronomy," *Proc. SPIE* **445** 535-542 (1983)

Bacon, R. et al., "3D spectrograph at high spatial resolution. I. Concept and realization of the integral field spectrograph TIGER," *Astron. Astrophys. Suppl. Ser.* **113** 347-357 (1995)

Barakat, R. and Houston, A., *J. Opt. Soc. Am.* **53**, 1244 (1963)

Barakat, R., *J. Opt. Soc. Am.* **54**, 38 (1964)

Barden, S.C., “Volume-phase holographic gratings and their potential for astronomical applications,” *SPIE Proc.* **3355** 1998

Bass, M., et al., Handbook of optics, Volume II, Chapter 18, McGRAW-HILL, Inc. (1995)

Bershady, M.A., et al., “Galaxy Kinematics with Integral-Field Spectroscopy and the Hobby-Eberly Telescope,” Fiber optics in Astronomy III Vol. **152** 253-257 (1998)

Boas, Mary L., Mathematical method in the physical sciences, John Wiley & Sons, Inc., 467-469 (1983).

Bobroff, N. and Rosenbluth, A. E., “Evaluation of highly corrected optics by measurement of Strehl ratio,” *Appl. Opt.* **31** 1523-1536 (1992)

Boulesteix, J. et al., “First results from CIGALE scanning Perot-Fabry interferometer,” *Proc. SPIE* **445** 37-41 (1983)

Bowen, I.S., *Ap. J*, **88**, 113 (1938)

Brodie, J.P., et al., “Optimum choice of fibre diameter for multiple-object spectroscopy,” *The Astronomical Journal* **96** 2005-2010 1988

Buchdahl, H.A., “Many-Color Correction of Thin doublets,” *Appl. Opt.* **22**,1878 (1985)

Buchroeder,R.A., “Tilted-Component Telescopes, Part I: Theory,” *Applied Optics* **19** 2169-2171 (1970).

Buchroeder, R., *Appl. Opt.* **11** 2968 (1972)

Carnell, K.H., et al., “Some experiments on precision lens centring and mounting,” *Opt. Acta* **21** 615-629 (1974)

Carvill J, Mechanical engineer’s data handbook, CRC Press, Inc. (1993)

Casse, M. et al., "Optical design of the FUEGOS high resolution spectrograph multiple fibre spectrograph," *SPIE Proc.* **2198** 1060-1070 (1994)

Chang, P.C., et al., "Multiple fibre interconnect using silicon G-grooves," *Proc. SPIE 836*, 311-318 (1987)

Clark, P., Howard, J.W. and Freniere, E.R., "Asymptotic approximation to the encircled energy function for arbitrary aperture shapes," *App. Opt.***23**, 353-357 (1984).

Connes, P., "Astronomical Fourier spectroscopy," *A. Rev. Astron. Astrophys.*, **8** (1970)

Content, R., "A new design for integral field spectroscopy with 8-m telescopes," *Proc. SPIE* **2871** 1295-1305 (1997).

Content, R. Allington-smith, J. et al., "ESA-NGST integral field and multiobject spectrograph slicer system," *Proc. SPIE* **4008** (2000).

Courtès, G, "An integral field spectrograph (IFS) for large telescopes", Instrumentation for astronomy with large optical telescopes, 123-128, *D. Reidel Publishing Company* (1982)

Dallier, R. and Cuby, J.G, Non-cooled near infrared spectroscopy, *Proc. SPIE* **3354** 833-844 (1998)

Danzer, U. et al., " High precision two dimensional fibre-array in silicon V-groove technique," Annual Report, Angewandte Optik, Physikalisches Institute der Universitat Erlangen (1992)

Dalton, G., Parry, I., Alling-Smith, J., Sharples, R., Ren, D., Taylor, K., Gillingham, P., Karoji, H., Iye, M., Noumaru, J., Akiyama, M., and Ohta, K., " FMOS: A Fibre-fed spectrograph for SUBARU," *FMOS design document* (1999)

Dohlen, K. et al., "Optical designs for the Rosetta narrow-angle camera," *Opt. Eng.* **35** 1150-1157 (1996)

Eisner, M. and Schwider, J., "Transferring resist microlenses into silicon by reactive ion etching," *Opt. Eng.* **35** 2979-2982 (1996)

.Elston, R., "FLAMINGOS: A Multi-Object Near-IR Spectrometer," *Proc. SPIE* **3354** 404-413 (1998)

Erdmann, L. and Efferenn, D., "Technique for monolithic fabrication of silicon microlenses with selective rim angles," *Opt. Eng.* **36** 1094-1098 (1997)

Faber, E.M., "The scientific case for a 10-meter telescope", Optical and Infrared telescope for the 1990s, 304-328 (1980)

Fabricant, D. et al., "The FAST spectrograph for the Tillinghast telescope," *PASP* **110** 79-85 (1998)

Felenbok, P., "The original FUEGOS project on the VLT," *Fiber Optics in Astronomy III*, ASP Conference Series, Vol. 152 (1998)

Feldman, A., Horowitz, D., Waxler, R.M., and Dodge, M.J., *Optical Materials Characterization*, National Bureau of Stands Technical Note 993,U.S. (1979)

Forbes, G.W., "Chromatic Coordinates in Aberration Theory," *J.Opt.Soc.Am.* **A 1**,344 (1984)

Frank, L. and Leno, S., Introduction to optics, Prentic-Hall Internation, Inc (1996)

Gambling, W.A., Payne, D.N., and Matsumura, H., *Appl. Opt.* **14** 1538 (1975)

Garth, D.I., et al., DEIMOS: A Wide-Field, Faint-Object Spectrograph for the Keck II Telescope, Preliminary design review, (1994)

Gelles, R., Unobscured-aperture two-mirror systems, *J. Opt. Soc. Am.* **65** 1141-1143 (1975).

Gloge, D., *Bell Syst Tech. J.*, **51** 1767 (1972)

Guérin, J., "AOIFU: AOB OSIS Infrared Fiber Unit," Fiber Optics in Astronomy III, *ASP Conference Series*, **152** 282-288 (1998)

Handbook of Optics Vol. II,McGraw-Hill, Inc (1995)

Hall, D.N.B. et al., “A 1.4 meter Fourier transform spectrometer for astronomical observations,” *Proc. SPIE* **172** (1979)

Hailash, C.S. et al., “A high resolution pressure scanned photoelectric Fabry-Perot spectrometer for velocity field studies of extended objects,” *Proc. SPIE* **445** 33-36 (1983)

Haselbeck, S., Schreiber, H, Schwider, J and Streibl, N, “Microlens fabricated by melting photoresist,” *Opt. Eng.* **6** 1322-1324 (1993)

Haynes, R. et al., “Charaterisation of cooled infrared fibres for the Gemini IRMOS,” *Proc. SPIE* **4008** (2000)

Haynes, R., Content, R., et al., “SMIRFS: Multiobject and integral field near-IR spectroscopy,” *Proc. SPIE* **3354** (1998).

Haynes, R., Content, R., Allington-Smith, J. and Lee, D., “Teifu: a thousand element integral field unit for the WHT,” *Proc. SPIE* **3355** (1998)

Haynes, R. and Allington-Smith, J., “SMIREF-Π: Multi-Object and Integral-Field Unit Spectroscopy at the UKIRT,” Fiber Optics in Astronomy III, *ASP Conference Series*, **152** 289-299(1998)

Heacox, W.D., “On the application of optical-fiber image scramblers to astronomical spectroscopy,” *Astron. J.* **92** 219-229 (1986)

Heacox, W., in Optical and Infrared Telescopes of the 1990s, 702 (1980).

Hecht, E., Optics, Eugene Hecht, 3rd ed. 258 (1998).

Herbst, T.M., “A micropupil-based near-infrared imaging spectrograph,” *Proc. SPIE* **3354** 720-728 (1998).

Herpe, G. et al., “The ARGUS mode of the ALBIREO spectrograph: Evaluation of its performance and first result,” Fiber optics in Astronomy III Vol. **152** 213-219 (1998)

Herzberger, M. and Salzberg, C.D., "Refractive indices of infrared optical material and color correction of infrared lenses ," *J. Opt .Soc .Am.* **52**,420 (1962)

Hill, J.M. and Angel, J.R.P., "Optical matching for fiber optic spectroscopy," *Proc. Of SPIE* **445** 85-92 (1983)

Hill, J.M. et al., *Astrophys. J.* **242**, L69 (1980)

Hill, J.M. et al., *SPIE Proc.* **331** 279 (1982)

Hubbard, E.N. et al., *Astrophysical Journal* **229** 1074 (1979)

Hutley, M. C. et al, "The testing of microlens array," *IOP short meeting in Microlens array* (1991)

Jacobs, Eddie L. and Edwards Timothy C., "Sampling criteria for sensor simulation," *Opt. Eng.* **38** 825-835 (1999)

Jacquinot, P., *J. Opt. Soc. Am,* **44** 761 (1954)

Jaramillo-Núñez, A. et al, "Apparatus for cementing doublet lenses," *Opt. Eng.* **35** 3432-3436 (1996)

Jay, T. R., Stern, M. B. and Knowlden, R. E., "Effect of refractive microlens array fabrication parameters on optical quality," *Proc. SPIE* **1751** 236-245 (1990)

Jay, T.R. et al., "Preshaping photoresist for refractive microlens fabrication," *Optical Engineering* **33** 3552-3555 (1994)

Joyce, R.R. et al., "Astronomical longslit spectrograph utilizing a 256x256 InSb focal plane array," *SPIE Proc.* **2198** 725-735 (1994)

Joyce, R.R. et al, Infrared astronomical spectroscopy with a non-cryogenic spectrograph, *Proc. SPIE* **3354** 741-749 (1998)

Kells,W., et al., COSMIC: A multiobject spectrograph and direct imaging camera for the 5 meter Hale Telescope prime focus, *PASP*, **110**, 1487-1498 (1998)

Kenworthy, M.A. et al., "COHSI: a lens array and fiber feed for the near infrared," *Fiber Optics in Astronomy III*, 300-305 (1998)

Kenworthy, M. A. and Parry, I. R. "SPIRAL phase A: A prototype integral field spectrograph for the Ango-Autralian Telescope," *PASP* **113** 215-226 (2001).

Khlebnikov, F. P. and Salbut, V. L., "Centring of lenses in optical systems," *Sov. J. Opt. Technol.* **55** 681-685 (1989).

Kingslake, R., *Lens Design Fundamentals*, Academic press, pp 81-85 (1978)

Koepf, G. and Markey, B.J., "Fabraction and characterization of a 2-D fibre array," *Applied Optics* **23** 3515-3517 (1984)

Kogelnik,H., "Coupled wave theory for thick hologram gratings," *The Bell System Technical Journal* **48** 2909-2946 (1969)

Kraft, Robert P., "A workshop on high-resolution spectroscopy with very large telescope: Introduction to the summarizing reports," *PASP* **107** 981-982 (1995)

Kurata, K., et al., "An optical fibre connector of physical contact using a glass capillary," 19-22, FOC/LAN' 87 Proceedings (1987)

Kutz M, ed. Mechanical engineerings' handbook. John Wiley & Sons, Inc. (1998)

Kyogoku, T. et al, "Ion beam assisted deposition of a thin film coating on a gradient-index lens array," *Appl. Opt.* **29** 4071-4076 (1990)

Lacy, W.A., Fibre optics, Prentice-Hall, INC. (1982)

Le Fevre, O. et al., "CFHT MOS/SIS spectrograph performance," *A&A* **282** 325-340 (1994)

Lee, D., PhD thesis, "New Techniques in astronomical spectroscopy for 8-M telescopes" (1998)

Lee, D. and Taylor, K., "Fibre developments at the Anglo-Australian Observatory for SPIRAL and AUSTRALIS," *Proc. SPIE* **4008** 268 – 276 (2000).

Lenzen, R. et al, "Omega Case: A new multi-mode NIR-imager/Spectrometer for the Calar Alto Observatory," *Proc. SPIE* **3354**, 493-499 (1998)

Lessing, N.v.d.W., "Selection of Optical Glasses in Apochromats," *J. Opt. Soc. Am.***47**,955 (1957)

Lessing, N.v.d.W., "Further Consideration on the Selection of optical Glasses in Apochromats," *J. Opt .Soc. Am.* **48**,269 (1958)

Lessing, N.v.d.W., "Selection of Optical Glasses in Superachromats," *Appl. Opt.* **9**, 1955 (1970)

Lund, G. and Enard, D., "Multiple object spectrograph at the 3.6 M telescope using OPTOPUS," *SPIE Proc.* **445** 70-76 (1983)

Mahajan, V. N.,Can. J. Phys. **57** 1426 (1979)

Mahajan, V. N., "Aberrated point-spread function for rotationally symmetric aberrations," *Appl. Opt.* **22** 3035-3041 (1983)

Maihara, T., Ohta, K., Tamura, N., Ohtani, H., Akiyama, M., Noumaru, J., Kaifu, N., Karoji, H., Iye, M., Dalton, G. B., Parry, I.R., Robertson, D., Sharples, R., Ren, D., Allington-Smith, J., Taylor, K., and Gillingham, P., "Fiber-Multi-Object Spectrograph (FMOS) for Subara Telescope," *SPIE Proc.* **4008** 1111-1118 (2000)

Maillard, J.P. and Michel, G., "A high resolution fourier transform spectrometer for the Cassegrain focus at the CFH telescope," Instrumentation for astronomy with large optical telescope, Humphries,C.M. editor, 213-222 (1982)

Malacara, D. (Editor), Optical shop testing, John Wiley & Sons, Inc. (1978)

Materials Characterization, National Bureau of Stands Technical Note 993,U.S. (1979)

Martin, P. J. et al, "Ion-beam-assisted deposition of thin films," *Appl. Opt.* **22** 178-184 (1983)

Mattsson, L., Introduction to surface roughness and scattering. Optical society of America (1989)

McGregor, Peter J. et al., "Near-infrared Integral-Field Spectrograph (NIFS): An Instrument Proposed for Gemini," *Publ. Astron. Soc. Aust.*, **16** 273-287 (1999),

Mclean I., Electronic imaging in astronomy. John Wiley & Sons Ltd (1997)

MEMs Optical catalogue (2000)

Mercado, R.I. and Robb, P.N., "Design of Thick Doublets Corrected at Four and Five wavelengths," *J .Opt. Soc. Am.***71**,1639 (1981)

Mersereau, K. et al, "Fabrication and mearurement of fused silica microlens arrays," *Proc. SPIE,* **1751**, 229-233 (1992)

Michael, T. Gale, et al, "Active alignment of replicated microlens array on a charge-coupled device imager," *Opt. Eng.* **36** 1510-1517 (1997)

Miller, C.M., "A fibre-optic-cable connector," *Bell Syst. Tech. J.* **54** 1547-1555 (1975)

Miyazawa, T. et al., "Aberration improvement of Selfoc lenses," *App. Opt.* **19** 1113 – 1116 (1980).

Moas, Mary L., Mathematical method in the physical sciences, John Wiley & Sons, Inc., pp 467-469 (1983).

Moorwood, A.F.M. and Delabre, B., "Infrared spectrometer/imager for the ESO VLT," *Proc. SPIE* **1235** (1990)

Motamedi, M. E., et al, "Micro-optic integration with focal plane arrays," *Opt. Eng.* **36** 1374-1381 (1997)

Multilayer Specification Sheet, Siltint Coating Catalogue (2000)

Murphy, T.W. et al., "A Cryogenic Integral Field Spectrograph for Palomer 200 Inch Telescope," *PASP* **111** 1176-1184 (1999)

Nicia, A., "Lens coupling in fiber-optics devices: efficiency limits," *App. Opt.* **20** 3136-3145 (1981)

Nussbaum, P. et al, "Design, fabrication and test of microlens array for sensors and microsystems," *Pure Appl. Opt.* **6,** 617-636, 1997

Oke, J.B. et al., "The Keck Low-Resolution Imaging Spectrometer," *PASP* **107** 375-385 (1995)

Oliva, E. and Gennari, S., "Achromatic lens systems for near infrared instrument," *Astro. Astrophys. Suppl. Ser.* **114**. 179 (1995)

Owen et al., "New spectroscopic instrument based on volume holographic optical elements," *Proc. SPIE* **2406** (1995)

Paek, U. C. and Weaver, A. L., "Formation of a spherical lens at optical fibre ends with CO_2 laser," *Appl. Opt.* **14** 294-298 (1990)

Palais, J.C, "Fibre coupling using gradient-index rod lenses," *App. Opt.* **19** 2011-2018 (1980)

Parry, I.R. et al. "CIRPASS: a NIR integral field and multi-object spectrograph," *Proc. SPIE* **4008** (2000)

Parry, IR, Kenworthy, M. and Taylor, K., "SPIRAL phase A: A prototype integral field spectrograph for the AAT," *Proc. SPIE* **2871** (1997)

Parry, IR, "Autofib-2 – a Robotic Multifibre Positioner for the WHT," *Proc. SPIE* **2198** (1994)

Parry, IR, "The astronomical uses of optical fibres," Fiber optics in Astronomy III Vol. **152** 3-13 (1998)

Parry, IR, “Some new techniques for faint object spectroscopy in astronomy,” PhD thesis, University of Durham (1986).

Parry, IR and Gray, PM, “An automated multiobject fibre optics coupler for the AAT,” *Proc. SPIE* 627 118-124 (1986)

Persson, S.E. and West,S.C., “A near-infrared camera for Las Campanas observatory,” *PASP.* **104**,204 (1992)

Philip, J. P., “Stray Light Control: An Integral Part of Optical Design,” *Proc. SPIE* **399** 50-58 (1983).

Pierce, A.K., “Construction of a Bowen image slicer,” *PASP* 77 216-217 (1965)

Pilachowski et al., “High-resolution spectrographs for large telescopes, *PASP* **107** 983-989 (1995)

Pogge, R.W. et al, “The MDM/Ohio State/ALADDIN Infrared Camera (MOSAIC),” *Proc. SPIE* **3354** 414-418 (1998)

Popivic, Z. D., Sprague, R. A. and Neville-Connell, G. A., “Techniques for monolithic fabrication of microlens arrays,” *Appl. Opt.* **27** 1281 (1988)

Prieto, E. et al, “A Wide-Field Integral-Spectroscopy Unit for the VLT-VIRMOS,” Fiber optics in Astronomy III Vol. **152** 229-2234 (1998)

Prieto, E. et al., “Very wide integral field unit of VIRMOS for the VLT: design and performances,” *Proc. SPIE* **4008** (2000)

Proudley, G. M., et al. “Fabrication of two-dimensional fiber optic arrays for an optical crossbar switch,” *Optical Engineering* **33** 627-635 (1994)

Rabarot, M. et al. “Fibre coupling of microchip laser with silica microlenses,” *Pure Appl. Opt.* 6 699-705 (1997)

Ren, D., Allington-Smith, J.R. and Rauscher B.J., "Compact all-reflective near-infrared spectrograph and imager," *Proc. SPIE* **3122** 280-286 (1997a)

Ren, D., "All-reflective Infrared camera", *Infrared Technology*, **No.2** (1997b)

Ren, D. and Allington-Smith, J.R., "Apochromatic lenses for near-infrared astronomical instruments," *Opt. Eng.* **38** 537-542 (1999).

Ren, D., Private communication with Laser Components (UK) LTD, September. (1999)

Ren,D. "The measurement of MEMs microlens array," internal report, Astronomical research group, University of Durham (2000a)

Rhorer, R. L. and Evans, C. J., "Chapter 41: Fabrication of optics by diamond turning," in Handbook of Optics I, McGraw-Hill, Inc. (1995)

Ridgway, S.H. and Brault, J.W., "Astronomical Fourier transform spectroscopy revisited," *A. Rev. Astron. Astrophys.*, **22** (1984)

Robb, P. N. and Mercado, R.I., "Glass Selection for Hyperachromatic Triplets," *J. Opt. Soc. Am* **73**, 1882 (1983)

Robb, P.N., and Mercado, R.I., "Calculation of Refractive Indices Using Buchdahl's Chromatic Coordinate," *Appl. Opt.* **22**,1198 (1983)

Robb, P.N., "Selection of Optical Glasses. 1: Two materials," *Appl. Opt.* **24**. 1864 (1985)

Robertson, J.G., "Optimal extraction of single-object spectra from observations with two-dimensional detectors," *PASP* **98** 1220-1231 (1986).

Rodgers, J.M. and McCarthy, J.K., Design of a high speed UV-transmitting camera for the Keck LRIS, *Proc. SPIE*, **2198**, 1096-1103 (1994)

Roth, M. M., et al, "PMAS DEsign and Integration," *Proc. SPIE* **4008** 277- 288 (2000)

Sakamoto, T, "Coupling loss analysis on a multimode fibre directional coupling using GRIN-rod lenses," *App. Opt.* **25** 2620-2625 (1986)

Sands, P.J., "Inhomogeneous Lenses, Chromatic Aberrations," *J.Opt. Soc.Am* **61**, 777 (1971)

Sammueller, R., "Silicon multi-fibre connector and multi-fibre splicing – two possibilities for quick and simple connection of a large number of fibres," *Proc. SPIE* ***468*** 19-28 (1984)

Sasian, J.M. et al., "Fabrication of fibre bundle arrays for free-space photo switching systems," *Optical Engineering* **33** 2979-2985 (1994)

Sasian, J.M. and Descour, M.R., "Power distribution and symmetry in lens systems," *Opt. Eng.* **37**,1001-004 (1998)

Schott Spec Sheet (1991)

Schroeder, D. J., Astronomical optics, Academic Press, Inc. (1987).

Severi, M. and Mottier, P., "Etching selectivity control during resist pattern transfer into silica for the fabrication of microlenses with reduced spherical aberration," *Opt. Eng.* **38** 146-150 (1990)

Shannon, R.R., "Spectral plots for optical glass selection," *Opt. Eng.* **35**,2995 (1996)

Sigler, R.D., "Glass selection for airspaced apochromats suing the Buchdahl dispersion equation," *Appl. Opt.* **23**, 4311 (1986)

Simmons,D.A. et al., "CFHT's imaging fourier transform spectrometer," In Ardeberg,A.L., editor, Optical telescopes of today and tomorrow, volume **2198** 185-193 (1997)

Stephens, R.E., "Selection of Glasses for Three-Colour Achromats," *J. Opt. Soc. Am.***49**.398 (1959)

Stephens, R.E., "Four-Colour Achromats and Superachromatas," *J. Opt. Soc. Am.***50**.1016 (1960)

Stern, M. B. and Jay, T. R., "Dry etching for coherent refractive microlens arrays," *Opt. Eng.* **33** 3547-3551 (1994)

Sugai, H., et al., "The Kyoto Tridimensional Spectrograph II: Progress," *Proc. SPIE* **4008** 558 - 567 (2000)

Sutton,L.E. and Stavroudis, O.N., "Fitting refractive index data by least squares," *J. Opt. Soc. Am* **51**, 901-905 (1961)

Szostak, T., "High performance injection molded ST compatible connector for L.A.N. application," 15-18, FOC/LAN' 87 Proceedings (1987)

Taylor, K., "AUSTRALIS: a multi-fiber near-IR spectrograph for the VLT," *Fiber Optics in Astronomy III*, 261-270 (1998)

Taylor, K., "The low dispersion survey spectrograph," in Modern Technology and its influence on astronomy, Cambridge University Press (1989)

Tecza, M. and Thatte, N., "SINFONI: a high-resolution near-infrared imaging spectrometer for VLT," Fiber Optics in Astronomy III, *ASP Conference Series*, **152** 271-281(1998)

Tomlinson, W. J., "Applications of GRIN-rod lenses in optical fibre communication systems," *Appl. Opt.* **19** 1127-1138 (1980)

Torr, D. G. et al., "Ultraviolet imager for the international Solar Terrestrial Physics Mission," *Opt. Eng.* **32** 3060-3068 (1993)

Tsai, R. et al, "Properties of optical thin films and coatings prepared by reactive electron-beam deposition with and without ion bombardments," *Opt. Eng.* **36** 3433-3438 (1997)

Vanderriest, C., *PASP* **92** 858-862 (1980)

Vanderriest, C., "Integral-field spectroscopy with optical fibre on medium-size (1.5-4-m) telescope," Fiber optics in Astronomy III, ASP Conference Series, Vol. **152** 123-134 (1998)

Vogt, S. S., et al., *Proc. SPIE* **2198** 223 (1994)

Wade, R., "A 1-5 microns cooled grating array spectrometer and Fabry Perot system for UKIRT," *Prco. SPIE* **445** 47-50 (1983)

Wakaki, M., Komachi, Y. and Kanai, G., "Microlens and microlens arrays formed on a glass plate by use of a CO_2 laser," Appl. Opt. **37**, 627-631 (1998)

Warren, D.W. and Rudy, R.J., "Refractive optical system for astronomical instruments using infrared array in the 0.8 to 2.5 micron bands," *Infrared Astronomy with Arrays,* 305-306 (1994)

Weitzel, L. et al., "3D: The next generation near-infrared imaging spectrometer," *Astron. Astrophys. Suppl. Ser.* **119** 531-546 (1996)

Willner, S.P., "A four lens camera design," *Infrared Astronomy with Arrays*, 307-308 (1994)

Wright, Gillian S. et al., "GIRMOS-an infrared multi-object spectrograph for Gemini," *Proc. SPIE* **4008** (2000)

Wynne, C. G., "Two-Mirror Anastigmats," *J. Opt. Soc. Am.* **59** 572-578 (1969).

Wyse, R.F.G. and Gilmore, G., "Sky subtraction with fibres," *Mon., Not. R. A. S.* **257** 1-10 (1992)

ZEMAX Optical Design Program, User's Guide, Version 7.0 (1998)

Zhu, Y. and Xu, W., "Low Resolution Spectrograph for LAMOST telescope," *Proc. SPIE* **4008** 141-147 (Zhu, Y. and Xu, W., 2000)